Theoretical Studies on Materials for Hydrogen Energy Applications

By

Brindaban Modak

(CHEM01201004003)

BHABHA ATOMIC RESEARCH CENTRE, MUMBAI

A thesis submitted to the

Board of Studies in Chemical Sciences

In partial fulfillment of requirements

for the Degree of

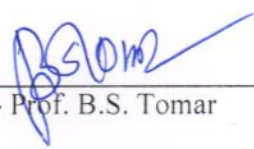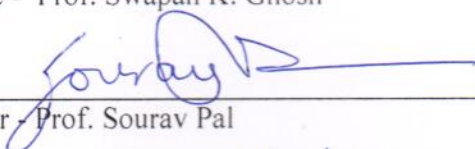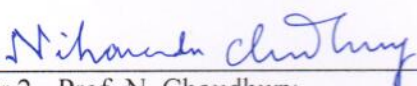DOCTOR OF PHILOSOPHY

of

HOMI BHABHA NATIONAL INSTITUTE

September, 2016

Homi Bhabha National Institute

Recommendations of the Viva Voce Committee

As members of the Viva Voce Committee, we certify that we have read the dissertation prepared by **Brindaban Modak** entitled "**Theoretical Studies on Materials for Hydrogen Energy Applications**" and recommend that it may be accepted as fulfilling the thesis requirement for the award of Degree of Doctor of Philosophy.

Chairman - Prof. Alok Samanta   Date: 28/09/2016

Guide / Convener - Prof. B.S. Tomar   Date: 28.9.2016

Co-guide - Prof. Swapan K. Ghosh   Date: 28.09.2016

Examiner - Prof. Sourav Pal   Date: 28.09.2016

Member 1- Prof. T. K. Ghanty   Date: 28.9.2016

Member 2- Prof. N. Choudhury   Date: 28/09/2016

Final approval and acceptance of this thesis is contingent upon the candidate's submission of the final copies of the thesis to HBNI.
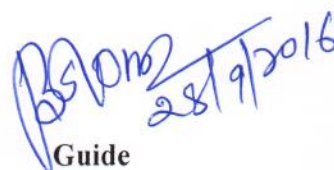
We hereby certify that we have read this thesis prepared under our direction and recommend that it may be accepted as fulfilling the thesis requirement.

Date: 28-09-2016

Place: Mumbai

Co-guide

Guide

STATEMENT BY AUTHOR

This dissertation has been submitted in partial fulfillment of requirements for an advanced degree at Homi Bhabha National Institute (HBNI) and is deposited in the Library to be made available to borrowers under rules of the HBNI.

Brief quotations from this dissertation are allowable without special permission, provided that accurate acknowledgement of source is made. Requests for permission for extended quotation from or reproduction of this manuscript in whole or in part may be granted by the Competent Authority of HBNI when in his or her judgment the proposed use of the material is in the interests of scholarship. In all other instances, however, permission must be obtained from the author.

Brindaban Modak

Brindaban Modak

DECLARATION

I, hereby declare that the investigation presented in the thesis has been carried out by me. The work is original and has not been submitted earlier as a whole or in part for a degree / diploma at this or any other Institution / University.

Brindaban Modak

List of Publications arising from the thesis

(A) Journals

(1) Photocatalytic Activity of NaTaO$_3$ Doped with N, Mo, and (N,Mo): A Hybrid Density Functional Study.

Brindaban Modak, K. Srinivasu and Swapan K. Ghosh

J. Phys. Chem. C **2014**, *118*, 10711−10719.

(2) Band Gap Engineering of NaTaO$_3$ by Density Functional Theory: A Charge Compensated Codoping Strategy.

Brindaban Modak, K. Srinivasu and Swapan K. Ghosh

Phys. Chem. Chem. Phys. **2014**, *16*, 17116−17124.

(3) A Hybrid DFT Based Investigation of the Photocatalytic Activity of Cation−Anion Codoped SrTiO$_3$ for Water Splitting under Visible Light.

Brindaban Modak, K. Srinivasu and Swapan K. Ghosh

Phys. Chem. Chem. Phys. **2014**, *16*, 24527-24535.

(4) Improving Photocatalytic Properties of SrTiO$_3$ through (Sb, N) Codoping: A Hybrid Density Functional Study.

Brindaban Modak, K. Srinivasu and Swapan K. Ghosh

RSC Adv. **2014**, *4*, 45703–45709.

(5) Improvement of Photocatalytic Activity of NaTaO$_3$ under Visible Light by N and F Doping.

Brindaban Modak, and Swapan K. Ghosh

Chem. Phys. Lett. **2014**, *613*, 54–58.

(6) Role of F in Improving the Photocatalytic Activity of Rh-Doped SrTiO$_3$.

Brindaban Modak, and Swapan K. Ghosh

J. Phys. Chem. C **2015**, *119*, 7215−7224.

(7) Origin of Enhanced Visible Light Driven Water Splitting by (Rh, Sb)-SrTiO$_3$.

Brindaban Modak, and Swapan K. Ghosh

Phys. Chem. Chem. Phys. **2015**, *17*, 15274-15283.

(8) Exploring The Role of La Codoping beyond Charge Compensation for Enhanced Hydrogen Evolution by Rh-SrTiO$_3$.

Brindaban Modak, and Swapan K. Ghosh

 J. Phys. Chem. B **2015,** *119,* 11089−11098.

(9) Enhancement of Visible Light Photocatalytic Activity of SrTiO$_3$: A Hybrid Density Functional Study.

Brindaban Modak, and Swapan K. Ghosh

 J. Phys. Chem. C **2015***, 119,* 23503−23514*.

(10) Improving Visible Light Photocatalytic Activity of KNbO$_3$ by using (N, W) as an Efficient Dopant Pair

Brindaban Modak, and Swapan K. Ghosh

RSC Adv. **2016**, 6, 9958–9966.

(11) An Efficient Strategy for Controlled Band Gap Engineering of KTaO$_3$

Brindaban Modak, and Swapan K. Ghosh

J. Phys. Chem. C **2016,** *120,* 6920−6929.

(12) Improving The Photocatalytic Activity of S-Triazine Based Graphitic Carbon Nitride through Metal Decoration: An ab Initio Investigation.

K. Srinivasu, **Brindaban Modak**, and Swapan K. Ghosh

Phys. Chem. Chem. Phys. **2016**,*18*, 26466-26474.

(13) Improving Visible Light Photocatalytic Activity of NaNbO$_3$: A DFT based Investigation

Brindaban Modak, Pampa Modak and Swapan K. Ghosh

RSC Adv. 2016, 6, 90188–90196.

(14) Improving Visible Light Photocatalytic Activity of $KTaO_3$ using Cation-Anion Dopant Pair.

Brindaban Modak, and Swapan K. Ghosh

Sol. Energy Mater Sol. Cells **2016**, (Accepted).

(15) Exploring Metal Decorated Porphyrin-like Porous Fullerene as Catalyst for Oxygen Reduction Reaction: A DFT Study

Brindaban Modak, K. Srinivasu, and Swapan K. Ghosh

Int. J. Hydrogen Energy (Under Review)

(B) Conferences

1. Improvement of Photocatalytic Activity of $NaTaO_3$ under Visible Light by Codoping with Mo, N: A Hybrid Density Functional Theory.

Brindaban Modak, K. Srinivasu, and Swapan K. Ghosh

Current Trends in Theoretical Chemistry, BARC (CTTC-2013).

2. Hybrid Density Functional Study on (Sb, N) codoped $SrTiO_3$ with Improved Photocatalytic Property.

Brindaban Modak, K. Srinivasu, and Swapan K. Ghosh

Trombay Symposium on Radiation & Photochemistry, (TSRP-2014), BARC

3. A Hybrid DFT Based Investigation of Tuning Band Gap: Compensated Vs Non-Compensated Codoping.

Brindaban Modak, K. Srinivasu and Swapan K. Ghosh

Proceedings of DAE-BRNS 5th Interdisciplinary Symposium on Materials Chemistry (ISMC-2014), BARC,

[Best Poster Presentation Award (Second Prize)]

4. Improvement of Photocatalytic activity of NaTaO$_3$ by codoping with Nitrogen and Halogen.

Brindaban Modak, and Swapan K. Ghosh.

Proceedings of DAE-BRNS Symposium on Multiscale Modeling of Materials and Devices (MMMD-2014), BARC, Page-97.

[Best Poster Presentation Award]

5. (Mo, N) Doping for Enhanced Photoelectrochemical Water Splitting of SrTiO$_3$.

Brindaban Modak, K. Srinivasu and Swapan K. Ghosh

Theoretical Chemistry Symposium (TCS-2014), CSIR-NCL, Pune

Brindaban Modak

Brindaban Modak

Dedicated

To My Beloved

Parents & Wife

ACKNOWLEDGEMENTS

Debobrata Da, Bablu Kaka, Hirakendu, and all others for their numerous help, support and wishes. I am very much lucky to get a caring and cooperative friend like *Swagata,* who offered me unconditional support from my college life. I also thank all the well wishers from my native place (*Lakshmipur*) for their blessings and inspiration.

Last but not the least, I would like to thank my family for being a constant source of support. I express my deep sense of gratitude and indebtedness to my parents (**Mr. Mahadev Modak,** and **Smt. Annapurna Modak**) for their love, inspiration, encouragement, blessings and support that helped me to achieve what I am today. I owe my heartfelt gratitude and indebtedness to my Wife **Pampa** for her love, caring, support, inspiration and good wishes to make my journey smoother. I gratefully acknowledge the sincere encouragement received from my elder brother **Sagar Modak,** who inspired me to choose chemistry in my academic carrier. I would like to thank all my relatives for their blessings and encouragement. Finally, I would like to thank the **God,** the **Almighty** for His blessings which helped me in fulfilling my desire in every aspect of my life.

....Brindaban

CONTENTS

SYNOPSIS

Development of alternate energy sources have become one of the major areas of interests due to limitation of long term availability of fossil fuels as well as environmental issues. There has been a growing interest on hydrogen energy as a renewable source. During past few decades extensive research activities including both experimental and theoretical are going on to make hydrogen energy realizable. However, there are few challenges for the so called hydrogen economy viz., designing efficient strategy for the generation of hydrogen, developing cost effective, durable, safe, and environment friendly storage system, and finally designing infrastructure for application of hydrogen. One of the most promising ways to produce hydrogen is the photocatalytic water splitting using solar energy.[1-4] However, finding a suitable catalyst which can split water and produce hydrogen under visible light is a major challenge in this field of research. Till now, a wide range of photocatalysts have been developed, most of which are oxide based semiconductors, and recently various perovskite type materials have also attracted immense interest due to their potential catalytic property to split water. Among them, $NaTaO_3$, $KTaO_3$, $KNbO_3$, $NaNbO_3$, $SrTiO_3$ have been shown to be an excellent photocatalyst for the generation of hydrogen as well as the degradation of organic pollutants.[5-9] However, their large band gap limits the photoactivity only to the range of UV light, which covers ~5% of the solar spectrum. Hence one of the biggest challenges is to modify its band gap so that it can utilize the visible light of solar spectrum for the photocatalytic applications. The introduction of foreign elements in the crystal lattice to change the band structure is observed to be one of the most promising ways to improve the visible light activity of the wide band gap semiconductor

photocatalysts.[10-12] However, the improvement of photocatalytic efficiency with mono doping is not very much in spite of significant enhancement of the visible light activity. Usually, monodoping involves introduction of localized states in between the conduction and valence bands, thus reducing the photoexcitaion energy. Unfortunately, these localized states can boost the electron hole recombination, thereby diminishing the photocatalytic efficiency. The second aspect, particularly in the case of charge imbalance, is the formation of vacancy, which is an efficient source for charge carrier trapping. Another major concern is the change of alignment of band edges of the doped systems, which may lead to hamper the oxidative or reductive power of the catalyst for the desired process. To overcome these problems, we employ the codoping strategy, which has been found to be very much successful in modifying the band structure of semiconductor photocatalysts.[13-21]

Although Hydrogen offers very high energy density per unit mass, its energy density per unit volume is very less i.e. it requires large volume to store. Hydrogen can be stored as gaseous form in pressure vessels, under several hundreds atmospheric pressure. In liquid form Hydrogen can be stored only at cryogenic temperature. Apart from the energy density both these methods are neither safe nor cost effective. The other approach of storing hydrogen is through chemical absorption in the form of metal hydride. The main disadvantages associated with these materials are their high decomposition temperature and poor recyclability. In the recent times, there have been shown emerging interest toward molecular hydrogen storage through physical adsorption of hydrogen. Due to low binding interaction between H_2 interaction molecule and substrate, this approach usually requires low temperature. The kinetics involved in this approach is quite fast as the adsorption process is almost barrier less. The quantity of absorber H_2 increases with the

increase of surface area of the most materials. This leads to development of various kinds of highly porous materials with high surface area.

There are two different approaches through which hydrogen can be used as a fuel in vehicles, are (i) hydrogen-fuelled internal combustion engines (H_2ICEs) and (ii) fuel cells (FCs). In case of internal combustion engines (ICEs), chemical energy is first converted to mechanical energy, which can then be transformed to electrical energy in the second step. In case of fuel cells the chemical energy is directly converted to electrical energy. The main reaction occurring at the cathode of the fuel cell is the oxygen reduction reaction (ORR), while at the anode there occurs oxidation of hydrogen. The cathodic reaction, the oxygen reduction reaction, is found to be almost 6 times slower in comparison to the anodic oxidation process. This is the rate limiting step in fuel cell. Pt is considered to be the best catalyst reported so far for fuel cell applications. But limited availability and high cost of Pt drives to develop alternate catalyst for this purpose. Numerous studies are going on to find efficient cocatalyst comparable to Pt.

In the present thesis, we have focused on all the three important aspects related the hydrogen economy as mentioned above. Using the density functional based electronic structure calculations, we have designed a perovskite based photocatalyst for the generation of hydrogen via visible light driven water splitting. To develop efficient materials for hydrogen storage, we have investigated different the light metal decorated carbon porous nanostructures which can adsorb molecular hydrogen. Finally, calculations for designing new materials for the efficient oxygen reduction reaction have been carried out. All these discussions are presented in the eight chapters, which are summarized as follows.

Chapter 1: This chapter provides a general introduction on challenges in using fossil fuels in long term, different strategies to harvest solar energy, hydrogen economy, different ways to generate hydrogen, particularly focusing on photocatalytic water splitting under visible light, how to improve the efficiency of the catalyst, storage of hydrogen, and applications of hydrogen as a fuel.

Chapter 2: This chapter provides a brief overview of the computational methodologies that have been used to investigate the systems. All the calculations based on density functional theory (DFT) have been carried out using VASP software. This chapter discusses the essential description of quantum mechanics, including DFT followed by some additional computational methods.

Chapter 3:

This chapter discusses the effect of codoping with different cation-anion pair and anion-anion pair to form charge compensated and noncompensated $NaTaO_3$ aiming to improve its photocatalytic activity under visible light. Among cation-anion pair (Cr, N), (Mo, N), and (W, N) from charge compensated system, while (S, N), (V, N), (Nb, N), (Mn, N) and (Tc, N) form charge non-compensated systems. In case of charge compensated system the calculated band gap follows the order (Cr, N)-codoped $NaTaO_3$ < (Mo, N)-codoped $NaTaO_3$ < (W, N)-codoped $NaTaO_3$. For (Cr, N) codoped $NaTaO_3$ impurity states are found to appear in the mid gap region, due to large difference between the d-orbital energy of Cr and Ta. Hence, codoping with this pair may not be suitable choice for improving photoconversion efficiency. However, for (Mo, N) and (W, N)-codoped $NaTaO_3$, the localized impurity states are completely passivated, and the

impurity states lie just adjacent to the band edges to form a continuum band structure. This ensures improved charge carrier mobility in the codoped system. These features are believed to be effective for longer life time of the photo-generated charge carrier. The narrowing of band gap is quite significant in both the cases to enable $NaTaO_3$ to absorb the visible light. Finally we showed that the positions of the band edges for the (Mo/W, N)-codoped $NaTaO_3$ are appropriate for the overall water splitting. On the other hand, charge non-compensated codoping involving (S, N), (V, N), (Nb, N), (Mn, N) and (Tc, N) leads to narrowing the band gap by a larger extent. In all the cases discrete mid gap states are found to appear in between VB and CB due to incomplete passivation of the individual impurity states. Hence, these dopant pair may be ineffective in overcoming the drawback of monodoping process, and hence may not be suitable for enhancing the photocatalytic property of $NaTaO_3$.

We also propose N, F codopant pair to improve the photoactivity of $NaTaO_3$ under visible light. F can be easily incorporated in place of oxygen lattice site due to size similarity. Codoping with N and F results formation of charge compensated and isoelectronic (with $NaTaO_3$) system, hence the tendency to form unwanted defects will be minimum, which would be beneficial for longer life time of the photogenerated charge carriers. This leads to complete passivation of N-induced unoccupied acceptor states in the band structure and thus improved photo-conversion efficiency is expected. In the (N, F)-codoped $NaTaO_3$, the N 2p states are found to appear just above the VB, resulting into an elevation of the band gap remarkably. This reduces the band gap to a significant extent and shifts the absorption curve by 117 nm towards the visible region as compared to that of the undoped $NaTaO_3$. Both the CBM and VBM for the (N, F)-codoped $NaTaO_3$ are in suitable positions with respect to the water redox levels to satisfy the thermodynamic criterion for overall water splitting.

Chapter 4: In this chapter, we have adopted codoping approach with various dopant pair to improve the photocatalytic behavior of $SrTiO_3$ under visible light. We have shown that codoping with either with pentavalent metal (Sb, V, Nb, and Ta) or hexavalent metal (Mo, W) successfully reduces the band gap without encountering any localized mid gap states, thus ensures enhanced photoconversion efficiency in comparison to that of the monodoped systems. Applicability of these modified $SrTiO_3$ for overall water splitting are checked by aligning their VBM and CBM positions with respect to water redox levels, showing that all satisfying the thermodynamic criteria to evolve both hydrogen and oxygen.

Recently, Rh-doped $SrTiO_3$ has been paid significant attention by several groups due to enhanced visible light activity. However, the photo-conversion efficiency achieved is relatively lower. This is due to the fact that Rh^{+4} state introduces localized acceptor states in between the valence band (VB) and conduction band (CB). On the other hand, in presence of Rh^{+3} state, acceptor states are found to disappear, consequently reducing the rate of charge carrier loss. However, the challenging job is to fix the oxidation state of Rh to +3 as both Rh^{+3} and Rh^{+4} states have been found to be present in the normally prepared Rh-doped $SrTiO_3$ sample. Here, we have investigated the origin of the acceptor states in case of Rh-doped $SrTiO_3$ in details, and the change in electronic structure of Rh-doped $SrTiO_3$ in presence of Sb thus attempting to find out the improvement of the photocatalytic activity. We also investigated the role of La codoping on the microscopic electronic structure of Rh-doped $SrTiO_3$. Finally we predicted that codoping with pentavalent ion, like, V, Nb, and Ta also stabilize the desired oxidation state of Rh, with reduction of band gap by a larger extent. We have also shown that codoping with F is successful for this purpose.

Chapter 5: This chapter describes a systematic investigation to explore the effect of several anionic dopants (individually as well as in combination) on the electronic structure of $KTaO_3$. In all the codoped cases, clear band structure is produced, ensuring good photoconversion efficiency. The present study reveals that the extent of band gap narrowing in case of codoping with N and F is quite significant (almost 1 eV) to improve the visible light activity of $KTaO_3$ effectively. More interestingly, this does not involve any considerable shifting of the conduction band minimum (CBM) in the downward direction. This is very crucial for $KTaO_3$ as its CBM potential is quite close to the hydrogen reduction potential.

This Chapter also discusses the effect of doping with N and W on the geometry and electronic structure of $KNbO_3$. Interestingly, a highly favourable band structure is produced with reduced band gap when both N and W are simultaneously doped into the crystal structure of $KNbO_3$. More importantly, the band edge shifting in presence of both N and W occurs in such a controlled fashion that $KNbO_3$ still remains suitable for overall water splitting.

Chapter 6: This chapter discusses the strategy of improving the photocatalytic activity of s-triazine based graphitic carbon nitride (g-CN), which is a potential photocatalyst for water splitting, through metal decoration. Graphitic carbon nitride of this variety shows band gap of 2.89 eV. Our aim is to reduce the band gap in a controlled way by decorating with different noble metal elements, Pt, Pd, Ag, and Au. We have extended this study, to investigate the electronic structure of graphitic carbon nitride decorated with the cluster (Pt_4, Pd_4, Ag_4, and Au_4). Among them Ag_4-graphitic carbon nitride is shown to be the most promising due to reduced band gap as well as suitable for overall water splitting.

Chapter 7: This chapter explores porus graphitic carbon nitride of the kind g-C_4N_3 functionalized with different metal as a potential material for hydrogen storage. The unique properties are due to the high adsorption energies of these elements over nitrogen triangular holes. The materials have the additional advantage that they are stable against clustering of the metal elements due to higher metal-carbon nitride adsorption energy in comparison to the metal-metal cohesive energy. The adsorption energies of hydrogen molecules on these metals are in the range for efficient hydrogen storage applications. Besides, they are nontoxic and pose no adverse effects on the environmental.

Chapter 8: This Chapter discusses the development of new catalyst for the oxygen reduction reaction (ORR) at fuel cells, which is almost 6 times slower in comparison to the anodic oxidation process, and is considered as the rate limiting step in fuel cell. Pt is considered to be the best catalyst reported so far for fuel cell applications. But limited availability and high cost of Pt drives to develop alternate catalyst for this purpose. Here, we have investigated the catalytic activity of the transition metal (Fe, Co and Ni) decorated porphyrene line fullerene ($C_{24}N_{24}$) for the ORR. Present study reveals that the Fe and Co decorated systems are active whereas the Ni decorated system is almost inert due to poor O_2 binding energy in the later case. A systematic study of the possible ORR paths are carried out on both Fe and Co decorated $C_{24}N_{24}$ system. The changes in free energy for all the steps discussed for both Fe and Co systems. The free energy profiles at different electrode potentials are also plotted to see whether all the reaction steps are downhill or not at zero potential, at higher potentials.

Chapter 9: This chapter provides some concluding remarks based on our study. This also gives some future directions to improve the efficiency of the materials involved in the three different stages of hydrogen economy by a further extent. The present work can be extended to the surface, so that the kinetic of the different steps involved during water splitting can be investigated thoroughly. Besides, heterojunction type materials may be of interest for the photocatalyst for water splitting due to efficient separation of photogenerated charge carriers. In addition, development of efficient cocatalyst is also considered to be one of the potential areas of research in this field.

References

(1) Kudo, A.; Miseki, Y. *Chem. Soc. Rev*. **2009**, *38*, 253–278.

(2) Chen, X.; Shen, S.; Guo, L.; Mao, S. S. *Chem. Rev.* **2010**, *110,* 6503–6570.

(3) Hisatomi, T.; Kubota, J.; Domen, K. *Chem. Soc. Rev*. **2014**, *43*, 7520-7535.

(4) Srinivasu, K.; Modak, B.; Ghosh, S. K. *J. Phys. Chem. C* **2014**, *118*, 26479−26484.

(5) Kato, H.; Kudo, A. *J. Phys. Chem. B*. **2001**, *105,* 4285-4292.

(6) Kato, H.; Asakura, K.; Kudo, A. *J. Am. Chem*. Soc. **2003**, *125*, 3082-3089.

(7) Domen, K.; Kudo, A.; Onishi, T.; Kosugi, N.; Kuroda, K. *J. Phys. Chem*. **1986**, *90*, 292-295.

(8) Zhang, P.; Zhang, J.; Gong, J. *Chem. Soc. Rev.,* **2014**, *43*, 4395.

(9) Li, K.; Handoko, A. D.; Khraisheh, M.; Tang, J. *Nanoscale*, **2014**, *6*, 9767–9773.

(10) Asahi, R.; Morikawa, T.; Ohwaki, T.; Aoki, K.; Taga, Y. *Science* **2001,** 293, 269-271.

(11) Khan, S. U. M.; Al-Shahry, M.; Ingler, W. B. J. *Science* **2002**, *297*, 2243-2245.

(12) Gai, Y.; Li, J.; Li, S.-S.; Xia, J.-B.; Wei, S.-H. *Phys. Rev. Lett.* **2009**, *102*, 036402.

(13) Modak, B.; Srinivasu, K.; Ghosh, S. K. *J. Phys. Chem. C* **2014**, *118,* 10711−10719.

(14) Modak, B.; Srinivasu, K.; Ghosh, S. K. *Phys. Chem. Chem. Phys.* **2014**, *16,* 17116−17124.

(15) Modak, B.; Ghosh, S. K. *Chem. Phys. Lett.* **2014**, *613*, 54–58

(16) Modak, B.; Srinivasu, K.; Ghosh, S. K. *RSC Adv.* **2014**, *4*, 45703–45709.

(17) Modak, B.; Srinivasu, K.; Ghosh, S. K. *Phys. Chem. Chem. Phys.* **2014**, *16*, 24527-24535

(18) Modak, B.; Ghosh, S. K. Exploring *J. Phys. Chem. B* **2015**, *119*, 11089−11098.

(19) Modak, B.; Ghosh, S. K. *J. Phys. Chem. C* **2015**, *119*, 7215−7224.

(20) Modak, B.; Ghosh, S. K. *Phys. Chem. Chem. Phys.* **2015**, *17*, 15274-15283.

(21) Modak, B.; Ghosh, S. K. *J. Phys. Chem. C* **2015**, *119*, 23503−23514.

SrTiO$_3$ with respect to the water redox levels.

to the water redox levels

side view

Chapter 1

Introduction

1.1. Challenges for Long Term Use of Fossil Fuels

Increasing energy demand and impact of global warming on the environment have been of major concern during the past decades.[1] Fossil fuels which are the largest among the energy sources available till date, mainly exist in the form of oil, natural gas and coal. The quantity of total energy obtained from these fuels are restricted by available reservoirs present on the planet. Although, the current reserves have ability to fulfil the global demand, there is serious concern regarding continuation of exploitation of fossil fuels solely because of their adverse effect on environment caused by sustained and increased carbon emissions.[2-4] Among the fossil fuels, consumption of coal releases maximum amount of CO_2 (88.3 kg/gigajoule of energy produced), while natural gas is the lowest CO_2 emitter (50 kg/GJ). It is predicted that at the global level carbon emission rate will increase to 13.5 gigatons of carbon per year by 2050 due to increase in population. The most adverse effect of increase of CO_2 in the atmosphere is the rise in global temperature due to green house effect. If the CO_2 concentration in the atmosphere becomes above 450 ppm, the global temperature will increase by 2° C, which can bring catastrophic changes in the environment, like melting glaciers, ice sheet, major changes in the seasonal event timing, and weather pattern.

To cap carbon emission at current rates and prevent further increase with the increasing demand of global energy consumption, it is proposed that at least 10 TW of energy should be provided by zero carbon emitting sources by 2050. To meet the challenge alternate sources for large scale energy production need to be developed. During the past few decades there has been enormous increase of research activities in the area of alternate source of energy, which is renewable and can deliver energy without sacrificing the environment. These can be achieved by utilizing even only a fraction of solar energy, which is an enormous source of energy.

1.2. Solar Energy

The average rate of sunlight energy reaching earth surface is so high (~120,000 TW), that even a very small fraction of it is enough to fulfil the global demand. However, in the current situation only 1.5% of global energy production is obtained from utilization of solar energy. So far, various technologies have been developed to capture solar light and convert it into usable light. Among them, photovoltaic route is the most popular one. These systems are composed of multiple number of solar cells connected in series to construct a module, which in turn is installed to form an array with many more modules to achieve total power output at the desired level. The photovoltaic cells absorb sunlight and convert it into an electrical current supporting a load. One of the major limiting factors for a solar cell is the lower photon to current conversion efficiency. The high cost for the materials, production and installation of the photovoltaic cells and modules increases the price of the electricity generated using this approach. Solar thermal power provides electricity at relatively lower cost in comparison to photovoltaic system. Here, sunlight is concentrated and focused onto a working fluid to produce thermal energy, which is utilized in steam turbine or heat engine to produce electricity. Another promising technology for solar energy conversion is the production of fuel using sunlight. In this approach, sunlight is captured and converted into chemical energy instead of electrical or thermal energy, as in the case for photovoltaics and solar concentrators, respectively. In this process, solar energy is utilized to split water into hydrogen, which is considered as a promising energy carrier.[5-11] Since, 70% of earth surface is covered with water, it can be used as unlimited source of hydrogen. The advantages[12] of hydrogen for use as a fuel are:

(i) Production of heat or electricity through combustion or electrochemical oxidation of hydrogen produces water as by-product. Therefore, no pollutants or greenhouse gases are emitted, allowing the zero emission vehicles to be practically achievable.

(ii) The chemical energy per mass is the highest for hydrogen among different liquid hydrocarbon fuels.

(iii) Hydrogen can be used directly as a fuel or via fuel cell.

During the past few decades, extensive research activities are going on to make hydrogen energy realizable. However, there are few challenges for the so called hydrogen economy viz., (i) designing efficient strategy for the generation of hydrogen (ii) developing cost effective, durable, safe, and environment friendly storage system. (iii) designing infrastructure for application of hydrogen.

1.3. Hydrogen Generation

There are various ways to generate hydrogen, which include natural resources like water through electrolytic, thermo-chemical, photocatalytic, etc.[13-15]

1.3.1. Water electrolysis with solar electricity

Generation of hydrogen by water electrolysis was first described by W. Nicholsor and A. Carlisle in 1800, just after the discovery of 'Voltaic' pile by Volta.[16, 17] In this case, one mole of water is split into one mole of hydrogen and half mole of oxygen gas as

$$H_2O(l) \xrightarrow{2F} H_2(g) + \frac{1}{2}O_2(g)$$
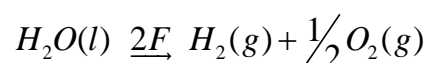
Where F represents the Faraday constant measuring one mole of electricity, 96485 Coulomb. An electrolyser, on application of sufficient (critical) voltage, produces O_2 at the anode and H_2 at the cathode.

Table1.1: Thermodynamic Data for Water, Hydrogen and Oxygen

Thermodynamic Potential	H$_2$O	H$_2$	½ O$_2$	Change
Enthalpy	-285.83 kJ	0	0	ΔH=285.83 kJ
entropy	69.91 JK^{-1}	130.68JK^{-1}	0.5× 205.14 JK^{-1}	TΔS= 48.7 kJ

The work done by the system at temperature 298 K and 1 atmosphere pressure,

W = P Δ V = (101.3 × 10^3 Pa) (1.5 moles) (22.4 × 10^{-3} m^3/mol^{-1}) = 3715 J

The change in internal energy (ΔU) is given by

ΔU = ΔH- PΔV = 285.83 kJ -3.72 kJ = 282.1 kJ

This change in internal energy must be accompanied by expansion of the produced gas, so the change in enthalpy represents the required energy for the electrolysis. The net energy that must be supplied by the external electricity source is given by the change in the Gibbs free energy as,

ΔG = ΔH- TΔS = 285.83 kJ – 48.7 kJ = 237.1 kJ

The rate of hydrogen evolution is limited by the kinetics of the oxygen and hydrogen evolution reaction at the electrodes and is strongly dependent on the chemical activity of the electrode. Metals like Pt, Pd show good performance as electrode material, but they are highly expensive. The major limiting factor for water splitting is the requirement of large overpotential for the evolution of oxygen. To enhance the rate of water electrolysis, an electrolyte is dissolved in water, which increases the water conductivity. Well known water electrolysers are: alkaline water electrolyser (AWE), polymer electrolyte membrane (PEM) water electrolyser, and solid oxide electrolyser. The economy of hydrogen generation through water electrolysis is driven by the cost of electricity and electrolyser. One of the promising solution is to use the photovoltaic (PV) energy to split water into hydrogen and oxygen. The

advantage of this approach is that both the gases can be used in a fuel cell to make electricity even in absence of sunlight. This has been first introduced in the year of 1970. Here, the PV module is directly connected to the electrolyser to generate hydrogen and oxygen. Water splitting using PV electricity is limited to low temperature electrolysers (AWE, and PEM technologies). Although, AWE is quite robust and well established technology, it has the drawback of corrosive nature of the electrolyte liquid. This limitation of AWE and less complex design of PEM drive the application of PEM technology in this field. The shortcomings of this approach are (i) decrease of activity with time, (ii) shutdown of the electrolytic cells leads to dissolution of Ni at the cathode because this electrode is driven towards more positive potential by short-circuit with anode. To overcome these shortcomings, Ni cathode is required to be activated by coating with a thin layer of more active and more stable material. Another interesting approach is to use wind turbine to provide electricity to the electrolyzers for the generation of hydrogen.

1.3.2. Thermochemical Water Splitting

Thermochemical splitting of water to hydrogen and oxygen needs very high temperature. considering thermodynamic restriction sufficient yield of hydrogen and oxygen from direct water splitting can only be attained by raising the temperature above 2500 K.[18, 19] This high temperature imposes restrictions on the choice of materials and design of reactor. During the past few decades, several thermodynamic cycles have been proposed.[20] In spite of some demonstrations at the laboratory scale and pilot scale, industrial scale production is still quite far. Popular schemes include simple oxide (iron, zinc, cerium oxide, etc) based cycle or mixed oxide (ferrite) based cycle between a lower and higher valence state, participating in an oxidation reduction process which generates hydrogen and oxygen in separate steps as

$$MO_{x-1} + H_2O(g) \rightarrow MO_{ox} + H_2(g) \qquad \text{(Exothermic)}$$

$$MO_x \rightarrow MO_{ox-1} + \frac{1}{2}O_2 \qquad \text{(Endothermic)}$$
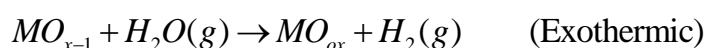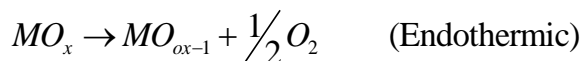
In the first step the activated redox reagent is oxidized by H_2O, which produces H_2. Second step is the catalyst regeneration step. The first step can take place at temperature lower than 700°C. However the second step needs temperature greater than 1600°C. Besides, solar reactors reported so far are based on particles fed into rotating cavity reactors, which are costly and complicated to operate. Hence, large scale production of solar hydrogen needs developing cost effective and efficient technology. This high tempareture can be achieved by using concentrating solar power (CSP) technology, which is therefore a natural choice for solar thermochemical reactor. The CSP technology shows the ability to produce large amount of energy at a small fraction of surface area required for photovoltaics. This consists of collection systems, which uses parabolic reflector (with trough, tower, dish, and more recently Fresnel's planar optical configuration). The expression for the flux concentration ratio (C) over a target area (A) at the focal plane, normalized with respect to the incident normal beam isolation can be written as

C= Q_{Solar}/IA

Higher the value of the concentration ratio, lower is the heat loss, and consequently higher is the attainable temperature at the receiver. First commercial CSP plant with capacity 354 MW was built in the Californian Majave Desert in the year 1980. In this approach the heat is utilized to invest feed water into superheated steam that drives a turbine generator to produce electricity. The steam is cooled by passing through a steam condenser, reverting back to water and the process is repeated. The heat generated can be utilized to generate hydrogen through thermosplitting of water. A typical solar tower may develop temperature ranging from 200 to 1000ºC. Significant concentration of hydrogen was produced, with a conversion of steam up to 30%. This demonstrated that the combination of CSP technology with thermochemical splitting of water will be one of the promising approaches to generate

hydrogen at a reasonable cost without emitting any greenhouse gas, thus making the dream of purely renewable solar hydrogen economy a reality. Further developement of this combined technology is in progress to scale-up the feasibility of solar hydrogen production plant. The advantage of this approach is that it can generate hydrogen and oxygen in separate steps, thus avoiding the separation stepand also possibility of formation of explosive mixtures.
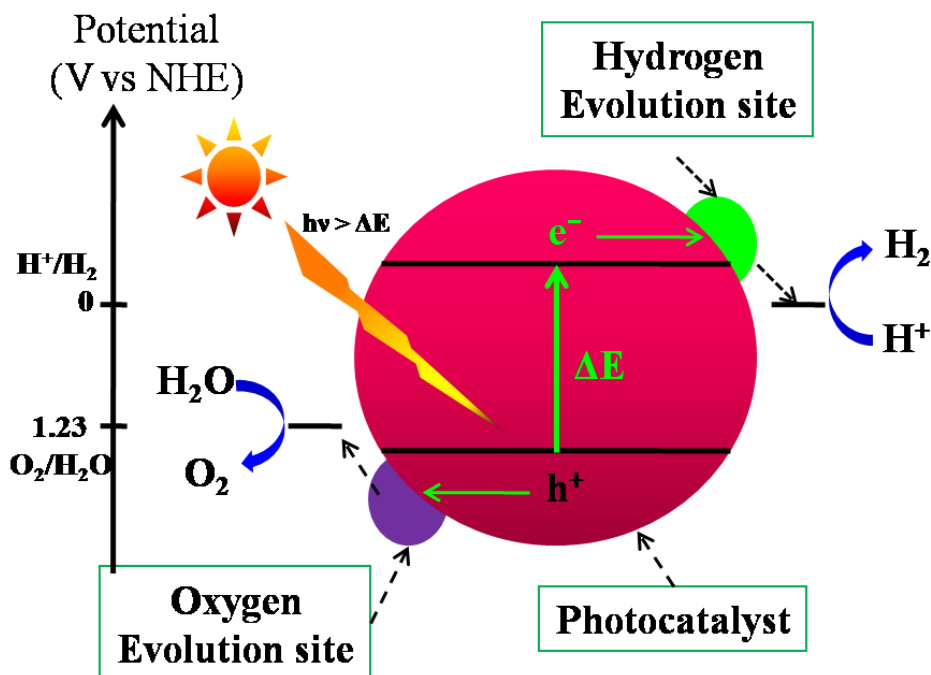
Figure 1.1: Schematics of different processes in Photocatalytic Water Splitting

1.3.3. Photocatalytic Water Splitting

Because of simplicity, water splitting using a photocatalyst is an attractive path for large scale production of hydrogen.[21-23] Therefore, it is considered as an effective solution towards green sustainable energy source. In this approach hydrogen can be readily obtained by dispersing a suitable photocatalyst in a pool of water under the exposer of sunlight. The process can be shown by simple schematics in Figure 1.1. To overcome the difficulties in separating the hydrogen and oxygen produced several strategies have been developed.

The conversion of photon energy into chemical energy in this path is accompanied by a large positive change in the Gibbs free energy. The reaction scheme is very similar to natural photosynthesis because both are uphill reactions. However, photocatalytic degradation processes are generally downhill reactions, also known as photoinduced reactions. Photocatalytic water splitting was first reported in the year 1970 by Honda and Fujishima using TiO_2 electrode.[23] Under the exposer of UV light electron and holes are generated in TiO_2. The photoexcited electron reduces water to generate hydrogen on a platinum electrode and the holes oxidise water to produce oxygen on the TiO_2 electrode with some external bias by power supply. During the past decades, numerous research activities are going on to develop efficient photocatalyst for the splitting of water under direct sunlight.

1.3.3.1. Mechanism of Photocatalytic Water Splitting

There are three main steps involved in the photocatalytic water splitting as has been shown in Figure 1.1.[25-27] In the first step (i) photocatalyst absorbs photon and electron-hole pair is formed. The heterogeneous catalyst developed so far are mostly semiconductor type, which consists of conduction band and valence band separated by a band gap. Incident light with energy higher than ΔE_{gap} is able to generate electron and hole in the conduction band (CB) and valence band (VB), respectively. These photogenerated electron and hole are utilized to split water. There are few important conditions that the material must satisfy to be suitable for water splitting. First and foremost, the bottom of the CB must be more negative than the redox potential of H^+/H_2 (0 V vs NHE), while the top of the VB must be more positive than the redox potential of O_2/H_2O (1.23 V). This implies that the theoretical minimum band gap for a material to be active for overall water splitting is 1.23 eV, which corresponds to the photon wavelength of around 1100 nm. Oxide materials like, TiO_2, $SrTiO_3$, $NaTaO_3$, $KTaO_3$, $NaNbO_3$, $KNbO_3$ have suitable band edge positions.[24] However, all are wide band gap materials. Although CdS has low band gap as well as proper band edge alignment they are

not sufficiently stable under photocatalytic condition. WO_3 has lower band gap but its conduction band minimum (CBM) position is not suitable for hydrogen evaluation. Hence, we can tell that proper band edge alignment is a necessary condition, but not sufficient. To utilize the solar spectrum, the band gap should be less than 3 eV.

The second step (ii) involves charge separation and migration of photogenerated electrons and holes. This step is strongly dependent on the particle size, crystallinity and nature of crystal structure. Better the crystalline quality, lesser is the number of defects, which are efficient centers for charge carrier trapping and recombination. In case of small particle size the migration length of the charge carriers to the reaction center is relatively short, and hence the probability of recombination is reduced.

The final step (iii) consists of surface chemical reaction. This step is mainly controlled by surface active sites and surface area. In absence of active sites for redox reaction the photogenerated electrons and holes recombine with each other. Various cocatalysts, like Pt, NiO and RuO_2 are often loaded to introduce active sites for hydrogen generation. This is essential for many photocatalysts, particularly for which the CBM levels are not too high to reduce H_2O to H_2. On the other hand, O_2 evolution involves four electron oxidation of H_2O. Materials which possess a deep enough valence band maximum (VBM) can oxidise H_2O to O_2 even in absence of any cocatalyst. H_2 and O_2 can recombine to form H_2O. Therefore, surface property for cocatalyst and photocatalyst should be such that the rate of back reaction is reduced. Normally, surface area decreases with the increase of particle size. Again smaller particle size lead to wider band gap due to quantum size effect. So, to obtain good photocatalytic activity one has to compromise some of the factors depending on the type of desired reaction. As for example, for water splitting a high degree of crystallinity is preferred over high surface area because electron-hole recombination process is one of the major limiting factors due to its uphill nature. However, for photocatalytic degradation of organic

pollutants high surface area is more essential because the extent of the absorbed reactant is very much important in this case.

Photocatalysts can also be used for the application in solar cell, phosphors, and dielectric. The major difference is that the photocatalytic processes involve chemical reaction, while others do not. For a successful photocatalyst process, all the three steps should be completed simultaneously. Therefore, the surface and bulk structure and associated electronic structure should be suitable for a good photocatalyst, which is considered to be a highly functional material.

1.3.3.2. Elements Constructing Heterogeneous Photocatalyst

The choice of elements varies depending on the requirements as discussed below.

(i) Most of the oxide, sulphide, and nitride based photocatalysts are composed of metal ions with d^0 and d^{10} configurations. VBM of the metal-oxide materials consists of O 2p orbital, while the CBM are composed of d and sp orbitals. On the other hand, VBM of the metal sulphide and nitride based materials are normally composed of S 3p and N 2p orbitals, respectively.

(ii) Alkali, alkaline earth and lanthanide ions do not directly contribute to the formation of band structure, but plays pivotal role in the construction of the crystal structure (e.g. 'A' site of perovskite compound).

(iii) Various transition metal cations with partially occupied d orbitals (Cr^{+3}, Ni^{+2}, Rh^{+3}, etc) are normally used as dopant. They can reduce the effective band gap by introducing impurity levels.

(iv) Noble metal (Pt, Rh, Au, etc.) and some metal oxide NiO and RuO_2 can act as cocatalyst for hydrogen generation through water splitting, while IrO_2 behaves as an oxygen evolving cocatalyst.

1.3.3.3: Methods for enhancing photocatalytic efficiency:

There are several strategies to improve the photocatalytic activity of a material. Among them the popular methods include; (i) sensitization (ii) morphology modification (iii) thermal annealing (iv) sacrificial reagent (v) loading cocatalyst (vi) utilization of plasmonic nanoparticles (vii) band gap narrowing. A brief description of these approaches is presented in the following sections.

(i) Sensitization: Sensitization of photocatalyst using suitable sensitizer is one of the popular techniques to expand the absorption range, particularly toward visible region to enhance the photoactivities under visible light.[28-31] Organic materials like 8-hydroxy quinoline, magnesium phthalocyanine (MgPc), ethylenediaminetetraacetic acid (EDTA), Eosin-Y, are commonly used for this purpose, since owing to low band gap, they absorb light of longer wave length. Absorption of photon of suitable wave length results into transfer of photo excitation electron to the LUMO of the sensitizer from HOMO, which is then transferred to the CB of the photocatalyst to undergo photocatalytic reaction. This process not only facilitates absorption of light of longer wavelength but also efficient separation of charge carriers.

Various low band gap semiconductors are also used for this purpose. Materials like CuO, CdSe, CdS, are often loaded onto a photocatalyst. They also play similar role as that of the sensitizer dyes. The enhancement of photocatalyst activity is attributed to the increasing quantity of free charge carrier available for the photocatalytic process.

(ii) Morphology modification: The strategy of morphology modification has been widely adopted for the improvement of photocatalytic activity.[32-38] Photocatalyst in the form of nanoparticles, nanorod, mesoporous structure or two-dimensional structure is very commonly used due to several advantages. As for example, nanoparticles are often preferred over the bulk structure. In this case, photo generated e^- and h^+ travel shorter distance to reach the

reaction site, thus minimizing the probability of their recombination. Moreover nanoparticles consist of highly crystalline structure (lower boundary defects) which is favourable to further charge carrier mobility. Nanorods have superior charge transport properties, resulting higher photocatalytic performance. A common feature of these two photocatalysis is that they possess a higher surface to volume ratio in comparison to bulk. This increases the photocatalytic activity by increasing the rate of photo excitation and generation of electron-hole pair, thus enhancing light harvesting capability. Another advantage is the increase in the number of active sites for photo-reaction with increasing the surface to volume ratio. As for example C_3N_4 can generate H_2 through water splitting, have surface area of 10 m^2 g^{-1} in the bulk form, while the surface area significantly increases to 84.2 m^2 g^{-1} then C_3N_4 nanosheet is formed leading to higher photocatalytic performance.

(iii) Thermal treatment: Normally defects (oxygen vacancy, reduced species, grain boundary) in the crystal structure are always associated with synthesis of the materials. These are efficient source for charge carrier trapping followed by their recombination. Thermal annealing is sometimes employed to reduce the defect density.[39-42] Besides, thermal annealing increases the crystalinity of the material, thus facilitating the charge carrier transport. It also enhances bonding or interfacial contact between two different materials, like photocatalyst and co-catalyst, thereby improving the photocatalytic performance.

(iv) Sacrificial reagent: To improve the photocatalytic activity for water splitting sacrificial reagents are often employed, which act as electron donor or hole scavenger.[43-48] The advantage is that the photo generated holes irreversibly oxidize the sacrificial reagent instead of water. Thus, it enriches the electron content in the photocatalyst, thereby improving photo activity. To improve O_2 evolution, one can use various oxidizing agents (electron acceptors or electron scavenger like Ag^+, Fe^{+3}) which can consume photogenerated electron in the CB.

(v) Loading cocatalyst: In order to improve the photocatalytic activity it is quite popular to employ cocatalyst.[49-52] Apart from noble metal (Au, Ag, Pt) various materials including reduced graphene oxide, MoS_2 etc. have been extensively used as cocatalyst. These materials act as electron accepting system due to lower Fermi energy level of these systems in comparison to CBM of the photocatalyst. Therefore photoexcited electron could be transferred to the cocatalyst, thus reducing the probability of electron-hole recombination rate. There also exists hole scavenging cocatalyst, which is often employed to enhance the process at the VBM. Materials like RuO_x, CoO_x are commonly used for this purpose.

(vi) Localised Surface Plasmon Resonance Effect (LSPR):

The LSPR effect arises from loading of certain types of plasmonic metal nanoparticles (Au, Ag, Cu, Pt) on the surface of a photocatalyst.[53-55] Their role is to improve light harvesting efficiency of the material. This approach has been extensively used for expanding the absorption behaviour of wide band gap semiconductor materials like TiO_2, $SrTiO_3$, $NaNbO_3$ etc towards visible region. In this case, the incident light spatially interact with the photocatalyst surface and temporarely confines the electromagnetic waves. To obtain such effects, the electromagnetic effect should be localized in an extremely small area (normally in the range of nanometer) that exceeds the diffraction limit, thus confining the radiation within the space for a certain period of time. Electron-holes are generated in the metal nanoparticles due to photoexcitation. The free electron is then transferred to the CB of the photocatalyst and migrate to the catalyst surface to undergo reaction. In summary, LSPR effect leads to separation of the photogenerated electron-hole pair through the interaction of photon with the plasmonic nanoparticle loaded photocatalyst.

(vii) Z-Scheme:

An alternative approach to one step visible light driven photocatalyst is Z-scheme approach.[56] The approach was inspired by natural photo-synthesis in green plants where the photosystems I and II utilize 700 nm and 680 nm photons, respectively to oxidise H_2O into O_2 under sunlight. The quantum yield for this process is chosen to be unity. In the Z-scheme, two different approaches are combined using a suitable shuttle redox mediator. The advantage of the scheme is that the photocatalyst allows absorption of visible light more efficiently in comparison to that in the one step overall water splitting system due to relaxation of the condition of minimum band gap criterion. Besides a large number of photocatalyst having potentiality to either water oxidation or reduction can be employed in this case.

The process involved in the Z-scheme water splitting can be illustrated by the schematic shown in Figure 2. In case of H_2 evolution system, the forward reactions occurring on the photocatalyst surface are the reduction of proton by conduction band electrons and the oxidation of an electron donor (D) by valence band holes to yield the corresponding electron acceptor (A),

$2H^+ + 2e^- \rightarrow H_2$ (Photo reduction)

$D + nh^+ \rightarrow A$ (Photo-oxidation)
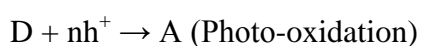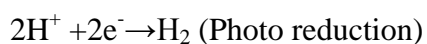
For O_2 evolving photocatalysis the respective reactions are,

$A + ne^- \rightarrow D$ (Photo reduction)

$2H_2O + 4h^+ \rightarrow O_2 + 4H^+$ (Photo-oxidation)
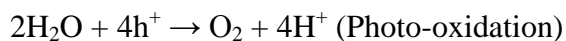
where, electron acceptor generated in the H_2 evolution photocatalytic system is converted to its reduced form (D) and water oxidation occurs by the VB holes. Therefore a cycle of redox pairs (D and A) is established and splitting of H_2O is achieved.

(viii) Band gap engineering:

The mismatch of optical absorption spectra of the photocatalytic semiconductor with the solar spectrum leads to poor solar conversion efficiency. As for example, wide band gap semiconductor shows poor photo conversion efficiency under visible light. Therefore tuning the band gap of wide band gap semiconductor is very much important for efficient utilization of visible light. The common approach widely used for band gap narrowing are (a) defect engineering (b) multicomponent solid solution (c) doping with foreign elements.[57]

(a) Defect Engineering: It is known that high crystallinity is always advantageous for enhancing the activity of photo splitting of water due to good charge carrier mobility and lower recombination of photogenerated charge carriers within the defect free solids. However several reports have demonstrated that an appropriate amount of defects like oxygen vacancies and step edges play important role in improving the transfer of photogenerated charge carriers, thereby increasing the photo activity. Moreover, the optical absorption, electrical conductivity, reducing properties and dissociative absorption of the metal oxide can also be significantly improved by oxygen vacancies. Usually oxygen vacancies can be effectively introduced on the metal oxide surface by thermal treatment under a reducing oxygen depleted atmosphere or vacuum, high energy particles bombardment and doping with metal or non-metal ions. All the oxygen deficient metal oxides including ZnO, TiO_2, WO_3, Fe_2O_3 and $BiVO_4$ showed improved activity for photoelectrochemical oxidation of water, due to enhanced electrical conductivity and separation of photo generated electron-hole pair. O-vacancy rich ultrathin In_2O_3 porous sheet type photoelectrode shows a significantly higher photo current under visible light than the O-vacancy poor and bulk samples due to smaller band gap and better charge carrier separation efficiency. Recently it has been shown that defects in TiO_2 created by a facile low-temperature vacuum process increased the photocatalytic activity for H_2 evolution by four fold. Even self-doped metal cation (Ti^{+3} in

TiO$_2$) is shown to be an effective strategy to enhance the photocatalytic activity of the parent material due to lowering of band gap and introduction of oxygen vacancy.

However, defects can also provide efficient centers for charge carrier recombination, thereby lowering the photo conversion efficiency. The role of defects in photocatalysis is not fully explored so far. There are various aspects related to defects chemistry including density, concentration, ratio of bulk vs surface concentration, stability should be investigated in future studies.

(b) Multicomponent Solid Solutions

Formation of solid solution between wide and narrow band gap semiconductor is an effective strategy to tune the band structure of the photo catalyst. This approach can not only narrow the band gap but also adjust the band edge positions by varying the ratio of the compositions of the semiconductor in the solid solution which will be advantageous for achieving an optical balance between visible light absorption and redox potential.

Till date a large number of solid solution have been developed such as $(Ga_{1-x}Zn_x)(N_{1-x}O_x)$, $BaTaO_2N$-$BaZrO_3$ or $CaTaO_2N$-$CaZrO_3$, ZnS-CdS, Ta_3N_5-$TaON_3$, $AgAl_{1-x}Ga_xO_2$ etc. Among them the most popular one is $(Ga_{1-x}Zn_x)(N_{1-x}O_x)$ developed by Dorver and coworker for photosplitting of water under visible light. Both ZnO and GaN are wide band gap semiconductor, therefore not active for visible light absorption while their solid solution shows significant activity for the photo splitting of water under visible light due to smaller band gap. The formation of GaN-ZnO solid solution has been confirmed by the shift of X-ray diffraction (XRD) peaks and optical absorption edges. In this case, p-d repulsion between N 2p and Zn 3d orbital elevated the VB maximum without affecting the CBM.

Among the sulphide solid solution $Cd_{1-x}Zn_xS$ exhibits high quantum yield for H$_2$ evolution under visible light even in absence of cocatalyst loading. Especially, the earth

abundant and non-toxic elements like Cu, W, Mo, Zn, Fe, Ta, and Ti are most desirable for the construction of multicomponent semiconductor.

However, most of these mixed oxides are prepared through high temperature solid state reaction, resulting into a very low activity and surface area. Therefore, it is prescribed to prepare these mixed oxides with mesoporous structure, high surface area and crystallinity by soft chemistry routes, like hydrothermal method, and polymerizable complex method. Besides, it is so far a great challenge to find a solid solution system with low cost, enhanced activity and sufficient stability under the exposure of visible light irradiation. In a recent study, using the first principle based calculation, Wu et al predicted Ti_3O_3N, $La_2TiO_2N_2$ and Li_5MoO_4N to have potential in the field of visible light driven water splitting which is expected to exhibit better photocatalytic activity than even the best oxinitride photocatalyst known today.

(c) Doping with Foreign Elements

Doping with foreign elements is found to be one of the most efficient strategies to narrow down the band gap of semiconductor photocatalyst.[58-63] There are two ways to reduce the band gap of a semiconductor, either by elevating the VBM or by lowering the CBM energy. Generally VB of metal oxide semiconductor is composed of O 2p orbital while CB is contributed by cation d-orbitals. Therefore, to elevate the VBM one has to choose anionic type dopant with higher p-orbital energy. Similarly, the energy of CBM can be lowered by cationic dopant with lower d-orbital energy than that of the host elements. Usually such foreign elements introduce donor above the VB or acceptor states below the CB, leading to a reduction in the band gap. In addition attempts by introducing impurity states in the forbidden region have also been made in many studies. To achieve good photocatalytic activity, one may set the following condition for the photo catalysts; (i) the VBM should be located below the H_2O/O_2 level while the CBM should be higher than the H^+/H_2 level to ensure spontaneous

photooxidation and photoreduction activities for water splitting respectively and (ii) the impurity states in the gap should be shallow enough or mixed with the band states of the host material, so that photo or thermally excited charge carrier can be transferred easily to the reactive sites of the catalyst within their lifetime. Probability of the electron-hole recombination increases with increase in concentration of the trapping centers that capture an electron in CB or hole in VB, as discussed by Shockless-Read-Hall model. Therefore, if the dopant introduces a localized state far away from the band edge with an energy gap higher than the thermal excitation energy k_BT, the lifetime of the photogenerated charge carrier may become shorter, resulting into poor photocatalytic activities. This requirement often limits the utility of scheme (c) for band gap narrowing in practical scenario, because such midgap states are often localized in space and the photogenerated carriers cannot be utilized for photocatalytic reaction on the surface. However, more detailed consideration follows to provide more insight into the aspect of doping.

Doping of semiconductor photocatalyst can usually be classified in the following categories; anionic monodoping, cationic monodoping, codoping.

Anionic monodoping: The valence band of metal oxide photocatalyst mostly consists of 2p states. Non metal like nitrogen, carbon, phosphorous and sulphur have larger p-orbital energy in comparision to the oxygen p-orbital. Therefore doping of N, C, P or S into the O lattice site elevates the VB edge and thus reduces the effective band gap, resulting into an enhancement of visible light activity. Although they contribute towards enhancing visible light activity of the host material, the underlying mechanism for the same and their optimum concentration, influence on the phase stability of the oxide material, and electron-hole recombination differ by a large extent. The substitutional doping of N is found to be most promising because its p state contributes to the band gap narrowing by mixing with O 2p state. Although, doping with S also reduces the band gap by similar mechanism, it would be energetically difficult to

introduce S at the O lattice site due to larger ionic radius. In case of doping with C and P, the impurity states are deep enough in the gap, and therefore leads to poor photo conversion efficiency in spite of strong visible light activity.

Cationic mono doping: The conduction band of the metal oxide semiconductor is composed of metal 'd' orbitals. Therefore, substitutional doping with transition metal of lower 'd' orbital energy can effectively reduce the band gap. Several studies have been performed with wide range of metal ions, including 3d, 4d, 5d, transition metals. It has been reported that these elements usually introduce additional defect state either below the CBM or above the VBM of the oxide. Therefore, the effective band gap is reduced resulting into an enhancement of the visible light activity. The dopant element should be chosen carefully so that it can lower the CBM by such an extent that the photocatalyst retains its water reducing behavior.

Codoping:

It has been reported in many studies that the most of the monodoping systems show poor photo conversion efficiency in spite of appreciable visible light activity. This is due to the presence of localized state in the forbidden region which can act as recombination centers and thus reduce the photogenerated current. Besides, monodoping often leads to formation of charge compensation vacancy defects, which are known to be efficient charge carrier trapping centers. To overcome this, the strategy of codoping with another element has been adopted widely.[64-73] The codoped systems may be broadly classified as (i) anion-anion, (ii) cation-cation and (iii) cation-anion. Normally the choice of the codopant should be such that it form charge compensated system, thus minimizing the formation of vacancy defects. An efficient codopant pair should be able to reduce the band gap without encountering any localized mid gap states, and thus ensure longer life time of the photogenerated charge carrier

along with enhanced visible light activity. More importantly, the narrowing of band gap should occur in this codoped system in such a controlled way that both water oxidizing and reducing behavior of the material can remain intact. Moreover, the presence of one codopant often facilitate the doping with other elements by reducing the formation energy. Sometimes, a codopant not only maintains the electrical charge neutrality but also leads to the formation of a crystal structure which enhances the probability of photo reaction over recombination. Therefore, the strategy of codoping is still one of the promising areas of interest in the technology related to visible light driven photocatalyst.

In the present thesis, the effect of doping and codoping for different metal oxide photocatalysts have been discussed illustratively.

1.4. Hydrogen Storage

The main obstacle for widespread application of hydrogen energy is the difficulty encountered in its storage and bulk transport. Although Hydrogen offers very high energy density per unit mass, its energy density per unit volume is very less, i.e. it requires large volume to store hydrogen. At ambient condition (Temperature=25^0C, pressure= 1 bar) the volume required to store 1 kg of Hydrogen is almost 11 m^3. Hence, the second major challenge for the progress of Hydrogen economy is the development of sufficiently good and compact, light weight Hydrogen storage system which can deliver hydrogen gas at nearly room temperature and at pressure not much higher than the atmospheric pressure. A material to be a good hydrogen storage system should satisfy the requirements[74] (i) enthalpies for hydrogen absorption and desorption should be in between the enthalpies for chemisorption and physisorption, (ii) at ambient condition the kinetics should be fast enough for quick uptake and release of Hydrogen (ii) the gravimetric and volumetric densities should be quite high for effective Hydrogen storage, (iv) effective heat transfer (v) the storage material

should be recyclable for considerable number of times (vi) high mechanical strength (vii) long lasting and (viii) safe use under operational conditions.

The possible ways to store Hydrogen are in gaseous, or liquid form and in solid state materials. Hydrogen can be stored as gaseous form in pressure vessels, under several hundred atmospheric pressure. In liquid form, Hydrogen can be stored only at cryogenic temperature. Apart from the energy density, both these methods are neither safe nor cost effective. The other approach of storing hydrogen is through chemical of physical absorption in the form of metal hydride or absorbing it into porous solid matrix.

1.4.1. Hydrogen Storage through Chemisorption: Metal Hydrides

Storage of hydrogen in the form of metal hydrides is well explored for transport application.[75,76] Wide range of metals and alloys form metal hydrides which can reversibly release hydrogen under different temperature and pressure. This approach is considered to be safer than gas or liquid state hydrogen storage technology, as the hydrogen release process is highly endothermic. Metal hydrides can be broadly classified as (i) ionic hydrides consisting of alkali and alkaline earth metals like Li, Mg, Be etc. (ii) Metallic or semiconductor hydrides mainly composed of transition metals, lanthanides and actinides (iii) complex metal hydrides including the complexes of group IA, IIA and III A elements, AlH_4^-, AlH_6^{3-}, NH_2^-, BH_4^- and NH^{2-} which form stable hydrides like $NaAlH_4$, $NaBH_4$, $LiNH_2$ etc. though ionic bonding with alkali and alkaline earth metals.

MgH_2 is considered to be one of the promising light metal hydrides for hydrogen storage due to its high hydrogen content (7.6 wt%), cost effectiveness and wide availability of Mg. However, the major drawback of this compound is the requirement of higher desorption temperature (300^0C) (due to sluggish kinetics for adsorption/desorption process).

Although, many transition metals can form hydrides, their dissociation pressure and temperature are not favorable for the practical scenario at ambient condition. To overcome

this, various intermetallic hydrides have been formed by alloying with other metal, so that the overall dehydrogenation enthalpy is reduced. So far a large number of intermetallics of 3d-transition metals like Ti-Fe, Ti-V based alloys or even higher multiple metal containing alloys have been developed for hydrogen storage application.

Although the hydrogen gravimetric densities are high in the complex metal hydrides, their dehydrogenation is highly irreversible and the system becomes unsuitable for further use.

Various metal borohydrides are also found to be promising materials for storing hydrogen with high gravimetric hydrogen densities due to low mass of B and large amount of hydrogen can be present in the system. As for example, $LiBH_4$ can store hydrogen with a gravimetric density of 18.4 wt% and its decomposition temperature is around 320—380^{0}C. $NaBH_4$ is another material which can store up to 10.8 wt% of hydrogen. Although $Be(BH_4)_2$ is found to contain highest hydrogen wt% (20%), the complexes of borohydrides are prohibited for use in hydrogen storage application due to high toxicity associated with Be metal. $Mg(BH_4)_2$ can also store hydrogen up to 14.8 wt%. The main disadvantages associated with these materials are their high decomposition temperature and poor recyclability.

1.4.2. Hydrogen Storage through Physisorption:

In recent times, there has been growing interest towards molecular hydrogen storage through physical adsorption of hydrogen. Although the hydrogen molecule is nonpolar (zero dipole moment), it can adsorbed on surfaces by means of weak Van der Waals interaction due to quadrupole moment and polarizability. The origin of these Van der Waals interaction is due to fluctuations in the charge distribution in between the adsorbing substrate and the interacting molecule. The enthalpy of physical adsorption varies in the range of 1 to 10 kJ/mole, which is too low to break the chemical bond in Van der Waals interaction molecule. Due to low binding interaction between H_2 molecule and the substrate, this approach usually

requires low temperature. The kinetics involved in this approach is quite fast as the adsorption process is almost barrierless. The quantity of absorbed H_2 increases with the increase in surface area of the host materials. This leads to the development of various kinds of highly porous materials with high surface area.

So far large number of light weight robust materials with high porosity have been developed for storing hydrogen through physisorption.[77-83] However this approach needs cryogenic temperature to achieve significant hydrogen uptake capacity. Materials like metal organic framework, porous carbons, zeolites, clathrates and organic polymeric compounds can absorb hydrogen on the surface of the pores. Carbon based materials are of prime interest due to low density, wide range of pores structure, efficient regeneration of substrate, long lasting property etc. The most promising carbon based materials include carbon nanotubes (CNTs), graphite, carbon nanofibers, activated carbon, ordered porous carbons etc.

Among the different porous materials discussed so far, metal organic frameworks (MOFs) and covalent organic frame works (COFs) materials are found to be promising because of their large surface area, robust nature and developed synthetic strategy. MOFs are crystalline materials where the metal ions are connected through organic ligand as linkers, generating micropores and channels. Depending on the choice of metal and organic ligand the framework topology, and pore size, the surface area of these materials varies. In contrast to MOFs, the COFs are based on strong covalent bond. Hydrogen storage in these materials is dictated by surface area and pore volume.

Recently, transition metal decorated carbon nanomaterials have been of emerging interest for hydrogen storage application.[84-86] In this case, the hydrogen adsorption energies are such that ambient temperature hydrogen storage is possible through well-established Kubas type of interactions. Wide range of transition metal decorated fullerenes and CNT have been developed and it has been reported that Sc, or Ti decorated materials can bind

molecular hydrogen with a binding energy of around 0.5 eV/H_2 and gravimetric density of nearly 8-9%. Although, the transition metal decorated carbon materials are found to be attractive for storing hydrogen due to their large cohesive energies and relatively smaller binding energies to the carbon host materials, they have certain limitations. Transition metals are often found to aggregate and form cluster which not only lowers the hydrogen adsorption storage efficiency but also change the materials in such a way that it becomes no longer suitable for recyclable hydrogen storage applications.

1.5. Application of Hydrogen as a Fuel

There are two different approaches through which hydrogen can be used as a fuel in vehicles,[87-89] viz. (i) hydrogen-fuelled internal combustion engines (H_2ICEs) and (ii) fuel cells (FCs). In the case of internal combustion engines (ICEs), chemical energy is first converted to mechanical energy, which can then be transformed to electrical energy in the second step. The advantages of ICE are lower weight, cost effectiveness, and they can be run even using impure fuel, and the only undesirable emission is nitrogen oxides (NO_x) generated due to thermal dissociation and oxidation of N_2 present in atmospheric air during combustion.

In the case of fuel cells, the chemical energy is directly converted into electrical energy. It is considered to be an important component to make hydrogen economy a reality. The overall reaction occurring in H_2/O_2 fuel cell can be written as

$$H_2 + \tfrac{1}{2}\,O_2 \longrightarrow H_2O, \quad \Delta G = -237 \text{ kJ/mol}$$
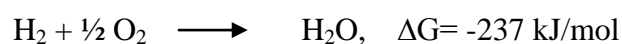
The equilibrium cell voltage is 1.23 V at standard condition. This is simply the difference in the electrode potential generated due to cathode and anode reaction at the equilibrium condition. However, the cell voltage achieved in practical scenario is found to be less due to losses at both the half cell reactions. In the fuel cell the two electrodes are connected by an external circuit. Inside the cell, an electrolyte solution separates the two electrodes. Based on the nature of electrolyte, fuel cells may be of different types as, polymer electrolyte

membrane fuel cells, solid oxide fuel cells, alkaline fuel cells, phosphoric acid fuel cells, direct methanol fuel cells, and molten carbonate fuel cells, etc. Fuel cells can also be broadly classified into two groups based on operational temperature, viz. (i) low temperature fuel cell, which includes alkaline fuel cell, polymer electrolyte fuel cell, direct methanol fuel cell, phosphoric acid fuel cell and (ii) high temperature fuel cell which includes molten carbonate fuel cell and solid oxide fuel cell. The main reaction occurring at the cathode of the fuel cell is the oxygen reduction reaction (ORR), while at the anode there occurs oxidation of hydrogen. The overall anodic reaction can be expressed as

$$H_2 \longrightarrow 2H^+ + 2e^-$$

The kinetics of oxidation on the Pt based catalyst is found to be quite fast, mainly controlled by mass transfer limitation. In the case of pure hydrogen, the rate of reaction is very fast (rate constant of the order of 10^{-5} mol sec^{-1} cm^{-2}), although the rate is retarded in presence of impurity.

The cathodic reaction, the oxygen reduction reaction, is found to be almost six times slower in comparison to the anodic oxidation process.[90,91] This is the rate limiting step in fuel cells. Depending on the reaction condition, the ORR may proceed either via four electron path or two electron path. In the case of four electron path, the reaction can be expressed as

$$O_2 + 2H_2O + 4e^- \longrightarrow 4OH^- \quad \text{(in alkaline medium)}$$
$$O_2 + 4H^+ + 4e^- \longrightarrow 2H_2O \quad \text{(in acid medium)}$$
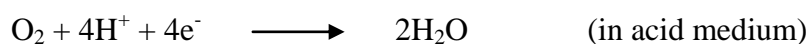
whereas, the two electron path proceeds through formation of hydrogen peroxide as

$$O_2 + H_2O + 2e^- \longrightarrow OOH^- + OH^- \quad \text{(in alkaline medium)}$$
$$O_2 + 4H^+ + 4e^- \longrightarrow H_2O_2 \quad \text{(in acid medium)}$$
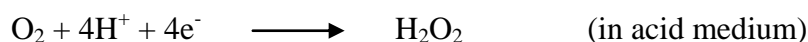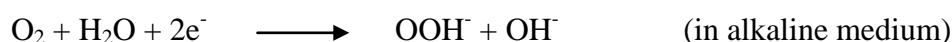
Usually, four electron path is more favorable in comparison to the two electron path.

Since, the kinetics of electrode reactions are very slow for the fuel cells, operating at low temperature requires an efficient catalyst like Pt, although, high temperature fuel cells can be operated using transition metal or their alloys as catalyst. Among the different fuel cells, the polymer electrolyte membrane fuel cells (PEMFC) and the alkaline fuel cell (AFC) are more promising due to their operation at room temperature. Pt is considered to be the best catalyst reported so far for fuel cell applications. But limited availability and high cost of Pt drives research for developing alternate catalyst for this purpose. Numerous studies are going on to find efficient cocatalyst comparable to Pt. Efforts towards making Pt-based alloys or anchoring Pt nanostructures onto carbon nanomaterials as active support have been shown to be interesting due to use of minimum amount of Pt. Apart from Pt various other metals anchored on carbon based nanomaterials are also under study for fuel cells applications.

1.6. Scope of the Present Thesis

In the present thesis (Chapter 3-8), we have focused on all the three important aspects related the hydrogen economy as mentioned above. Using the density functional based electronic structure calculations, we have designed a perovskite based photocatalyst for the generation of hydrogen via visible light driven water splitting. To develop efficient materials for hydrogen storage, we have investigated different the light metal decorated carbon porous nanostructures which can adsorb molecular hydrogen. Finally, calculations for designing new materials for the efficient oxygen reduction reaction have been carried out. All these discussions are presented in the eight chapters, which are summarized as follows.

Chapter 3 deal with the effect of codoping with different cation-anion pair and anion-anion pair to form charge compensated and noncompensated $NaTaO_3$ aiming to improve its photocatalytic activity under visible light. Among cation-anion pair (Cr, N), (Mo, N), and (W, N) from charge compensated system, while (S, N), (V, N), (Nb, N), (Mn, N) and (Tc, N) form charge non-compensated systems. For (Mo, N) and (W, N)-codoped $NaTaO_3$, the

localized impurity states are completely passivated, and the impurity states lie just adjacent to the band edges to form a continuum band structure. This ensures improved charge carrier mobility in the codoped system. On the other hand, charge non-compensated codoping leads to narrowing the band gap by a larger extent. In all the cases discrete mid gap states are found to appear in between VB and CB due to incomplete passivation of the individual impurity states. Hence, these dopant pair may not be suitable for enhancing the photocatalytic property of $NaTaO_3$. We also propose N, F codopant pair to improve the photoactivity of $NaTaO_3$ under visible light. Codoping with N and F results formation of charge compensated and isoelectronic (with $NaTaO_3$) system, hence the tendency to form unwanted defects will be minimum, which would be beneficial for longer life time of the photogenerated charge carriers.

In chapter 4, we have adopted codoping approach with various dopant pair to improve the photocatalytic behavior of $SrTiO_3$ under visible light. We have shown that codoping with either with pentavalent metal (Sb, V, Nb, and Ta) or hexavalent metal (Mo, W) successfully reduces the band gap without encountering any localized mid gap states, thus ensures enhanced photoconversion efficiency in comparison to that of the monodoped systems. Applicability of these modified $SrTiO_3$ for overall water splitting are checked by aligning their VBM and CBM positions with respect to water redox levels, showing that all satisfying the thermodynamic criteria to evolve both hydrogen and oxygen. We have also investigated the origin of the acceptor states in case of Rh-doped $SrTiO_3$ in details, and the change in electronic structure of Rh-doped $SrTiO_3$ in presence of Sb thus attempting to find out the improvement of the photocatalytic activity. We also investigated the role of La codoping on the microscopic electronic structure of Rh-doped $SrTiO_3$. Finally we predicted that codoping with pentavalent ion, like, V, Nb, and Ta also stabilize the desired oxidation state of Rh, with

reduction of band gap by a larger extent. We have also shown that codoping with F is successful for this purpose.

Chapter 5 describes a systematic investigation to explore the effect of several anionic dopants (individually as well as in combination) on the electronic structure of $KTaO_3$. In all the codoped cases, clear band structure is produced, ensuring good photoconversion efficiency. The present study reveals that the extent of band gap narrowing in case of codoping with N and F is quite significant (almost 1 eV) to improve the visible light activity of $KTaO_3$ effectively. It also discusses the effect of cation-anion codoping on the electronic structure of $KTaO_3$. This Chapter also discusses the effect of doping with N and W on the geometry and electronic structure of $KNbO_3$. Interestingly, a highly favourable band structure is produced with reduced band gap when both N and W are simultaneously doped into the crystal structure of $KNbO_3$. The same strategy has been applied for controlled band gap narrowing of $NaNbO_3$.

Chapter 6 discusses the strategy of improving the photocatalytic activity of s-triazine based graphitic carbon nitride (g-CN), which is a potential photocatalyst for water splitting, through metal decoration. Our aim is to reduce the band gap in a controlled way by decorating with different noble metal elements, Pt, Pd, Ag, and Au. We have extended this study, to investigate the electronic structure of graphitic carbon nitride decorated with the cluster (Pt_4, Pd_4, Ag_4, and Au_4).

Chapter 7 explores porus graphitic carbon nitride of the kind $g-C_4N_3$ functionalized with different metal as a potential material for hydrogen storage. The unique properties are due to the high adsorption energies of these elements over nitrogen triangular holes. The materials have the additional advantage that they are stable against clustering of the metal elements due to higher metal-carbon nitride adsorption energy in comparison to the metal-

metal cohesive energy. The adsorption energies of hydrogen molecules on these metals are in the range for efficient hydrogen storage applications.

Chapter 8 discusses the development of new catalyst for the oxygen reduction reaction (ORR) at fuel cells, which is almost 6 times slower in comparison to the anodic oxidation process, and is considered as the rate limiting step in fuel cell. Here, we have investigated the catalytic activity of the transition metal (Fe, Co and Ni) decorated porphyrene line fullerene ($C_{24}N_{24}$) for the ORR. Present study reveals that the Fe and Co decorated systems are active whereas the Ni decorated system is almost inert due to poor O_2 binding energy in the later case. A systematic study of the possible ORR paths are carried out on both Fe and Co decorated $C_{24}N_{24}$ system. The changes in free energy for all the steps discussed for both Fe and Co systems. The free energy profiles at different electrode potentials are also plotted to see whether all the reaction steps are downhill or not at zero potential, at higher potentials.

Finally, in chapter 9 we provide some concluding remarks based on our study. This also gives some future directions to improve the efficiency of the materials involved in the three different stages of hydrogen economy by a further extent.

Chapter 2

Theoretical Background

This chapter provides a brief overview of the computational methodologies that have been used to investigate the systems. All the calculations based on density functional theory (DFT) have been carried out using Vienna ab-initio simulation Package (VASP) software. This chapter discusses the essential description of quantum mechanics, including DFT followed by some additional computational methods.

2.1. The Schrödinger Equation

The chemistry of elements and compounds is solely dependent on their electronic configuration. To get an independent understanding of the structure, stability, property of the chemical species as well as to predict the properties of new materials, it is therefore important to evaluate the electronic properties. In the year 1926, Austrian physicist Erwin Schrödinger using wave mechanics as a tool proposed an equation to determine the exact energy of a system.[92] The non-relativistic Schrödinger equation of a many body system is considered to form the basis of electronic structure of matter and provide the basic tool to calculate the electronic properties of atoms, molecules and materials. The Schrödinger Equation in its time-independent non-relativistic form is defined as an Eigen value problem of the form,

$$\hat{H}\psi_i = E_i\psi_i \tag{2.1}$$

where $\hat{H}$ stands for the Hamiltonian operator which operates on the wave function of the system (ψ_i) to deliver the energy Eigen value (E_i). Equation 2.1 is a second order differential equation. The wave function of the ith state of a system composed of N electron and M nuclei can be expressed as

$$\psi_i = \psi_i(\vec{x}_1, \vec{x}_2, \vec{x}_3, \ldots \vec{x}_N, \vec{R}_1, \vec{R}_2, \vec{R}_3, \ldots \vec{R}_M) \tag{2.2}$$

and is dependent on both electronic coordinates $\{\vec{x}_i\}$ and nuclear coordinate $\{\vec{R}_i\}$. Electronic coordinates consist of 3N number of spatial coordinates $\{\vec{r}_i\}$ and N number of spin

coordinates, while nuclear coordinate consist of 3N spatial coordinates. The Hamiltonian operator ($\hat{H}$) consists of the following terms.

(i) The kinetic energy operator of the electron ($\hat{T}$)

$$\hat{T} = -\frac{h^2}{8\pi^2 m_e} \sum_{i=1}^{N} \nabla_i^2 \tag{2.3}$$

(ii) The kinetic energy operator of the nuclei ($\hat{T}_{nuc}$)

$$\hat{T}_{nuc} = -\frac{h^2}{8\pi^2} \sum_{A=1}^{M} \frac{1}{M_A} \nabla_A^2 \tag{2.4}$$

(iii) The potential due to interaction between the electron and nuclei ($\hat{V}_{ext}$) (known as external potential in DFT)

$$\hat{V}_{ext} = -e^2 \sum_{i=1}^{N} \sum_{A=1}^{M} \frac{Z_A}{r_{iA}} \tag{2.5}$$

(iv) The repulsive interaction between the electrons ($\hat{V}_{ee}$)

$$\hat{V}_{ee} = e^2 \sum_{i=1}^{N} \sum_{j>1}^{N} \frac{1}{r_{ij}} \tag{2.6}$$

(v) The nuclei-nuclei repulsive term ($\hat{V}_{NN}$)

$$\hat{V}_{NN} = e^2 \sum_{A=1}^{M} \sum_{B>A}^{M} \frac{Z_A Z_B}{R_{AB}} \tag{2.7}$$

and thus can be expressed as

$$\hat{H} = \hat{T}_e + \hat{T}_{nuc} + \hat{V}_{ext} + \hat{V}_{ee} + \hat{V}_{NN} \tag{2.8}$$

Here, m_e and M_A represent the mass of electron and A^{th} nucleus, respectively, e and $Z_A e$ indicate the magnitude charge of an electron and A^{th} nucleus, respectively, h stands for the Planck's constant. Subscripts A and B have been used for nuclei, while i, j for the electrons.

The Laplacian operator (∇_q^2) is expressed as a sum of differential operators in Cartesian coordinate as

$$\nabla_q^2 = \frac{\partial^2}{\partial x_q^2} + \frac{\partial^2}{\partial y_q^2} + \frac{\partial^2}{\partial z_q^2} \tag{2.9}$$

Conventionally the quantum mechanical equation is written without the use of fundamental physical constant. Hence m_e, e, $h/2\pi$, $4\pi\varepsilon_0$, are all set to unity, while other physical quantities are represented as multiplication of these constants. Therefore one can write the Hamiltonian operator of a system, in atomic units, as,

$$\hat{H} = -\frac{1}{2}\sum_{i=1}^{N}\nabla_i^2 - \frac{1}{2}\sum_{A=1}^{M}\frac{1}{M_A}\nabla_A^2 - \sum_{i=1}^{N}\sum_{A=1}^{M}\frac{Z_A}{r_{iA}} + \sum_{i=1}^{N}\sum_{j>1}^{N}\frac{1}{r_{ij}} + \sum_{A=1}^{M}\sum_{B>A}^{M}\frac{Z_A Z_B}{R_{AB}} \tag{2.10}$$

In principle, the exact solution of Schrödinger equation can be achieved for any system of interest. However in reality it is impossible to obtain analytical solution for system with more than one electron due to involvement of larger number of variables (3N electronic spatial coordinates, N electronic spin coordinates and 3N nuclear spatial coordinates. Therefore, studies of systems of interest which are mostly multi-atomic, are very difficult to obtain even through computation and hence require simplified schemes. The Schrödinger equation can be simplified with the help of several approximations discussed below.

2.2. Born-Oppenheimer Approximation

The first approximation was given by Max Born and J. Robert Oppenheimer[93] in the year of 1927. With this approximation, the wave function can be split into nuclear and electronic components as,

$$\psi_{Total}(\vec{x},\vec{R}) = \psi_{electronic}(\vec{x})\ \psi_{nuclear}(\vec{R}) \tag{2.11}$$

The Born-Oppenheimer approximation takes into account the large difference in the mass of electron and nuclei. The mass of the electron is nearly 1880 times lower than that of lightest

nucleus (i.e., mass of a proton, ^{1}H) and therefore movement of electron is much faster than that of the nuclei. Consequently the kinetic energy of nuclei is negligible in comparison to that of the electron. According to Born-Oppenheimer approximation the kinetic energy of the nucleus is taken as zero and electrons are considered as moving in the field of fixed nuclei ($\vec{R}_A$). Hence the Hamiltonian takes the form

$$\hat{H} = -\frac{1}{2}\sum_{i=1}^{N}\nabla_i^2 - e^2\sum_{i=1}^{N}\sum_{A=1}^{M}\frac{Z_A}{r_{iA}} + \sum_{i=1}^{N}\sum_{j>1}^{N}\frac{1}{r_{ij}} + \sum_{A=1}^{M}\sum_{B>A}^{M}\frac{Z_A Z_B}{R_{AB}} \tag{2.12}$$

where the last term is a constant. The Hamiltonian can be split into nuclear component and electronic component, and the electronic Hamiltonian can be expressed as,

$$\hat{H}_{elec} = -\frac{1}{2}\sum_{i=1}^{N}\nabla_i^2 - \sum_{i=1}^{N}\sum_{A=1}^{M}\frac{Z_A}{r_{iA}} + \sum_{i=1}^{N}\sum_{j>1}^{N}\frac{1}{r_{ij}} = \hat{T}_{elec} + \hat{V}_{Ne} + \hat{V}_{ee} \tag{2.13}$$

Therefore, the electronic wave function does not explicitly depend on the nuclear coordinate and can be described solely by the electronic coordinate, although it depends on the nuclear coordinate parametrically. The electronic structure calculation has thus been simplified to the solution of only the electronic Schrödinger equation, viz.

$$\hat{H}_{elec}\psi_{elec} = E_{elec}\psi_{elec} \tag{2.14}$$

where

$$\psi_{elec} = \psi_{elec}(\vec{x}_1, \vec{x}_2, \ldots, \vec{x}_N) \tag{2.15}$$

It should be noted that the E_{elec} stands for the energy of electronic component of the total energy which consists of electronic energy, which along with the nucleus- nucleus repulsive energy, forms the total energy, viz.

$$E_{Total} = E_{elec} + E_{nuc}. \tag{2.16}$$

which serves as the potential for the Schrödinger equation for the nucleus.

2.3.The Variational Principle

According to the Schrödinger equation

$$\hat{H}\psi_i = E\psi_i$$
(2.17)

Multiplying both sides by complex conjugate (ψ_i^*) of ψ_i and integrating over all spaces

$$\int \psi_i^* \hat{H} \psi_i d\vec{x}_1 \ d\vec{x}_2 ..... d\vec{x}_N = \int \psi_i^* E_i \psi_i d\vec{x}_1 \ d\vec{x}_2 ..... d\vec{x}_N$$
(2.18)

In the normalized condition one has

$$\int \psi_i^* \psi_i d\vec{x}_1 \ d\vec{x}_2 ..... d\vec{x}_N = 1$$
(2.19)

and hence

$$E_i = \int \psi_i^* \hat{H} \psi_i d\vec{x}_1 \ d\vec{x}_2 ..... d\vec{x}_N$$
(2.20)

which can be expressed using Dirac notation as,

$$E_i = \left\langle \psi_i \mid \hat{H} \mid \psi_i \right\rangle$$
(2.21)

Therefore the total energy E_i can be obtained by determining ψ_i. Unfortunately this job is tremendously challenging and can be solved only for selected trivial cases. One of the important approaches involve the variational principle, which is widely used to obtain the ground state eigen function (ψ_0). According to this principle, the expectation value (E) of the Hamiltonian operator ($\hat{H}$) using any trial wave function (ψ_{trial}) is always greater than or equal to the true energy of the ground state of the system i.e. $\tilde{E} \geq E_0$, where $\tilde{E}$ is defined as

$$\tilde{E} = \frac{\left\langle \psi_{trial} \mid \hat{H} \mid \psi_{trial} \right\rangle}{\left\langle \psi_{trial} \mid \psi_{trial} \right\rangle}$$
(2.22)

Since, lower the value of the variation integral, the better is the approximation to the ground state energy, usually different parameters are used for the construction of a trial wave function to finally minimize the variation integral with respect to these parameters.

2.4. The Hartree Approximation

According to the Hartree approximation,[94] the given N electron problem is separated into N-one electron problems, leading to N-one electron Schrödinger-like equations. In this approximation, the Hamiltonian operator can be expressed as $\hat{H} = \sum_{i=1}^{N} \hat{h}(i)$

where,

$$\hat{h}(i) = -\frac{1}{2}\sum_{i=1}^{N}\nabla_i^2 - \sum_{a=1}^{M}\frac{Z_A}{r_{iA}} + V_{Coul}(\vec{r_i}) \tag{2.23}$$

with

$$V_{Coul}(\vec{r_i}) = \sum_{j=1}^{N}\int \frac{1}{r_{ij}}\left|\phi_j(\vec{r_j})\right|^2 d\vec{r_j} \tag{2.24}$$

Assuming the electrons as non-interacting to each other, the total wave function is defined as a product of one electron wave functions which is known as Hartree product wave function.

$$\psi^{HP}(\vec{x_1}, \vec{x_2}, ..., \vec{x_N}) = \chi_1(\vec{x_1})\chi_2(\vec{x_2})......\chi_N(\vec{x_N}) \tag{2.25}$$

where $\chi_1(\vec{x_1})$ consists of the spatial orbital $\phi_i(\vec{r_i})$ and spin function ($\alpha(s)$ or $\beta(s)$)

$$\chi_i(\vec{x_i}) = \phi_i(\vec{r_i})\sigma(s) \tag{2.26}$$

where each one electron wave function can be obtained using the one-electron equation,

$$\hat{h}(i)\chi_i(\vec{x_i}) = \varepsilon_i\chi_i(\vec{x_i}) \tag{2.27}$$

The total energy of the system can be calculated as

$$E = \sum_{i=1}^{N}\varepsilon_i - \frac{1}{2}\sum_{i=1}^{N}\int\left|\phi_i(\vec{r_i})\right|^2 V_{Coul}(\vec{r_i})d\vec{r_i} \tag{2.28}$$

Although, the Hartree approximation simplifies the electronic structure calculation by a significant extent, it has several drawbacks. Neither the antisymmetry principle nor the Pauli Exclusion Principle is obeyed in this approximation. In contrast to the indistinguishable character of the electron, particular electrons are assigned to particular orbital in this

approximation. Besides, electronic correlation is completely ignored in the Hartree approximation, and the probability of finding an electron, in the neighbourhood is completely independent of finding another electron which is invalid in the real situation.

2.5 The Hartree-Fock Approximation

In the Hartree-Fock (HF) method,[95] the N electron wave function is expressed by a Slater determinant to incorporate the antisymmetric nature of the electronic wave function

$$\phi_{SD} = \frac{1}{\sqrt{N!}} \begin{vmatrix} \chi_1(\vec{x}_1) & \chi_2(\vec{x}_1) & \cdots & \chi_N(\vec{x}_1) \\ \chi_1(\vec{x}_2) & \chi_2(\vec{x}_2) & \cdots & \chi_N(\vec{x}_2) \\ \vdots & \vdots & \cdots & . \\ \chi_1(\vec{x}_N) & \chi_2(\vec{x}_N) & \cdots & \chi_N(\vec{x}_N) \end{vmatrix}$$

2.29

Here, ϕ_{SD} is an antisymmetrised product of N one electron wave functions, ($\chi_1(\vec{x}_1)$ known as apin orbital and composed of both spatial orbitals and spin functions). Here, $1/\sqrt{N!}$ is the normalization factor.

Equation 2.29 indicates that exchanging the coordinates of ith and j^{th} particles involves interchanging i^{th} and j^{th} rows of the determinant. Hence, the wave function ϕ_{SD} is antisymmetric as interchanging two rows or columns in the Slater determinant changes its sign. If two electrons are assigned to the same orbital, then $\chi_i = \chi_j$ and the resulting $\phi_{SD} = 0$. Hence, ϕ_{SD} obeys the Pauli Exclusion Principle. By minimizing E[ϕ_{SD}] with respect to ϕ_{SD} (i.e. the orbitals), the Hartree-Fock energy can be obtained using the variation principle under the condition of the orthonormality of the wave function and hence the orbitals $\chi_i(\vec{x}_i)$. This produces a set of N one electron Schrödinger-like Hartree-Fock equation of the form

$$\hat{f}(i)\chi_i(\vec{x}_i) = \varepsilon_i \chi_i(\vec{x}_i) \qquad i=1, N \qquad (2.30)$$

where ε_i represents the eigenvalues of $\hat{f}(i)$, which is an effective one electron operator, known as Fock operator and is expressed as

$$\hat{f}(i) = -\frac{1}{2}\nabla_i^2 - \sum_{A=1}^{M}\frac{Z_A}{r_{iA}} + V_{HF}(i) \qquad (2.31)$$

Here, $V_{HF}(i)$ is called the Hartree-Fock potential which is generated due to repulsive interaction between an electron with the remaining electrons (N-1). Now the complex two electron operator ($1/r_{ij}$) simplifies to a one electron operator $V_{HF}(i)$, which consists of the Coulomb operator $\hat{J}$ and the exchange operator $\hat{K}$, that can be expressed as,

$$V_{HF}(\vec{x}_1) = \sum_{j=1}^{N}\left(\hat{J}_j(\vec{x}_1) - \hat{K}_j(\vec{x}_1)\right) \qquad (2.32)$$

where

$$\hat{J}_j(\vec{x}_1) = \int\left|\chi_j(\vec{x}_1)\right|^2\frac{1}{r_{12}}d\vec{x}_2 \qquad (2.33)$$

and

$$\hat{K}_j(\vec{x}_1)\chi_i(\vec{x}_1) = \int\chi_j^*(\vec{x}_2)\frac{1}{r_{12}}\chi_i(\vec{x}_2)d\vec{x}_2\chi_j(\vec{x}_1) \qquad (2.34)$$

The Coulomb operator stands for the potential experienced by an electron at a position due to another electron in another spin orbital, and is integrated over all space. The exchange operator takes into account the modification of the energy due to exchanging position between two electrons. It should be noted that interchanging positions is restricted only to the electrons of the same spin. Exchange potential is zero when the electrons involved in the interchange process are of different spin. It should be pointed out from the equation (Coulomb term) that electron can interact with itself when *i=j*. However for *i=j* the Coulomb and exchange integrals become equal in magnitude but opposite in sign, and thus self-interaction is cancelled out.

The Hartree-Fock procedure employs the self consistent method to calculate the energy. In this approach, first a set of guess orbitals is used to construct $V_{HF}(i)$. The Hartree-

Fock equation is then solved using $V_{HF}(i)$ and a new set of orbital is generated. This procedure is iteratively continued till the input and output sets of orbitals match within a certain degree of precision and the energy values as well as the wavefunction are said to be self consistent.

The error in calculating the total energies using the Hartree-Fock method lies in the range of 0.5% to 1%. However, the error is in the range of the chemical bond-energies, and hence one needs some correction of the Hartree-Fock theory. The error appears due to negligence of dynamic correlation between the electrons arising out of inter-electronic repulsion within a short range. The difference between the Hartree-Fock energy (E_{HF}) and true ground state non-relativistic energy (E_0) is known as the correlation energy (E_{corr}), viz.

$$E_{corr} = E_0 - E_{HF} \tag{2.35}$$

To incorporate dynamic correlation, the wave function is better represented as a linear combination of large number of Slater determinants. Various methods like Moller-Plesset perturbation, configuration interaction coupled cluster etc. have been developed to take care of the electron correlation energy.[96,97] Unfortunately, all these post Hartree-Fock methods are computationally too expensive to use for large systems of practical interest.

2.6. Density Functional Theory

As the wave function is dependent on the 3N spatial coordinates and N electronic spin coordinate, solution of Schrödinger equation for many body system (using even Hartree-Fock methods) is limited by huge computational cost. The development of DFT greatly simplifies this problem by replacing the much complicated N electron wave function and the associated Schrödinger equation with the simpler single particle-density $\rho(\vec{r})$, and the equation for the direct determination of this density variable.

2.6.1. Thomas -Fermi -Dirac Approximation

In the year 1927 , Thomas and Fermi [98,99] showed that the kinetic energy of an electronic system E_{TF} can be expressed as a functional of the electron density $\rho(\vec{r})$. The Thomas-Fermi model is quantum statistical model, where the electrons are assumed to be distributed uniformly over the six dimensional phase space.

The electron density can be expressed similar to the probability density function as

$$\rho(\vec{r}_1) = N \int \left| \psi(\vec{x}_1, \vec{x}_2, ..., \vec{x}_i, \vec{x}_j, ...\vec{x}_N) \right|^2 ds_1 d\vec{x}_2 d\vec{x}_3 ....d\vec{x}_N \qquad (2.36)$$

where $\rho(\vec{r})$ follows the relation $\int \rho(\vec{r})d\vec{r} = N$ and indicates the probability density of finding an electron, normalised to N, the number of electrons.

The relation between the kinetic energy and the total electron density in the Thomas-Fermi model is given by

$$T_{TF}[\rho(\vec{r})] = \frac{3}{10}(3\pi^2)^{\frac{2}{3}} \int [\rho(\vec{r})]^{\frac{5}{3}} d\vec{r} \qquad (2.37)$$

The total energy of the system can be expressed (in atomic units) as

$$E_{TF}[\rho(\vec{r})] = \frac{3}{10}(3\pi^2)^{\frac{2}{3}} \int [\rho(\vec{r})]^{\frac{5}{3}} d\vec{r} - Z\int \frac{\rho(\vec{r})}{r} d\vec{r} + \frac{1}{2}\iint \frac{\rho(\vec{r}_1)\rho(\vec{r}_2)}{r_{12}} d\vec{r}_1 d\vec{r}_2 \qquad (2.38)$$

The second and third terms stand for the electron-nucleus attractive interaction and electron-electron repulsive interaction respectively, treated through simple classical electrostatics. It is to be noted that electron-electron exchange energy is not incorporated in this expression.

In the year 1930, Dirac made a modification of the Thomas-Fermi enrgy equation by introduction of the exchange term[100] as

$$E_{TFD}[\rho(\vec{r})] = E_{TF}[\rho(\vec{r})] + K_{D[\rho]} \qquad (2.39)$$

where $K_{D[\rho]} = -\frac{3}{4}\left(\frac{3}{\pi}\right)^{\frac{1}{3}} \int [\rho(\vec{r})]^{\frac{4}{3}} d\vec{r} \qquad (2.40)$

Although, this model reduces the computational cost, the accuracy of this method in calculating the energy is still low. This may be due to the assumption that the electrons are distributed uniformly in the space as a gas. To improve the accuracy of this model several modification have been proposed. Important breakthrough in density based theory came after the pioneering work of Hohenberg and Kohn in the year 1964.

2.6.2. Hohenberg-Kohn Formulation

Modern day density functional theory is based on two theorems proposed by Hohenberg and Kohn.[101] These theorems are applicable to a many-electron system, where the electrons are moving under the influence of an external potential $[V_{ext}(\vec{r})]$.

The first theorem states,

For any system of interacting particles in an external potential $V_{ext}(\vec{r})$, the single-particle density $\rho(\vec{r})$ uniquely determines the external potential (apart from an additive constant). In other words, the external potential $V_{ext}(\vec{r})$ is a unique functional of density $\rho(\vec{r})$ for a many electron system, and thus two different external potentials $V_{ext}(\vec{r})$ and $V_{ext}^{'}(\vec{r})$ cannot lead to the same $\rho(\vec{r})$. The external potential $V_{ext}(r)$ along with the number of electrons (obtainable from the density integral $\int \rho(\vec{r})d\vec{r} = N$), is sufficient to define the Hamiltonian operator for the electronic part as

$$\hat{H}_{elec} = \hat{T}_{elec} + \hat{V}_{Ne} + \hat{V}_{ee} = -\frac{1}{2}\sum_{i=1}^{N}\nabla_i^2 - \sum_{i=1}^{N}V_{ext}(\vec{r_i}) + \sum_{i=1}^{N}\sum_{j>1}^{N}\frac{1}{r_{ij}} \qquad (2.41)$$

which is thus uniquely determined (apart from an additive constant) by the density. They further demonstrated that the ground state energy and hence the kinetic energy as well as the

inter-electronic repulsion energy can thus be defined as unique functional of $\rho(\vec{r})$. The total

ground state energy can be expressed as a functional of the electron density as,

$$E[\rho] = T[\rho] + V_{ext}[\rho] + V_{ee}[\rho] \qquad (2.42)$$

The three terms in the right hand side of this equation indicate the kinetic energy of the

electrons, external potential contribution (electron-nucleus attractive interaction), and

electron-electron repulsion energy respectively. The electron-electron repulsion term can be

expressed as a sum of the classical Coulomb interaction and non-classical exchange

correlation energy (E_{XC}) as

$$V_{ee} = \frac{1}{2} \iint \frac{\rho(\vec{r_1})\rho(\vec{r_2})}{r_{12}} d\vec{r_1} d\vec{r_2} + E_{XC} \qquad (2.43)$$

One can also write the energy expression as

$$E[\rho] = F_{HK}[\rho] + \int \rho(\vec{r}) V_{ext}(\vec{r}) d\vec{r} \qquad (2.44)$$

where, $E_{HK}[\rho] = T[\rho] + V_{ee}[\rho] \qquad (2.45)$

Since, $F_{HK}[\rho]$ is independent of the external potential, its functional form is identical for all

systems and is thus a universal functional of density.

The second theorem of Hohenberg and Kohn applies the variational theorem to the

ground state energy which is a functional of the electron density.

The density that minimizes the energy functional is the exact ground state density.

Thus the ground state energy can be calculated as

$$E_0[\rho] = \min\left(F_{HK}[\rho] + \int \rho(\vec{r}) V_{ext}(\vec{r}) d\vec{r} \right) \qquad (2.46)$$

Although the Hohenberg-Kohn thoerem states that the kinetic energy and the Hamiltonian can be constructed from the electron density, it does not provide the functional form of $F_{HK}[\rho]$. This issue has been addressed by Kohn and Sham in the year 1965, who prescribed a practical scheme for the calculation of density.

2.6.3. Kohn-Sham Equations

Kohn and Sham have formulated DFT as an efficient tool for solving many body problem by involving an indirect way of calculating the kinetic energy functional.[102] First time they have introduced the concept of orbitals in DFT. Based on Hohenberg and Kohn theorem they have proposed the simplified idea that an interacting many body system can be replaced by an auxiliary independent non-interacting particle problem. According to them the ground state of the original interacting system can be mapped into a reference system of non-interacting electrons with the same ground state density. In this approach, each electron is considered to move independently in an effective potential created by the nuclei and the rest of the electrons. The kinetic energy is computed with reasonable accuracy, while the remaining part is taken care of through the exchange-correlation energy functional.

The Kohn-Sham operator representing the one-electron Hamiltonian for the non-interacting system can be written as:

$$\hat{h}_{KS}(\vec{r}) = \left[-\frac{1}{2}\nabla^2 + \hat{V}_{eff}(\vec{r}) \right] \qquad (2.47)$$

where the first term of the right hand side represents the kinetic energy operator and the second term stands for the effective potential, consisting of the external potential (electron-

nuclei interaction), electron-electron Coulomb repulsion and the exchange correlation. The Kohn-Sham orbitals $\{\phi_i(\vec{r})\}$ satisfy the Kohn-Sham equations

$$\left[-\frac{1}{2}\nabla^2 + \hat{V}_{eff}(\vec{r}) \right]\phi_i = \varepsilon_i\phi_i \tag{2.48}$$

where the effective potential is given by

$$\hat{V}_{eff}(\vec{r}) = V_{ext}(\vec{r}) + \int \frac{\rho(\vec{r}\,')}{\left|\vec{r} - \vec{r}\,'\right|}d\vec{r} + \frac{\delta E_{XC}}{\delta\rho(\vec{r})} \tag{2.49}$$

The electron density is defined as the sum of orbital densities given by,

$$\rho(\vec{r}) = \sum_{i=1}^{N}\left|\phi_i(\vec{r})\right|^2 \tag{2.50}$$

The total energy of the interactions system can be written as

$$E_{KS} = T_s[\rho] + E_{Ne}[\rho] + J[\rho] + E_{XC}[\rho] \tag{2.51}$$

where,

$$T_s[\rho] = \sum_{i=1}^{N}\left\langle \phi_i \left| -\frac{1}{2}\nabla^2 \right| \phi_i \right\rangle, \tag{2.52}$$

indicates the exact kinetic energy of the non-interacting system. The electron-nucleus attractive interaction energy can be given by exact expression

$$E_{Ne}[\rho] = -\sum_{i=1}^{N}\int\sum_{A=1}^{M}\frac{Z_A}{\vec{r}_{1A}}\left|\phi_i(\vec{r}_1)\right|^2 d\vec{r}_1 = -\int\sum_{A=1}^{M}\frac{Z_A}{\vec{r}_{1A}}\rho(\vec{r})d\vec{r}_1 \tag{2.53}$$

The electron-electron Coulomb repulsion can also be given by the exact expression, written as

$$J[\rho] = \frac{1}{2}\sum_{i=1}^{N}\sum_{\substack{j=1 \\ i \neq j}}^{N}\iint\frac{\left|\phi_i(\vec{r}_1)\right|^2\left|\phi_i(\vec{r}_2)\right|^2}{r_{12}}d\vec{r}_1 d\vec{r}_2 = \frac{1}{2}\iint\frac{\rho(\vec{r}_1)\rho(\vec{r}_2)}{r_{12}}d\vec{r}_1 d\vec{r}_2 \qquad (2.54)$$

The exact form of the exchange-correlation functional $E_{XC}[\rho]$ is however not known and therefore this has to be approximated using a suitable expression. The beauty of the Kohn-Sham method is that it converts a many body problem into a number of independent particle problem. The Kohn-Sham orbitals are used to calculate the electron density. Although the wave function for the many body interacting system is not determined by the Slater determinant of the Kohn-Sham orbitals, the density can be constructed from these Kohn-Sham orbitals.

According to the Kohn-Sham approach, the system of non-interacting electrons move under the effective field created by the nuclei and other electrons. Thus, one can solve the Kohn-Sham equations self-consistently by first constructing the effective potential from the chosen initial density by using the suggested functional form. Then the Kohn-Sham equation is solved to generate the Kohn-Sham orbitals, which are used to calculate the density. The calculated density is mixed with the old density from the previous loop to yield new initial density for the next loop. This procedure is iteratively continued till the self-consistency is reached according to the desired tolerance where the output density becomes nearly same as the input density. Finally, the converged density is utilized to calculate the energy and other physical properties.

The importance of the Kohn-Sham method lies in the fact that the total energy depends only on the electron density $\rho(\vec{r})$ and all the components of the total energy except E_{XC}, have known explicit functional forms. Several approximation have thus been made to construct the functional form of the exchange-correlation functional E_{XC}.

2.6.4. Functional for Exchange Correlation

In DFT, the exchange correlation energy (E_{XC}) is defined as a functional of the electron density. However, the major problem is that the exact functional form of E_{XC} is unknown. Therefore, several approximation have been made to obtain the expression for E_{XC}. A suitable approach is to separate E_{XC} into two components, one representing the exchange energy (E_X) and other the correlation energy (E_C).

$$E_{XC}[\rho] = E_X[\rho] + E_C[\rho] \tag{2.55}$$

It should be noted that the numerical value for the exchange energy is higher than that of the correlation energy.

2.6.4.1. The Local Density Approximation (LDA)

The simplest approach for defining E_{XC} is the local density approximation (LDA), where the inhomogeneous electronic system is assumed to be locally homogeneous, i.e. the electron density is considered to be a slowly varying function of $\vec{r}$. In this approach the exchange correlation energy corresponding to the homogeneous system, which is known to good accuracy is used to calculate the same for the actual inhomogeneous system.

Thus the exchange correlation functional can be expressed as,

$$E_{XC}^{LDA}[\rho] = \int \rho(\vec{r}) \varepsilon_{XC}[\rho(\vec{r})] d\vec{r} \tag{2.56}$$

where,

$$\varepsilon_{XC}(\rho) = \varepsilon_{XC}^{hom}(\rho) = \varepsilon_X^{hom}(\rho) + \varepsilon_c^{hom}(\rho) \tag{2.57}$$

The exchange part for the LDA functional has been obtained from the Dirac exchange energy functional as,

$$\varepsilon_X(\rho) = -\frac{3}{4}\left(\frac{3}{\pi}\rho(r)\right)^{\frac{1}{3}} \tag{2.58}$$

The analytical expression for the correlation energy (E_C) is unknown even for a homogeneous electron gas. However, it can be obtained almost accurately using quantum Monte Carlo methods. One of the most widely used LDA functional for E_C is the VWN potential, as prescribed by Vosko, Wilk and Nusuir. [103]

The advantage of the LDA approach is that it is computationally inexpensive. This approach has been found to be successful in describing systems of nearly uniform density such as nearly free electron metals. The major disadvantage of LDA method is that it overestimates chemical bonding and underestimates equilibrium volume of the crystal lattice and band gap. The reaction energy barrier calculated using this approach shows significant error. This may be due to the fact that the exchange energy is underestimated by about 10% and the correlation energy is overestimated to nearly double of the actual value.

2.6.4.2. The Generalized Gradient Approximation (GGA)

In order to account for the inhomogeneity of the electron density, generalized gradient approximation has been developed, where one considers dependence of E_{XC} on density $\rho(\vec{r})$ as well as its gradient $\nabla\rho(\vec{r})$. Mathematically, the typical gradient corrected exchange correlation energy function can be expressed as,

$$E_{XC}^{GGA}[\rho] = \int \rho(\vec{r})\varepsilon_{XC}(\rho, \nabla\rho)d\vec{r} \tag{2.59}$$

In the gradient corrected functional the main feature of LDA is preserved and simultaneously inhomogeneity contribution is incorporated. This improves the electron correlation description. A large variety of GGA functionals have been developed so far among which, the popular GGA functional includes Perdew, Burke and Enzerhof (PBE),[104] Perdew and Wang (PW91),[105] Becke (B88)[106], etc. Although, GGA functional overcomes many limitations of LDA, it underestimates the band gap of semiconductor materials. This has led to the development of hybrid functional or GW-approximation which will be discussed in the following sections.

2.6.4.3. Hybrid Density Functional

It is well known that standard density functional theory using HF or LDA or GGA approach cannot reproduce the exact band gap of semiconductors and insulators. This problem can be overcome considerably by using appropriate hybrid density functional which includes a certain fraction of the HF exchange and PBE correlation. However, it is computationally very expensive tool, the HF exchange in hybrid DFT for larger system. This is due to the fact that the HF exchange decays slowly with respect to distance. The delay has been found to be highly system dependent and the range can vary from a few Å to 1000 Å. To overcome this, Heyd-Scuseria-Ernzerhof developed screened Coulomb hybrid functional, which can be used for larger variety of systems.[107] In this approach, the spatial decay of the exchange interaction is accelerated, making the calculation for the HF exchange feasible even for the extended system. For this purpose, the full 1/r Coulomb potential has been substituted by a screened potential which is based on the splitting of the Coulomb operator into two components, short range (SR) and long range (LR). The splitting function may be arbitrarily chosen provided

the sum of the SR and LR components give original Coulomb operator. Heyd-Scusseria-Ernzerhof uses the error function for the splitting as given by

$$\frac{1}{r} = \underbrace{\frac{erfc(\mu r)}{r}}_{SR} + \underbrace{\frac{erf(\mu r)}{r}}_{LR} \qquad (2.60)$$

where $erfc(\mu r)$ denotes the complementary error function, $erfc(\mu r) = 1 - erf(\mu r)$. Here, μ is an adjustable parameter defining the extent of short range interactions known as screening parameter. The extreme limits are as follows: For $\mu = 0$, the long range term vanishes and the short range becomes equivalent to the full Coulomb operator, while the reverse is true for $\mu = \infty$.

The exchange correlation energy for the PBE0 hybrid functional which is based on the Perdew-Burke-Ernzerhof (PBE) exchange correlation functional, can be expressed as,

$$E_{XC}^{PBE0} = aE_X^{HF} + (1-a)E_X^{PBE} + E_C^{PBE} \qquad (2.61)$$

where a stands for the mixing coefficient. The expression for the exchange energy can be expressed as, $E_X^{PBE0} = aE_X^{HF} + (1-a)E_X^{PBE}$ $\qquad (2.62)$

Splitting all the terms of equation (A) into short range and long range results

$$E_X^{PBE0} = aE_X^{HF,SR}(\mu) + aE_X^{HF,LR}(\mu) + (1-a)E_X^{PBE,SR}(\mu) + E_X^{PBE,LR}(\mu) - aE_X^{PBE,LR}(\mu) \qquad (2.63)$$

Numerical test calculation based on realistic value of the parameter μ reveals that the contribution of the long range component of the HF exchange is very small (only a few percent), and these terms tend to cancel each other. Neglecting these terms results into screened Coulomb potential of hybrid density functional, known as Heyd-Scuseria-Ernzorhof

(HSE) functional. The exchange correlation energy functional in the HSE approach can be written as,

$$E_{XC}^{HSE} = a E_X^{HF,SR}(\mu) + (1-a) E_X^{PBE,SR}(\mu) + E_X^{PBE,LR}(\mu) + E_C^{PBE}$$

(2.64)

where μ is an adjustable parameter determining the extent of short range interactions. For the HSE method, value of μ lies within the range of 0.2 Å^{-1} to 0.3 Å^{-1}. In the functional HSE03 and HSE 06, the μ value is fixed at 0.2 Å^{-1} and 0.3 Å^{-1} respectively. The HSE functional becomes equivalent to PBE0 when $\mu = 0$ and asymptotically reaches PBE at the limit $\mu \to \infty$.

The description of the lattice parameter and bulk modulus are greatly improved using HSE hybrid functional within the framework of plane-wave projector-augmented wave (PAW) formation. This may be due to the fact that the fixed amount of HF exchange contribution decreases the self interaction error of standard DFT. Usually the electronic properties of semiconductors with small and medium band gap, are almost accurately predicted by using the HSE functional, while for the large band gap systems this functional overestimates the band gap. The reason is probably that the systems with wide band gap posses very weak screening so that the non-local exchange term becomes almost equivalent to the full Fock exchange term. On the other hand, the fractional amount of HF exchange term provides the appropriate balance for the systems with medium band gap which posses intermediate screening.

2.6.4.4. GW Approximation

To overcome the limitation of conventional DFT using LDA or GGA for the determination of band gap, an accurate method based on the quasiparticle (QP) concept accompanying the

Green's function has been developed.[108] In a solid system, a positive charged polarization cloud around an electron is always formed due to Coulomb repulsion with other electrons. The assembly of the bare electron and positively screening charge cloud is defined as quasiparticle. There exist weak interactions between these quasiparticles via screened Coulomb force. For a solid system, the quasiparticle energies can be determined by solving

$$(T + V_{ext} + V_H)\psi_{nk}^{QP}(r) + \int d^3r' \sum \left(r, r', E_{nk}^{QP}(r') \right) = E_{nk}^{QP}\psi_{nk}^{QP}(r) \qquad (2.65)$$

where $\psi_{nk}^{QP}(r)$ represents the quasiparticle wave function which is usually taken from LDA or GGA wave function as an initial input to carry out the quasiparticle calculations. Here $\sum$ represents the self energy operator for quasiparticle and describes the non-local exchange correlation effects. In the GW approximation, $\sum$ is defined as the product of Green's function G and the dynamically screened Coulomb interaction W,

$$\sum_{GW}(r, r'; t) = iG(r, r'; t)W(r, r'; t) \qquad (2.66)$$

The Green's function $G(r, r'; t)$ indicates the probability of finding an electron at position r at time t when previously there was an electron at position r' and time t=0. The set of energy term $\sum_{GW}$ can be written in terms of the energy as

$$\sum_{GW}(r, r'; t) = i\int G(r, r'; E + E')W(r, r'; E)dE', \qquad (2.67)$$

$$G(r, r'; E) = \sum_n \frac{\psi_n^{KS}\psi_n^{KS*}}{E - \varepsilon_n'} \qquad (2.68)$$

$$W(r, r'; E) = \int \varepsilon^{-1}(r, r_1; E)V_C(r_1, r')dr_1 \qquad (2.69)$$

where ψ_n^{KS} represents the single particle eigenfunctions with energy ε_n, ε^{-1} indicates the dielectric function calculated within the framework of random phase approximation, V_C

stands for the bare Coulomb potential. To carry out the calculation for screened Coulomb interaction a full dielectric matrix is required which can be obtained from DFT.

2.7. Correlation and Hubbard U

The electronic structure of strongly correlated materials containing elements with partially occupied d or f states is poorly described by LDA or GGA. These approaches predict that rare earth insulator materials should show metallic property. The reason is due to inaccurate description of the correlation part of the DFT exchange correction functional for the localized states (3d, 4f). A significant improvement of the description of the localized 3d and 4f states can be made by using (LDA+U) or (GGA+ U) approach where the parameter U is used as an on-site replacement of LDA or GGA.[109, 110] The Coulomb U is defined as the difference in energy required to remove an electron from the occupied state to vacuum and to insert one electron to the unoccupied state from vacuum, referred to as the energy of the unperturbed system. Accuracy of this method is strongly dependent on the choice of the Coulomb U value. The expression for the generalized energy functional can be written as,

$$E^{LDA+U}[\rho^\sigma(r), n^\sigma] = E^{LDA}[\rho^\sigma(r)] + E^{ee}[n^\sigma] - E_{dc}[n^\sigma] \qquad (2.70)$$

where $E^{LDA}[\rho^\sigma(r)]$ represents the total energy functional according to local density approximation, ρ^σ is the total electron spin density, $E^{ee}[n^\sigma]$ stands for electron-electron interaction energy and $E_{dc}[n^\sigma]$ is double counting term, which takes care of the electron-electron interaction energy term already included in E^{LDA}.

$$E_{dc}[\rho^\sigma] = \frac{U}{2} n(n-1) - \frac{J}{2} \sum_\sigma n^\sigma(n^\sigma - 1) \qquad (2.71)$$

where U and J represent the screened Coulomb Hubbard and exchange parameters, respectively.

2.8. Basis Set

Basis set is the set of mathematical functions used to construct any unknown arbitrary wave function. Molecular orbitals are often expressed as a linear combination of atomic orbitals (LCAO) as,

$$\psi_i = \sum_{\mu=1}^{N} C_{\mu i} X_u \qquad (2.72)$$

where X_u indicates a predefined set of basis functions for the μ th orbital and $C_{\mu i}$ represents expression coefficients. A complete basis set should contain infinite number of basis functions to accurately represent the wave function. But in the practical scenario, a finite number of basis functions is employed due to computational limitation. The eror due to incomplete basis set is known as basis set truncation error. A good computational strategy should be such that the basis set truncation error is minimum, even though the number of basis function lies within the computational limit. The basis function should be such that the wave function is single valued, finite, continuous and quadratically integrable. The most popular basis sets for the electronic structure calculation includes

(i) Slater type orbital (STO)

(ii) Gaussian type orbital (GTO)

(iii) Plane wave basis set

2.8.1 Slater Type Orbital

The Slater Type Orbitals decay exponentially as a function of distance from the nucleus.[111] The mathematical form of STO can be written as

$$X(r,\theta,\phi) = Nr^{n-1}e^{-\xi r}Y_{l,m}(\theta,\phi) \qquad (2.73)$$

where (r,θ,φ) are the spherical coordinates, $Y_{l,m}$ stands for the conventional spherical harmonics, N is the normalization constant and ξ is known as the Slater orbital exponent.

The mathematical form of STO is closely related to that of the hydrogenic orbital, making it attractive for electronic structure calculation. The disadvantage of STO is that it contains no radial node and therefore, to introduce radial modes, atomic orbitals are given as a linear combination of STOs. Electrons near the nucleus are well described by the STOs. However non-availability of analytical solution of the general four centre integral in case of STO basis set, drastically limit their application in molecular systems of practical interest.

2.8.2. Gaussian type orbital (GTO)

In the year 1950, S.F boys proposed the Gaussian type functions for the atomic orbitals,[112] where the radial decay behaviour is changed to $e^{-\alpha r^2}$. The general functional form of a normalized Gaussian type orbital (GTO) in polar coordinate can be expressed as,

$$\psi_{\xi,h,l,m}(r,\theta,\phi) = NY_{l,m}(\theta,\phi)r^{2n-2-l}e^{-\xi r^2} \qquad (2.74)$$

where the exponent ξ controls the width of the GTO.

The main advantage of GTO basis set is that the analytical solution of the general four-index integral is available. Since, the product of two GTO results another GTO, many

centred two electron integrals can be expressed into much simpler form. Faster calculation is possible even for the electronic structure of polymeric system using GTO basis set. Although GTOs are computationally feasible, there exist certain limitations for their use as basis function. One of the major issues is related to the shape of the radial portion of the orbital. For example, as GTOs for S type functions are smooth and differentiable at r = 0 (nucleus), differing significantly from the real hydrogenic AOs which have a cusp. Also, the radial decay of all hydrogenic orbital is quite slow (exponential in r), while the decay of GTOs, is too fast (exponential in r^2) leading to reduction in amplitude with the distance. Therefore tail behaviour for GTOs is poorly described.

To overcome these limitations, the basis sets have been constructed as a building block to approximate STO, which retain the best features STOs (appropriate radial shape). In this case, the basis functions are expressed as a linear combination of several GTOs to give as good a fit as possible to the Slater orbital. The basis function defined as a linear combination of Gaussians is known as a contracted' basis function while the individual Gaussians involved to construct the controlled basis function is known as primitive Gaussian.

2.8.3. Plane Wave Basis Set

According to Bloch's theorem, the wave function for a periodic solid, must be composed of a phase factor and a periodic part that obeys $u_k(\vec{r}) = u_k(\vec{r} + \vec{a}_i)$, where $\vec{a}_1, \vec{a}_2, \vec{a}_3$ are the lattice vectors. Plane waves build a complex and orthonormal basis with periodicity. They are solutions of Schrödinger Equation under the influence of constant external potential, which is also approximately valid in the interstitial region in a periodic solid. However closer to the atomic nuclei the external potential is no longer a constant quantity and hence the solution of the Schrödinger Equation is written as a linear combination of plane waves.

In general a function in real space can be expressed as the Fourier transform of a function in reciprocal space,

$$u_k(\vec{r}) = \int e^{i.\vec{g}.\vec{r}} \tilde{u}_k(\vec{g}) d\vec{g} \qquad (2.75)$$

To maintain the periodicity of $u_k(\vec{r})$, values of $\vec{g}$ are restricted by the relation, $e^{i\vec{g}.\vec{a}_j} = 1$, i.e. $\vec{g}.\vec{a}_j = 2\vec{n}\pi$ for $\vec{a}_j$ with $j=1$, 2, 3, the three main lattice vectors. This indicates that, $\vec{g} = n_1\vec{b}_1 + n_2\vec{b}_2 + n_3\vec{b}_3$, where $\vec{a}_i.\vec{b}_j = \delta_{ij}$ and hence

$$\vec{b}_i = 2\pi \frac{\vec{a}_j \times \vec{a}_k}{\Omega} \text{ with } \Omega = \vec{a}_i.(\vec{a}_j \times \vec{a}_k) \text{ and } \vec{n} = (\vec{n}_1, \vec{n}_2, \vec{n}_3) \text{ represents a vector of integer}$$

numbers. Therefore, the $\vec{g}$ vectors in the Fourier transform are restricted precisely to the reciprocal lattice vector $\vec{G}$. The general expression for the wave function can be written as

$$\psi^{(k)}(r) = \frac{e^{i\vec{k}.\vec{r}}}{\sqrt{\Omega}} \sum_{G=0}^{\alpha} C_k(G) e^{i\vec{G}.\vec{r}} \qquad (2.76)$$

To maintain periodicity, the Fourier transform becomes a Fourier series, and $C_k(G)$ represents the Fourier coefficients. This restriction of $\vec{g}$ values to the reciprocal lattice vectors ensures that periodic boundary conditions are satisfied automatically. We now express plane wave basis function as

$$\phi_G(\vec{r}) = \frac{1}{\sqrt{\Omega}} e^{i\vec{G}.\vec{r}} \qquad (2.77)$$

For a periodic system one can write

$$\psi_k(\vec{r}) = \sum_G C_{k,G} e^{i(\vec{G}+k).\vec{r}} \qquad (2.78)$$

In principle, an infinite number of reciprocal lattice vectors G is required to define the wave function with infinite accuracy. However, the Fourier coefficient of the wave function become negligible at larger value of $|k + G|$, leading to truncation of plane wave expansion at a finite number of terms. Hence, the plane wave expansion is limited to all waves with kinetic energy lower than energy cut off (E_{cut}) as

$$\frac{\hbar^2}{2m}|k + G|^2 < E_{cut} \qquad\qquad (2.79)$$

In case of Γ-point (k=0) the above relation defines a sphere with a radius G_{cut} in the wave vector space, where, $|G| < G_{cut} = \sqrt{\frac{2mE_{cut}}{\hbar^2}}$ $\qquad\qquad$ (2.80)

In atomic units $(\hbar = m = 1), G_{cut} = \sqrt{2E_{cut}}$. Conventionally it is expressed in Rydberg unit (1 Ry = 0.5 a.u.= 13.6 eV) as $G_{cut} = 2\sqrt{E_{cut}(Ry)}$.

The error due to truncation of basis set can be minimized by increasing the cutoff.

There are several advantages of using plane wave basis: (i) Easy conversion of real space representation (the potential energy V has a diagonal representation) to momentum-space (the kinetic energy T is diagonal) via a Fast Fourier transform. (ii) convergence of physical properties is controlled by a single parameter, the cutoff energy, and can be monitored. (ii) straightforward calculation for Hellmann-Feynman forces acting on the atoms and the stress on the unit cell in terms of the expectation value of derivative of the Hamiltonian with respect to the ionic coordinates. (iv) avoid basis set superposition errors.

There are certain disadvantages of using plane wave basis set; (i) For systems of low dimensionality, such as molecules, wires, or surfaces, a significant computational effort is utilized to represent the vacuum, which is not particularly relevant. (ii) A very high energy cut off is required for the system, where the wave function close to the nuclei vary rapidly.

(iii) It is practically impossible to study charged systems in absence of any kind of charge compensating background using standard plane wave approach. Even for neutral molecules with a dipole moment, a spurious electrostatic interaction exists between the periodic images in the adjacent cells as the periodic boundary condition is automatically embedded into the plane wave scheme. As the decay of dipole-dipole interaction is not slow (R^{-3}), the cell size should be large enough to minimize this, which will again increase the computational cost due to involvement of large number of plane waves. Similar thing happens for non polar molecules with non zero quadruple moment, although quadruple-quadruple interaction decays relatively faster (R^{-5}).

2.9. Pseudo-Potential Approximation

The electronic wave function has complex nodal structure closer to the ionic cores. In the plane wave approach, this requires very high cut off energy in the k-space to describe the wave function at an acceptable accuracy. In general, the electronic wave function only outside the core region vary with the variation of chemical environment and contribute to the physical and chemical properties of the materials, so it is desirable to smoothen the nodal behaviour closer to the inter core region. This has led to the development of pseudopotential, where the core state is replaced by an effective potential. The size of basis set can be reduced considerably by using pseudopotential, which consequently reduces the computational cost without sacrificing much on the accuracy. Various pseudopotentials have been developed aiming at replacing the true atomic potential and reproducing the effect of the core electrons outside the core region in different chemical environment, while being computationally efficient. Pseudopotential can be generated empirically or using ab initio approach. In the empirical method, the parameters of the pseudopotential are obtained by fitting the experimental data. Hence, its accuracy is strongly dependent on the fitting process and its

application is also restricted to the material, from which the parameter has been calculated. On the other hand, pseudopotential in the ab initio method are calculated from the inner electronic states of atoms and independent of any other information of a chemical system. Therefore, ab initio pseudopotentials are more universal.

The basic idea of the ab initio pseudopotential approach can be illustrated by the concept of orthogonalized plane waves. In case of solid, the energy levels of the valence electrons can be calculated from a weak effective potential Vp, in which a major part of the potential energy (negative) inside the atomic core is cancelled by the kinetic energy of the valence electron (positive) in the same region.

The original nodal wave function can be expressed as

$$H|\psi_V\rangle = (T+V)|\psi_V\rangle = E_V|\psi_V\rangle \qquad (2.81)$$

The equivalent pseudo wave function can be written as

$$(H+V_R)|\phi_V\rangle = (T+V+V_R)|\phi_R\rangle \equiv (T+V_{PS})|\phi_R\rangle = E_V|\phi_R\rangle \qquad (2.82)$$

The smooth potential $(H+V_R)$ is referred to as pseudopotential V_{PS}, in the Phillips-Kleinman (PK) form, which can be defined as

$$V_{PS}^{PK} = V + \sum_c (E_V - E_c)|\psi_c\rangle\langle\psi_c| \qquad (2.83)$$

In case of orthogonalized plane wave form of the pseudopotential, the pseudo wave function is still quite 'hard core' and is proportional (not equal) to the real wave function outside the core region.

In the pseudopotential approach, the core is like a 'black box' from which the valence wave function is generated with some logarithmic derivative. Here, any core pseudopotential yielding the same logarithmic derivative should be a valid pseudopotential. However, the constructed pseudopotential must satisfy the following conditions: (i) pseudopotential should not oscillate within the core region, i.e., it should be smooth. The pseudopotential valence

wave function (Ψ_{PS}) does not contain any radial nodes. (ii) all electron and pseudopotential valence wave functions must be equal. (iii) all electron and atomic wave function are equal beyond a cutoff radius; (iv) integrated charge within the sphere of cut off radius for all electron atom and pseudoatom must be equal. Through a Fridel sum rule, the charge conserving feature is mapped into another feature: the logarithmic derivative of the real and pseudo wave function and their first energy derivative agree beyond the cutoff radius. Pseudopotential constructed using such a method is known as norm-conserving pseudopotential.[113, 114] They are relatively soft core and almost independent of energy, and the resulting ionic pseudopotential can be transferred to various atomic environment. However, to represent the charge distribution and moment of the potential energy wave function by the pseudowave function accurately, there is need for a core radius around the outermost maximum of the all electron wave function. Hence, the resulting pseudo potentials (e.g. first row, 3d, and rare-earth elements) require a large plane wave basis set. To handle this, the core radius is often significantly increased beyond the outermost maximum in the all electron wave function. Unfortunately, the transferability is adversely affected by the increase of core radius. Moreover, additional test calculations are required to demonstrate the reliability of such soft pseudopotentials for any new chemical systems. This leads to the development of new pseudopotential discussed below.

Ultra soft Pseudopotentail

To overcome the problem of norm-conserving pseudopotential, Vanderbilt and co-workers proposed a new kind of pseudopotential, known as ultrasoft pseudopotential.[115, 116] In this approach, the norm-conservation is relaxed and the resulting charge deficit is compensated by introducing localized atom-centred augmentation charges, which are defined as the difference in the charge density between the all electron and pseudo wave function. But for the sake of

convenience they are pseudized to treat the augmentation charges efficiently on a regular grid. The core radius of the pseudopotential can now be chosen around the half distance between the nearest neighbours and is independent of the location of the maximum of the all electron wave function. However, a small cutoff radius must be used only for the augmentation charges to restore the charge distribution and moment of all electron wave function accurately. The pseudized augmentation charges are normally treated on a regular grid in real space, which is not necessarily identical with that used for the representation of the wave function.

Vanderbilt's approach has been adopted extensively, especially for the calculation of 3d-transition metal elements due to reduction in the computational cost and improvement of accuracy by a significant extent. But the wide spread application of this approach is partly limited by the complex procedure for the construction of pseudopotential, which involves too many parameters, like several cutoff radii, etc. Therefore, extensive test calculations are essential to achieve an accurate and highly transferable pseudopotential.

Drawback of pseudopotential

There are certain drawback of pseudopotentials

(i) The pseudopotentials are not unique and hence test calculations should be performed before using them.

(ii) Some pseudopotential can be generated but they suffer from low accuracy and give rise to the ghost states.

(iii) Some properties, particularly, those strongly influenced by the core can not be described using pseudopotentials.

2.10. Projector Augmented Approach

To avoid the disadvantages of ultrasoft pseudopotential Blochl proposed projector augmented wave (PAW) method.[117-119] Blöchl introduced a linear transformation from pseudo wave function to all electron wave function and then applied this transformation to the Kohn-Sham functional to derive the PAW total energy functional in a consistent manner.

The basic concept of PAW method can be defined as follows

$$|\psi_n\rangle = \hat{T}|\tilde{\psi}_n\rangle \qquad (2.84)$$

where, $|\psi_n\rangle$ and $|\tilde{\psi}_n\rangle$ are the true wave function and auxiliary function, respectively. $\hat{T}$ represents the transformation operator, expressed as

$$\hat{T} = 1 + \sum_i (|\phi_i\rangle - |\tilde{\phi}_i\rangle)\langle\tilde{p}_i| \qquad (2.85)$$

where, $|\phi_i\rangle$ and $|\tilde{\phi}_i\rangle$ stand for all electron partial waves from true atomic potential and pseudo partial waves from pseudo potential, respectively. $\langle\tilde{p}_i|$ stands for the projection operator.

Here, the whole wave function for each electron is evaluated, in contrast to the other pseudo potential based approaches, where only the pseudo wave function is calculated. All integrals are evaluated as a combination of integral of smooth function extending through space and localized contribution calculated over Muffin-tin sphere, as in the case of augmented plane wave approach. Thus,

$$|\psi_n\rangle = |\tilde{\psi}_n\rangle + \sum_i (|\phi_i\rangle - |\tilde{\phi}_i\rangle)\langle\tilde{p}_i|\tilde{\psi}_n\rangle \qquad (2.86)$$

The full valence electron wave function is split into three parts. The construction of PAW data set is relatively easier as the PAW approach works directly with the complete all electron wavefunction and all electron potential, thus avoiding pseudization of the augmentation charges. Thus has been achieved by utilizing radial support grids around each atom instead of regular grids. The decomposition into regular grid and radial grid is complete

to such an extent that no cross term between the grids need to be evaluated. The PAW approach has been found to be a very powerful tool for the calculation of electronic structure within DFT. While retaining the correct description of nodal behaviour of the valence electron wave function, it shows the ability to incorporate upper core state in addition to the valence state in the self consistent iteration, without adding significant amount of computational cost.

2.11. Density of States

The actual number of electrons in a given energy states is determined by the number of states in the system, which is defined as[120,121]

$$N(E)dE = F(E)g(E)dE \qquad (2.87)$$

where $N(E)dE$ stands for the actual number of electrons present in the energy range E and $(E+dE)$ at any temperature, $F(E)$ is the probability function of the electron in the energy state E and $g(E)dE$ represents the number of available quantum states in the above energy range.

If we consider two spheres with radii n and n+dn in the n-space, the number of states of the energy less than E is given by the positive octant of the sphere

$$g'(E) = \frac{1}{8}\frac{4\pi n^3}{3} \qquad (2.88)$$

Since, all the points on the surface of a sphere with radius n ($n^2 = n_x^2 + n_y^2 + n_z^2$) will have same energy, one can write

$$g'(E) = \frac{1}{8}\frac{4\pi}{3}\left(\frac{8ma^2E}{h^2}\right)^{3/2} = \frac{4\pi V}{3h^3}(2m)^{3/2} E^{3/2} \qquad (2.89)$$

where $a^3 = V$. Differentiation of both sides of the above equation results into expression for the density of states $g(E) = (\partial g'(E)/\partial E)$ in the energy range of dE as,

$$g(E)dE = \frac{2\pi V}{h^3}(2m)^{3/2}E^{1/2}dE \qquad\qquad (2.90)$$

According to Pauli's exclusion principle, maximum two electrons can be accommodated in each state. So the actual density of state in a volume V is given by

$$g(E)dE = \frac{4\pi V}{h^3}(2m)^{3/2}E^{1/2}dE \qquad\qquad (2.91)$$

Thus density of states per unit volume and in a unit energy range is,

$$g''(E) = \frac{4\pi}{h^3}(2m)^{3/2}E^{1/2} \qquad\qquad (2.92)$$

which is a highly important quantity and is known as the density of states, given by

$$Density\ of\ states = \frac{4\pi}{h^3}(2m)^{3/2}E^{1/2} \qquad\qquad (2.93)$$

2.12. Optical Property

The optical processes like absorption, reflection, and transmission are observed in the case of solid materials.[122] There are various parameters in the solid to quantify these processes, which can be described by the properties of solid at macroscopic level or microscopic level. At the microscopic level, the complex dielectric function defined as

$$\varepsilon = \varepsilon_1 + i\varepsilon_2 \qquad\qquad (2.94)$$

is strongly correlated with the band structure and can be calculated either by density functional perturbation theory, or by summing over the conduction band states. Both the methods however deliver identical results and the convergence with respect to the number of conduction band states has also been found to be rather fast. In Vienna ab-initio simulation (VASP), the imaginary part of the complex dielectric function is calculated by summing over the conduction band using the expression below

$$\varepsilon_{\alpha\beta}^{(2)}(\omega) = \frac{4\pi^2 e^2}{\Omega} \lim_{q \to 0} \frac{1}{q^2} \sum_{C,V,K} 2w_K \delta(\varepsilon_{CK} - \varepsilon_{VK} - \omega) \langle u_{CK} + e_{\alpha q} | u_{VK} \rangle \langle u_{CK} + e_{\beta q} | u_{VK} \rangle^* \quad (2.95)$$

where the indices V and C refer to valence and conduction band states, respectively, u_{CK} indicates the cell periodic part of the orbital at the k-point K, and Ω is the volume of the primitive cell. The k-point weights, w_K, are defined such that they sum to unity, ω represents the frequency with dimension of energy, the vectors e_α indicates unit vectors for the three Cartesian directions, and q represents the Bloch vector of the incident wave. The real part of the dielectric tensor $\varepsilon_{\alpha\beta}^{(1)}$ is obtained from the imaginary part using Kramers-Kronig relation as

$$\varepsilon_{\alpha\beta}^{(1)}(\omega) = 1 + \frac{2}{\pi} P \int_0^\infty \frac{\varepsilon_{\alpha\beta}^{(2)}(\omega')\omega'}{\omega'^2 - \omega^2 + i\eta} d\omega' \quad (2.96)$$

where P denotes the principal value. The expression for the absorption coefficient, $\alpha(\omega)$, is given by

$$\alpha(\omega) = \sqrt{2}\omega \left(\sqrt{\varepsilon_1(\omega)^2 + \varepsilon_2(\omega)^2} - \varepsilon_1(\omega) \right)^{1/2} \quad (2.97)$$

2.13. Force Theorem and Geometry Optimization

The equilibrium geometry of a crystal structure can be obtained by minimizing the forces acting on each atom. These forces can be calculated using the Hellmann-Feynman theorem, which states that the force exerting on the ith nucleus in the electronic steady state is defined as

$$F_\alpha = -\frac{\partial E(R)}{\partial R_\alpha} = -\int \psi^*(\{\vec{r}_j\}; R) \frac{\partial H}{\partial R_\alpha} \psi(\{\vec{r}_j\}; R) d\tau \quad (2.98)$$

where, $E(R)$ represents the total energy of the system as a function of the nuclear coordinates $R = \{R_\alpha\}$, H stands for the Hamiltonian of the interacting electrons in presence of

external potential created by the nuclei, $\psi(\{\vec{r}_j\};R)$ indicates the electronic wave function for the ground state and the integration over τ represents integration over all electronic coordinates. The equilibrium crystal geometry is reached when the total force acting on the atoms is zero,

$$F_\alpha = -\frac{\partial E(R)}{\partial R_\alpha} = 0 \text{, for all } R_\alpha \tag{2.99}$$

Therefore, the optimized geometry can be obtained by calculating the first derivative of Bohr-Oppenheimer energy surface. However, in practical scenario, it is very difficult to obtain exactly zero forces. So, usually the desired force tolerance is set to 10^{-3} eV/Å to perform geometry optimization at a satisfactory level.

2.14. Bader Charges

The properties of materials are often correlated with the amount of charge transfer between atoms and ionic charges on atoms. Quantum mechanical theory cannot define the atomic charges in molecules or solid as it is not a observable quantity. Quantum mechanical calculations provide the introduction on the electronic charge density as a continuous distribution. The main difficulty is to partition the electrons among the constituent atoms. There are different schemes, namely Mulliken analysis, Bader analysis, etc., to extract this information. In the Mulliken analysis, the charge associated with the basis functions centered on a particular atom is assigned to that atom. This has been found to be a fast and useful approach to calculate the partial charges on the atoms. But, it is only applicable when the basis functions are centred on atoms and not applicable for the plane wave based calculations. A different approach has been proposed by Bader, which focuses entirely on the charge density. For a given geometry X, the gradient of the electron density, $\Delta\rho$ (r;X), through a trajectory are calculated in the direction of maximum increase/decrease of the density starting

from an arbitrary point r_0. As a result, the space is separated into basins (atoms) in different sets of trajectories where the path is terminated at the critical point, i.e., $\Delta\rho$ (r)=0. Bader proposed the concept that each atom (basin) is described by a region in real space enclosed by the surface through which there is no flux in the gradient vector field of ρ (r). This is known as zero-flux surface that every point in the surface satisfies $\Delta\rho$ (r). n(r)=0

where, n(r) is the unit vector perpendicular to the surface. then, the Bader charge on the atoms are determined through integration over the electron density within individual basins. Because, this approach is based solely on the charge density, it is independent to the choice of basis set used in the calculation. So, it can be applicable for the plane wave based calculation, as well as atomic wave function based calculation. However, the major problem is the computational effort and the complexity of the algorithm. Henkelman proposed an efficient, robust approach for the decomposition of electronic charge density into atomic contributions.[123-125] Later on, he developed a grid-based Bader analysis algorithm for partitioning a charge density grid into Bader volume. The partitioning algorithm follows the steepest ascent path along the charge density gradient from one grid point to another grid point unitil a charge density maximum is reached. As the algorithm assigns grid points to charge density maxima, subsequent parts are terminated when they reach previously assigned grid points. This algorithm scales linearly with the number of grid points. It is very much efficient and even allows for the analysis of large grid generated from DFT calculation using plane wave basis set.

2.15. Introduction to VASP

The Vienna ab-initio simulation Package (VASP) is one of the powerful tools for performing first principles based calculations within DFT.[126] It involves either ultrasoft pseudopotential or the PAW method, and a plane wave basis set. VASP uses efficient schemes for matrix

diagonalisation and an efficient Pulay/Broyden charge density mixing. Thus it avoids all problems associated with the original Car-Parrinello method, where integration of electronic and ionic equation of motion occurs simultaneously. The ion-electron interaction is described either by ultrasoft pseudopotentail or PAW method, which considerably reduces the number of plane waves per atom for the transition metal and first row elements. Generally in the case of bulk material, the number of plane waves per atom required does not cross 100 and in most cases even 50 plane waves per atom is sufficient. In the VASP, the prefactor for the cubic part (N^3, N is the number of valence electrons in the system) is too small to be neglected, and thus scaling with respect to system size occurs in an efficient way. This becomes possible because the nonlocal contribution to the potential is evaluated in real space and the number of orthogonalisation is kept small. VASP can handle systems containing up to 400 valence electrons. VASP uses self consistency cycle to calculate the electronic ground state and this scheme is combined with efficient numerical methods to evaluate the self consistent solution for the Kohn-Sham orbitals in an efficient, robust and fast manner. VASP uses fastest scheme currently available for the matrix diagonalization iteratively. A full featured symmetry code is implemented to determine the symmetry of arbitary configuration automatically. The symmetry code is also utilized to set up the Monkhorst Pack special k-point leading to an efficient calculation of bulk materials and symmetric clusters. The integration of the band structure energy over the Brillion zone can be carried out either with smearing method or tetrahedron method. Tetrahedron method with Blöchl's correction remove the quadratic errors of linear tetrahedron method and significantly enhances the convergence speed with respect to the number of special k-points.

Chapter 3

Improving Visible Light Photocatalytic Activity of NaTaO₃

3.1 Introduction:

Till now, a wide range of photocatalysts have been developed, most of which are oxide based semiconductors, and recently various perovskite type materials have also attracted immense interest due to their potential catalytic property to split water. Among them, $NaTaO_3$ has been shown to be an excellent photocatalyst for the generation of hydrogen as well as the degradation of organic pollutants.[127-131] However, its large band gap (4.1 eV) limits the photoactivity only to the range of UV light, which covers ~5% of the solar spectrum. Hence one of the biggest challenges is to modify its band gap so that it can utilize the visible light of the solar spectrum for photocatalytic applications. The introduction of foreign elements in the crystal lattice to change the band structure, has been observed to be one of the most promising ways to improve the visible light activity of the wide band gap semiconductor photocatalysts. Till date several efforts have been made to develop a wide range of doped $NaTaO_3$ materials, which have appreciable visible light activity. Thus, Zhou et al theoretically predicted that the doping of Fe in the Ta lattice site of $NaTaO_3$ crystal significantly improves the visible light activity by reducing the band gap by 2 eV,[132] while Li et al and Kang et al introduced Bi at the Ta lattice site to reduce the band gap for the utilization of visible light.[133,134] Later on, Kanhere et al showed that the reduction of band gap is much more prominent when the Bi substitution is implemented in both Na and Ta sites.[135,136] Very recently, Su et al synthesized Cr doped $NaTaO_3$ by replacing both Ta and Na and observed significant increase of visible light activity.[137] However, mono-doping, particularly when the valence of the dopant element and that of the host element are different, is associated with the formation of defects, which are known to be an effective source for electron hole recombination. In the case of, anion doping, the N doped systems have been studied by different groups. [138-142] For example, Fu et al synthesized N doped $NaTaO_3$ for the

decomposition of formaldehyde under visible light.[138] Wang et al reported that the incorporation of N can significantly enhance the visible light activity and photocurrent density as compared to undoped $NaTaO_3$.[139] Recently, Jiang and his group observed an improved photocatalytic activity of N doped $NaTaO_3$ for the degradation of Methylene Blue under visible light.[140,141] There are several reports which have shown that N doping in an oxide based semiconductor creates discrete intra-band gap states, resulting into the narrowing of band gap.[143-146] However, these states can promote undesirable electron hole recombination, and thus reduce the photoactivity.[147] The replacement of O^{-2} by N^{-3} can promote the creation of oxygen vacancy due to charge mismatch and such vacancy related defects are known to be efficient centre for trapping charge carriers.[148-150] To overcome this, co-doping strategy has been employed extensively for various semiconductor photocatalysts.[151-155]

3.2. Computational Methods

Projected augmented wave (PAW) method has been employed throughout the calculation using Vienna ab initio simulation package (VASP) software. During geometry optimization, we use generalized gradient approximation (GGA) with Perdew-Burke-Ernzerhof (PBE) functional for the exchange correlation contribution. The integration over the first Brillouin zone was carried out using Monkhorst and Pack scheme and 6 x 6 x 6 grid was used for k-point sampling. For the calculation of band structure, density of states (DOS) and optical property, we employ screened hybrid functional as prescribed by Heyd, Scuseria, and Ernzerhof (HSE) functional. In the HSE functional, the exchange-correlation energy is expressed as

$$E_{XC}^{HSE} = \frac{1}{4} E_X^{SR}(\mu) + \frac{3}{4} E_X^{PBE,\, SR}(\mu) + E_X^{PBE,\, LR}(\mu) + E_C^{PBE} \qquad 3.2.1$$

In this functional, the electron-electron interaction is separated into short ranged (SR) and long ranged (LR) parts, defined by the screening parameter μ. In hybrid density functional based calculations, different mixing of the exchange parameter and the screening parameter has been tested to reproduce the experimental band gaps. In the present hybrid functional study, we employ the standard exchange mixing parameter of 25% and calculate the band gap of undoped $NaTaO_3$ with three different screening parameter values, viz., 0.20 Å^{-1}, 0.15 Å^{-1} and 0.10 Å^{-1}.

The screening parameter was then kept fixed at 0.15 Å^{-1} since it was found to successfully reproduce the experimental band gap of $NaTaO_3$. The k-point mesh 3 x 3 x 3 was set for the hybrid functional calculations. The cutoff energy of 500 eV has been chosen for the plane wave basis sets. Spin polarized calculations were performed for pure as well as doped systems. To investigate the change in optical behavior due to co-doping we have performed the frequency-dependent dielectric matrix calculation, as implemented in VASP.

3.3 Photocatalytic Activity of NaTaO$_3$ Doped with N, Mo and (N, Mo)

Introduction of nitrogen in place of oxygen leads to a system deficient by one electron since the valence shell of N consists of one less electron than oxygen. Hence the co-dopant atom should introduce one extra electron to form a charge compensated system. In this study, we propose to use the N, Mo co-dopant pair to improve the photoactivity of NaTaO$_3$ under visible light. We investigate theoretically the electronic structure of (N, Mo) co-doped NaTaO$_3$ and compare the results with those of undoped and mono-doped NaTaO$_3$ systems. In the co-doped system, the presence of Mo will nullify the electron deficiency in the N doped NaTaO$_3$ by providing one more extra electron to the system, and hence the formation of charge related defect should be minimum. To investigate the effect of relative distance between N and Mo, we consider two different configurations for the co-doped systems. The crystal structure of NaTaO$_3$ varies depending on the synthetic conditions, forming mainly cubic (Pm-3m), monoclinic (P2/m), and orthorhombic (Pcmn) phases having different photocatalytic behavior.[156-159] The present study focuses on the orthorhombic structure, with Pcmn space group, which is the most stable structure at room temperature, and is described by tilted TaO$_6$ octahedra.

3.3.1. Results and Discussion

The valence states of Na ($3s^1 2p^6$), Ta ($6s^2 5d^3$), Mo ($5s^2 4d^4$), O ($2s^2 2p^4$), and N ($2s^2 2p^3$) were considered for the construction of the PAW potentials. The DFT based electronic structure calculations, using different density functionals, have been carried out for the NaTaO$_3$ and its

doped counterparts with mono-doping using either N or Mo and co-doping using both N and Mo. The calculated results on the band gaps, density of states and other related energy properties, optical properties and photocatalytic activity are discussed below.

3.3.1.1. Electronic Structure of Pure NaTaO$_3$ and its Doped Counterparts

The initial geometry for the orthorhombic structure of NaTaO$_3$ has been obtained using the structural data from ICSD database.[160] To model the doped NaTaO$_3$, we consider 2 x 1 x 1 supercell for the orthorhombic structure (Figure 3.3.1), which consists of 8 Na, 8 Ta, and 24 O atoms. The mono-doped systems were modeled by replacing one of the oxygen or tantalum atom by N or Mo atom, respectively in the supercell, while for co-doping one oxygen atom and one Ta atom have been substituted by one N and one Mo atom, respectively. Geometry optimization has been carried out using DFT procedure with PBE functional and the band structure related properties are discussed here for undoped NaTaO$_3$ as well as its mono- and co-doped counterparts.
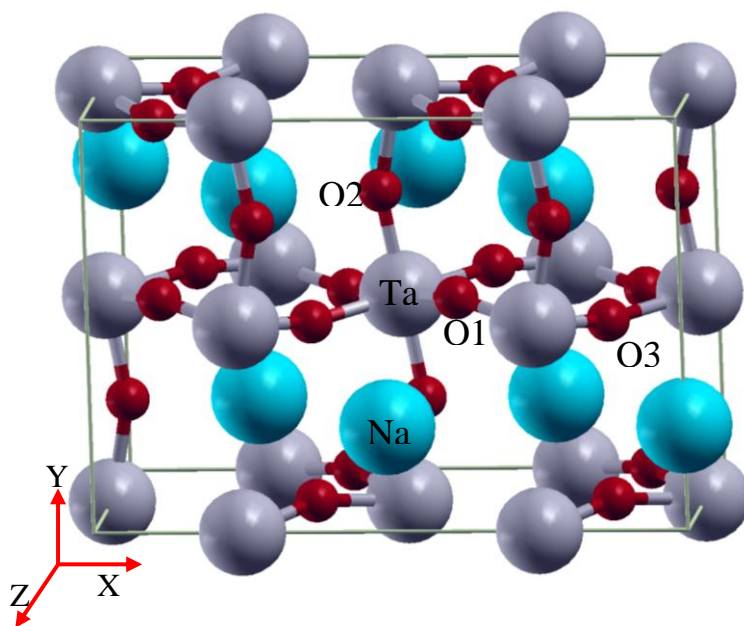
Figure 3.3.1: Supercell structure for orthorhombic $NaTaO_3$. The lattice sites of the dopant are marked by Ta1, O1, O2, and O3.

3.3.1.1.1. Pure NaTaO$_3$

The optimized lattice parameters are found to be a=5.52 Å, b=7.86 Å and c=5.57 Å (experimental lattice constants are: a=5.48 Å, b=7.79 Å and c=5.52 Å). Table 3.3.1 reports the band gap values calculated using different energy density functionals, such as the HSE functional (with different screening parameter), PBE0 and PBE functionals. The results indicate that the band gap obtained using HSE functional with μ =0.15 Å^{-1} (4.05 eV) is closer to the experimental value (4.1 eV). The band structure plot for 2 x 1 x 1 supercell has been presented in Figure 3.3.2a. Figure 3.3.3a displays the projected density of states (PDOS) which indicate that the top of valence band is mainly contributed by O 2p state, while the conduction band minimum is dominated by Ta 5d state. This is also evident in the isosurface plot for the valence band maximum (VBM) and conduction band minimum (CBM) (Figure 3.3.4).
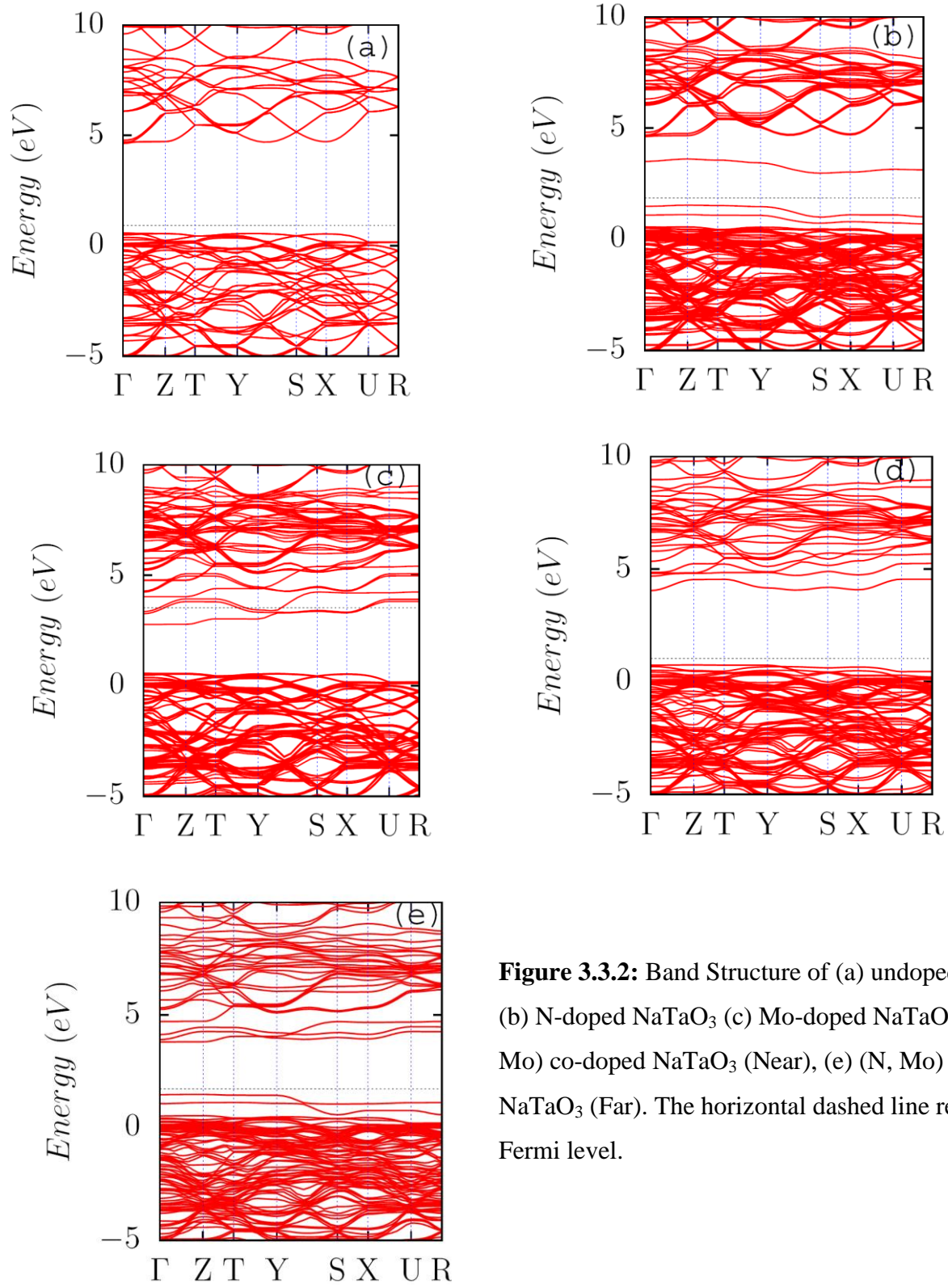
Figure 3.3.2: Band Structure of (a) undoped $NaTaO_3$ (b) N-doped $NaTaO_3$ (c) Mo-doped $NaTaO_3$ (d) (N, Mo) co-doped $NaTaO_3$ (Near), (e) (N, Mo) co-doped $NaTaO_3$ (Far). The horizontal dashed line represents Fermi level.

Hence band gap narrowing by the upward shifting of the valence band can be attained by anionic doping, with a dopant having higher p orbital energy than O 2p energy, while, for a shift in the conduction band position to lower energy, cationic doping using a dopant, with lower d orbital energy than that of Ta 5d should be implemented. In the next subsection, we discuss the effect of doping on the electronic structure of $NaTaO_3$.
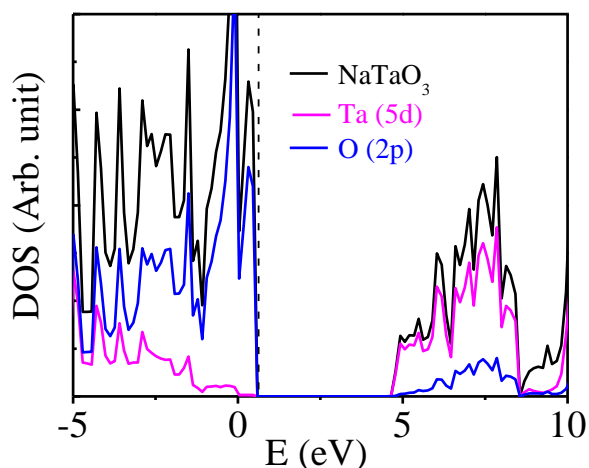
Figure 3.3.3: Total and projected density of states of $NaTaO_3$. Vertical dashed line indicates Fermi level.

Table 3.3.1. The calculated band gap for $NaTaO_3$ at the level of PBE, HSE (μ=0.2, 0.15, 0.1) and PBE0 method and experimental result (Ref 7)

Method	Band Gap (eV)
Experimental	4.1
PBE	2.57
HSE (μ=0.2 $\mathring{A}^{-1}$)	3.90
HSE (μ=0.15 $\mathring{A}^{-1}$)	4.05
HSE (μ=0.1 $\mathring{A}^{-1}$)	4.23
PBE0	4.67
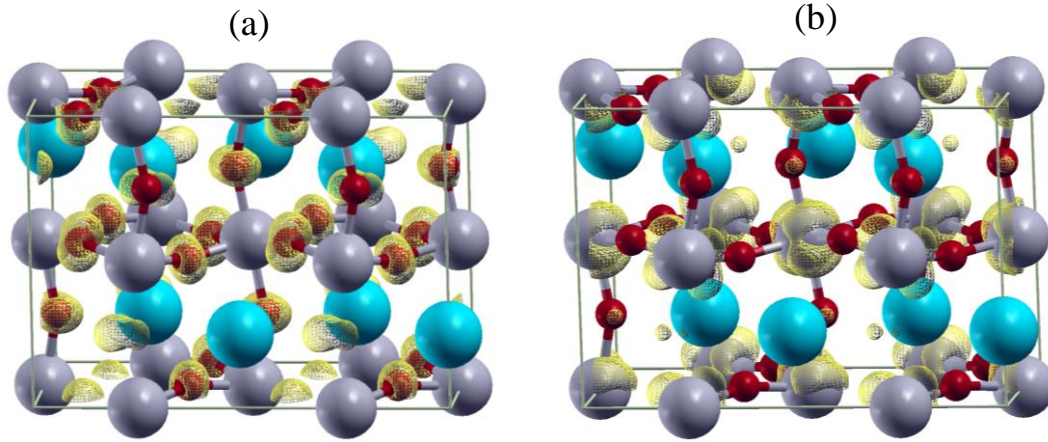
Figure 3.3.4: The isosurface plot of the (a) valance band maxima and (b) conduction band minima for $NaTaO_3$ (isovalue considered for the contour plot is 0.02 electron/$Å^3$).

3.3.1.1.2. N-doped $NaTaO_3$

We have considered two different configurations for the N doped system by introducing N at the O1 and O2 positions, respectively (Figure 3.3.1). The introduction of N in place of oxygen does not lead to much structural changes, as the size of nitrogen is almost same as that of oxygen. To get an idea about the stability of the mono-doped systems, we calculate the defect formation energy (E_f) using the following relation:

$$E_f = E_{N-NaTaO3} + \mu_O - E_{NaTaO3} - \mu_N, \qquad (3.3.1)$$

where E_{NaTaO3} and $E_{N-NaTaO3}$ are the total energies of the pure and N-doped $NaTaO_3$, respectively. The quantities μ_O, and μ_N, represent the chemical potential for oxygen and nitrogen atoms, respectively. The defect formation energy varies with the nature of synthesis condition (i.e. O-rich to Ta-rich). In the case of $NaTaO_3$, the chemical potential of the constituent elements must satisfy the relationship

$$\mu_{Na} + \mu_{Ta} + 3\mu_O = \mu_{NaTaO3}, \qquad (3.3.2)$$

where μ_X denotes the chemical potential of the species X.

Under the environment of O-rich condition, μ_O is calculated from the energy of an oxygen molecule (μ_O = ½ μ_{O2}) and μ_{Ta} is calculated from equation (3.3.2). In the case of Ta-rich condition, μ_{Ta} is obtained from the energy of the Ta atom in the bulk crystal and μ_O is determined from equation (3.3.2). μ_N has been calculated as the energy of the nitrogen atom in the homonuclear diatomic molecules in gas phase, i.e., μ_N = ½ μ_{N2}. The calculated formation energy for the N doping is found to be 5.16 eV/supercell and 1.18 eV/supercell for the oxygen-rich and oxygen-poor (Ta-rich) cases, respectively. The formation energy data indicate that the first structure (O1 substitution) is energetically more stable (by 0.04 eV) as compared to the other (O2 substitution).

We now discuss the changes in the electronic structure due to N doping in the $NaTaO_3$ crystal considering the lower energy structure. The positions of the band edges indicate that the N substitution does not bring any shift in the position of the conduction band edge as compared to the pure system. Figure 3.3.2b displays the band structure plot, where the discrete states above the valence band, localized above and below the Fermi level are observed. The calculated band gap for the structure is 3.09 eV, which is 0.96 eV lower as compared to that of undoped $NaTaO_3$. Analysis of PDOS (Figure 3.3.5a) indicates that the impurity states just above the valence band are contributed by both O 2p and N 2p states.

The photoexcited electron now requires lower energy to be transferred to the conduction band due to the presence of these localized states. However, the empty states (above the Fermi level) are highly undesirable for photocatalytic activity as they can trap the charge carriers and enhance the electron-hole recombination process. In addition, N doping leads to the formation of oxygen vacancy in the crystal structure to compensate for the additional charge. The presence of oxygen vacancy in such semiconductors also plays crucial role in reducing the photocatalytic

efficiency by promoting the recombination of photogenerated charge carriers. These factors limit

the photocatalytic efficiency of N doped NaTaO$_3$.
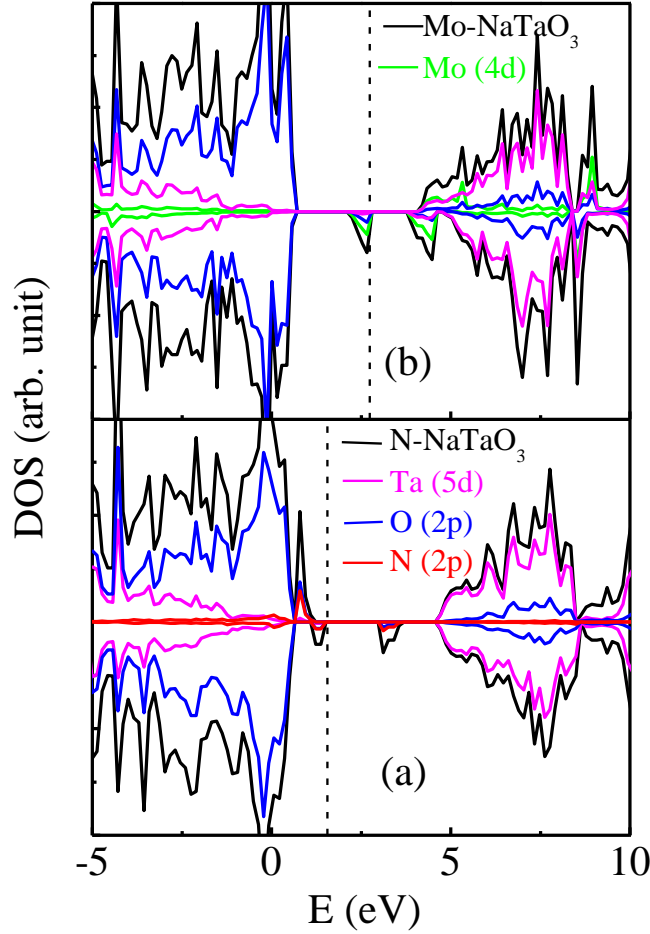
Figure 3.3.5: Total and projected density of states of (a) N doped NaTaO$_3$ (b) Mo doped NaTaO$_3$. Vertical dashed line indicates Fermi level.

3.3.1.1.3. Mo-doped NaTaO$_3$

To model the Mo-doped NaTaO$_3$ we replace Ta1 (Figure 3.3.1) by Mo. The cell volume for the

Mo doped system is slightly less due to smaller radius of Mo as compared to that of Ta. The Mo-

O distance (1.97 Å) is also shorter than the Ta-O bond length. The defect formation energy for

the Mo-doped system is calculated using the relation

$$E_f = E_{Mo\text{-}NaTaO3} + \mu_{Ta} - E_{NaTaO3} - \mu_{Mo,} \qquad (3.3.3)$$

where, μ_{Mo} denotes the chemical potential of Mo and is calculated from the energy of an Mo atom in the bulk crystal. $E_{Mo-NaTaO3}$ stands for the energy of the Mo-doped $NaTaO_3$. The quantity μ_{Ta} , the chemical potential of Ta, is calculated from the energy of the Ta atom in the bulk crystal in the case of Ta-rich condition, while in the O-rich condition it is calculated using equation (2). The formation energies for Mo doping are calculated to be 4.08 eV/supercell and -7.91 eV/supercell under Ta-rich and O-rich conditions, respectively. Figure 3.3.2c shows the band structure plot for the Mo doped system. The impurity states appear just below the conduction band, leading to the reduction of band gap to 1.42 eV, which is ideal for visible light absorption. The Fermi level is found to be within the conduction band, which indicates excess electron in the system as the valence shell of Mo contains one more electron than that of Ta. Analysis of the PDOS (Figure 3.3.5b) indicates that the mid gap states located just below the Fermi level, are mainly contributed by Mo 4d and O 2p states. The mid gap states have an adverse effect on the photocatalytic property of the material, as the mobility of the charge carrier is hindered due to the presence of such isolated states.

3.3.1.1.4. (N, Mo) co-doping

As discussed in the earlier section, the mono-doping with either anion (N) or cation (Mo) introduces isolated states in between the valence and conduction bands, and thus can increase the electron hole recombination rate. The charge imbalance due to doping may also lead to the formation of defects, which are known to be efficient source of charge carrier trapping. To overcome these problems, we adopt charge compensated co-doping approach to modify the band structure of $NaTaO_3$ in a controlled manner. In the present study we consider two different configurations obtained by varying the N-Mo distance to model the co-doped system. In one

case, Mo and N are directly attached occupying Ta1 and O1 lattice sites (Figure 3.3.1), respectively [N-Mo-NaTaO$_3$ (Near)], while in the other configuration they are located far from each other (Ta1 and O3 in Figure 1 [N-Mo-NaTaO$_3$ (Far)]). The optimized Mo-N distances for the 'Near' and 'Far' configurations are 1.75 Å and 4.08 Å, respectively. We have calculated the formation energy for both the configurations under Ta-rich as well as O-rich conditions using the relation below

$$E_f = E_{Mo,N\text{-}NaTaO3} + \mu_{Ta} + \mu_O - E_{NaTaO3} - \mu_{Mo} - \mu_N \qquad (3.3.4)$$

where $E_{Mo,N\text{-}NaTaO3}$ is the energy of the (Mo, N) co-doped NaTaO$_3$. This indicates that the co-doping is most favored under O-rich conditions owing to large negative values of formation energy with values of -5.08 eV/supercell and -4.13 eV/supercell for the 'Near' and 'Far' configuration, respectively. (The formation energies are 2.92 eV/supercell and 3.88 eV/supercell under Ta-rich condition.) The formation energy results indicate higher stability of the 'Near' co-doped configuration as compared to the 'Far' co-doped configuration.

Since the 'Near' configuration is energetically more stable, one might expect to get the 'Near' configuration more easily. While this may be true for experimental techniques like sol-gel method or other wet chemistry methods,[161] the situation may be different if the synthetic procedure involves techniques like magnetron sputtering or supersonic cluster beam deposition.[162] In the present context, in the 'Near' case, the co-dopant N is located in a site which is nearest neighbor of the other co-dopant Mo, while in the 'Far' configuration there is no direct Mo-N bonding. In the NaTaO$_3$ supercell, there are 24 oxygen lattice sites and 8 tantalum lattice sites. In the magnetron sputtering or supersonic cluster beam deposition techniques, the dopants Mo and N are considered to be distributed among the lattice sites randomly. Once Mo is introduced into the crystal structure, the number of lattice sites available for N to occupy is 6 for

the nearest neighboring sites around Mo and 18 for the other sites. Thus, the probability of the N atom to occupy a site which is nearest neighbor of Mo atom is (6/24), i.e. (1/4), while, the probability of its occupying sites other than a nearest neighboring site is (18/24), i.e. (3/4). This can provide an interpretation for the formation of the 'Far' configuration as the major fraction in these techniques.

Thus, the possibility of obtaining the 'Far' configuration is quite evident, which is also supported by analogous situation, encountered in the recent experimental and theoretical studies on (Cr, N) and (Cr, C)-co-doped TiO_2 by McDonnell et al[163] as well as the synthesis of (Cr, N) co-doped TiO_2 by Chiodi et al[55] using supersonic cluster beam deposition technique. In the first study[54], although DFT predicted lowest energy configuration was the "Near" one, no experimental evidence of Cr-N or Cr-C bond was found. Analogously, in the second study[164] as well, there was no evidence of direct bonding between Cr and N, indicating that the N is not in the neighboring lattice site of Cr.

We have calculated the binding energy of the dopant pair to get an idea about the stability of the co-doped systems using the formula

$$E_b = E_{N\text{-}NaTaO3} + E_{Mo\text{-}NaTaO3} - E_{Mo\text{-}N\text{-}NaTaO3} - E_{NaTaO3} \qquad (3.3.5)$$

The positive binding energy values for the 'Near' configuration (2.33 eV) and the 'Far' configuration (1.37 eV) indicate the stability of the co-doped systems.

Figures 3.3.2d and 3.3.2e represent the band structure plots for the co-doped system with 'Near' and 'Far' configurations, respectively. The calculated band gap for the 'Near' configuration reduces to 3.31 eV due to shift in the conduction band and the valence band with respect to that of undoped $NaTaO_3$. The analysis of PDOS (Figure 3.3.6a) indicates that the valence band maxima are mainly contributed by O 2p and N 2p states, while the bottom of the

conduction band is composed of Mo (4d), Ta (5d) and O (2p) states. However, the reduction of the band gap is much more significant in the case of 'Far' configuration. The calculated band gap is 2.33 eV, which ensures the suitability for absorption of visible light. A critical inspection of the PDOS plot (Figure 3.3.6b) indicates that the contribution of some Ta 5d states, which was not seen in earlier case, along with O 2p and N 2p states, is responsible for the large shift in the valence band. The shifting of the conduction band is also higher than the 'Near' configuration.
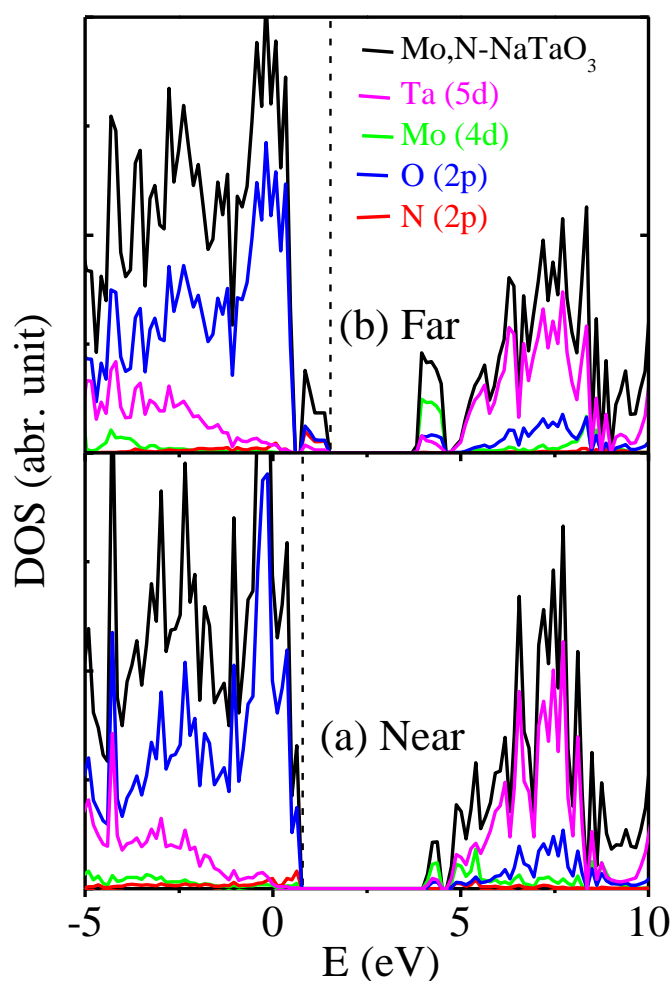
Figure 3.3.6: Total and projected density of states of (a) (N, Mo) co-doped NaTaO$_3$ (Near) (b) (N, Mo) co-doped NaTaO$_3$ (Far). Vertical dashed line indicates Fermi level.

The isosurface plots (Figure 3.3.7 and 3.3.8) for the VBM indicate that when Mo and N are directly attached ('Near' co-doping), the electron density is found to be distributed on both oxygen and nitrogen centers, while in the 'Far' co-doped case, the electron density is more localized on the N center. This indicates that the hybridization of N 2p and O 2p is stronger in the first case. To get a detailed insight, we have performed Bader charge density analysis, which reveals that the electronic charge on the N center is -1.06 for the 'Near' configuration which is less as compared to -1.42 in the 'Far' configuration. This indicates higher ionic character of the metal-nitrogen bond in the 'Far' configuration. This is also supported by the total charge density distribution plots (Figure 3.3.9), where we can see that the nitrogen charge density is more delocalized towards the metal center in the case of 'Near' configuration. This leads to more stabilization of N 2p orbital, resulting in less reduction in the band gap in 'Near' configuration. The most interesting outcome from the results presented in this subsection is that the discrete states, as observed in the case of mono-doped systems due to charge mismatch, disappear and a continuum band structure is formed.
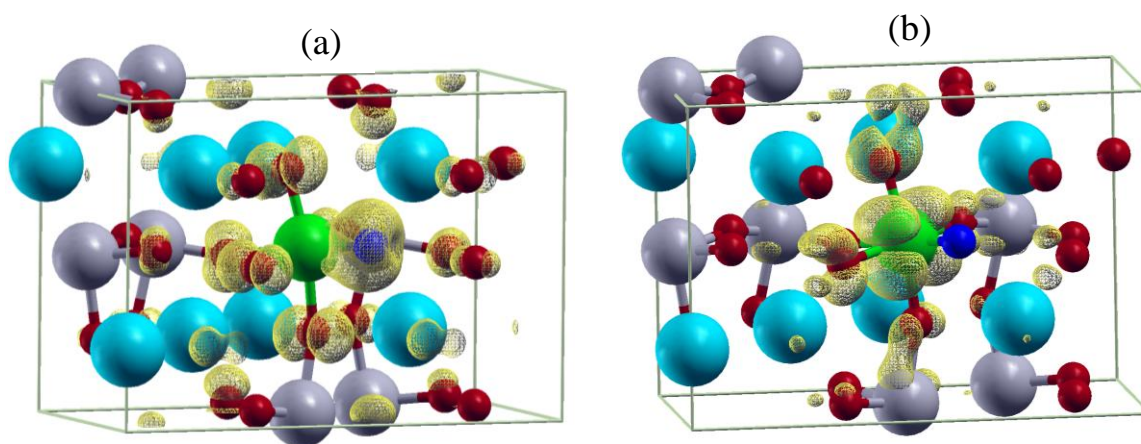
Figure 3.3.7: The isosurface plot of the (a) valance band maxima and (b) conduction band minima for (N, Mo) co-doped NaTaO$_3$ (Near).   (● Mo, ● N)
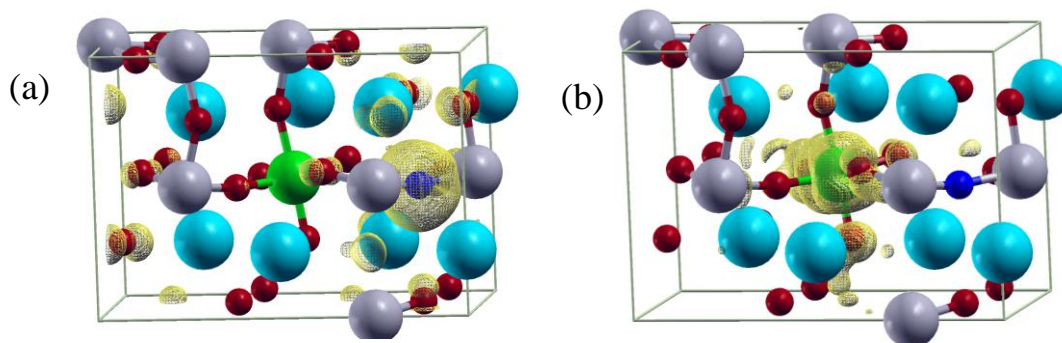
Figure 3.3.8: The isosurface plot of the (a) valance band maxima and (b) conduction band minima for (N, Mo) co-doped $NaTaO_3$ (Far).

This is clearly due to the presence of Mo, which compensates for the electron deficiency in the N-doped $NaTaO_3$. Thus, the presence of both Mo and N leads to the formation of a charge compensated system, which is also isoelectronic with the undoped system. Thus the impurity induced mid gap states are passivated by introducing both N and Mo simultaneously in the $NaTaO_3$ crystal lattice.
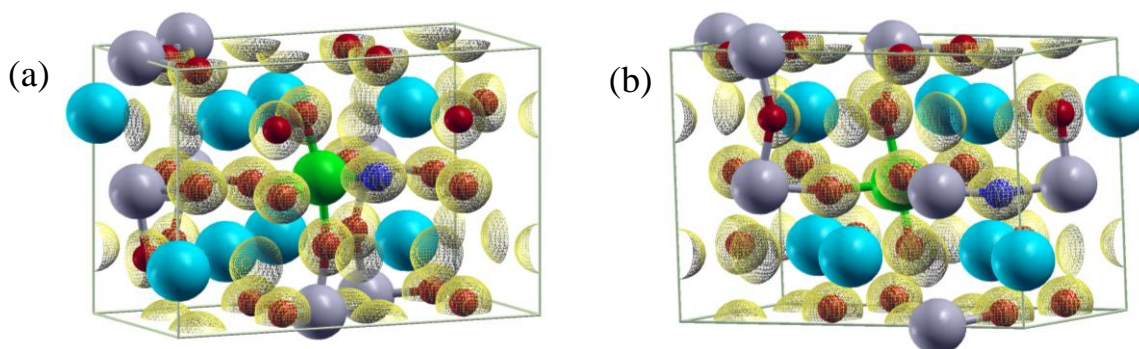
Figure 3.3.9. The isosurface plot of the total charge density of (N, Mo) co-doped $NaTaO_3$ (a) 'Near' and (b) 'Far' configurations.

3.3.1.2. Optical Property

Now we discuss the absorption properties based on frequency dependent dielectric function calculation. The absorption coefficient $\alpha(\omega)$ has been calculated using the relation

$$\alpha(\omega) = \sqrt{2}\omega\left(\sqrt{\varepsilon_1(\omega)^2 + \varepsilon_2(\omega)^2} - \varepsilon_1(\omega)\right)^{\frac{1}{2}}$$

(3.3.6)

where, ε_1 and ε_2 are the real and imaginary parts of the dielectric tensor, respectively. Figure 3.3.10 shows that the absorption curves are shifted to the visible region due to co-doping with (Mo, N). The (Mo, N) co-doped systems with 'Far' configuration shows appreciable visible light activity, and hence is expected to be a good catalyst for visible light driven photochemical processes.
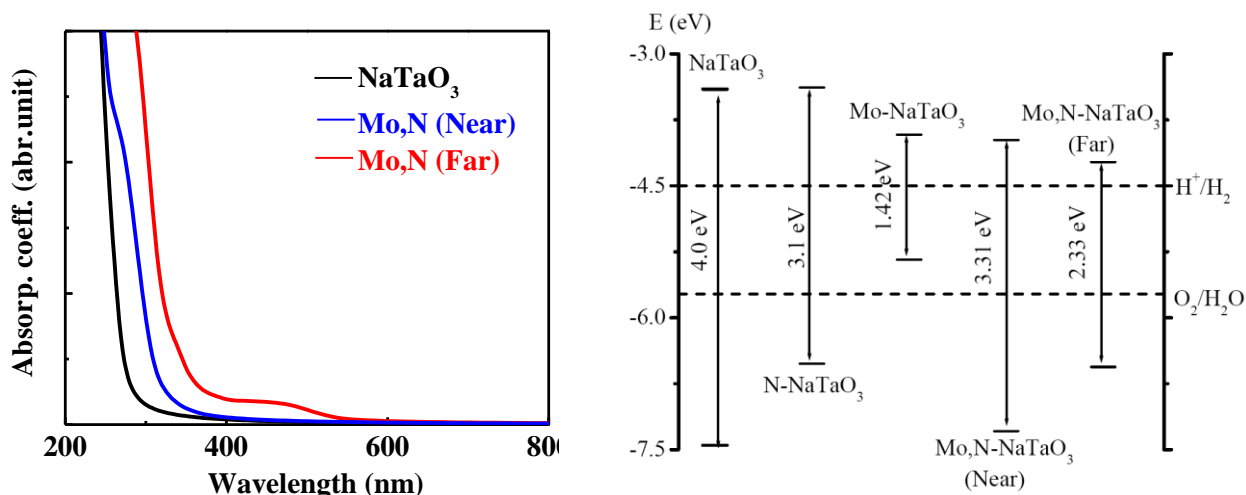
Figure 3.3.10: The calculated optical absorption curves for the undoped and co-doped NaTaO₃.

Figure 3.3.11: The calculated VBM and CBM positions of mono-doped and co-doped NaTaO₃ with reference to the respective experimental values of undoped NaTaO₃.

3.3.1.3. Photocatalytic Activity

While modifying the band gap of a semiconductor, one should be aware of the positions of the band edges for a spontaneous redox process. To assess the photocatalytic performance we align the CB and VB energy levels of the mono-doped and co-doped systems with respect to that of the undoped $NaTaO_3$. It is observed that for the undoped $NaTaO_3$ the CBM position is 1.1 eV higher than the hydrogen reduction level and the VBM is 1.77 eV lower than the water oxidation level. The CBM values for the doped and co-doped systems are obtained from the corresponding DOS plots by taking into account the relative location with reference to the undoped $NaTaO_3$. The VBM levels are calculated from the respective energy gaps. Figure 3.3.11 shows that the VBM level for the N doped $NaTaO_3$ is 0.79 eV lower and the CBM level is 1.12 eV higher than the water oxidation and reduction levels, respectively. On the other hand, the VBM of the Mo doped $NaTaO_3$ lies 0.39 eV above the water oxidation level, indicating the possibility of no oxygen evolution activity of the system. However, the position of CBM (0.58 eV above the water reduction level) allows hydrogen release. In the case of co-doped system, the positions of both CBM and VBM are favorable for the water reduction and oxidation processes, respectively. For the (Mo,N) co-doped 'Near' configuration, there has been a small upward shift of the VBM, which is relocated at 1.56 eV below the water oxidation level, while the CBM move downward by 0.52 eV with respect to that of $NaTaO_3$. However, in case of (Mo,N) co-doped 'Far' configuration, the VBM is located below the water oxidation level by 0.83 eV and the CBM position is 0.27 eV higher with respect to water reduction level. Thus, the present study indicates that co-doping with Mo, N modifies the band structure of $NaTaO_3$, making it more suitable to absorb the visible light, maintaining its photocatalytic activity.

3.3.2. Conclusion

We have investigated here the effect of co-doping to improve the photocatalytic performance of NaTaO$_3$ by using hybrid density functional calculations. The role of the individual dopants on the band structure has been explored. The formation energy for the incorporation of N is shown to be higher than that in the case of Mo doping. Although the mono-doping of either N or Mo is successful in improving the visible light activity, the impurity induced intraband gap states may promote electron hole recombination and consequently reduce the photocatalytic efficiency. To avoid those undesirable states, we adopt a charge compensated co-doping approach by introducing Mo and N in the NaTaO$_3$ crystal lattice. The band gap is reduced significantly for the Mo, N co-doped system with 'Far' configuration, to shift the absorption curve to the visible region. In this case, the impurity states lie just adjacent to the band edges to form a continuum band structure. As the co-doped system remains isoelectronic with the pure system, the formation of charge imbalance defects will be minimum. The band alignment plot indicates that both water oxidation and reduction are thermodynamically allowed in the case of Mo, N co-doped system. Finally, the present theoretical study reveals that the N, Mo codoping can be a promising way to improve the photocatalytic activity of NaTaO$_3$ under visible light.

3.4. Band Gap Engineering of NaTaO₃: Charge Compensated vs Charge Non-Compensated Codoping Strategy

In the present section, we propose the codoping of W and N to modify the band structure of NaTaO$_3$. Basically introduction of N ($2s^22p^3$) in place of O ($2s^22p^4$) leads to one electron deficiency, which can be compensated by replacing one Ta ($6s^25d^3$) by W ($6s^25d^4$). Being very similar in atomic size, W can be easily fitted into the Ta lattice site without any major distortion in the crystal structure. The other interest for choosing W is due to lower energy of W 5d orbital in comparison to Ta 5d, which may be effective for downward shifting of the CBM and thus reducing the band gap of NaTaO$_3$. We have extended our study with several dopant pair, which can form charge compensated (Cr, N) and non-compensated (S/V/Nb/Mn/Tc, N)-codoped systems. Here we perform a detailed systematic calculation exploring the role of the indiviual dopant elements as well as in combination of both using density functional theory, which is very much popular tool for describing electronic structure of semiconductor materials. We employed sophisticated hybrid functional of Heyd, Scuseria, and Ernzerhof (HSE) to obtain an accurate description of the band structure of undoped, monodoped and codoped NaTaO$_3$. The effect of monodoping and codoping on the electronic structure is reflected in the band structure plots. The characteristic changes due to introduction of the dopant element have been explained by analyzing the partial density of states (PDOS) plots. Stability of the codoped system has been assessed by calculating the defect-pair binding energy. To find the most suitable growth condition for the formation of monodoped as well as codoped NaTaO$_3$ we calculate the formation energies under different conditions. The calculated absorption spectrum has been presented to display the shift of the absorption curves of the codoped systems with respect to the

undoped NaTaO$_3$. We have also checked the band alignment of (W, N) codoped NaTaO$_3$ with respect to water redox levels.

3.4.1. Results and Discussions

The doped and codoped systems have been modeled with 40 atoms (8 Na, 8 Ta, and 24 O) supercell (2 x 1 x 1) of the orthorhombic (Pcmn, 62) NaTaO$_3$, which is the dominating phase at room tempareture. The valence states of the elements included in the PAW potentials are Na ($3s^1 2p^6$), Ta ($6s^2 5d^3$), W ($6s^2 5d^4$), O ($2s^2 2p^4$), N ($2s^2 2p^3$), S ($3s^2 3p^4$), Cr ($3d^5\ 4s^1$), V ($3d^4\ 4s^1$), Nb ($4p^6 5s^2 4d^3$), Mn ($3d^6\ 4s^1$), and Tc ($5s^2 4d^5$). Since the undoped system and N-doped system is discussed in section 3.3.1 the same is not discussed here.

3.4.1.1. W Monodoped NaTaO$_3$

Thus to compensate for the electron deficiency induced due to N-doping we propose to introduce W as a codopant which can inject an extra electron due to the presence of one more electron in the valence shell of W ($6s^2 5d^4$) than that in Ta ($6s^2 5d^3$). Before discussing the combined effect of both the dopants we will present a short picture of the electronic structure of W-doped NaTaO$_3$. Figure 3.4.1a shows that the Fermi level is shifted to the conduction band edge, indicating that W-doped NaTaO$_3$ will behave as a n-type semiconductor. W-doping introduces occupied impurity states 0.91 eV below the conduction band. PDOS (Figure 3.4.1b) analysis indicates that these states are mainly contributed by W 5d state with some dispersed states of Ta 5d. Hence introduction of both p-type and n-type dopant elements passivates the adverse effect of the individual element.
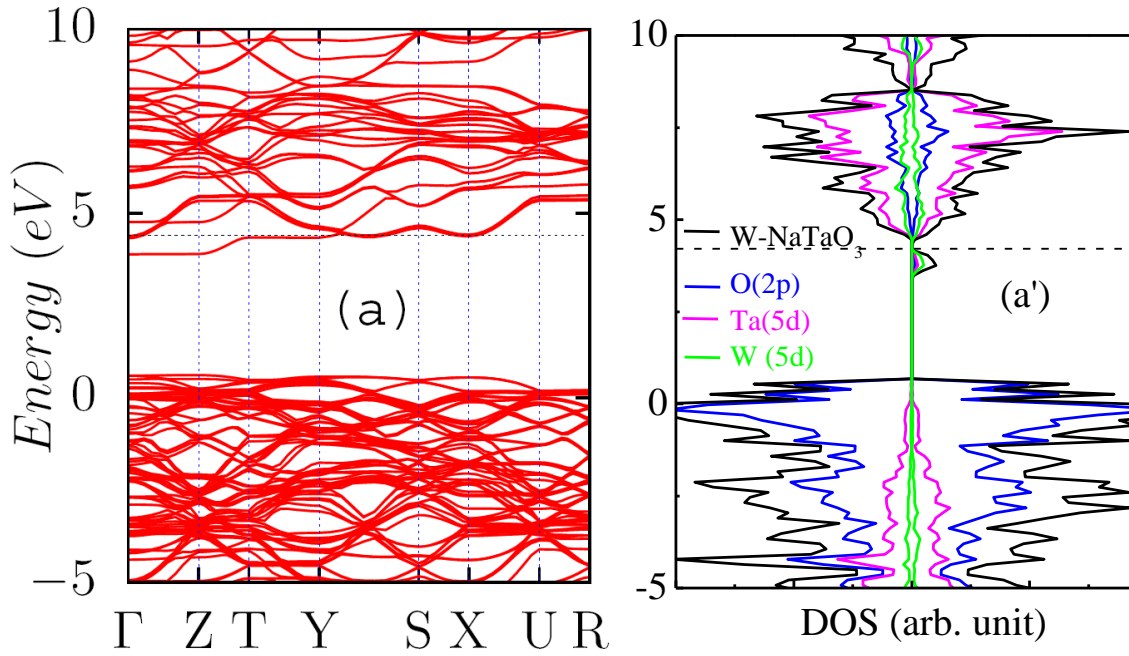
Figure 3.4.1: Band Structure and density of states of W-doped $NaTaO_3$ (a and a′).

3.4.1.2. (W, N)-codoping

In this section, we will investigate how the presence of both n-type (W) and p-type (N) dopants can improve the photocatalytic activity of $NaTaO_3$ under visible light without contributing to the charge carrier loss. Both N and W have been simultaneously introduced in the supercell to model the codoped system. We consider two model structures I ('Str. I') and structures II ('Str. II') corresponding to two different distances between the dopant atoms, W and N. The W to N distances are found to be 1.78 Å and 4.49 Å in the optimized geometries of 'Str. I' and 'Str. II', respectively. The binding energy for the codoped system is calculated using the relation

$$E_b = E_{N\text{-}NaTaO3} + E_{W\text{-}NaTaO3} - E_{W\text{-}N\text{-}NaTaO3} - E_{NaTaO3} \tag{3.4.1}$$

where $E_{N-NaTaO3}$, $E_{W-NaTaO3}$, $E_{W-N-NaTaO3}$ and E_{NaTaO3} are the total energy of N-doped, W-doped, (W, N) codoped and undoped $NaTaO_3$ supercell, respectively. The binding energies (2.38 eV and 1.57 eV) indicate that both the codoped systems are sufficiently stable.
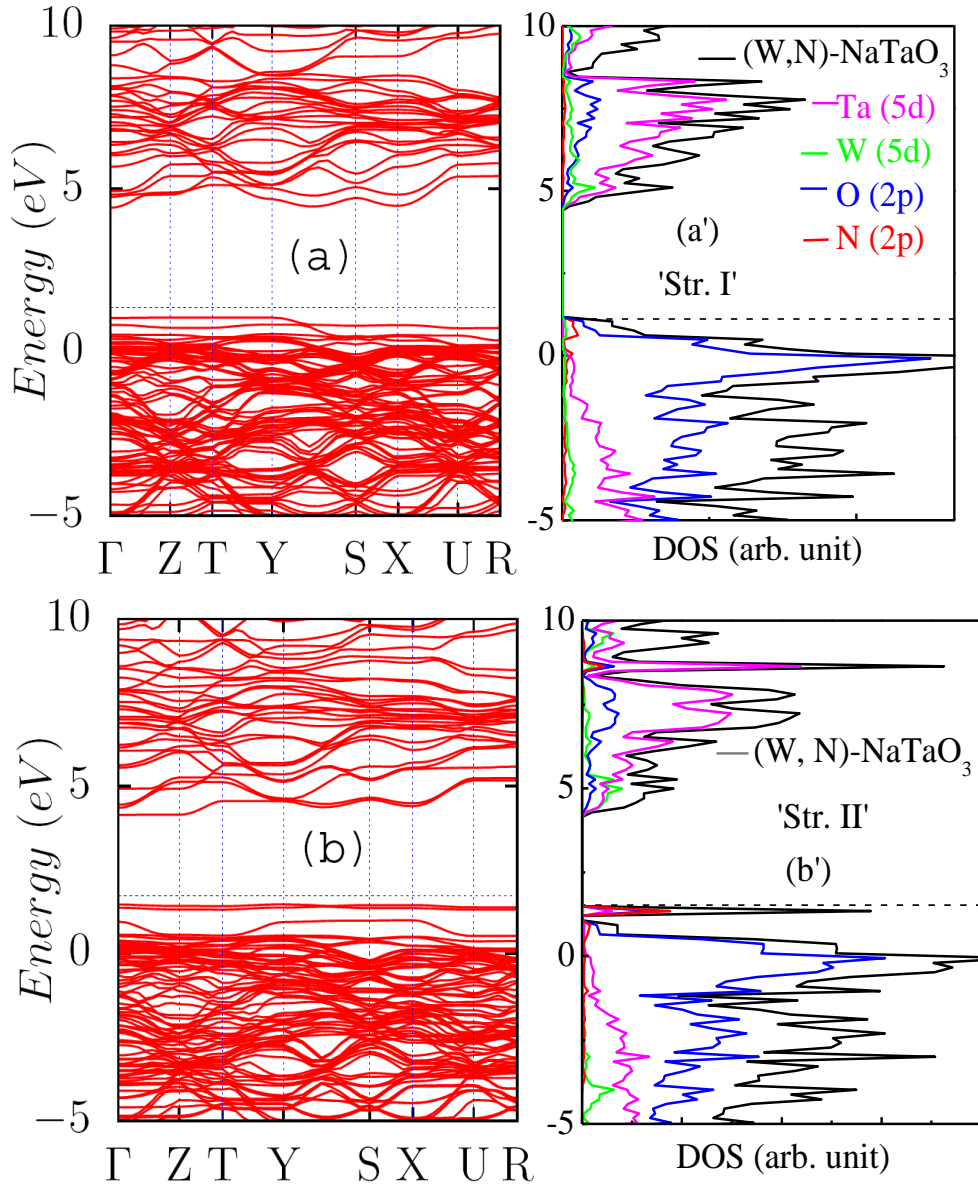
Figure 3.4.2: Band Structure and density of states of 'Str. I'-(a and a′) and 'Str. II' (b and b′) for (W, N)-codoped $NaTaO_3$. Horizontal dashed line indicates Fermi Level.

Formation of continuous band structures (Figure 3.4.2a and b) with significant reduction of band gap in (W, N) codoped $NaTaO_3$ is one of the most important outcome of the present study. Presence of both W and N compensates for the individual effects resetting the intrinsic semiconducting character of $NaTaO_3$ (Fermi level resides above the valence band). However, the extent of band gap reduction in case of 'Str. II' is more prominent than that in 'Str. I'. The calculated band gaps for the structures I and II are 3.36 eV and 2.67 eV, respectively. Analysis of PDOS plots (Figure 3.4.2a′ and b′) for the codoped system indicates that the impurity states, N 2p and W 5d are now shifted to the VB and CB edges, respectively. This causes an upward shifting of VBM and a downward shifting of CBM, resulting in decrease in the band gap. In the case of 'Str. I' the VB edge is dominated by O 2p state, similar to the case of undoped $NaTaO_3$. This feature is in contrast to the case of 'Str. II', where the dominating contribution for the VBM is N 2p state. Besides, W 5d state is also found to appear at the VB edge of the 'Str. II'. These lead to elevation of the VBM by larger extent for 'Str. II' (0.89 eV) in comparison to that in 'Str. I' (0.48 eV). This may be due to difference in the nature of the metal element bonded to nitrogen (M-N-M′) for the two model codoped systems. In the case of 'Str. I', 'M' and 'M′'represents Ta and W respectively, while for 'Str. II', both 'M' and 'M′' stand for Ta. As shown in Figure 3.4.3, the delocalization of N charge density towards metal centre is much more when it is bonded to W ('Str. I'), indicating a higher covalent character of the W-N bond in comparison to the Ta-N bond. To confirm this, we go for Bader charge density analysis, which reveals that the calculated charges on the N centre are -1.23 |e| and -1.45 |e| in case of W-N and Ta-N bonds, respectively. This observation supports our inference on the nature of two different M-N bonds. Thus, we can justify the band gap variation with better stabilization of the N 2p states when N is bonded to W resulting into less lifting of the VBM in case of 'Str. I'. The nature of CBM also differs slightly

for the two model structures. The CBM for the 'Str. I' has more Ta 5d character, while that for the 'Str. II' has more W 5d character. This leads to the difference in downward shifting of the CBM (0.21 eV and 0.49 eV) for the respective structures.
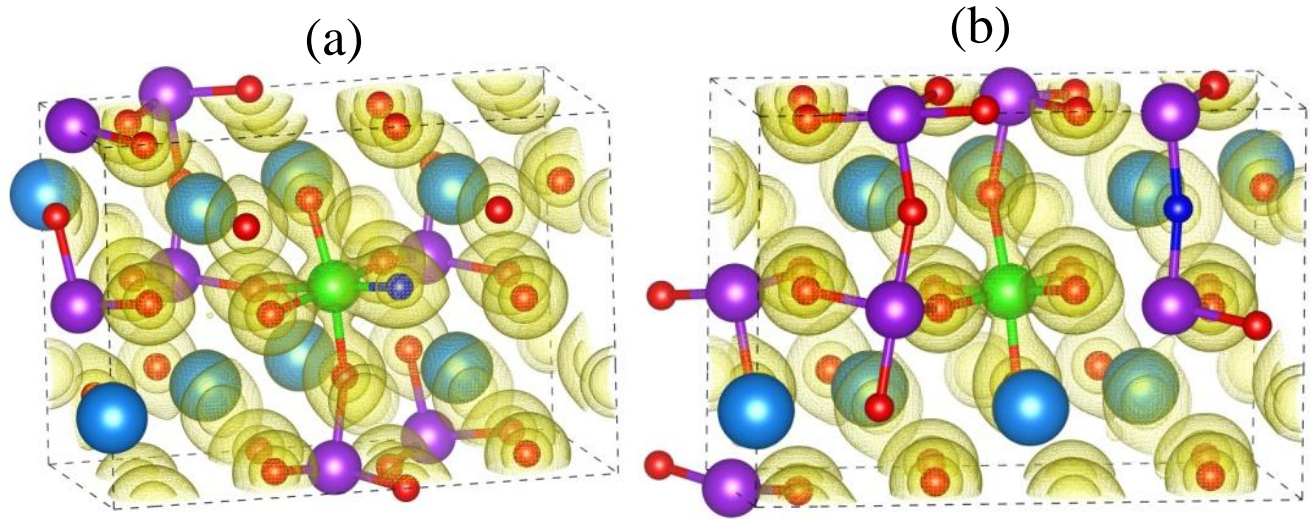
Figure 3.4.3: The isosurface plot of the total charge density of (N, W) codoped NaTaO$_3$ (a) 'Str. I' and (b) 'Str. II' (the density value considered for the isosurface contour plot is 0.07 electron/Å^3). The spherical balls with color magenta, red, sky-blue, green, and deep blue represent Ta, O, Na, W and N, respectively.

3.4.1.3. Defect Formation Energy of (W, N)-codoped NaTaO₃

To find the suitable growth condition for (W, N) codoping, the calculation for defect formation energy has been carried out and the result is compared with that of monodoping with W or N. The defect formation energy (ΔH_f) can be expressed as

$$\Delta H_f = E_{doped} - E_{NaTaO3} + \sum n_X \, \mu_X \qquad (3.4.2a)$$

where, E_{doped} stands for the energy of $NaTaO_3$ supercell in presence of individual/both the dopant element/elements, μ_X is the chemical potential of the element X, and n_X defines the number of elements introduced ($n_X = -1$) or replaced ($n_X = +1$) during defect formation. Usually defect formation energies are expressed in terms of chemical potential of the elemental bulk/ gaseous state, and hence we define $\Delta\mu_X = \mu_X - \mu_X^{bulk/gas}$. Equation (3a) thus takes the form

$$\Delta H_f = E_{doped} - E_{NaTaO3} + \sum n_X (\mu_X^{bulk/gas} + \Delta\mu_X). \qquad (3.4.2b)$$

When there exists equilibrium between $NaTaO_3$ and the reservoir of Na, Ta and O the following relation must be obeyed

$$\mu_{Na} + \mu_{Ta} + 3\mu_O = \mu_{NaTaO3(bulk)}. \qquad (3.4.3)$$

The chemical potential of the element Na (μ_{Na}), Ta (μ_{Ta}) and O (μ_O) cannot exceed those of the Na bulk ($\mu_{Na(bulk)}$), Ta bulk ($\mu_{Ta(bulk)}$) and O gas ($\mu_{O(gas)}$), i.e., $\mu_{Na} \leq \mu_{Na(bulk)}$ [$\Delta \mu_{Na} \leq 0$], $\mu_{Ta} \leq \mu_{Ta(bulk)}$ [$\Delta \mu_{Ta} \leq 0$], and $\mu_O \leq \mu_{O(gas)}$ [$\Delta \mu_O \leq 0$]. The condition $\mu_X = \mu_X^{bulk/gas}$ refers to a situation when chemical potential of X becomes equal to that of elemental X in bulk or gaseous state (i.e. X-rich condition).

For a stable compound, the heat of formation (Δ) must satisfy the following relation

$$\Delta = \Delta\mu_{Na} + \Delta\mu_{Ta} + 3 \Delta\mu_O \qquad (3.4.4a)$$

which can be rewritten as

$$\Delta = \mu_{Na} + \mu_{Ta} + 3\mu_O - \mu_{Na(bulk)} - \mu_{Ta(bulk)} - 3\mu_{O(gas)}. \qquad (3.4.4b)$$

Using equations (4) and (5b), one can write

$$\Delta = \mu_{NaTaO3(bulk)} - \mu_{Na(bulk)} - \mu_{Ta(bulk)} - 3\mu_{O(gas)} \qquad (3.4.4c)$$

Since the heat of formation for $NaTaO_3$ is a negative quantity, the following relations must be obeyed

$$\mu_{Na(bulk)} + \Delta \leq \mu_{Na} \leq \mu_{Na(bulk)} \qquad (3.4.5a)$$

$$\mu_{Ta(bulk)} + \Delta \leq \mu_{Ta} \leq \mu_{Ta(bulk)} \tag{3.4.5b}$$

$$3\mu_{O(gas)} + \Delta \leq 3\mu_O \leq 3\mu_{O(gas)} \tag{3.4.5c}$$

In the present study, $\mu_{Na(bulk)}$, $\mu_{Ta(bulk)}$, and μ_W have been calculated from the energy of the respective atoms in their bulk structure. For $\mu_{O(gas)}$ and μ_N we calculate the energy of an atom (½ E_{O2} or ½ E_{N2}) in the respective diatomic gas molecule, considered at the centre of a 20 x 20 x 20 $Å^3$ cubic box.
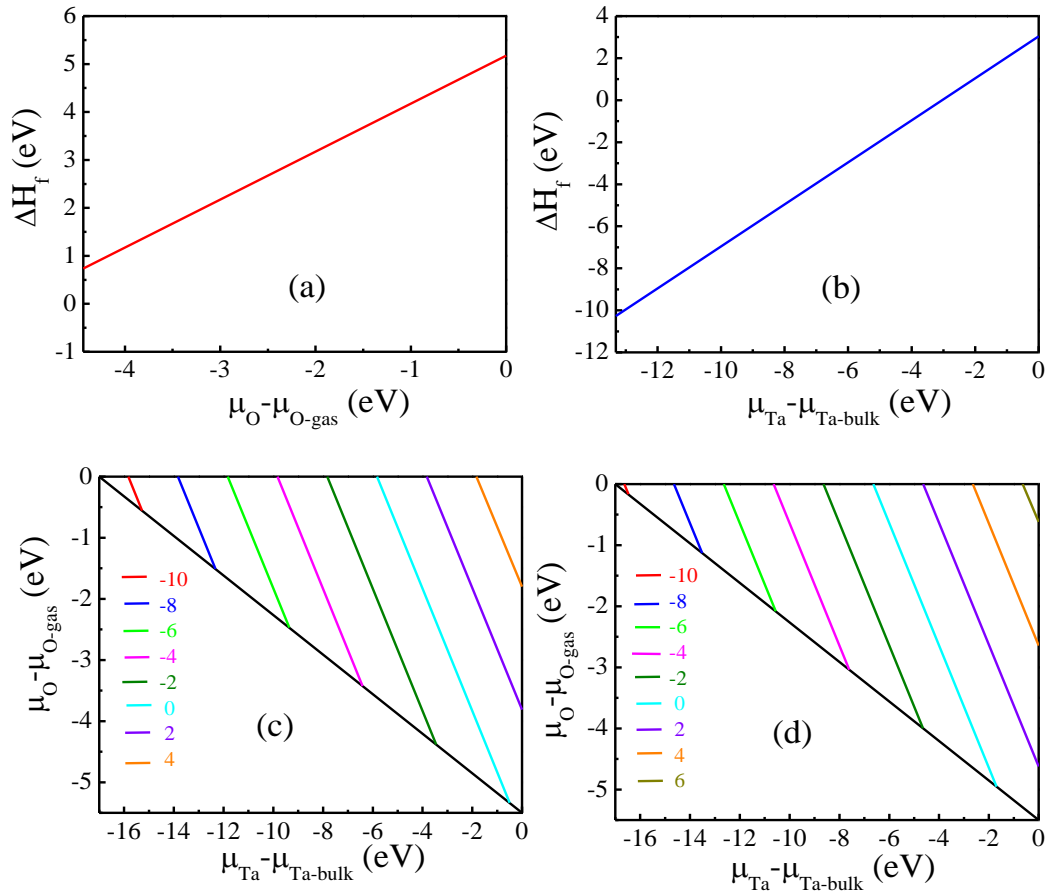
Figure 3.4.4: The variation of defect formation energy with the chemical potential of O (μ_O- μ_{O-gas}) and Ta (μ_{Ta}- $\mu_{Ta-bulk}$) for (a) N-doped $NaTaO_3$ (b) W- doped $NaTaO_3$ (c) (W, N)- codoped $NaTaO_3$ 'Str. I' (d) (W, N)- codoped $NaTaO_3$ 'Str. II'. The color lines (c) and (d) correspond to different formation energies for the (W, N)- codoped $NaTaO_3$.

Figures 3.4.4a and b show the formation energy plots for the monodoped cases, N-doped

$NaTaO_3$ and W-doped $NaTaO_3$, respectively. In both the cases the doping formation energy is

found to be highly positive under the respective host-rich condition. This is due to difficulty in

vacancy formation under host-rich condition. The N-doping is favored under O-poor condition,

while W-doping under Ta-poor condition. In presence of W, the defect formation energy for N-

doping is found to be energetically favorable. This may be due to formation of charge

compensated system in presence of both the cationic and anionic dopants into the $NaTaO_3$ crystal

structure. As shown in Figure 3.4.4c and Figure 3.4.4d, the favorable growth condition for both

the codoped systems is O-rich and Ta-poor condition. Comparison of Figure 3.4.4c and Figure

3.4.4d indicates that the 'Str. I' is energetically more favorable than the 'Str. II'. Hence, for the

synthesis of 'Str. I' and 'Str. II' one has to employ different experimental techniques.[53-56]

3.4.1.4. Effect of dopant concentration

We have also investigated the effect of codoping with large supercell ($2 \times 2 \times 1$)

containing total 80 atoms. In this case also we consider both 'Str. I' and 'Str. II' for (W, N)

codoped $NaTaO_3$. We have calculated the formation energies as discussed in the case of smaller

supercell. The variation of formation energies as a function of chemical potential of the host

elements have been displayed in Figure 3.4.5a and b. A Comparison of Figure 3.4.5a and b with

Figure 3.4.4a and b indicates that the formation energies are hardly affected by the increase in

supercell size. This justifies the calculation of formation energies using $2 \times 1 \times 1$ supercell. To

investigate the role of concentration of the dopant elements on the band gap we calculated the

electronic structure of (W, N)-codoped $NaTaO_3$ using $2 \times 1 \times 1$ supercell. The DOS and PDOS

for both 'Str. I' and 'Str. II' have been presented in the Figure 3.4.5a' and b', respectively. As

shown in the DOS plot, there are no mid-gap states in between VB and CB, indicating complete passivation of the impurity induced states. However, the extent of band gap reduction is little bit less (calculated band gap for 'Str. I' and 'Str. II' are 3.43 eV and 2.89 eV, respectively) due to lower concentration of the dopant elements.
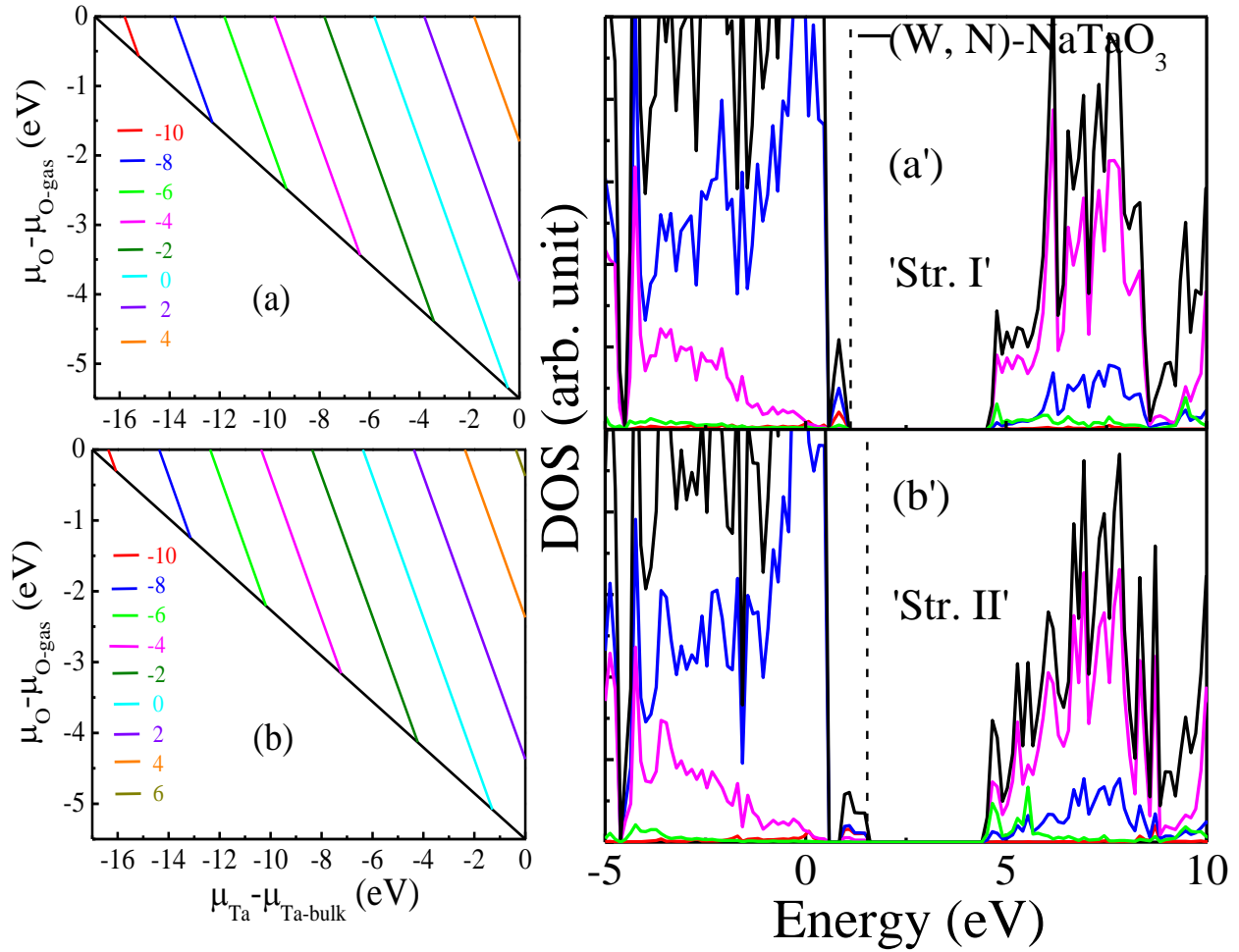
Figure 3.4.5: The variation of defect formation energy with the chemical potential of O (μ_O- $\mu_{O\text{-gas}}$) and Ta (μ_{Ta}- $\mu_{Ta\text{-bulk}}$) for (a) (W, N)- codoped $NaTaO_3$ Str. I (b) (W, N)- codoped $NaTaO_3$ Str. II with $2 \times 2 \times 1$ supercell. The Key is the same as in Figure 3.4.4. Density of states of (N, W) codoped $NaTaO_3$ for the Str. I (a') and Str. II (b') with $2 \times 2 \times 1$ supercell.

3.4.1.5. Compensated and non-compensated codoping with different dopant pair

In this section we have investigated how the electronic structure of $NaTaO_3$ is modified with the compensated and non-compensated codoping involving different dopant pairs.

3.4.1.5.1. Compensated codoping with Cr and N:

In this case we have constructed a charge compensated system by introducing one Cr and one N in place of one of the Ta lattice sites and O lattice sites, respectively. The calculated DOS and PDOS for the 'Str. I' and 'Str. II' have been displayed in Figure 3.4.6a and b, respectively. In case of 'Str. I' Cr 3d states are found to appear below the conduction band, while in case of 'Str. II' hybrid states composed of Cr 3d and O 2p are observed in the mid gap region. This may be due to large difference in the orbital energies between Cr 3d and Ta 5d.
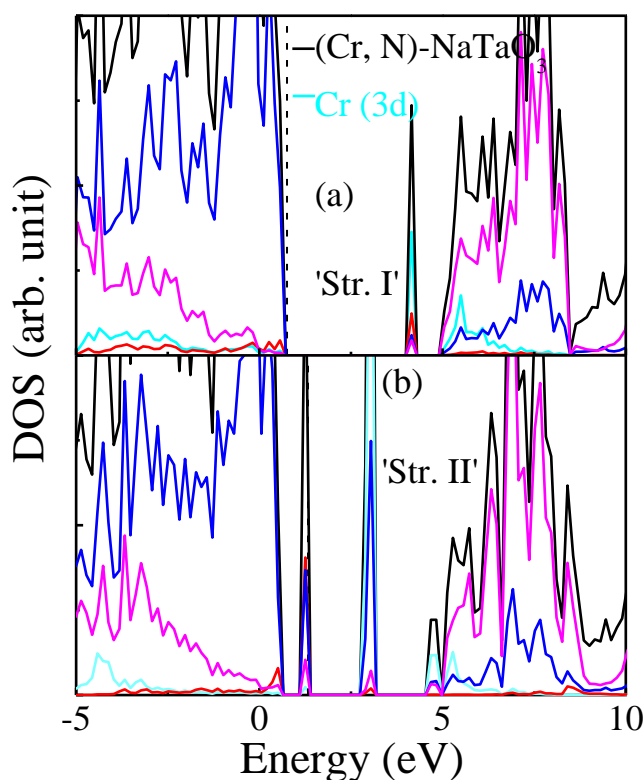
Figure 3.4.6: Density of states of (N, Cr) codoped $NaTaO_3$ for the Str. I (a) and Str.II (b)

3.4.1.5.2. Non-compensated codoping with (S, N), (V, N), and (Nb, N):

In case of (S, N) codoped $NaTaO_3$ two oxygen atoms have been replaced by one S and one N, while, for (V, N) and (Nb, N) codoped cases one oxygen atom and one tantalum atom have been substituted by one N and one V/ Nb atom, respectively. The common feature between all the three systems is that they are deficient by one electron and are thus charge non-compensated. To observe the effect of this type of doping we have calculated DOS and PDOS. As shown in Figure 3.4.7, in all the cases impurity induced states are found to appear in the forbidden region. They form discrete localized states in between VB and CB. This arises due to incomplete passivation of the impurity states in the charge non-compensated codoping.
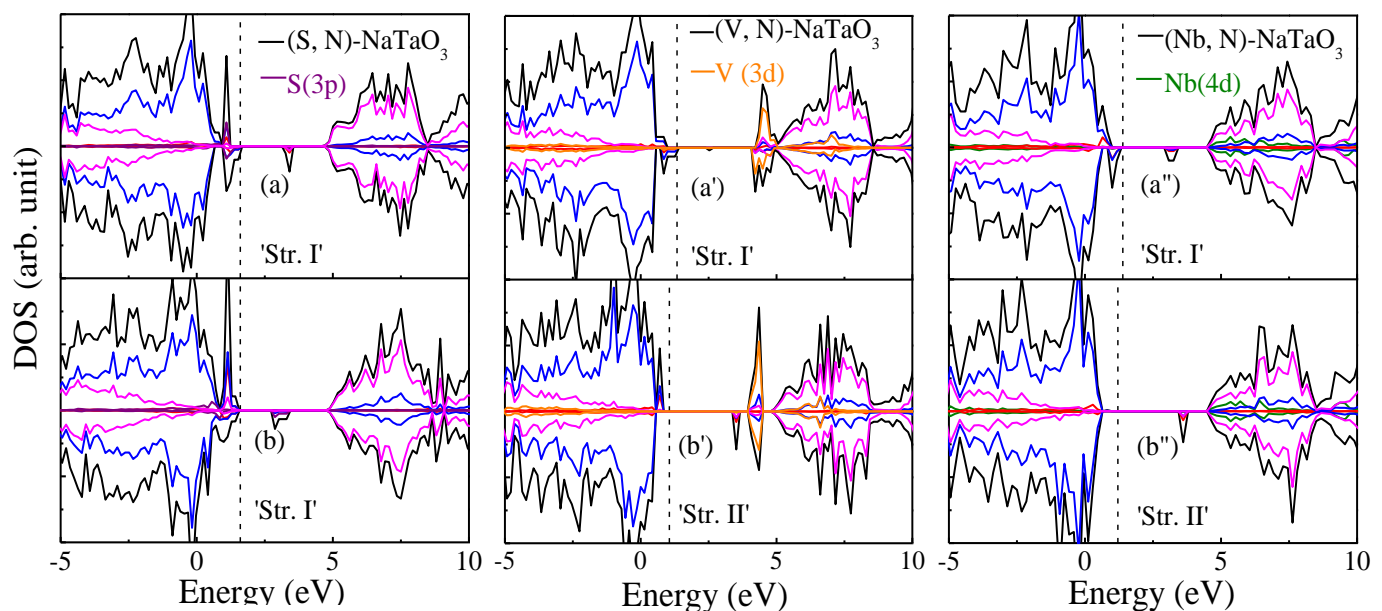
Figure 3.4.7: Density of states of (N, S) codoped $NaTaO_3$ for the Str. I (a) and Str.II (b), (N, V) codoped $NaTaO_3$ for the Str. I (a′) and Str.II (b′), (N, Nb) codoped $NaTaO_3$ for the Str. I (a″) and Str.II (b″)

3.4.1.5.3. Non-compensated codoping with (Mn, N) and (Tc, N):

In these cases one Mn/ Tc and one N have been introduced in one Ta and one O lattice sites, respectively. Both the systems are charge non-compensated. To investigate the effect of these codopant pair on the electronic structure, we have calculated DOS and PDOS (Figure 3.4.8). In both the cases discrete mid gap states are found to appear in between VB and CB. Analysis of PDOS indicates that these states are mainly contributed by the dopant elements. Appearance of these localized states in the forbidden region can be explained by incomplete passivation of the individual impurity states.
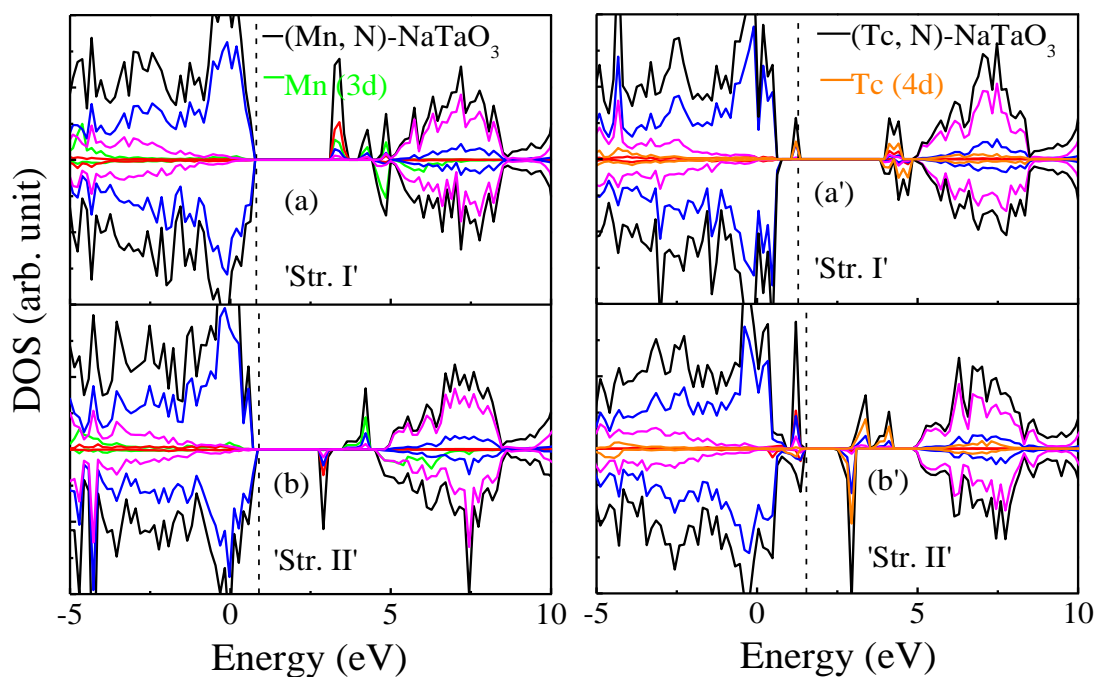
Figure 3.4.8: Density of states of (N, Mn) codoped $NaTaO_3$ for the Str. I (a) and Str.II (b), (N, Tc) codoped $NaTaO_3$ for the Str. I (a′) and Str.II (b′).

Based on the study of all these systems, it may be concluded that, although these localized states effectively reduce the band gap, they may trap the charge carrier and thus accelerate the recombination process. They also hinder the mobility of charge carriers. This may lead to reduction in life time of the photogenerated charge carriers, which in turn will affect the photocatalytic property. So these states are undesirable for photocatalytic purpose. Another major drawback of charge non-compensated codoping is the formation of defect states, which is known to be one of the sources for charge carrier loss. Hence these non-compensated codoping may not be successful in overcoming the disadvantages of monodoping.

3.4.1.6. Optical Property of (W, N)-codoped NaTaO$_3$

To quantify the shift in absorption spectrum we employ the frequency dependent dielectric function calculation. The calculated absorption spectra for the codoped systems have been shown in Figure 3.4.9 and compared with that of the undoped NaTaO$_3$. The absorption curve for the NaTaO$_3$ is limited to the UV region, while for the (W, N)-NaTaO$_3$ the maximum shift is found to be 158 nm towards visible region. Hence codoping of W and N successfully make NaTaO$_3$ visible light active by reducing the band gap. We have also checked the optical behavior of the codoped system with larger supercell. The calculated absorption spectrum as shown in the inset of Figure 3.4.9, indicates that the absorption shift towards visible region is quite significant even in presence of lower concentration of the dopant elements.
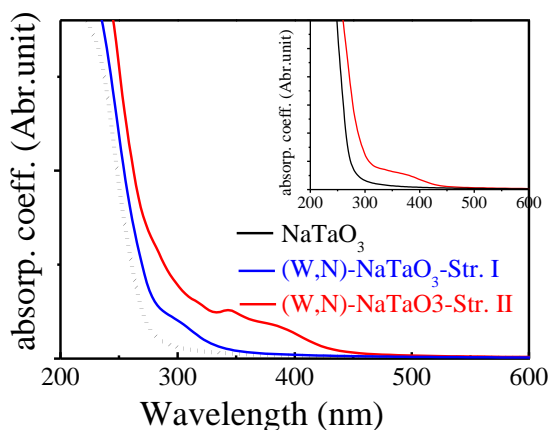
Figure 3.4.9: The calculated absorption curves for the undoped and (W, N) codoped NaTaO$_3$. Inset figure refers to calculated absorption using $2 \times 1 \times 1$ supercell.
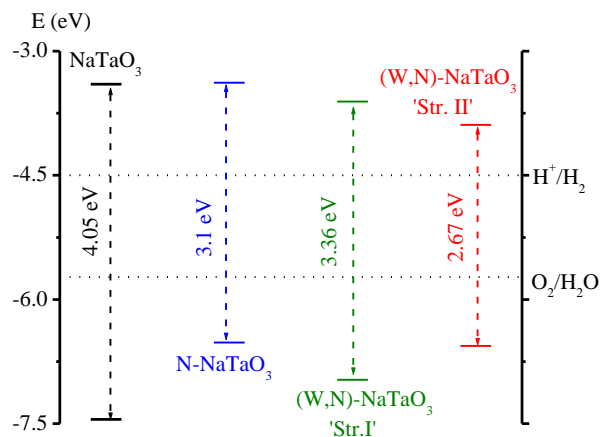
Figure 3.4.10: The calculated VBM and CBM positions of N-doped and (W, N) codoped NaTaO$_3$ with reference to that of undoped NaTaO$_3$.

3.4.1.7. Photocatalytic activity of (W, N)-codoped NaTaO$_3$

As discussed earlier, the improvement of visible light absorption may not always lead to enhancement of photocatalytic activity. The CBM and VBM should be in proper position with respect to the water redox levels so that both photooxidation and photoreduction of water become thermodynamically allowed. Hence we have checked the criterion for our proposed photocatalyst. In the case of undoped NaTaO$_3$, the VBM is found to be 1.77 eV lower than the O$_2$/H$_2$O level and CBM is located at 1.1 eV higher than the H$^+$/H$_2$ level. The band edges for the modified systems have been plotted with respect to the undoped NaTaO$_3$ on the basis of their energy levels in Figure 3.4.10, which indicates that the codoping of W, N modifies the band structure of NaTaO$_3$ in such a way that both the photooxidation and photoreduction properties remain intact. Thus, for 'Str. I', the VBM is located 1.24 eV lower than the O$_2$/H$_2$O level, and the CBM resides 0.89 eV higher than the H$^+$/H$_2$ level. For the 'Str. II' VBM lies 0.83 eV below the

water oxidation level and CBM lies 0.61 eV above the water reduction level. Hence the codoping of W and N into $NaTaO_3$ is expected to make it a good photocatalytic material.

3.4.2. Conclusion

In this study, we present a detailed electronic structure calculation to understand the effect of W, N codoping on the band structure of $NaTaO_3$ and compare the results with the same for individual dopants. Although N doping is able to extend the absorption region to some extent, the localized impurity states introduced in between the bands may inhibit the photocatalytic process. On the other hand, the doping with W leads to introduction of occupied impurity states below the CB. We have systematically examined the origin of appearance of the discrete states, which are completely passivated in presence of both the dopants. This ensures improved charge carrier mobility in the codoped system. Although the (Cr, N) codoped $NaTaO_3$ is a charge compensated system, there exist mid gap states in between the VB and CB. On the other hand, charge non-compensated codoping involving (S, N), (V, N), (Nb, N), (Mn, N) and (Tc, N) is found to be ineffective in overcoming the drawback of monodoping process, and hence may not be suitable for enhancing the photocatalytic property of $NaTaO_3$. As the (W, N) codoped system is a charge compensated system, formation of vacancy related defect states is expected to be minimum. These features are believed to be effective for longer life time of the photo-generated charge carrier. This codoping significantly reduces the band gap to enable $NaTaO_3$ to absorb the visible light. Finally we showed that the positions of the band edges for the (W, N) codoped $NaTaO_3$ are appropriate for the overall water splitting. Thus, based on this investigation, we can predict that the codoping with W and N is one of the promising ways to improve the photocatalytic property of $NaTaO_3$ under visible light.

3.5. Improvement of Photocatalytic Activity of NaTaO₃ under Visible light by N and F Doping

The compensated codoping has been found to be one of the successful strategies for controlled band gap engineering. There are few studies involving this approach for the case of $NaTaO_3$. In this study, we propose N, F codopant pair to improve the photoactivity of $NaTaO_3$ under visible light. Presence of both F and N will lead to the formation of a charge compensated system, which is also isoelectronic with the undoped $NaTaO_3$. Thus, defect formation due to charge mismatch can be avoided. The other interest of choosing F is that it can be easily incorporated in place of oxygen lattice site due to their size similarity (R_{O-2} = 1.35 Å, R_{F-1} = 1.285 Å). Besides, the presence of F reduces the electron-hole recombination process and thus enhances the photoactivity. As can be seen from previous theoretical and experimental studies, the codoping of N and F successfully improves the photocatalytic activity under visible light for several wide band gap semiconductors. Very recently, it has been seen that codoping of N and F significantly increases the strength of water absorption and enhances the photodecomposition of water on the TiO_2 surface. Here, we investigate theoretically the electronic structure of (N, F)-codoped $NaTaO_3$ and compare with that of undoped and monodoped $NaTaO_3$ systems.

3.5.1. Results and Discussion

3.5.1.1. Electronic Structure

To investigate the effect of individual dopant elements, we have studied the N-doped $NaTaO_3$ and F-doped $NaTaO_3$, separately. The optimized geometries for these doped systems indicate that the substitution of either N or F in place of oxygen lattice site does not result into

significant structural changes to the $NaTaO_3$ system. This is due to their closeness in ionic radius (R_{O-2} = 1.35 Å, R_{N-3} = 1.46 Å, and R_{F-1} = 1.285 Å). The Ta-N bond length (2.02 Å) and the Ta-F bond length (2.10 Å) are slightly longer than the Ta-O bond length (1.99 Å).
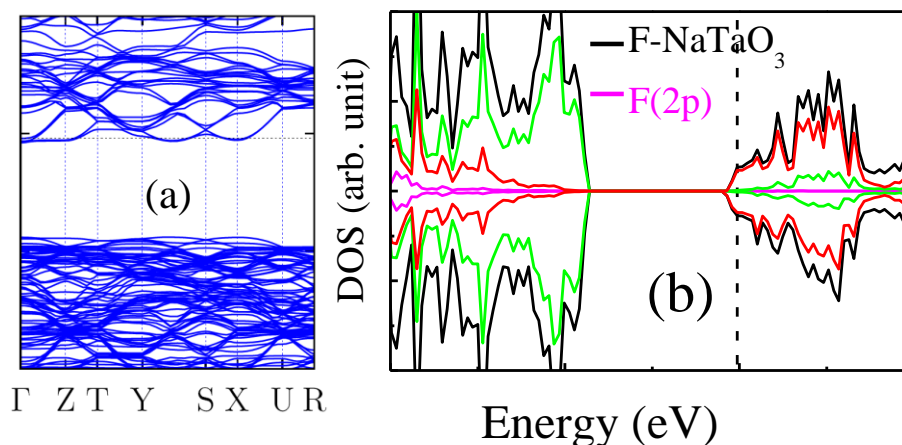
Figure 3.5.1: Band Structure and density of states of F-doped $NaTaO_3$.

As has been seen in the previous section, N doping is associated with the introduction of localized states in between the VB and CB. Although, these midgap states are beneficial for visible light absorption, they may trap charge carriers and hinder their mobility. As the N-doped $NaTaO_3$ is charge non-compensated, the tendency to form defects like oxygen vacancy will be higher in comparison to the parent crystal. All these factors are responsible for the lower photo-conversion efficiency than expected in the practical situations. In the following section, we will see how the presence of F can suppress these adverse effects. Thus, it is useful to study the effect of only F doping on the electronic structure of $NaTaO_3$. The band structure of F-doped $NaTaO_3$ is shown in Figure 3.5.1a. The calculated band gap for F-doped $NaTaO_3$ is found to be 4.02 eV, i.e., F doping plays hardly any role towards band gap narrowing. Analysis of electronic energy

levels indicates that there occurs no significant perturbation at the positions of the band edges of

$NaTaO_3$. The PDOS plot (Figure 3.5.1b) for the F-doped $NaTaO_3$ shows that the F 2p states

appear in the lower region of the VB and the band edges are still dominated by Ta 5d and O 2p

states, which is similar to the case of undoped $NaTaO_3$. As the valence shell of F ($2s^2 2p^5$)

contains one additional electron than O valence shell ($2s^2 2p^4$), F-doping introduces one extra

electron to the system. The Fermi level lies in the CB region similar to the case of n-type

semiconductor. However, the formation of reduced metal centre, as indicated by the presence of

localized Ti 3d states just below the CB in case of $F-TiO_2$, is not observed in case of $F-NaTaO_3$.

The extra electron might be distributed in the crystal lattice, instead of being localized on a

particular metal centre. Now, we will discuss the collective effect of both the n-type and p-type

dopants for the modification of the band gap of $NaTaO_3$. The calculated band structure of (N, F)-

codoped $NaTaO_3$ has been presented in Figure 3.5.2a. The first thing to be mentioned is that the

acceptor states appearing in the case of N-doped $NaTaO_3$ are completely passivated in presence

of F. This is obviously due to presence of F, which compensates for the electron deficiency

originated due to N-doping. This is supported by the Bader charge density analysis. The

calculated Bader charge on the N centre is -1.14 |e| in the N-doped $NaTaO_3$, while, in the (N, F)-

codoped $NaTaO_3$ the charge density on the N centre is increased to $-$ 1.43 |e|, and the band gap is

reduced by 1.12 eV, which will improve the absorption behavior in the visible region. Figure

3.5.2b shows the PDOS of (N, F)-codoped $NaTaO_3$, where N-induced states are found to appear

immediately above the VB, thus elevating the VBM significantly. The band gap narrowing is

attributed here to this upward shifting of the VB as the CB merely faces any shift. The F 2p

states are deeper inside the VB and do not contribute to the band edges of the (N, F)-codoped

$NaTaO_3$.
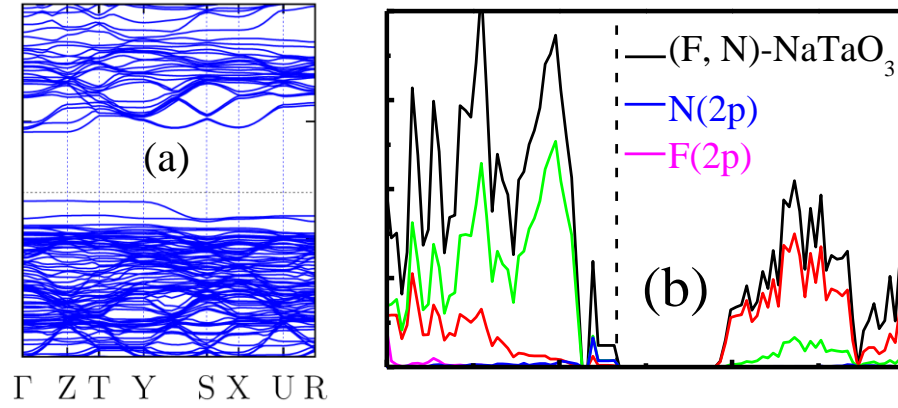
Figure 3.5.2: Band structure and total density of states of (N, F) codoped NaTaO₃.

3.5.1.2. Optical Property

To observe the shift in optical absorption spectrum due to codoping in comparison to the undoped system, we have calculated the frequency-dependent dielectric function. As shown in Figure 3.5.3, the absorption curve for the (N, F) codoped NaTaO₃ is found to be shifted to the visible region by 117 nm with respect to that of the undoped NaTaO₃.
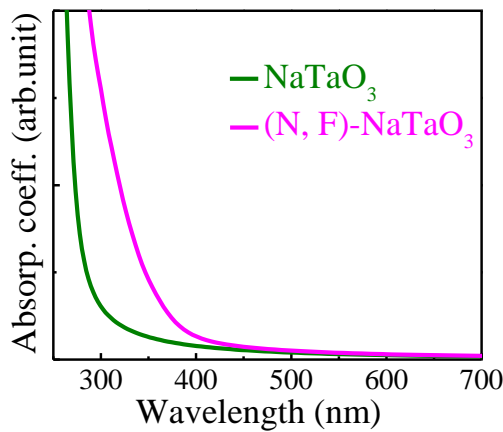
Figure3.5.3: The optical absorption curves for the undoped and (N, F) codoped NaTaO₃.
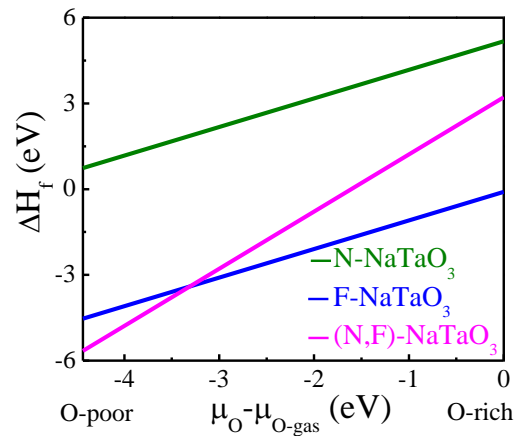
Figure3.5.4: The variation of defect formation energy with the chemical potential of O (μ_O- $\mu_{O\text{-gas}}$) for N-doped NaTaO₃, F-doped NaTaO₃ and (F, N)-codoped NaTaO₃.

3.5.1.3. Defect Pair Binding Energy

To assess the stability of the codoped systems we calculate the defect pair binding energy (E_b), which can be defined as

$$E_b = E_{N\text{-}NaTaO3} + E_{F\text{-}NaTaO3} - E_{F\text{-}N\text{-}NaTaO3} - E_{NaTaO3} \qquad (3.5.1)$$

where, $E_{N\text{-}NaTaO3}$, $E_{F\text{-}NaTaO3}$, $E_{F\text{-}N\text{-}NaTaO3}$, and E_{NaTaO3} represent the energy of N-doped, F-doped, (F, N)-codoped and undoped $NaTaO_3$ with same supercell size, respectively. The calculated binding energy for (N, F)-codoped $NaTaO_3$ is found to be 1.85 eV. The positive value indicates that the defect pair is stable in the codoped system.

3.5.1.4. Formation Energy

To get an insight into the feasibility of incorporating dopant element/elements under different synthetic conditions, we calculate the defect formation energy (ΔH_f) using the same procedure as discussed in section 3.4.1.3. Thus, ΔH_f can be defined as

$$\Delta H_f = E_{doped} + n_O\,\mu_O - E_{NaTaO3} - n_N\,\mu_N - n_F\,\mu_F \qquad (3.5.2)$$

where, E stands for the energy of the supercell, μ, the chemical potential of the elements and n_X indicates the number of atoms of element X inserted or substituted during defect formation.

As shown in Figure 3.5.4, in all the cases, defect formation is found to be energetically more favorable under O-poor condition. This is quite natural as the substitution of oxygen in the O-rich condition needs high energy. The doping with F is found to be more feasible than N-doping under both O-rich and O-poor conditions. Figure 3.5.4 indicates that the presence of F facilitates the introduction of N by reducing the formation energy significantly. Under O-poor condition, the formation of (N, F)-codoped $NaTaO_3$ is found to be more favorable than either of

the monodoping cases. This may be due to mutual passivation of the additional charge and formation of charge compensated system in presence of both the dopant elements.
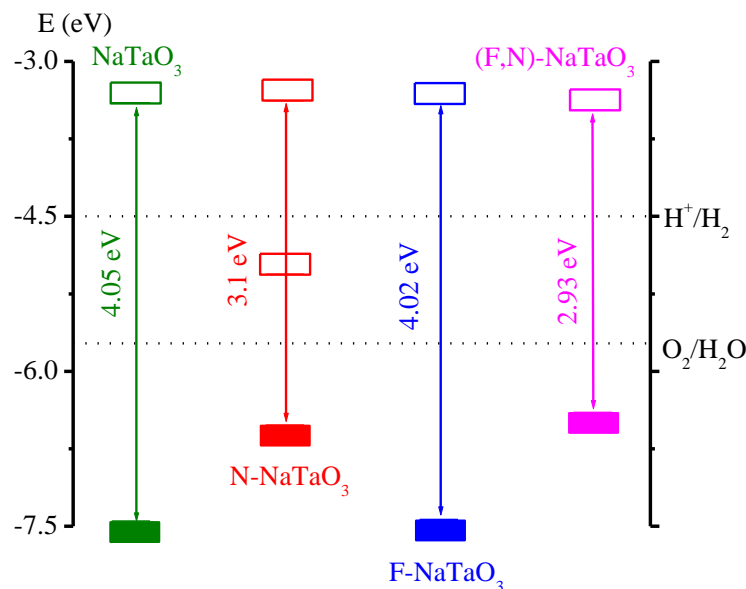
Figure3.5.5: The calculated VBM and CBM positions of N-doped, F-doped and (N, F) codoped NaTaO$_3$ with reference to the respective experimental values of undoped NaTaO$_3$.

3.5.1.5. Photocatalytic Activity

To know whether (N, F)-codoped NaTaO$_3$ is active for overall water splitting or not, we need to observe the positions of the band edges with respect to water redox levels. As can be seen from Figure 3.5.5, the VBM for N-doped NaTaO$_3$ is elevated with respect to that of the undoped NaTaO$_3$, while the position of the CBM remains almost unchanged. For F doped NaTaO$_3$, the difference between the band edges and the water redox levels are nearly same as that in the case of undoped NaTaO$_3$. Figure 3.5.5 indicates that the VBM is elevated by 1.05 eV with respect to that of undoped material due to (N, F)-codoping, while there is a small downward shift in the CBM. Hence, both the CBM and VBM of the (N, F)-codoped NaTaO$_3$ are in suitable positions to make water reduction as well as oxidation thermodynamically feasible.

3.5. 2. Conclusion

In this present study, we have investigated the synergistic effect of introducing two anionic dopants, N (p-type) and F (n-type), to improve the photocatalytic activity of $NaTaO_3$ under visible light. The incorporation of N into $NaTaO_3$ crystal structure is also found to be more feasible in presence of F. Codoping with N and F results into the formation of charge compensated and isoelectronic (with $NaTaO_3$) system, and hence the tendency to form unwanted defects will be minimum, which would be beneficial for longer life time of the photogenerated charge carriers. This leads to complete passivation of N-induced unoccupied acceptor states in the band structure and thus improved photo-conversion efficiency is expected. In the (N, F)-codoped $NaTaO_3$, the N 2p states are found to appear just above the VB, resulting into an elevation of the band gap remarkably. This reduces the band gap to a significant extent and shifts the absorption curve by 117 nm towards the visible region as compared to that of the undoped $NaTaO_3$. Both the CBM and VBM for the (N, F)-codoped $NaTaO_3$ are in suitable positions with respect to the water redox levels to satisfy the thermodynamic criterion for overall water splitting. Thus, based on the present investigation, we can conclude that doping with both N and F is one of the effective approaches for the enhancement of photoactivity of $NaTaO_3$ under visible light.

Chapter 4

Improving Photocatalytic

Activity of SrTiO$_3$ for Water

Splitting under Visible Light

4.1. Introduction

Among the perovskites, $SrTiO_3$ has been extensively studied for its potential applications in this field. The advantages of $SrTiO_3$ are that it is highly robust and can split water even in absence of external bias potential.[165] One of the biggest limitations of these materials is their poor response towards exposer of visible light, which covers a significant portion of the solar spectrum. The band gap of $SrTiO_3$ has been reported to be 3.20 eV with the conduction band maximum (CBM) lying 0.80 eV above the water reduction (H^+/H_2) level and the valence band minimum (VBM) located 1.17 eV below the water oxidation (H_2O/O_2) level.[166, 167] Band gap narrowing can be done either by elevating the valence band maximum (VBM) or by shifting the conduction band minimum (CBM) in the downward direction. But the shifting of band edge by a large extent may affect the reducing or oxidizing property of the material adversely, which are strongly related to hydrogen and oxygen evolution, respectively. Hence, one needs to employ a controlled band gap engineering. During the past few decades, extensive research has been carried out to reduce the band gap, the most successful way for which is the doping with one or more elements. There exist lots of reports exploring different strategies to shift the absorption region of $SrTiO_3$, mainly by introducing foreign element/elements in any of the two cationic sites (Sr and Ti) or in the anionic lattice site (O). Among nonmetal doping, effect of N has been studied by several experimental as well as theoretical groups.[168-174] A series of N-doped $SrTiO_3$ with varying N concentration have been synthesized by Wang et al and significant improvement of photocatalytic activity has been observed during the oxidative elimination of nitric oxide. It has been pointed out that this enhancement of visible light activity is attributed to the presence of N-induced localized mid gap states which reduce the effective band gap. However, these states are considered to be detrimental for the photocatalytic activity as they can hinder the charge carrier

mobility and thus reduce the photoconversion efficiency. Besides, defects like oxygen vacancy are known to be formed spontaneously to compensate for the charge imbalance in N-doped oxide semiconductor, and may trap photo-generated electron-hole pair and accelerate their recombination. Nowadays, codoping approach has been shown to be one of the successful approaches in designing new photocatalyst with improved photoresponse. This has also been shown to be popular for improving the photocatalytic activity of $SrTiO_3$ involving either anion-cation, anion-anion, or cation-cation pairs. Recently, significant attention has been paid to improve the photocatalytic activity of N-doped $SrTiO_3$ by introducing either a nonmetal (H, F, Cl, Br, I) or a metal (Cr, V, Nb, Ta, Sc, Y, La) as a codopant.[175-177] Although they are found to be successful in suppressing the N-induced undesirable states by forming charge compensated system, their potentiality towards overall water splitting is still to be tested.

In this chapter, we have adopted various metal-nonmetal codoping approach to improve the photocatalytic behavior of $SrTiO_3$ under visible light. While choosing the codopant pair for this purpose, we consider some important aspects, viz., (a) they should not bring significant distortion in the parent crystal structure, (b) they should reduce the band gap to such an extent that the visible light absorption will be appreciable, (c) they should not perturb the CB edge of $SrTiO_3$ significantly to make large downward shifting, (d) they should not introduce discrete mid gap states.

Among the transition metal doped systems, Cr-doped $SrTiO_3$ has been extensively studied due to its potential application to split water and organic compounds under visible light.[178-182] However, there exist some major issues that limit the photocatalytic efficiency of Cr-doped $SrTiO_3$. Improved photocatalytic activity has been observed only when chromium is in trivalent state (Cr^{+3}), although chromium is more stable in hexavalent state (Cr^{+6}). Hence keeping

chromium in trivalent state is a challenge as it has tendency to be converted in the hexavalent state. Secondly, localized mid gap states, introduced due to Cr doping, not only hinder the mobility of the charge carriers, but also bring significant changes in the band edge positions, thus affecting the overall water splitting property. Other metal cations of interest for this purpose include Mn, Ru, Rh, Pb, Ag, Ir, Pd and Pt.[183-191] Although they are able to shift the absorption spectra towards the visible region, there are cases, where hydrogen evolution has not been observed at all. This may be due to, as emphasized in previous studies, large perturbation at the band edge positions associated with introduction of undesirable localized states in the forbidden region. Owing to attractive visible light activity, Rh-doped $SrTiO_3$ has been found to be studied by several groups. However, photoactivity of Rh-doped $SrTiO_3$ is limited by the presence of Rh^{+4} species, which plays significant role in the electron-hole recombination. Here, we will discuss various strategies to improve the photocatalytic activity of Rh-doped $SrTiO_3$ under visible light. In the last part of the chapter we attempt to consider improvement of the visible light photocatalytic activity of $SrTiO_3$ by doping with pentavalent cation in combination with other ions.

In summary the strategies to improve the visible light photocatalytic activity of $SrTiO_3$ are discussed in this order:

(i) Codoping with Sb and N

(ii) Codoping with Mo/W and N

(iii) Codoping with Rh and Sb

(iv) Codoping with Rh and La

(v) Codoping with Rh and F

(vi) Codoping with Rh and V/Nb/Ta

4.2. Computational Methods

Spin-polarized DFT calculations have been carried out using Vienna ab initio simulation package (VASP) electronic structure code. The electron-ion interaction has been treated by projector augmented wave (PAW) potential, which is widely used for the studies of electronic structure of semiconductor materials. For the Brillouin zone integration, we employ Monkhorst and Pack scheme to generate gamma-centered k-point sets. The exchange and correlation energy density functionals were defined by generalized gradient approximation (GGA) with Perdew-Burke-Ernzerhof (PBE) scheme during geometry optimization. The total energy convergence tolerance was set to 10^{-6} eV/atom for the self consistent iteration. Electronic structure calculations have been carried out by employing the HSE hybrid functional, where the short-range interactions are calculated with exact exchange mixing in both HF and DFT. The exchange-correlation energy is expressed as

$$E_{XC}^{HSE} = a\, E_X^{SR}(\mu) + (1-a)\, E_X^{PBE,\,SR}(\mu) + E_X^{PBE,\,LR}(\mu) + E_C^{PBE} \qquad (4.1)$$

where, 'a' stands for the mixing coefficient. The screening parameter μ defines the short ranged (SR) and long ranged (LR) part of the interaction. In the present study, we use the mixing exchange parameter of 28% and standard screening parameter of 0.2 $\mathring{A}^{-1}$ to reproduce the experimental band gap of $SrTiO_3$. k-point mesh of 3 x 3 x 3 was set for the hybrid functional calculations. The energy cutoff of 600 eV has been chosen for the plane wave basis sets. To investigate the absorption behavior, the frequency-dependent dielectric function calculation has been carried out for the codoped and undoped $SrTiO_3$.

4.3. Improving Photocatalytic Property of SrTiO$_3$ through (Sb, N) Codoping

In this section, we discuss the effect of Sb as codopant to improve the photoactivity of N doped SrTiO$_3$ under visible light. The advantages for choosing Sb as codopant are: (a) being very similar in ionic radius (Sb^{+5}: R$_{ef}$ = 0.60 Å; Ti^{+4}: R$_{ef}$ = 0.605 Å), Sb can be easily fitted at the Ti lattice site without causing major lattice distortion in the host crystal structure; (b) introduction of Sb into the N doped system is expected to maintain charge balance in the codoped SrTiO$_3$ (Ti^{+4} + O^{-2}= Sb^{+5} + N^{-3}); (c) use of a non transition metal (Sb) may be more preferable over transition metal to avoid localized 'd'-states in the forbidden region. It has been successfully shown in the earlier reports that introduction of Sb as a codopant significantly increases the photocatalytic property of the monodoped entity. As for example, codoping of Sb into the Cr-doped SrTiO$_3$ has been found to enhance the photoactivity for H$_2$ evolution by suppressing the formation of hexavalent chromium (Cr^{+6}) as well as vacancy, which are known to diminish the photoactivity of SrTiO$_3$. However, detailed theoretical studies exploring the effect of Sb on the electronic structure of SrTiO$_3$ are rare. Here, we present a systematic study to investigate the synergistic effect of both N (as a substituent of O) and Sb (as a substituent of Ti) as codopants, and compare the results with that of the N-doped, Sb-doped and undoped SrTiO$_3$, using density functional theory as a tool.

4.3.1. Results and Discussions

The mono-doped system is modeled by replacing either one of the Ti or O atoms by Sb or N, respectively from a 2 x 2 x 2 supercell (40 atoms) of the cubic (space group: $Pm\overline{3}m$) SrTiO$_3$ crystal structure. In the case of codoping, we simultaneously introduce both Sb and N into

$SrTiO_3$. This corresponds to Sb concentration of 12.5 % and N concentration of 4.17 %. k-point mesh of 8 x 8 x 8 was found to be sufficient to attain convergence. The valence states considered during the calculations are: Sr $(4s^24p^65s^2)$, Ti $(4s^23d^2)$, Sb $(5s^25p^3)$, O $(2s^22p^4)$, and N $(2s^22p^3)$.

4.3.1.1. Geometry

The crystal structure of $SrTiO_3$, which mainly exists as cubic form ($Pm\overline{3}m$; Space group No. 221) at room temperature, is shown in Figure 4.3.1, where strontium and titanium are coordinated with 12 and 6 oxygen anions, respectively.
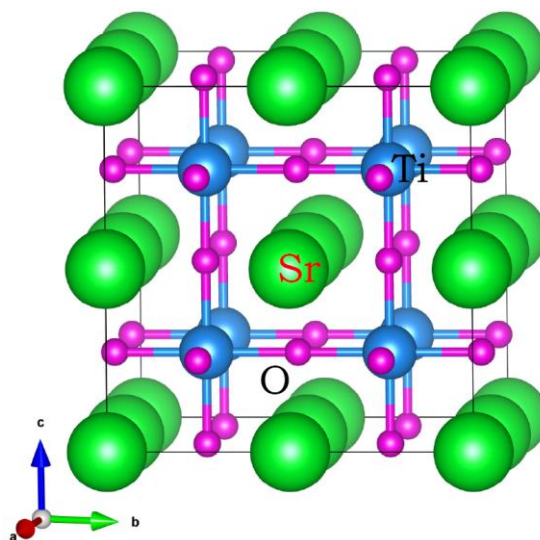
Figure 4.3.1: $2 \times 2 \times 2$ supercell for the cubic $SrTiO_3$ crystal structure.

The structural framework is based on corner sharing TiO_6 perfect octahedra and the Sr ion occupying the center position. Unit cell of $SrTiO_3$ contains one strontium, one titanium and three oxygen atoms. The lattice parameter of the optimized undoped $SrTiO_3$ is found to be a= 3.948 Å within the spin polarized GGA approach, in reasonable agreement with the previous reported results. The calculated Ti-O bond length is 1.974 Å. Since, doping of nitrogen in the oxide based material mainly involves replacement of oxygen by nitrogen, we consider only substitutional

doping. From the optimized cell structure, obtained in our calculation, it is found that N doping does not make any significant change in the $SrTiO_3$ crystal structure. The Ti-N bond length (1.976 Å) in N-doped $SrTiO_3$ is slightly higher than the Ti-O bond length (1.974 Å) in undoped crystal. This leads to increase in lattice parameter by only a small extent. Previous experimental reports show that, Sb occupies exclusively Ti lattice site in the Sb-doped $SrTiO_3$ as the ionic size of Sb^{+5} (R_{ef} = 0.60 Å) is closer to the ionic size of Ti^{+4} (R_{ef} = 0.605 Å) than that of Sr (R_{ef} = 1.44 Å). The introduction of Sb into the Ti lattice site does not lead to much change in the lattice structure. After full relaxation, it has been observed that the change in geometrical structure due to Sb-doping is limited to local region only, consistent with the experimental observation. Therefore, geometry of the (Sb, N)-codoped $SrTiO_3$ does not differ much from the basic crystal structure of the host material.

4.3.1.2. Defect pair binding energy

Before going to the discussion on the electronic structure of (Sb, N) codoped $SrTiO_3$, we calculate the defect pair binding energy (E_b) using the relation

$$E_b = E_{Sb\text{-}SrTiO3} + E_{N\text{-}SrTiO3} - E_{(Sb, N\text{-}SrTiO3)} - E_{SrTiO3} . \qquad (4.3.1)$$

where, $E_{N\text{-}SrTiO3}$, $E_{Sb\text{-}SrTiO3}$, $E_{(Sb, N)\text{-}SrTiO3}$ and E_{SrTiO3} represent the energy of the N-doped, Sb-doped, (Sb, N) codoped, and undoped $SrTiO_3$ supercell, respectively. The positive value of the defect pair binding energy (1.58 eV/ supercell) indicates that the codoped system is sufficiently stable.

4.3.1.3. Defect Formation Energy

In order to find favorable growth condition for doping of the individual element as well as both, we calculate the defect formation energy in each case. The defect formation energy relates chemical potential of the elements as

$$\Delta H_f = E_{doped} + n_O\, \mu_O + n_{Ti}\, \mu_{Ti} - E_{SrTiO3} - n_N\, \mu_N - n_{Sb}\, \mu_{Sb} \qquad (4.3.2)$$

where, E_{doped} represents total energy for the doped/ codoped $SrTiO_3$ supercell. μ stands for chemical potential of the element, n is the number of elements inserted or removed for the construction of doped/ codoped structure. At the equilibrium condition between the reservoir of Sr, Ti and O and $SrTiO_3$ equation (4.3.3) must be satisfied

$$\mu_{Sr} + \mu_{Ti} + 3\mu_O = \mu_{SrTiO3(bulk)} \qquad (4.3.3)$$

The chemical potential of the element cannot exceed that of the respect bulk (Sr/ Ti) or gaseous (O) state, i.e. $\mu_{Sr} \le \mu_{Sr(bulk)}$, $\mu_{Ti} \le \mu_{Ti(bulk)}$ and $\mu_O \le \mu_{O(gas)}$.

The expression for the heat of formation $SrTiO_3$ is given by

$$\Delta = \mu_{SrTiO3(bulk)} - \mu_{Sr(bulk)} - \mu_{Ti(bulk)} - 3\mu_{O(gas)} \qquad (4.3.4)$$

Since the heat of formation for $SrTiO_3$ is a negative quantity we can write

$$\mu_{Sr(bulk)} + \Delta \le \mu_{Sr} \le \mu_{Sr(bulk)} \qquad (4.3.5a)$$

$$\mu_{Ti(bulk)} + \Delta \le \mu_{Ti} \le \mu_{Ti(bulk)} \qquad (4.3.5b)$$

$$3\mu_{O(gas)} + \Delta \le 3\mu_O \le 3\mu_{O(gas)} \qquad (4.3.5c)$$

The chemical potential, $\mu_{Sr(bulk)}$, $\mu_{Ti(bulk)}$, and μ_{Sb} have been calculated from the energy of an atom in the respective bulk structure. On the other hand, $\mu_{O(gas)}$ and μ_N have been calculated from the energy of an oxygen atom ($\frac{1}{2}\,E_{O2}$) and nitrogen atom ($\frac{1}{2}\,E_{N2}$) in the corresponding gaseous molecule confined at the centre of a 20 x 20 x 20 Å^3 cubic box.
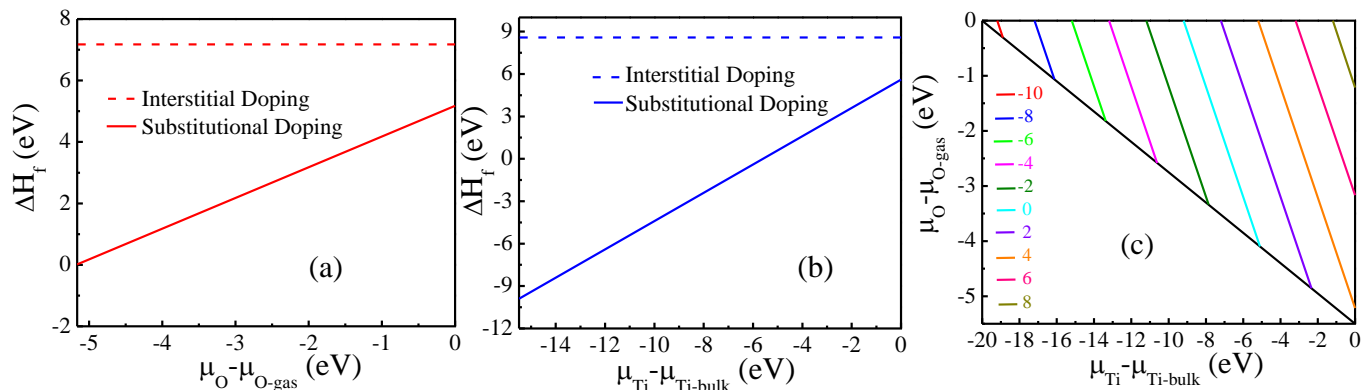
Figure 4.3.2: The variation of defect formation energy with the chemical potential of O (μ_O- $\mu_{O\text{-}gas}$) and Ti (μ_{Ti}- $\mu_{Ti\text{-}bulk}$) for (a) N-doped SrTiO$_3$ (b) Sb-doped SrTiO$_3$ (c) (Sb,N)-codoped SrTiO$_3$. The color lines in panel (c) corresponds to different formation energies for the (Sb, N)-codoped SrTiO$_3$.

The calculation of the formation energy (Figure 4.3.2a and 4.3.2b) indicates that in both the cases substitutional doping is energetically more favored in comparison to the interstitial doping. Figure 4.3.2a shows the variation of formation energy for N-doped SrTiO$_3$ as a function of oxygen chemical potential (μ_O - $\mu_{O(gas)}$). Under O-rich condition the formation energy has a large positive value, which shows a decreasing trend as we proceed towards O-poor condition. As shown in Figure 4.3.2b, the formation energy for Sb-doping is highly positive under Ti-rich condition. This indicates that the doping with individual element is highly unfavorable under host rich condition, may be due to requirement of large energy for vacancy formation in the substitution process. However, this is found to be feasible in presence of both the dopant elements as shown in Figure 4.3.2c. The calculation indicates that the O-rich condition is more suitable than the Ti-rich condition for the growth of the (Sb, N)-codoped SrTiO$_3$.

4.3.1.4. Electronic Structure

Figure 4.3.3 shows the band structure plot for the undoped $SrTiO_3$ along high symmetric k-path of the Brillouin zone (the horizontal dashed line represents the Fermi level). The calculated band gap (3.19 eV) shows excellent agreement with the experimental value (3.2 eV). Analysis of the projected density of states (Figure 4.3.3) indicates that the valence band maximum (VBM) is dominated by O 2p states while conduction band minimum (CBM) is composed of Ti 3d states. We will now discuss the effect of doping and codoping on the electronic structure of $SrTiO_3$.
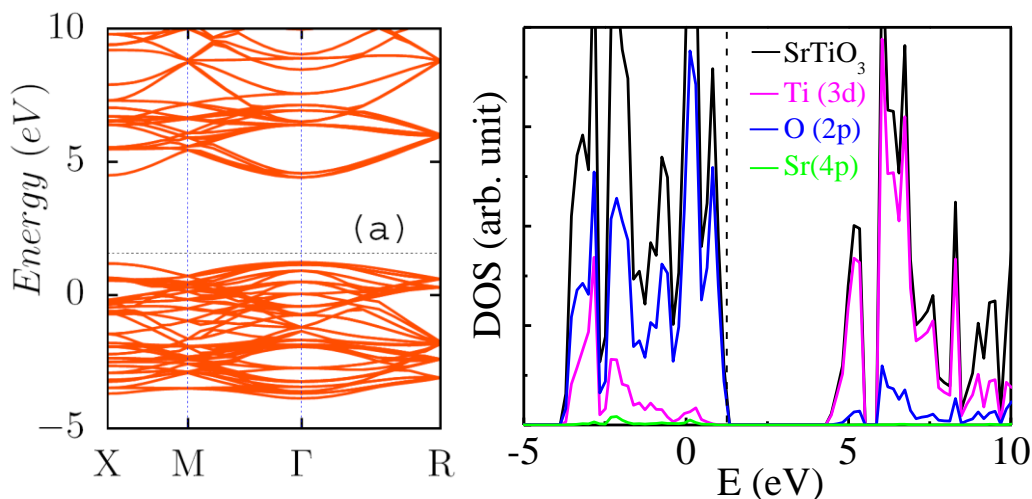
Figure 4.3.3: Band structure and density of state plot for undoped $SrTiO_3$

Introduction of N $(2s^2 2p^3)$ in place of O $(2s^2 2p^4)$ is found to bring significant changes in the electronic structure of $SrTiO_3$. The N-doped $SrTiO_3$ is deficient by one electron. Analysis of PDOS plot (Figure 4.3.4a) indicates that localized mid gap states are formed due to mixing of N 2p state with O 2p state along with small contribution from Ti 3d state. Consequently, the band gap (energy difference between the occupied impurity states and the conduction band) is reduced

to 2.31 eV, which is responsible for the visible light absorption of N-doped $SrTiO_3$. However, these isolated localized states are highly undesirable for the photocatalytic purpose as they may hinder the mobility of the charge carriers. Therefore one needs to introduce a codopant to passivate these discrete states for better photocatalytic property. Since the CBM of $SrTiO_3$ (prominent Ti 3d character), is located just 0.8 eV above the water reduction level (H^+/H_2), we carefully choose Sb as the codopant, which is expected not to perturb the conduction band (CB) level largely. Before discussing the results of the codoped system, it will be instructive to first discuss the monodoped system with Sb as the dopant.
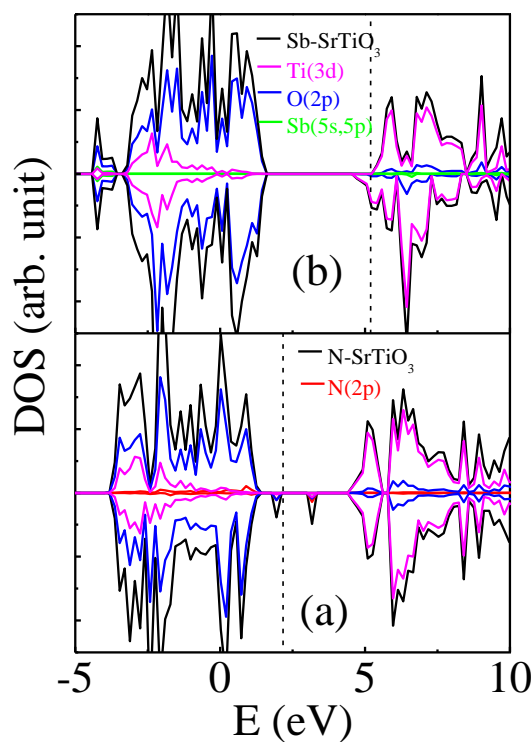
Figure 4.3.4: Density of state plot for N-doped $SrTiO_3$ (a) and Sb-doped $SrTiO_3$ (b).

As the stable oxidation state for Sb is the pentavalent state (Sb^{+5}), it leaves one extra electron to the system. This is manifested in the DOS plot (Figure 4.3.4b), with the Fermi level

located in the conduction band. Analysis of PDOS plot (Figure 4.3.4b) clearly indicates that the defects states are contributed by Ti 3d state. This is due to localization of the extra unpaired electron in the Ti 3d orbital. One more thing we should point out is that the respective band edges are still dominated by the O 2p and Ti 3d states, as observed in the case of undoped $SrTiO_3$. The contribution of the Sb 5s and 5p states to the band edges is found to be less significant. This may be due to more ionic character of the Sb-O bond. This is again supported by the analysis of Bader charge density. In the case of undoped $SrTiO_3$, the calculated Bader charges on Ti and O centers are 2.04 |e| and -1.23 |e|, respectively, while, for Sb-doped $SrTiO_3$, the values on the Sb and O centers are 2.80 |e| and -1.29 |e|, respectively. Let us discuss the synergistic effect of both N and Sb on the electronic structure of $SrTiO_3$.
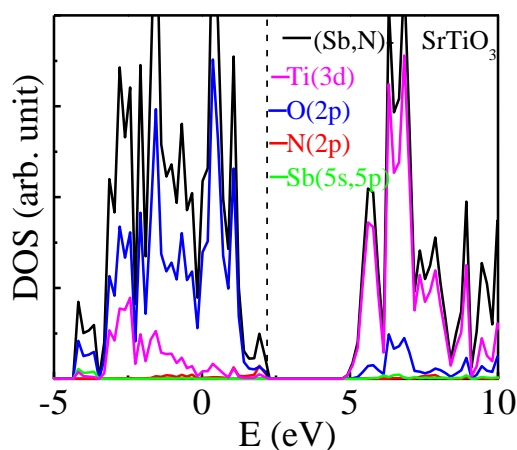
Figure 4.3.5: DOS and PDOS plots for (Sb, N) codoped $SrTiO_3$. The vertical dashed lines indicate the Fermi level.

The band structure plot (Figure 4.3.5) for the codoped $SrTiO_3$ shows that the Fermi level resides above the VBM, similar to that of an intrinsic semiconductor. It is interesting to observe that the band gap reduces significantly to 2.66 eV, which ensures the absorption of visible light. This is the consequence of elevation of valence band (VB) edge associated with the formation of

(N 2p, O 2p) hybridized state (Figure 4.3.5). The discrete acceptor states as appearing in the case of N-doped $SrTiO_3$ are completely passivated, resulting into a continuum band structure. This is due to the presence of Sb which compensates for the electron deficiency introduced through N-doping. It has been quantified by Bader charge analysis, which indicates a higher electronic charge at the N centre in the (Sb, N)-codoped $SrTiO_3$ (-1.36 |e|) as compared to that in N-doped $SrTiO_3$ (-1.15 |e|). On the other hand, the Ti 3d defect states arising in the case of Sb-doped $SrTiO_3$ is no longer present in the (Sb, N)-codoped $SrTiO_3$. Presence of both Sb and N leads to the formation of charge compensated system, which will minimize formation of undesired defects and thus reduce charge carrier loss.

4.3.1.5. Optical Property

To investigate the absorption property we calculate the frequency dependent dielectric function, $\varepsilon(\omega) = \varepsilon_1(\omega) + i\varepsilon_2(\omega)$. The real part ($\varepsilon_1$) and imaginary part ($\varepsilon_2$) of the dielectric tensor are obtained from Kramers–Kronig transformation, and using summation over the empty states, respectively, as implemented in VASP. The absorption coefficient $\alpha(\omega)$ has been evaluated using the formula

$$\alpha(\omega) = \sqrt{2}\omega \left(\sqrt{\varepsilon_1(\omega)^2 + \varepsilon_2(\omega)^2} - \varepsilon_1(\omega) \right)^{\frac{1}{2}} \qquad (4.3.6)$$
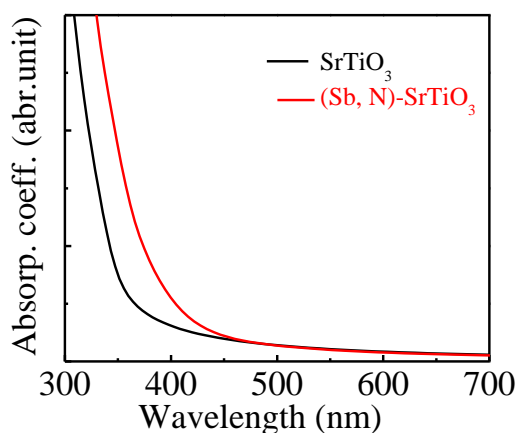
Figure 4.3.6: The calculated optical absorption curves for the undoped and codoped SrTiO$_3$
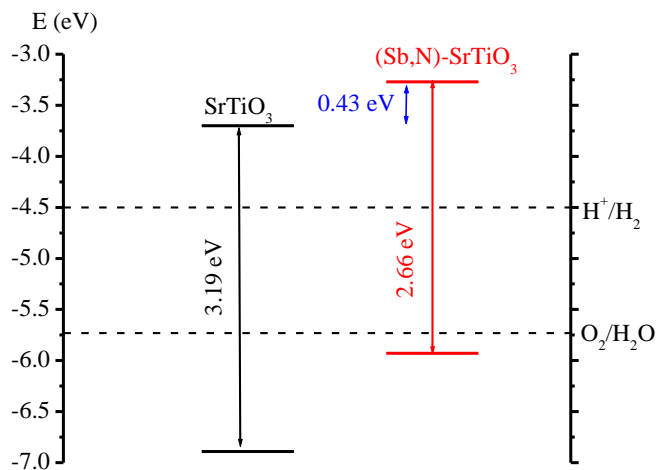
Figure 4.3.7: The band alignment of the undoped, and (Sb, N)-codoped SrTiO$_3$ with respect to the water redox levels.

Figure 4.3.6 shows that the absorption curve for the nondoped SrTiO$_3$ is limited to the UV region, while it is shifted towards the visible region in presence of both Sb and N dopants. This observation supports the band gap reduction of SrTiO$_3$ due to codoping with Sb and N as discussed in the earlier section.

4.3.1.6. Photocatalytic Activity

As we know, reduction in the band gap is sufficient to improve the visible light activity, but not necessarily to achieve high photocatalytic activity for water splitting. The conduction band potential should be more positive than the H$^+$/H$_2$ potential and the valence band potential should be more negative than the H$_2$O/O$_2$ potential, i.e. CB should be located above the water redox potential (H$^+$/H$_2$) and VB should be located below the water oxidation level (H$_2$O/O$_2$). To check this criterion for our proposed system we align the positions band of the band edges with respect to that of the undoped SrTiO$_3$. For undoped SrTiO$_3$ the CBM is located 0.8 eV above the water reduction (H$^+$/H$_2$) level and the VBM is 1.17 eV below the water oxidation level (H$_2$O/O$_2$). The

VBM and CBM for the (Sb, N) codoped $SrTiO_3$ is now placed by considering the relative shifts of the corresponding electronic energy levels with respect to that of the undoped $SrTiO_3$. As can be seen from Figure 4.3.7, the VBM of (Sb, N)-codoped $SrTiO_3$ is located 0.20 eV below the water oxidation level and the CBM position is 1.23 eV above the water reduction level. Hence, overall water splitting is thermodynamically feasible in the (Sb, N)-codoped $SrTiO_3$. Interestingly, the CBM of the (Sb, N)-$SrTiO_3$ is located even 0.43 eV above the CBM of the undoped $SrTiO_3$. This implies that the modified system should be more feasible for H_2 evolution due to enhancement of reducing power with respect to the undoped $SrTiO_3$.

4.3.2. Conclusion

The hybrid DFT calculations reported here reveal the significance of codoping of Sb and N into $SrTiO_3$ for improving the photocatalytic activity under visible light. The positive defect pair binding energy indicates that the (Sb, N)-codoped $SrTiO_3$ is sufficiently stable. The band gap is found to be reduced significantly without introducing any isolated midgap states. As the codoped system is charge compensated, it is expected to reduce undesirable vacancy formation, and consequently defect assisted carrier loss can be avoided. Presence of Sb also facilitates the introduction of N into the $SrTiO_3$ crystal structure by reducing the formation energy. The band alignment for the codoped $SrTiO_3$ is such that both the photo-oxidation and photo-reduction processes associated with water splitting are thermodynamically feasible. Moreover, the reducing power of the modified $SrTiO_3$ is higher than that of the undoped material, making it more suitable for H_2 generation. Hence we can propose that codoping of Sb and N into the $SrTiO_3$ crystal is one of the promising approaches to enhance the efficiency for photo splitting of water using visible light.

4.4. Investigation of Photocatalytic Activity of Cation-Anion codoped SrTiO₃ for Water Splitting under Visible Light

In this section, we have adopted metal-nonmetal codoping approach to improve the photocatalytic behavior of SrTiO$_3$ under visible light. We carefully choose Mo and W for the Ti lattice site and N for the O lattice site due to similarity in their ionic sizes. As the energy of N 2p orbital is higher than the O 2p orbital, N doping is effective for elevation of the valence band maximum (VBM). In fact, it has been successfully shown that the codoping of Mo/ W and N significantly increases the photocatalytic activity of TiO$_2$ under visible light. The substitution of N ($2s^2 2p^3$) for O ($2s^2 2p^4$) will add one hole to the system, while substitution of Mo ($5s^2 4d^4$) or W ($6s^2 5d^4$) for Ti ($4s^2 3d^2$) will add two extra electrons. Hence, equimolar proportion (1:1) of both the dopant elements, Mo/W and N will lead to the formation of a non-compensated codoped system. However, to form a compensated codoped system the proportion of Mo/W and N should be 1:2. Since the photocatalytic property may alter with the type of codoping, viz., compensated or non-compensated, we have studied here both the varieties.

4.4.1. Results and Discussions

The valence states included for the construction of PAW potential are: Sr ($4s^2 4p^6 5s^2$), Ti ($4s^2 3d^2$), Mo ($5s^2 4d^4$), W ($6s^2 5d^4$), O ($2s^2 2p^4$), and N ($2s^2 2p^3$).

4.4.1.1. Geometry and Electronic Structure

In the previous section we have shown that the doping with N does not bring much structural changes in the parecnt crystal structure. To investigate the effect of increasing concentration, we introduce two N atoms. The (N, N)-doped SrTiO$_3$ is deficient by two electrons. The change in

crystal structure is found to be small even in presence of higher N concentration (8.33 %). The calculated (N, N) distance is found to be 2.663 Å, which is shorter than the (O, O) distance (2.792 Å) in the undoped $SrTiO_3$.
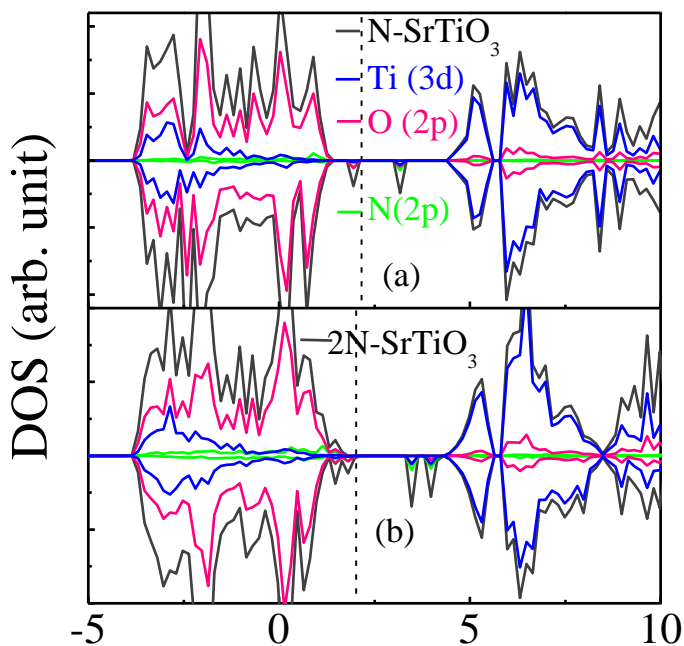
Figure 4.4.1: Density of states of N-doped $SrTiO_3$ (a) and (N, N)-doped $SrTiO_3$ (b)
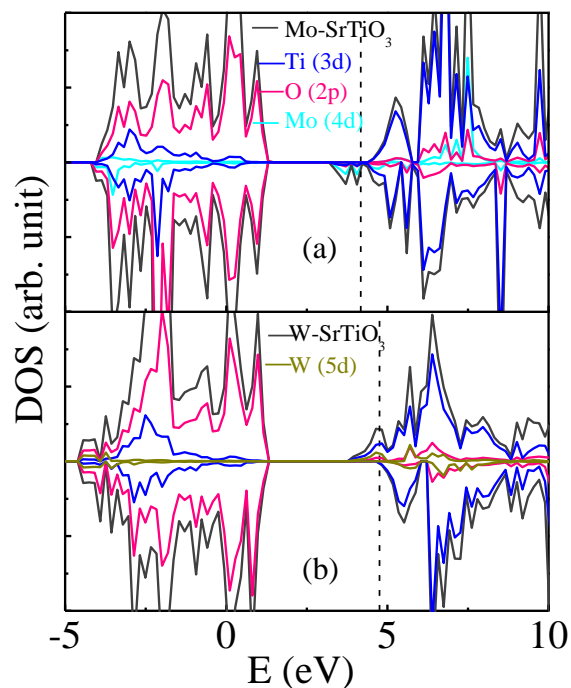
Figure4.4.2: Density of states of Mo-doped $SrTiO_3$ (a) and W-doped $SrTiO_3$ (b).

Figure 4.4.1 shows the comparison of density of N-doped $SrTiO_3$ and (N, N)-doped $SrTiO_3$. The electronic structure for (N, N)-doped $SrTiO_3$ is characterized by the presence of the fully occupied impurity states near the VB and unoccupied states near to the CB. Higher concentration of N results formation of continuum states at the band edges. As the unoccupied states are very close to the CB, we assume the band gap as the difference between these unoccupied states and the VB, and calculated as 1.58 eV. Although, increasing concentration improves the visible light activity, significant downward shifting of the CB edge may affect the reducing behavior severely. Now we will discuss the effect of doping with only Mo/ W on the electronic structure

of SrTiO$_3$. The Mo/W-doped SrTiO$_3$ modeled by introducing Mo or W at the Ti lattice site of a 2 × 2 × 2 SrTiO$_3$ supercell, corresponds to a dopant concentration of 12.5 %. Due to similarity in ionic size between the host element (R$_{Ti+4}$= 0.605 Å) and the substituent element (R$_{Mo+6}$= 0.59 Å and R$_{W+6}$= 0.60 Å) the perturbation in the cubic structure is found to be very small. The calculated Mo-O bond length (d$_{Mo-O}$= 1.972 Å) is comparable to the Ti-O bond length (d$_{Ti-O}$= 1.974 Å). However, Mo introduces partially occupied impurity states just below the CB (Figure 4.4.2a). This is due to presence of two more electrons in the valence cell of Mo (5s^2 4d^4) than that in Ti (4s^2 3d^2). Since these donor states are closer to the CBM, we assume the band gap as the difference between the VBM and the occupied impurity states, which is calculated as 1.86 eV.

In case of doping with W, the calculated W-O bond distance (d$_{W-O}$= 1.948 Å) is found to slightly shorter than the Ti-O bond length in undoped SrTiO$_3$. The characteristic DOS (Figure 4.4.2b) is found to be almost similar to the case of Mo-doped SrTiO$_3$. However, the impurity states appear as continuous state at the conduction band edge, rather than collection of isolated states as appearing in the case of Mo-doped SrTiO$_3$. Analysis of PDOS indicates that, the impurity states are composed of hybridized states of Ti 3d state and W 5d state, i.e., the mixing of Ti 3d states and W 5d states is relatively stronger in this case. This can be interpreted by the closeness of the Ti 3d orbital energy to the W 5d orbital energy, while differs significantly from Mo 4d orbital energy. The effective band gap for W-doped SrTiO$_3$ is calculated as 2.40 eV. Although, from the point of band gap narrowing, doping with only Mo/W seems to be attractive, the presence of partially occupied impurity states as well as formation of charge compensating defects are the limiting factors for the improvement of photocatalytic performance. Now, we

examine the scenario when both the anionic dopant and cationic dopant are present in the same supercell.

We start this discussion with 1:1 (Mo/W, N)-codoped $SrTiO_3$, which is constructed by replacing one Ti and one O atom from the $2 \times 2 \times 2$ supercell with one Mo/W and N, respectively (dopant concentration N is 4.17 % for N-doping and is 12.5% for Mo/W doping). As Mo/W leaves two more electrons and N introduces only one hole, the (Mo/W, N)-codoped $SrTiO_3$ is charge non-compensated and is excess by one electron. The Mo-N bond distance (d_{Mo-N}= 1.762 Å) in the (Mo, N)-codoped $SrTiO_3$ is found to be significantly shorter than the Ti-N bond length (d_{Ti-N}=1.976 Å) in the N-doped $SrTiO_3$.
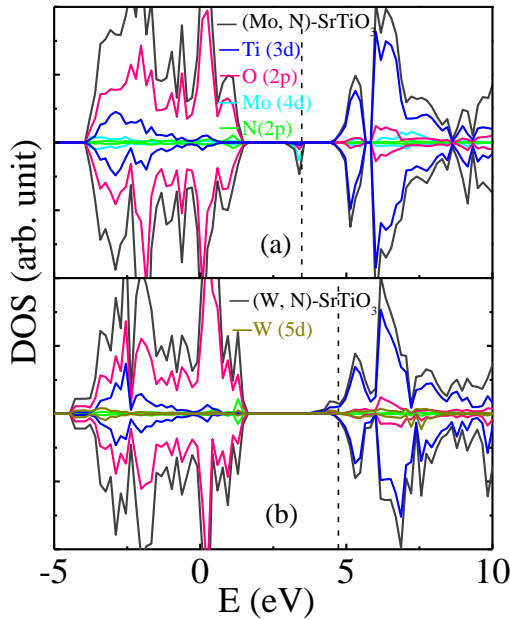
Figure 4.4.3: Density of states of (Mo, N)-codoped (a) and (W, N)-codoped $SrTiO_3$ (b).
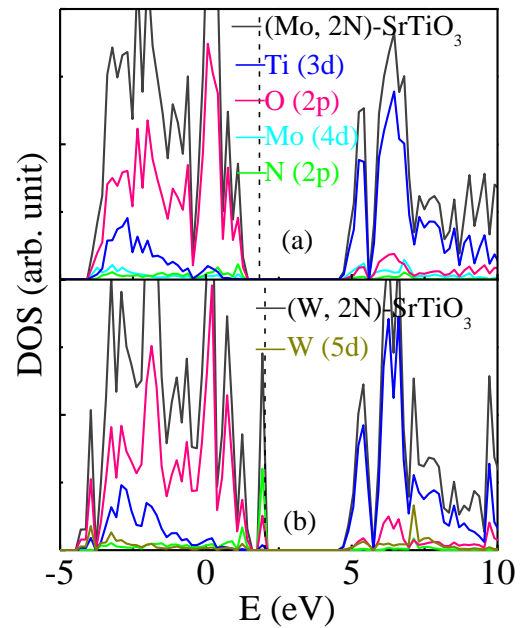
Figure 4.4.4: Density of states of (Mo, 2N)-codoped (a) and (W, 2N)-codoped $SrTiO_3$ (b).

Figure 4.4.3a shows the DOS plot for (Mo, N)-$SrTiO_3$. Although, presence of Mo is found to be effective in passivating the N-induced acceptor states completely, partially occupied

Mo-4d states are introduced in between the VB and CB. Due to lower Mo 4d orbital energy with respect to Ti 3d orbital energy, it appears as discrete state, far below the CB. The CBM is hardly affected by this codoping, and still has Ti 3d character. Although these partially occupied impurity states reduce the excitation energy to 1.06 eV, they may reduce the photoconversion efficiency by trapping the charge carriers. Now we will discuss the case of W and N doping in 1:1 proportion. In the optimized geometry of (W, N)-codoped $SrTiO_3$ the W-N distance is calculated as 1.809 Å. The DOS plot for the (W, N)-codoped $SrTiO_3$ has been shown in the Figure 4.4.3b. In contrast to the previous case, partially occupied impurity states are appeared just below the CB. This is again due to closeness in energy of the Ti 3d orbital and W 5d orbital. However, the nature of VBM is almost similar to the case of (Mo, N)-codoping. The energy difference between the VBM and the occupied impurity state is calculated as 2.07 eV. Although, in this case no discrete state in between VB and CB are observed, the impurity states significantly lower the CBM and thus may affect the reducing behavior severely. Besides, non-compensated codoping is accompanied by the formation of vacancy states, which are known to be efficient source for electron-hole recombination. Hence, 1:1 (Mo/ W, N)-codoped $SrTiO_3$ may show poor photocatalytic performance.

To overcome these problems, we have considered charge compensated (Mo/W, 2N)-codoped $SrTiO_3$. The (Mo/W, 2N)- $SrTiO_3$ is modeled with $2 \times 2 \times 2$ supercell by introducing one Mo/W and two N in the Ti and O lattice sites, respectively (dopant concentration for Mo/W is 12.5 % and for N it is 8.33 %). The calculated Mo-N bond distances (d_{Mo-N} = 1.800 Å and 1.808 Å) and W-N bond distances (d_{W-N} = 1.825 Å and 1.840 Å) in these cases are found to be slightly longer than that in their 1:1 analogues. The N, N distance (d_{N-N} = 2.803 Å and 2.814 Å) in both cases is found to be longer than that in 2N- $SrTiO_3$ (d_{N-N} = 2.663 Å), while closer to the

corresponding O, O distance (d_{O-O} = 2.792 Å) in the undoped $SrTiO_3$. This may be due to the isolelectronic nature of the (Mo/W, 2N)-codoped $SrTiO_3$ with the undoped $SrTiO_3$. The DOS plot (Figure 4.4.4a and b) shows that the Fermi level is shifted to the top of the VB, i.e., both (Mo, 2N)-$SrTiO_3$ and (W, 2N)-$SrTiO_3$ systems will behave as intrinsic semiconductor. It is interesting to observe that both the impurity induced states are completely passivated in these cases, ensuring improved charge carrier mobility as well as photoconversion effieciency due to elimination of the local trapping centers. As the (Mo/W, 2N) codoped $SrTiO_3$ is a charge compensated system, vacancy related defects formation is expected to minimum, which is beneficial for lower electron-hole recombination rate. Analysis of PDOS indicates that the nature of CBM is similar in both the cases. However, the characteristics of the VBM for (Mo, 2N)-codoped $SrTiO_3$ and (W, 2N)-codoped $SrTiO_3$ differs significantly. In case of (Mo, 2N)-codoped $SrTiO_3$ the VBM is composed of (N 2p, O 2p) hybridized state, with the majority contribution from O 2p state, while, in case of (W, 2N)-codoped $SrTiO_3$ the VBM is dominated by N 2p state. Analysis of energy levels indicates that the lowering of N 2p orbital energy occurs by larger extent in presence of Mo than that in presence of W. Consequently the band gap for (Mo, 2N)-codoped $SrTiO_3$ (2.82 eV) differs from that of (W, 2N) codoped $SrTiO_3$ (2.62 eV).
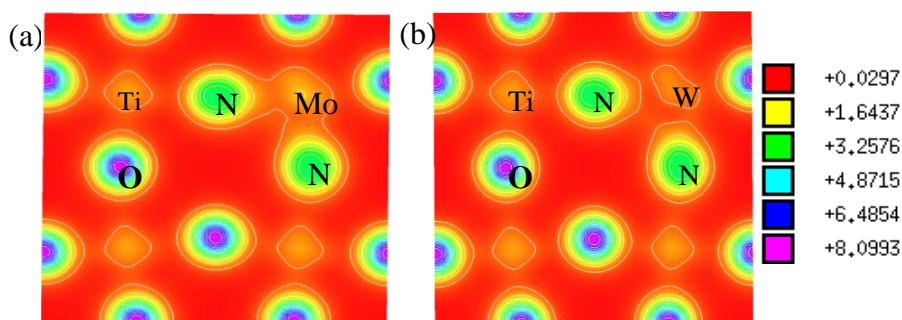
Figure 4.4.5: Part of total charge density distribution for (Mo, 2N)-codoped $SrTiO_3$ (a) and (W, 2N)-codoped $SrTiO_3$ (b).

To investigate this in more details, we analyze the charge density distribution (Figure 4.4.5). In case of (Mo, 2N)-codoped SrTiO$_3$ (Figure 4.4.5a), N electron density is found to be more delocalized towards Mo and a significant overlapping of electron cloud is observed. While, in case of (W, 2N) codoped SrTiO$_3$, although the N electron density is polarized towards W, there is no significant overlapping of the electron cloud (Figure 4.4.5b). This indicates the higher degree of covalent character in the bonding between Mo and N than that in between W and N. This is again supported by Bader charge density analysis. The calculated Bader charges on the N centers are -1.27 |e| and -1.26 |e| for (Mo, 2N)-codoped SrTiO$_3$, while -1.38 |e| and -1.37 |e| for (W, 2N)-codoped SrTiO$_3$. We should also point out that the band gap narrowing in both the cases are the result of elevation of VBM only, as the CBM also moves to the upward direction. This also justifies the choice of our doping strategy to improve the photocatalytic behavior of SrTiO$_3$, for which the CBM is only 0.80 eV above the water reduction level.

4.4.1.2. Defect Pair Binding Energy

To obtain an insight into the coupling strength between the impurity species in the codoped SrTiO$_3$ we have calculated the defect pair binding energy (E$_b$), defined as

$$E_b = E_{mono-doped\ (X@O)} + E_{mono-doped\ (Y@Ti)} - E_{codoped} - E_{SrTiO3} \qquad (4.4.1)$$

where E represents the total energy of the respective systems calculated for the same supercell size. The calculated binding energies for the (Mo, N)-SrTiO$_3$ and (W, N)-SrTiO$_3$ systems are 2.27 eV, and 2.31 eV, respectively. The binding energies are relatively higher in case of (Mo, 2N)-SrTiO$_3$ (4.04 eV) and (W, 2N)-SrTiO$_3$ (4.03 eV) systems. The positive binding energies indicate that the codoped systems are sufficiently stable. The extra stabilization in case of 1:2 codoping may be due to the formation of charge compensated system.

4.4.1.3. Defect Formation Energy

We have also calculated the formation energy for the monodoped as well as the codoped $SrTiO_3$ to explore the optimal growth condition in each case using the same procedure discussed in section 4.3.1.3. For μ_{Mo} and μ_{W}, we have taken the energy of a Mo/W atom in the bulk molybdenum/tungsten metal.

The formation energy for the monodoped and codoped $SrTiO_3$ has been shown in Figure 4.4.6 as a function of the chemical potential of the host element. The dopant formation energy follows an increasing trend with the chemical potential of the host element (Figure 4.4.6a and 4.4.6b). This is due to the fact that the host rich condition is unfavorable for vacancy formation, required for the insertion of the dopant element.
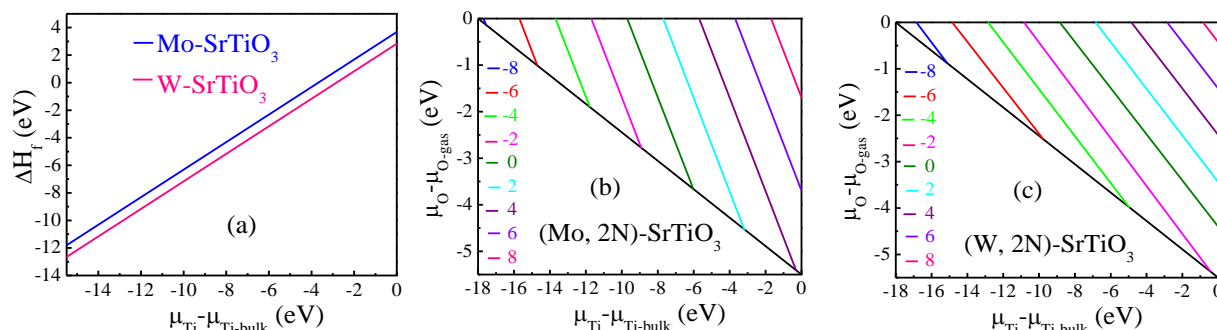
Figure 4.4.6: The variation of defect formation energy for Mo-doped $SrTiO_3$ and W-doped $SrTiO_3$ (a) (Mo, 2N)- codoped $SrTiO_3$ (b) (W, 2N)- codoped $SrTiO_3$ (c).

As can be seen from Figure 4.4.6a, the introduction of W in the $SrTiO_3$ crystal structure is more feasible than that of Mo. Figures 4.4.6b and c indicate that introduction of N in the $SrTiO_3$ crystal lattice is facilitated by the presence of Mo/W, i.e. codoping is energetically more favorable. This may be due to the stronger coupling between Mo/W and N. The formation

energy for the codoped system is found to be much lower when the growth condition is O-rich rather than Ti-rich.

4.4.1.4. Effect of Concentration

To investigate the effect of concentration calculation with different super cell size has been carried out. We consider two higher concentration cases using $2 \times 1 \times 1$ supercell and $2 \times 2 \times 1$ supercell and one lower concentration case using $2 \times 2 \times 3$ supercell. Here, we will discuss the case of codoping with W and N in 1:2 proportion. In each case, we consider the geometry, where both the N are directly attached to W, has been found to be lowest energy configuration for the $2 \times 2 \times 2$ supercell. In case of $2 \times 1 \times 1$ supercell, the dopant concentration corresponds to 50 % for W and 33.33 % for N. The calculated band gap is drastically reduced to 0.78 eV. The VBM is elevated by 1.58 eV and the CBM is lowered by 0.83 eV with respect to that of the undoped $SrTiO_3$ due to higher concentration of the dopant. Hence, this highly doped $SrTiO_3$ may not be suitable for both water oxidation and reduction. In case of $2 \times 2 \times 1$ supercell the dopant concentration corresponds to 25 % for W and 16.67 % for N. The calculated band gap (2.65 eV) is found to be close to that obtained using $2 \times 2 \times 2$ supercell. For lower dopant concentration we increase the supercell size to $2 \times 2 \times 3$, which corresponds to the dopant concentration of 8.33 % for W and 5.55 % for N. The calculated band is 2.66 eV. This indicates that even at lower dopant concentration the reduction of band gap is quite significant to achieve appreciable visible light activity.

4.4.1.5. Optical Property

Figure 4.4.7 shows the calculated absorption curves for the undoped $SrTiO_3$, (Mo, 2N)- $SrTiO_3$, and the (W, 2N)-$SrTiO_3$. The absorption curves for both the codoped systems are extended to the visible region with respect to that of the undoped $SrTiO_3$. This is due to decrease in photo-excitation energy with codoping as discussed in the electronic structure part. The absorption shift for the (W, 2N)-$SrTiO_3$ is relatively higher than that of the (Mo, 2N)-$SrTiO_3$. Hence, (W, 2N) codoping should be better choice to achieve more enhancement in the visible light activity.
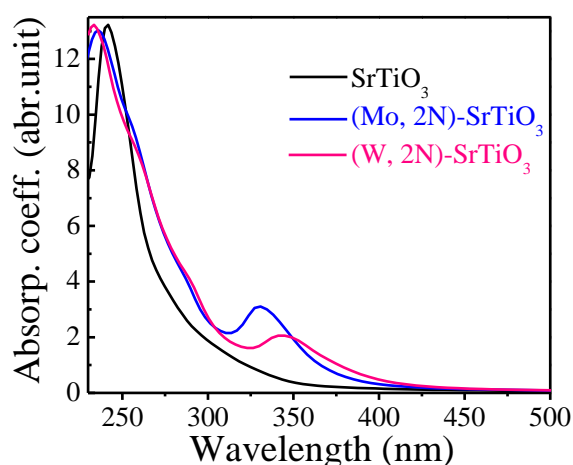
Figure 4.4.7: The calculated absorption curves for the undoped and codoped $SrTiO_3$.
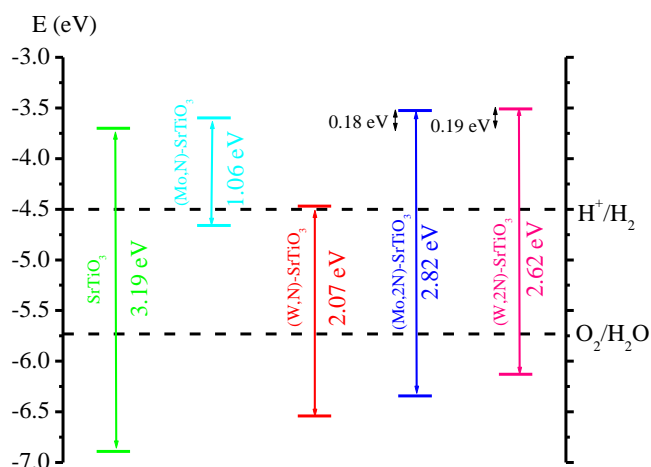
Figure 4.4.8: Band edge alignment for the undoped and codoped $SrTiO_3$.

4.4.1.6. Photocatalytic Activity

To check whether both non-compensated and compensated codoped $SrTiO_3$ are suitable for overall water splitting or not we align their band edges using same procedure as discussed in section 4.3.1.6. As shown in Figure 4.4.8, the VB edge of (Mo, N)-$SrTiO_3$ is located above the water oxidation level (H_2O/O_2). Hence, (Mo, N)-codoped $SrTiO_3$ will not be able to release O_2 in

the water splitting process, while, in case of the (W, N)-codoped $SrTiO_3$ the CB edge lies very close to the water reduction level. This indicates that the (W, N)-codoped $SrTiO_3$ may not be suitable for hydrogen production through water splitting. On the other hand, the band edge positions for both (Mo, 2N)-$SrTiO_3$ and (W, 2N)-$SrTiO_3$ are such that they are suitable for overall water splitting. Figure 4.4.8 indicates that the CBM for both the systems are located even above that of the undoped $SrTiO_3$, resulting into an enhancement of reducing power as well. Thus, the (Mo, 2N)-codoped $SrTiO_3$ and (W, 2N)-codoped $SrTiO_3$ systems are expected to be thermodynamically more suitable for H_2 evolution in comparison to the undoped $SrTiO_3$.

4.4.2 Conclusion

In this section, we have reported the results on investigation using hybrid DFT, the effect of codoping of Mo/W and N in different proportions aiming at improving the photocatalytic activity of $SrTiO_3$ under visible light. The presence of Mo or W is shown to favor the N-doping by reducing the formation energy. In the codoped systems, strong coupling between N and Mo or W is established, which is responsible for making the systems sufficiently stable. In the case of 1:1 codoping, although the band gap decreases significantly, incomplete passivation of the localized impurity states may lead to poor photocatalytic response. The band edge positions are also perturbed significantly, making (Mo, N)-$SrTiO_3$ inactive for oxygen evolution and (W, N)-$SrTiO_3$ unsuitable for hydrogen evolution in the water splitting process. As the (Mo/W, N)-$SrTiO_3$ is charge non-compensated, carrier loss due to defect states cannot be avoided. Thus codoping of Mo/W and N in 1:1 proportion should not be suggested for the improvement of photocatalytic efficiency of $SrTiO_3$ towards solar water splitting. On the other hand, introduction of Mo/W and N in 1:2 proportion results into charge compensated codoped system, which is

isoelectronic with the undoped $SrTiO_3$ and both the dopant-induced localized states are completely passivated. Hence good mobility behavior as well as improved photoconversion efficiency are expected for the (Mo/W, 2N) $SrTiO_3$ system. The reduction in band gap is solely due to the elevation of the VBM. The CBM is also found to be shifted in the upward direction, indicating that the reducing property at the CB will be stronger than the undoped $SrTiO_3$. As the codoping of (W, 2N) extends the absorption curve of $SrTiO_3$ towards visible region by larger extent than (Mo, 2N) codoping, it may be concluded that the (W, 2N)-codoped $SrTiO_3$ should be better choice to achieve improved photocatalytic behavior for solar driven water splitting.

4.5. Origin of enhanced visible light driven water splitting by (Rh, Sb)-SrTiO₃

In this section, we investigate recent observation of enhanced photo-conversion efficiency of Rh-doped SrTiO₃ with addition of Sb.[192-194] Owing to good visible light activity, Rh-doped SrTiO₃ has been paid significant attention by several groups. It shows relatively higher photocatalytic activity for hydrogen generation as compared to the (Mn/Ru/Ir/Pt/Pd)-doped SrTiO₃. Various attempts have been made to improve the photocatalytic efficiency of Rh-doped SrTiO₃ by further extent. As for example, Iwashina et al found a significant increase of photocurrent as well as rate of water splitting when Rh-doped SrTiO₃ was pasted on an electrode with respect to that in powdered form.[186] Shen at al adopted polymerizable complex method for the preparation of Rh-doped SrTiO₃ and observed better photocatalytic activity than that prepared by using conventional route.[183] Later on Kawasaki et al found that photocatalytic performance of Rh-doped SrTiO₃ is significantly higher when Rh exists in the +3 state than in the +4 state.[187,188] It has been revealed that Rh^{+4} state introduces localized acceptor states in between the valence band (VB) and conduction band (CB). Since these states are very efficient in trapping the charge carriers and promoting their recombination, the photo-conversion efficiency achieved is relatively lower. On the other hand, in presence of Rh^{+3} state, acceptor states are found to disappear, consequently reducing the rate of charge carrier loss. Thus, the oxidation state of Rh should be +3 for achieving a high photocatalytic activity of Rh-doped SrTiO₃. However, the challenging job is to fix the oxidation state of Rh to +3 as both Rh^{+3} and Rh^{+4} states have been found to be present in the normally prepared Rh-doped SrTiO₃ sample. Codoping with Sb has been shown to be one of the successful approaches for the stabilization of Rh^{+3} state in the Rh-doped SrTiO₃ system, which has been explained in terms of the formation of charge compensated

system in presence of Sb^{+5} with Rh^{+3}. Thus, the formation of Rh^{+4} state is suppressed, leading to an increase of lifetime of the photo-generated charge carriers and hence the photocatalytic activity to a significant extent. However, detailed description of the change in electronic structure of Rh-doped $SrTiO_3$ in presence of Sb is yet to be explored. Here, we have investigated the origin of the acceptor states in case of Rh-doped $SrTiO_3$ in details, thus attempting to find out how they are passivated in presence of Sb. A systematic quantum chemical calculation using density functional theory (DFT) has been presented describing the effect of the individual as well as both the dopant elements on the electronic structure of $SrTiO_3$.

4.5.1. Results and Discussions

To model the doped systems, we consider $2 \times 2 \times 3$ supercell (60 atoms) of the cubic $SrTiO_3$ crystal structure. All the model structures have been fully relaxed (both ionic positions as well as cell parameter) using conjugate gradient algorithm with k-point mesh of $6 \times 6 \times 4$ generated by using Monkhorst and Pack scheme and energy convergence of 10^{-6} eV. To construct the potential, we have considered the valence states: Sr $(4s^2 4p^6 5s^2)$, Ti $(4s^2 3d^2)$, Rh $(5s^1 4d^8)$, Sb $(5s^2 5p^3)$, and O $(2s^2 2p^4)$.

4.5.1.1. Geometry and Electronic Structure

A $2 \times 2 \times 3$ supercell structure of $SrTiO_3$ is shown in Figure 4.5.1. The calculated cell dimensions are found to be 7.897 Å (in the X and Y direction) and 11.846 Å (in the Z direction).
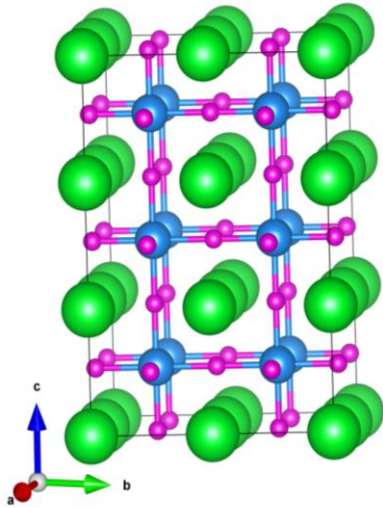
Figure 4.5.1: $2 \times 2 \times 3$ supercell structure of cubic $SrTiO_3$. Largest sphere (green): Sr; Medium sphere (sky blue): Ti; smallest sphere (magenta): O.

In section 4.3.1.4, we have shown that the calculated band gap (3.19 eV) of $SrTiO_3$ matches well with the experimentally reported value (3.2 eV) and the VBM and CBM have mainly O 2p character and Ti 3d character, respectively. In the following subsections, we will first discuss the effect of the individual dopant elements (Rh and Sb), and then the combined effect of both.

Previous experimental studies have shown that, Rh substitutes Ti^{+4} and occupies the octahedral lattice site in the $SrTiO_3$ crystal structure. Hence, we model Rh-doped $SrTiO_3$ by replacing one of the Ti atoms in the $2 \times 2 \times 3$ supercell by Rh (dopant concentration corresponds to 8.33 %). Full geometric relaxation indicates that the deviation from ideal structure is very small (cell dimensions increase by 0.002 Å in the in the X/ Y direction, and 0.005Å in the Z direction), which is due to the closeness of ionic radii of Ti^{+4} ($R_{Ti^{+4}} = 0.605$ Å) and Rh^{+4} ($R_{Rh^{+4}} = 0.60$ Å).This is consistent with the observation of similar single phase XRD pattern of Rh-doped $SrTiO_3$ with that of undoped $SrTiO_3$ crystal structure. However, the presence of Rh brings significant changes in the electronic structure of $SrTiO_3$. As can be seen from the DOS plot (Figure 4.5.2a), the impurity states appear as partially unoccupied states above the VB, and are contributed by O 2p and Rh 4d orbital. This is due to strong hybridization between O 2p and Rh 4d states. The unsymmetrical nature of the spin-up and spin-down part of DOS is the

consequence of unpaired electron in the Rh-doped SrTiO$_3$ system (Rh^{+4}: 4d^5). A more detailed description of the nature of the gap states is presented in Figure 4.5.2a. In the octahedral crystal field, Rh 4d orbitals split into t$_{2g}$ subset and e$_g$ subset. Figure 4.5.3a reveals that the t$_{2g}$ subset of orbitals contribute to these gap states. So, one can describe the electron distribution in the Rh 4d orbital as t$_{2g}^5$ e$_g^0$, i.e., low spin configuration. This is supported by the calculated total magnetic moment value of 1.0 μ$_B$ per supercell.
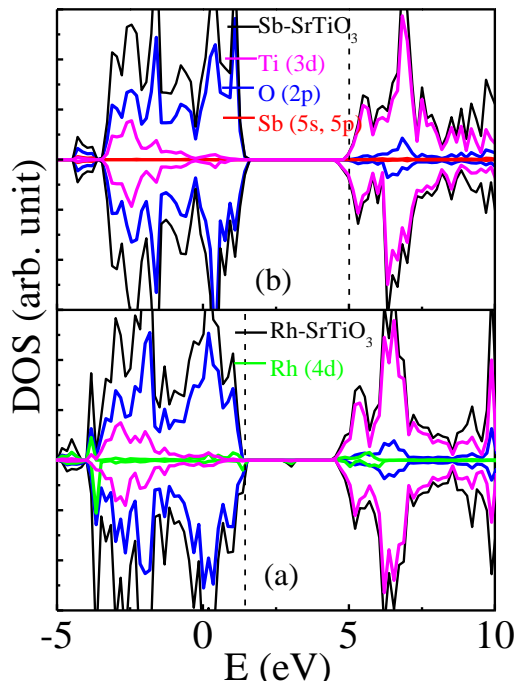
Figure 4.5.2: Density of states of Rh-doped SrTiO$_3$ (a) and Sb-doped SrTiO$_3$ (b) using $2 \times 2 \times 3$ supercell structure. Vertical dashed line indicates the Fermi Level.
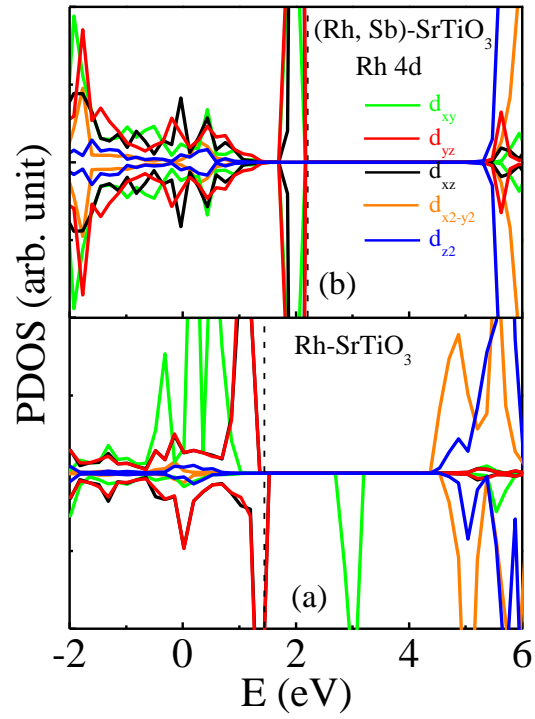
Figure 4.5.3: Projected density of states on the Rh 4d orbital for Rh-doped SrTiO$_3$ (a) and (Rh, Sb)-codoped SrTiO$_3$. Vertical dashed line indicates the Fermi Level.

The photoexcitation of electron in the Rh-doped $SrTiO_3$ occurs with light of even lower energy due to the presence of the mid gap states. This attributes to the experimental observation of significant enhancement of the visible light activity of $SrTiO_3$ with Rh doping. Unfortunately, these acceptor states provide an efficient source for charge carrier trapping centers and thus reduce the mobility of the charge carriers drastically. This causes the photo-conversion efficiency of Rh-doped $SrTiO_3$ to be lower than expected. Besides, it may have significant role in the observation of poor oxygen evolution activity of Rh-doped $SrTiO_3$. Hence, to improve the photocatalytic activity, these acceptor states must be passivated, which can be done by suppressing the formation of Rh^{+4} state. Introduction of Sb has been reported to be successful in stabilizing Rh^{+3} state, and increasing the lifetime of the photo-generated charge carriers. Here we want to investigate the role of Sb from the electronic structure point of view, which has not been discussed so far. We first discuss the individual effect of Sb on the electronic structure of $SrTiO_3$. Similar to the case of Rh, Sb also prefers to occupy the Ti lattice site of $SrTiO_3$ crystal structure. To model Sb-doped $SrTiO_3$, we replace one of the Ti from a $2 \times 2 \times 3$ $SrTiO_3$ supercell by Sb (dopant concentration corresponds to 8.33 %). After full relaxation, it has been observed that the change in geometrical structure due to Sb-doping is limited to local region only (cell dimensions increase by 0.02 Å in the in the X/ Y direction and 0.033 Å in the Z direction), consistent with the experimental observation. This is due to the similarity in ionic size of Ti^{+4} ($R_{Ti^{+4}} = 0.605$ Å) and Sb^{+5} ($R_{Sb^{+5}} = 0.60$ Å). The DOS plot (Figure 4.5.2b) shows the introduction of partially occupied impurity states due to Sb doping adjacent to the CBM of $SrTiO_3$. The Fermi level shifts near to the CB, indicating the presence of extra electron. This is obvious because Sb ($5s^2 5p^3$), which is more stable in +5 state, occupies lattice site of Ti^{+4} and introduces one extra electron. As can be seen from Figure 3b, the impurity states have mainly Ti 3d character, i.e., the extra

electron is localized on the Ti center. The total magnetic moment of Sb-doped $SrTiO_3$ is calculated to be - 0.715 μ_B, which is mainly contributed by Ti, indicating localization of the unpaired electron on the Ti center.

Now, we will proceed to discuss the scenario when both Rh and Sb dopants are present in $SrTiO_3$. According to recent XRD analysis of (Rh, Sb)-codoped $SrTiO_3$, both Rh and Sb occupy Ti lattice sites, maintaining the basic crystal structure of the host. It also rules out the formation of any other defect states due to codoping with Rh and Sb. In this study, we model (Rh, Sb)-codoped $SrTiO_3$ by introducing one Rh and one Sb at the Ti lattice site in a $2 \times 2 \times 3$ $SrTiO_3$ supercell (concentration for both the dopants corresponds to 8.33 %). Geometry optimization indicates that the cell dimensions increase by 0.019 Å in the in the X/ Y direction, and 0.043Å in the Z direction.
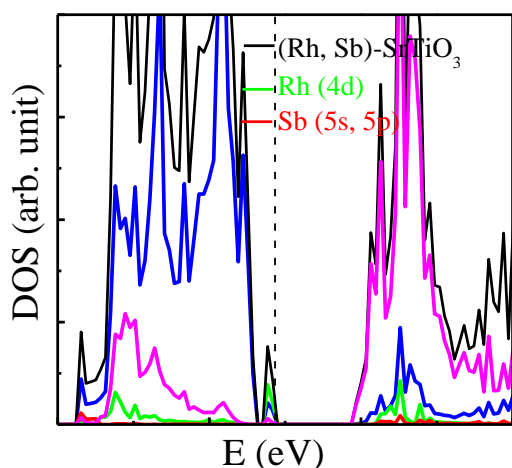
Figure 4.5.4: Density of states of (Rh, Sb)-codoped $SrTiO_3$ using $2 \times 2 \times 3$ supercell structure. Vertical dashed line indicates the Fermi Level.
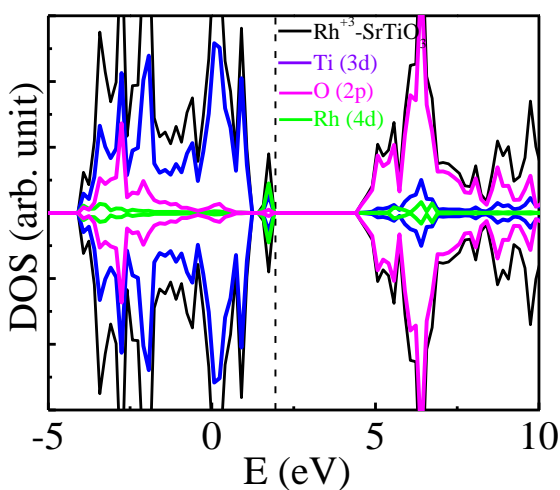
Figure 4.5.5: Density of states of Rh^{+3}-doped $SrTiO_3$ using $2 \times 2 \times 3$ supercell structure. Vertical dashed line indicates the Fermi Level.

The DOS plot for (Rh, Sb)-codoped $SrTiO_3$ (Figure 4.5.4) shows the formation of a clean band structure without encountering any localized states. Analysis of partial density of states (PDOS) indicates that the VBM is composed of Rh 4d and O 2p hybridized states, with higher contribution of Rh 4d state as compared to the O 2p states. This elevates the VBM with respect to that of the undoped $SrTiO_3$, resulting into a band gap narrowing to 2.62 eV. The spin up and spin down part of DOS are found to be symmetrical, indicating the absence of unpaired electron in the (Rh, Sb)-codoped $SrTiO_3$. This is supported by the total magnetic moment value of zero, in agreement with the observation of Niishiro et al.[194] As can be seen from Figure 4.5.3b, the t_{2g} set of Rh 4d orbital is completely occupied ($t_{2g}^6 e_g^0$). This is the consequence of transferring the extra electron to the Rh center. To demonstrate the phenomenon of charge transfer more clearly, we analyse the Bader charge density at the Rh center in absence and presence of Sb. We employ grid based Bader analysis algorithm as implemented in VASP 5.2 version to calculate the charge on the atom center. The decrease in Bader charge on the Rh center from 1.61 (Rh-doped $SrTiO_3$) to 1.45 ((Rh, Sb)-codoped $SrTiO_3$) indicates the lower oxidation state of Rh in the latter, consistent with the experimental observation. Thus, the present study unambiguously explains the evidence of Rh^{+3} state in the (Rh, Sb)-codoped $SrTiO_3$.

By comparing the band structure of Rh-doped $SrTiO_3$ in absence and presence of Sb, one can explain the origin of improved photocatalytic activity of (Rh, Sb)-codoped $SrTiO_3$. In presence of Sb, the acceptor states are completely passivated, thereby reducing the rate of electron-hole recombination. Due to continuous band structure at the band edges, the charge carriers have better mobility in the (Rh, Sb)-codoped $SrTiO_3$. Besides, Sb^{+5} stabilized Rh^{+3} state by forming charge compensated system. This will reduce the formation of vacancy, which has been found to be present in the Rh-doped $SrTiO_3$ sample. All these factors go in favor of

increased lifetime of the charge carriers in the (Rh, Sb)-codoped $SrTiO_3$ system, thus enhancing the photocatalytic activity significantly.

4.5.1.2. Rh^{+3} doped $SrTiO_3$

We have also studied the effect of doping with only Rh^{3+} and compared the results with that of (Rh, Sb)-codoped $SrTiO_3$. Rh^{3+}-doped $SrTiO_3$ is modelled by adding one extra electron, while keeping the positive background charge same. The DOS plot for the Rh^{3+}-doped $SrTiO_3$ is shown in Figure 4.5.5. Unlike the case of Rh^{4+}-doped $SrTiO_3$ (Figure 4.5.2a), no acceptor states in between the VB and CB is found in this case. The VBM is composed of hybridised state of Rh 4d and O 2p, while the CBM is mainly contributed by Ti 3d state. The band gap for Rh^{3+}-doped $SrTiO_3$ is calculated as 2.60 eV. All these characteristics are very much similar to the case of (Rh, Sb)-codoped $SrTiO_3$ (Figure 4.5.4). However, the CBM position of $SrTiO_3$ is hardly affected by doping with only Rh^{3+}, while it is significantly shifted in the upward direction due to codoping with both Rh and Sb, thus increasing the reducing behaviour at the CB. Hence, a better hydrogen evolution efficiency is expected in case of (Rh, Sb)-codoped $SrTiO_3$ than Rh^{3+}-doped $SrTiO_3$. Besides, Rh^{3+}-doped $SrTiO_3$, being a charge non-compensated system may have tendency to form undesirable vacancy defects in the crystal structure, promoting electron-hole recombination rate. This may be one of the limiting factors for achieving higher photo-conversion efficiency of Rh^{3+}-doped $SrTiO_3$.

4.5.1.3. (Rh, N)-codoped $SrTiO_3$

We have extended our study to investigate the role of N as a codopant of Rh-doped $SrTiO_3$. As can be seen from previous experimental studies, N plays the role as an anionic dopant and

occupies the oxygen lattice site. Hence, we first investigate the electronic structure of (Rh, N)-codoped $SrTiO_3$ considering N as anionic dopant. This has been modelled by replacing one of the Ti atoms and O atoms by Rh and N, respectively in the $2\times2\times3$ supercell. Full geometry optimization of (Rh, N)-codoped $SrTiO_3$ indicates that N is more closer to Rh than Ti. This leads to shortening of Rh-N bond length (1.83 Å) and enlarging the Ti-N bond length (2.15 Å). The cell volume is increased by 0.64 % with respect to that of undoped $SrTiO_3$. The DOS plot has been shown in Figure 4.5.6a and the calculated energy difference between VBM and impurity states is calculated as 2.59 eV. The acceptor states are shifted in the upward direction and appear closer to the bottom of the CB. This leads to the lowering the CBM level by a significant extent. Analysis of electronic energy levels indicates that the CBM position for (Rh, N)-codoped $SrTiO_3$ is 0.65 eV lower than that of (Rh, Sb)-codoped $SrTiO_3$. This will make a difference in the reducing behaviour at the CB. Besides, (Rh, N)-codoped $SrTiO_3$ being a charge non-compensated system will form vacancy defects spontaneously.
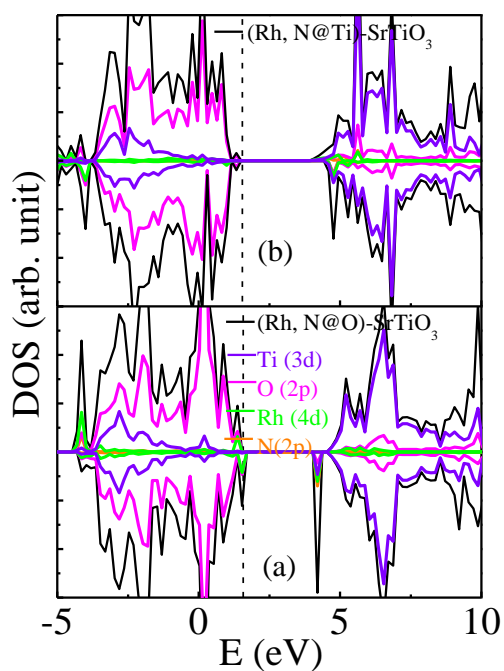
Figure 4.5.6: Density of states of (Rh, N@O)-codoped $SrTiO_3$ (a) and (Rh, N@Ti)-codoped $SrTiO_3$ (b) using $2 \times 2 \times 3$ supercell structure. Vertical dashed line indicates the Fermi Level.

Now, we will consider N as cationic dopant, which has not been explored experimentally till date. Here, (Rh, N)- codoped SrTiO$_3$ model structure has been constructed by replacing two Ti from a 2×2×3 supercell with one Rh and one N. In this case, a significant distortion in the host crystal structure is observed due to large difference between the ionic size of Ti^{+4} (0.605 Å) and N^{+5} (0.13 Å). The cell volume is increased by 1.27 %. The N-O bond length varies in the range 1.20 Å -2.573 Å. The DOS plot has been shown in Figure 4.5.6b. In this case, the Rh-induced acceptor states are found to be completely passivated. The calculated band gap is found to decrease to 2.47 eV due to shifting of the CBM in the downward direction. Analysis of energy levels indicates that the CBM for (Rh, N)- codoped SrTiO$_3$ is 0.84 eV lower than that of the (Rh, Sb)- codoped SrTiO$_3$. This will lead to poor reducing behavior at the CB. Hence, based on this discussion we can justify the choice of Sb as a codopant of Rh-doped SrTiO$_3$.

4.5.1.4. Oxygen Deficient Rh-doped SrTiO$_3$

We have also investigated the role of oxygen vacancy on the electronic structure of Rh-doped SrTiO$_3$. To model the Rh-doped SrTiO$_3$ with neutral oxygen vacancy we remove one oxygen atom from a 2×2×3 SrTiO$_3$ supercell and replacing one of the Ti by Rh. The magnetic moment calculation (-0.94 μ_B) indicates that there is excess electron, which is localized on the Ti centers. The DOS plot for the oxygen-deficient Rh-doped SrTiO$_3$ has been shown in Figure 4.5.7. The Fermi level is shifted to the CB region due to excess electron. The nature of VBM (Rh 4d+ O 2p) looks very much similar to that of Rh^{+3}-doped SrTiO$_3$, while partially occupied Ti-3d states introduced adjacent to the CBM in case of oxygen-deficient Rh-doped SrTiO$_3$. The energy difference between the (Rh 4d, O 2p)-hybridized states and Ti 3d state is calculated and found to be 2.34 eV. This will extend the absorption curve towards the visible region by larger extent than

that of Rh^{+3}-doped $SrTiO_3$. Unfortunately, the oxygen vacancy is well known charge carrier trapping center, and will diminish the photoconversion efficiency severely.
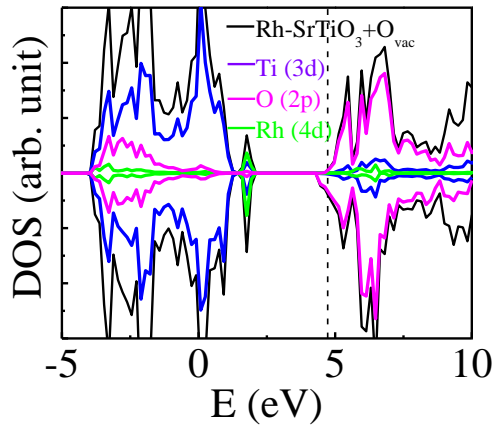
Figure 4.5.7: Density of states of Rh-doped $SrTiO_3$ with neutral oxygen vacancy using $2 \times 2 \times 3$ supercell structure. Vertical dashed line indicates the Fermi Level.
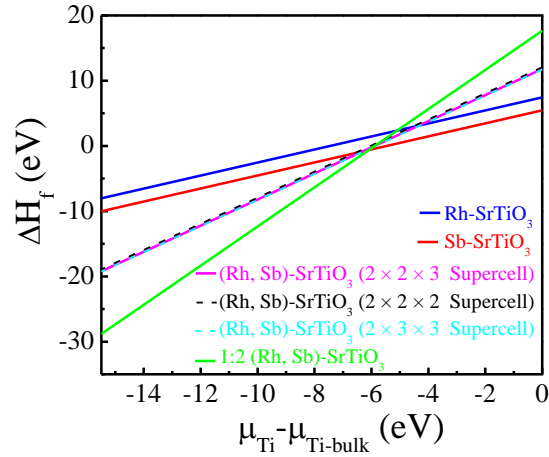
Figure 4.5.8: The variation of defect formation energy with the chemical potential of Ti (μ_{Ti}- $\mu_{Ti-bulk}$) for Rh-doped $SrTiO_3$, Sb-doped $SrTiO_3$, (Rh, Sb)- codoped $SrTiO_3$ (using $2 \times 2 \times 2$, $2 \times 2 \times 3$ and $2 \times 3 \times 3$ supercell) and 1:2 (Rh, Sb)- codoped $SrTiO_3$.

4.5.1.5. Defect Pair Binding Energy

The defect pair binding energy (E_b), which provides useful information about the stability of (Rh, Sb)-codoped $SrTiO_3$ is defined as

$$E_b = E_{Rh-SrTiO3} + E_{Sb-SrTiO3} - E_{(Rh, Sb)-SrTiO3} - E_{SrTiO3} \qquad (4.5.1)$$

where, the total energy (E) of the undoped, monodoped and codoped system has been calculated using supercell of equal dimension. The positive value of the calculated binding energy (1.13 eV/ supercell) for the (Rh, Sb)-codoped $SrTiO_3$ justifies its stability in the real scenario.

4.5.1.6. Defect Formation Energy

Calculation of the defect formation energy has been carried out by using the same procedure as in section 4.3.1.3 to find out the relative feasibility of the synthesis of Rh-doped $SrTiO_3$ sample in absence and presence of Sb. Since all the cases involve substitution of Ti, we define the defect formation energy as

$$\Delta H_f = E_{doped} + n_{Ti}\,\mu_{Ti} - E_{SrTiO3} - n_{Sb}\,\mu_{Sb} - n_{Rh}\,\mu_{Rh,} \qquad (4.5.2)$$

where, E_{doped} represents the total energy of the mono-doped /codoped $SrTiO_3$. Here n_x defines the number of atoms of (Rh/Sb) introduced or Ti removed during formation of doped materials, while μ_X is the elemental chemical potential of the species Ti, Rh and Sb.

Figure 4.5.8 presents the defect formation energy profile for the monodoped as well as codoped $SrTiO_3$. The common characteristics for all the cases is that the defect formation energy increases as we proceed from Ti-poor to Ti-rich condition. This is expected as the formation of Ti vacancy is energetically unfavorable under Ti-rich condition. The formation energy calculation indicates that doping with Sb is energetically more favorable by 2.0 eV than Rh-doping. It is interesting to note that the cost of Rh doping significantly decreases in presence of Sb at the Ti-poor condition. Hence, the formation of (Rh, Sb)-codoped $SrTiO_3$ is energetically more favorable than the (Rh/ Sb)-monodoped $SrTiO_3$.

4.5.1.7. Effect of Concentration

We extended our study to have a look at the scenario when the concentrations of Rh and Sb are increased or decreased by equal extent. For this purpose, we consider $2 \times 2 \times 2$ supercell and $2 \times 3 \times 3$ supercell to introduce one Rh and one Sb at the Ti lattice sites, which corresponds to dopant concentration of 12.5% and 5.5%, respectively. Both the structures are relaxed fully using

the same functional as well as energy convergence criteria, as discussed in the earlier section. The k-point mesh used for sampling the Brillouin zone are $8 \times 8 \times 8$ and $6 \times 4 \times 4$, respectively. The defect formation energy (Figure 4.5.8) is found to be of the same order as that calculated using $2 \times 2 \times 3$ supercell. This justifies our choice of supercell size in the present calculation. The VBM is mainly contributed by Rh 4d and O 2p hybridized states and CBM is composed of Ti 3d state. However, the impurity states at the VBM are found to be less delocalized in case of lower concentration of Rh and Sb. The band gap of (Rh, Sb)-codoped $SrTiO_3$ at the higher concentration and lower concentration of the dopant elements found to be are 2.62 eV and 2.65 eV, respectively.

4.5.1.8. Effect of Different Dopant Proportion

In a recent experimental study, Niishiro et al synthesized a series of (Rh, Sb)-codoped $SrTiO_3$ samples with different proportions of Rh and Sb and investigated their efficiency to produce hydrogen and oxygen during water splitting reaction. According to their report, the material with relatively higher proportion of Rh shows poor oxygen evolution efficiency. On the other hand, Sb rich codoped sample shows moderate efficiency for both hydrogen evolution and oxygen evolution. Finally they suggested that the ratio of Sb and Rh should be unity for achieving highest oxygen evolution efficiency. To explain these observations more clearly, one needs to investigate the electronic structure of $SrTiO_3$ codoped with different ratio of Rh and Sb. For this purpose, we consider here 2:1 and 1:2 (Rh, Sb)-codoped $SrTiO_3$. In the present study, 2:1 codoped system has been modeled by introducing two Rh and one Sb at the Ti lattice sites of $2 \times 2 \times 3$ supercell (dopant concentration: Rh: 16.67%, Sb: 8.33%). The computational parameters are kept fixed at the same values as used in the case of 1:1 codoping. The DOS plot for the 2:1

(Rh, Sb)-codoped $SrTiO_3$ has been shown in Figure 4.5.9a, where it is clear that the spin-up and spin-down parts are unsymmetrical, indicating the presence of unpaired electron. Calculation of magnetic moment also shows the existence of unpaired electron in the 2:1 (Rh, Sb)-codoped $SrTiO_3$, which is rather obvious because of insufficient amount of Sb, which is responsible for providing extra electron to pair the d electrons of Rh. The DOS plot shows the presence of partially occupied and unoccupied states, similar to the case of doping with only Rh. This divides the band gap in two regions, with energy gap of 1.05 eV and 1.15 eV. Although, it improves the visible light activity significantly, affect the oxygen evolution drastically. Analysis of PDOS indicates that these states are hybrid states, composed of Rh 4d orbital and O 2p orbital.

On the other hand, model for 1:2 codoping is constructed by replacing three Ti atoms with one Rh and two Sb from a $2 \times 2 \times 3$ $SrTiO_3$ supercell, which corresponds to dopant concentration for Rh and Sb of 8.33% and 16.67%, respectively. The DOS plot for the 1:2 (Rh, Sb)-codoped $SrTiO_3$ is shown in Figure4.5.9b. The Fermi level is in the CB region, indicating the presence of excess electron, which is a consequence of unequal proportion of electron donor and acceptor. This leads to a net total magnetic moment of -0.9 μ_B, which is contributed by Ti, i.e., the extra electron is localized on the Ti centers, which is also responsible for the appearance of occupied Ti 3d states at the bottom of the CB, similar to the case of Sb-doping. The VBM is contributed by Rh 4d and O 2p hybrid states, similar to the case of 1:1 codoping. The calculated energy difference between the VBM and occupied state at the CB is found to be 2.39 eV. Hence, from a consideration of the utilization of visible region of solar light, both 2:1 and 1:2 codoping approaches are attractive. However, due to charge non-compensated nature, there is a possibility of spontaneous formation of vacancy defects, which are known to work as electron-hole

recombination centers. Hence, both are expected to achieve lower photo-conversion efficiency in comparison to the case of 1:1 codoping.
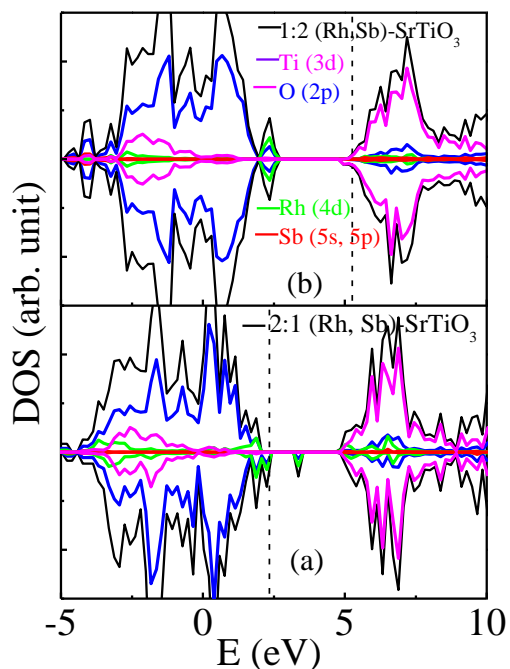
Figure 4.5.9: Density of states of 2:1 (Rh, Sb)-codoped $SrTiO_3$ (a) and 1:2 (Rh, Sb)-codoped $SrTiO_3$ (b) using $2 \times 2 \times 3$ supercell structure. Vertical dashed line indicates the Fermi Level.

4.5.1.9. Optical Property

To investigate the change in the optical property of $SrTiO_3$ due to codoping with Rh and Sb, we calculate the frequency dependent dielectric function to obtain absorption coefficient. Figure 4.5.10 shows the optical spectrum for the undoped and codoped $SrTiO_3$. The absorption curve for the undoped $SrTiO_3$ is found to be shifted towards visible region due to codoping with Rh and Sb. This is due to reduction of band gap with codoping. This explains the observation of improved photocatalytic activity of (Rh, Sb)-codoped $SrTiO_3$ under visible light.
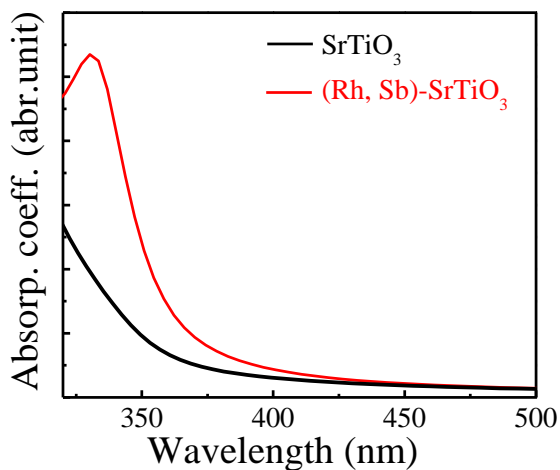
Figure 4.5.10: The calculated absorption curves for the undoped and (Rh, Sb)-codoped SrTiO₃.
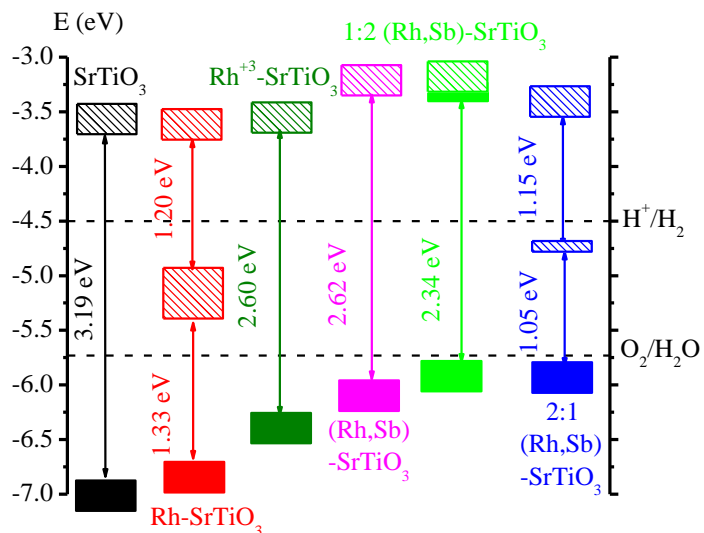
Figure 4.5.11: The band edge alignment of the undoped, Rh-doped SrTiO₃, Rh^{+3}-doped SrTiO₃, (Rh, Sb)-codoped SrTiO₃, 2:1 (Rh, Sb)-codoped SrTiO₃, and 1:2 (Rh, Sb)-codoped SrTiO₃ with respect to the water redox levels.

4.5.1.10. Band Edge Alignment

As can be seen from the experimental studies, the introduction of Sb to Rh-doped SrTiO₃ not only improves the photo-conversion efficiency but also makes it active for oxygen evolution. To explain this, we align the band edge positions of all the model systems with respect to the water redox levels using the same procedure as discussed in section 4.3.1.6. As can be seen from Figure 4.5.11, in case of Rh-doped SrTiO₃ although the CBM position is suitable for hydrogen evolution, an unoccupied state is located just above the H₂O/O₂ level, which may be responsible

for the experimental observation of poor oxygen evolution property of Rh-doped SrTiO$_3$. In the case of Rh^{+3}-doped SrTiO$_3$ the VBM is significantly elevated with respect to that of undoped SrTiO$_3$, while the CBM position is hardly affected. In the case of (Rh, Sb)-codoped SrTiO$_3$, both CBM and VBM are found to be located in suitable positions with respect to water redox levels for spontaneous release of both hydrogen and oxygen. As can be seen from Figure 4.5.11, the positions of VBM and CBM for 1:2 (Rh, Sb)-codoped SrTiO$_3$ are such that it is active for overall water splitting, consistent with the experimental observation. Lower oxygen evolution efficiency with respect to the 1:1 codoped SrTiO$_3$ can be explained by the elevation of the VBM by larger extent. On the other hand, in case of 2:1 (Rh, Sb)-codoped SrTiO$_3$, the presence of unoccupied states above the water oxidation level may be responsible for the poor oxygen evolution activity. Thus, the present theoretical study reproduces the experimental outcomes as well as explains their origin properly.

4.5.2. Conclusion

In this section, we have reported our findings on the origin of improved photocatalytic property of Rh-doped SrTiO$_3$ towards overall water splitting in presence of Sb. In the Rh-doped SrTiO$_3$, the formal oxidation state of Rh is +4, which introduces localized mid-gap states due to partially occupied t$_{2g}$ subset. These states not only act as charge carrier trapping centers but also affect the oxygen evolution (water oxidation) drastically. However, they are found to be completely passivated when Sb is introduced as a codopant. Sb, when occupies Ti^{+4} lattice site, leaves one extra electron to achieve its most stable +5 oxidation state. This extra electron is utilized to lower the oxidation state of Rh to +3, which is indicated in the Bader charge analysis, where Bader charge on the Rh center is found to be reduced upon codoping with Sb. This also brings a change

in the magnetic behavior, thus converting paramagnetic Rh-doped $SrTiO_3$ to diamagnetic (Rh, Sb)-codoped $SrTiO_3$. The t_{2g} subset of Rh 4d orbital in the (Rh, Sb)-codoped $SrTiO_3$ is found to be fully occupied. The activity of (Rh, Sb)-codoped $SrTiO_3$ towards evolution of both oxygen and hydrogen has been explained by its suitable band edge alignment with respect to the water redox levels. It is observed that the band gap of the codoped system is hardly influenced by the change in concentration of both the dopant elements by equal extent in between the range studied here. The electronic structure of the codoped system is however found to be strongly dependent on the ratio of the concentration of the dopant elements. Thus, codoping of Rh and Sb in 2:1 ratio results into a band structure, which has characteristics almost similar to that of Rh-doped $SrTiO_3$, limiting the photocatalytic behavior towards overall water splitting. On the other hand, electronic structure analysis of 1:2 (Rh, Sb)-codoped $SrTiO_3$ indicates its ability to produce both hydrogen and oxygen during water splitting, in agreement with the experimental studies.

4.6. Exploring The Role of La Codoping beyond Charge Compensation for Enhanced Hydrogen Evolution by Rh-SrTiO$_3$

The major challenge is to narrow the band gap, but at the same time, maintaining the overall water splitting activity of the material. As for example, the elevation of valence band maxima (VBM) by large extent may affect the oxygen evolution efficiency, while lowering of the conduction band minima (CBM) may slow down the reducing behavior (hydrogen evolution) of the material. However, this problem can be overcome by employing two different photocatalyst for the hydrogen evolution and oxygen evolution, known as the Z-scheme photocatalysis system.[195, 196] In the case of Z-scheme system, the photocatalyst allows absorption of visible light more efficiently in comparison to that in one step overall water splitting system due to relaxation of the condition of minimum band gap criterion. Besides, a large number of photocatalysts, having potentiality to either water oxidation or reduction, can be employed in this case. During the past few years, numerous investigations have been carried out to increase the solar energy to hydrogen conversion efficiency. This includes not only developing new photocatalyst, but also finding new redox mediator systems, which can transfer charge carriers from oxygen evolving photocatalyst to hydrogen-evolving photocatalyst more efficiently. However, competitive redox behavior of the electron-mediators and their role in accelerating the backward reaction and shielding of the incident light limit the efficiency of the Z-scheme photocatalyst system. This led to the development of redox-mediator free Z-scheme system.[197-200] As for example, Sasaki et al constructed Z-scheme system using powder photocatalysts suspended in a reactor. They find that the aggregation of these powders with suitable contact has a significant role in improving the photocatalytic activity. Among various hydrogen evolution catalysts, Rh-doped SrTiO$_3$ has

attracted significant interest due to its unique absorption behavior. It has been employed in the Z-scheme system with a large number of oxygen-evolving photocatalyst, like WO_3, Ta_3N_5, $BiVO_4$, Bi_2MoO_6, etc. Various attempts have been made to improve the efficiency of the Z-scheme photocatalyst system involving Rh-doped $SrTiO_3$. Kato et al synthesized Rh-doped $SrTiO_3$ using hydrothermal method (HT) and polymeric complex (PC) method and compared their photocatalytic activity with that prepared through solid state reaction. They observed a remarkable enhancement of photoactivity in the case of Rh-doped $SrTiO_3$ prepared through HT and PC methods due to formation of highly homogeneous and fine photocatalyst particles. Sasaki et al investigated the effect of cocatalyst and concluded that Ru is a better cocatalyst than Pt due to suppression of back reaction, leading to enhancement of photoactivity for water splitting.

Previous studies show that Rh introduces localized states in between the valence band (VB) and conduction band (CB), thus reducing the effective band gap. This extends the absorption property of $SrTiO_3$ towards the visible region of the solar spectrum. Unfortunately, these localized states are working as recombination centers for the photogenerated electron-hole pair. As a result, photoconversion efficiency of Rh-doped $SrTiO_3$ is lowered below the expected level. It has also been reported in the earlier studies that Rh in the Rh-doped $SrTiO_3$ exists in both +3 and +4 oxidation states. Rh^{3+} species, which introduces impurity states just above the VB, is shown to be photochemically active. However, Rh^{4+} species, which introduces localized state in the midgap region, is found to be photochemically inert. Hence, to improve the photocatalytic activity of Rh-doped $SrTiO_3$, formation of Rh^{+4} state should be suppressed. One of the most promising approaches to control the valence of a dopant is codoping with another dopant element. In the case of $SrTiO_3$, there are three possible lattice sites (Sr, Ti, and O) to introduce the codopant. The choice of the codopant should be such that a charge compensated

system is formed. Hence, the preferred valence of the codopant for the Sr, Ti and O lattice site should be +3, +5 and -1, respectively. A number of attempts have been made by using pentavalent codopant. As for example, Furuhashi et al synthesized (Rh, Sb)-codoped $SrTiO_3$ and observed that the rate of electron hole recombination is significantly decreased in presence of Sb. Recently (Rh, Sb)-codoped $SrTiO_3$ has been synthesized loaded with IrO_2 cocatalyst using conventional solid-state reaction to investigate the overall water splitting under visible light. Although, codoping with Sb activates the oxygen evolution ability of Rh-doped $SrTiO_3$, it lowers the hydrogen evolution rate significantly. In our previous study, we have investigated the effect of F-codoping at the O lattice site into the crystal structure of Rh-doped $SrTiO_3$. Recently, Wang et al reported an unique redox-mediator free Z-scheme photocatalyst system which consists of core/shell structure of (Rh, La)-codoped $SrTiO_3$ as hydrogen evolving photocatalyst. They observed an enhancement of hydrogen production rate, which is even 3.8 times higher than that of Rh-doped $SrTiO_3$. This is due to codoping with La, which forms charge compensated system with Rh^{+3}, thus suppressing the formation of Rh^{+4} species as well as oxygen vacancy, resulting in an improvement of photocatalytic activity. However, the origin of enhanced hydrogen evolution activity is not explored definitely.

In the present theoretical study, we investigate the role of La codoping on the microscopic electronic structure of Rh-doped $SrTiO_3$ by employing the quite accurate (but computationally expensive) hybrid density functional calculation. We examine systematically the defect formation energy, band structure, density of states (DOS), projected density of states (PDOS), positions of band edges with respect to the water redox levels in presence of individual as well as both Rh and La. Based on this study, the origin of improved photoconversion efficiency, band gap narrowing and higher hydrogen evolution activity have been illustrated.

Thus present study provides useful informations, which are very much important for the development of highly efficient photocatalyst.

4.6.1. Results and Discussion

The valence electrons considered in this study during construction of the pseudo potential include: Sr ($4s^2\ 4p^6\ 5s^2$), Ti ($4s^2\ 3d^2$), Rh ($5s^1 4d^8$), La ($5s^2\ 5p^6\ 5d^1\ 6s^2$), and O ($2s^2 2p^4$). All the model structures were fully relaxed with $8 \times 8 \times 8$ set of Monkhorst and Pack k-point mesh.[48]

At room temperature, SrTiO$_3$ has a perfect cubic perovskite structure and belongs to $Pm\overline{3}m$ symmetry group. The dopants are introduced in a supercell of $2 \times 2 \times 2$ order, consisting of 40 atoms. We also consider larger supercells ($2 \times 2 \times 3$, and $2 \times 3 \times 3$) to check the reliability of the calculations presented here. For all the cases, we have first performed the structural optimization and then calculated the defect formation energy to have an idea about the feasibility of their synthesis. Next, we describe the electronic structure by analyzing the band structure, DOS and PDOS. Finally we have tried to explain the relative water splitting activity of the doped, codoped, and undoped SrTiO$_3$ by aligning their CBM and VBM with respect to the water redox levels.

4.6.1.1. Geometry

Rh-doped SrTiO$_3$ is modeled by introducing one Rh at the Ti lattice site in the $2 \times 2 \times 2$ SrTiO$_3$ supercell (12.5 % dopant concentration), which is found to be most preferable site for Rh according to available experimental reports. The cubic structure is found to be maintained even after Rh doping, and only a small increment in the lattice parameter is observed. This is due to closeness in ionic size of Ti ($R_{Ti^{+4}} = 0.605$ Å) and Rh ($R_{Rh^{+4}} = 0.60$ Å). The Rh-O bond length is

calculated as 1.996 Å, which is slightly longer than the Ti-O bond distance in the pure host lattice. For the construction of La-doped SrTiO$_3$ we replace one Sr atom from a $2 \times 2 \times 2$ SrTiO$_3$ supercell by La (12.5 % dopant concentration). As the ionic sizes of La^{+3} ($R_{La^{+3}} = 1.36$ Å) and Sr^{+2} ($R_{Sr^{+2}} = 1.44$ Å) are close to each other, doping with La has very little effect on the parent crystal structure. However, the Ti-O-Ti bond angle in the La-doped SrTiO$_3$ is found to be slightly smaller (177°) than that in the undoped SrTiO$_3$. When both Rh and La atoms are introduced in the SrTiO$_3$ crystal structure, the Rh-O bond length is enlarged to 2.02 Å and Ti-O-Ti bond angle is reduced to 176°. The lattice constant in all the doped cases are comparable to that of the undoped SrTiO$_3$ crystal structure.

4.6.1.2. Defect Formation Energy

To examine the relative feasibility of doping with either Rh or La and both Rh and La, we calculate the defect formation energy using the procedure discussed in section 4.3.1.3

$$\Delta H_f = E_{doped} + n_{Ti}\,\mu_{Ti} + n_{Sr}\,\mu_{Sr} - E_{SrTiO3} - n_{La}\,\mu_{La} - n_{Rh}\,\mu_{Rh,} \qquad (4.6.1)$$

where E$_{doped}$ and E$_{SrTiO3}$ stand for the total energy of doped and undoped SrTiO$_3$, calculated by using same supercell size. Here, n$_X$ and μ$_X$ define the number of elements removed/introduced to obtain the doped structure and chemical potential of the dopant element, respectively. Here, μ$_{Sr(bulk)}$, μ$_{Ti(bulk)}$, μ$_{Rh}$ and μ$_{La}$ have been evaluated by calculating the energy of an atom in the pure metallic Sr, Ti, and Rh (body centered cubic crystal structure, F m -3 m) and La (hexagonal close-packed structure, P63/mmc), respectively.

      The variation of defect formation energy for Rh-doped SrTiO$_3$ and La-doped SrTiO$_3$ with the chemical potential of Ti and Sr has been presented in Figure 2a and 2b, respectively. In both the cases, the host rich condition is relatively unfavorable than the host poor condition, due to the

requirement of higher energy for the vacancy formation under host rich condition. Also a comparison of Figure 4.6.1a and 4.6.1b indicates that La doping is energetically more favorable than Rh doping. The defect formation energy profile for the (Rh, La)-codoped SrTiO$_3$ has been shown in Figure 4.6.1c, where each line stands for a particular formation energy, calculated by using $2 \times 2 \times 2$ supercell. Dashed line (black) and dotted line (green) represent the same, calculated by using $2 \times 2 \times 3$ and $2 \times 3 \times 3$ supercell, where Rh and La occupying the nearest lattice sites, respectively.
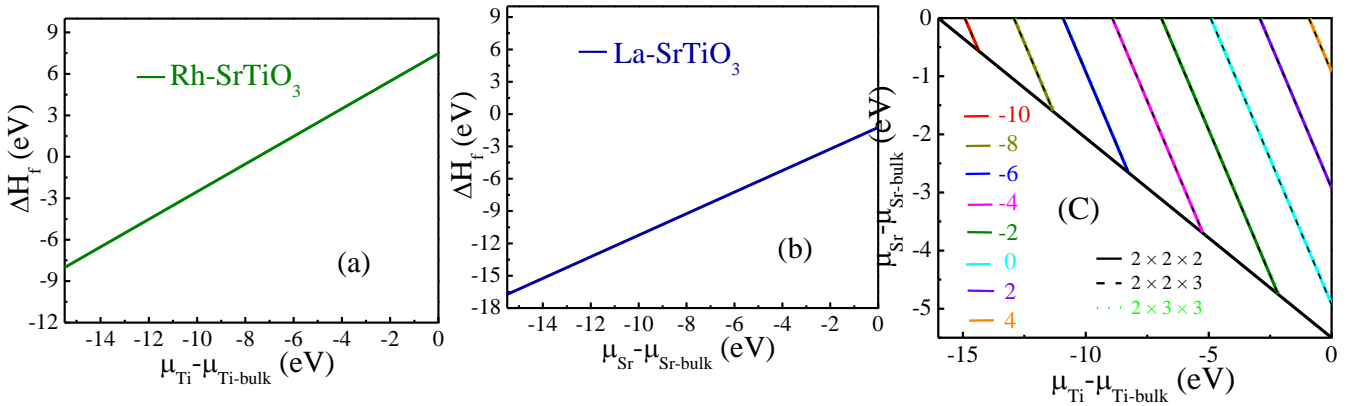
Figure 4.6.1: The variation of defect formation energy with the chemical potential of Ti (μ_{Ti}- $\mu_{Ti\text{-}bulk}$) and Sr (μ_{Sr}- $\mu_{Sr\text{-}bulk}$) for (a) Rh-doped SrTiO$_3$, (b) La-doped SrTiO$_3$ and (c) (Rh, La)-codoped SrTiO$_3$. The color lines (C) corresponds to different formation energies for the (Rh, La)-codoped SrTiO$_3$ using $2 \times 2 \times 2$ supercell. In panel 'c' dashed lines and dotted lines indicate different formation energies for the (Rh, La)- codoped SrTiO$_3$ using $2 \times 2 \times 3$ and $2 \times 3 \times 3$ supercell, respectively.

It is shown that the defect formation energy for the (Rh, La)-codoped SrTiO$_3$ is almost independent of increasing supercell size beyond $2 \times 2 \times 2$. This justifies the choice of supercell size in the present study. The defect formation energy is found to be energetically more favorable under Sr-rich condition than Ti-rich condition. A sharp decrease in defect formation energy for

Rh doping is observed in presence of La, leading to the possibility of synthesis of (Rh, La)-codoped $SrTiO_3$ more feasible.

4.6.1.3. Electronic Structure

In this section, we discuss the effect of dopant on the electronic structure of $SrTiO_3$. The band structures for Rh-doped, La-doped and (Rh, La)-codoped $SrTiO_3$ are shown in Figure 4.6.2 along with the band structure of undoped $SrTiO_3$ for comparison. The calculated band gap for undoped $SrTiO_3$ (3.19 eV) shows an excellent agreement with the experimentally observed value (3.2 eV). In case of Rh-doped $SrTiO_3$, the VBM is found to be elevated significantly due to introduction of new states on the top of VB. This leads to reduction in band gap to 2.70 eV, which is in agreement with the experimental observation for Rh^{+4}-doped $SrTiO_3$. However, the effective band gap is significantly smaller than this value due to the presence of localized unoccupied states in between VB and CB, which is responsible for observation of sharp enhancement of visible light absorption of Rh-doped $SrTiO_3$.
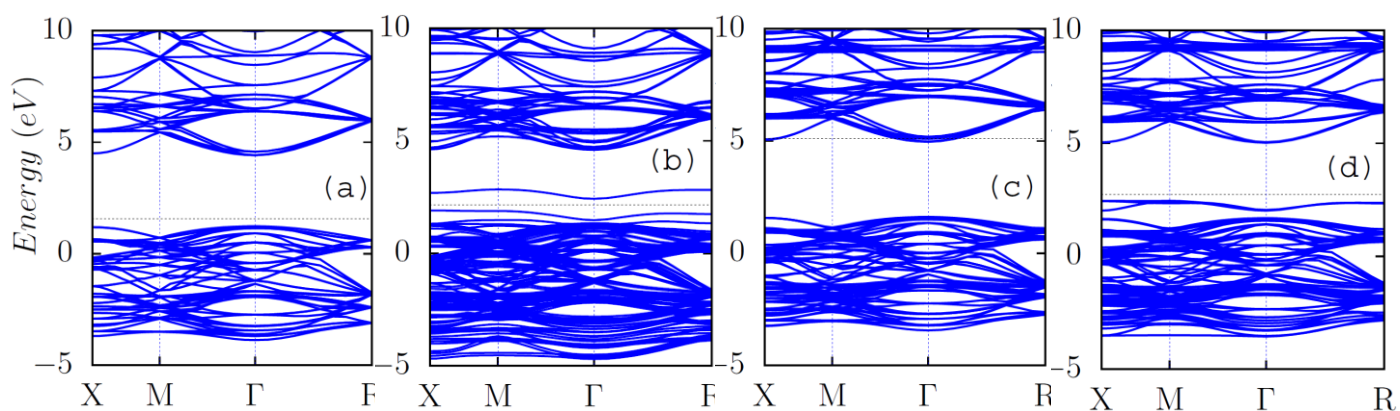
Figure 4.6.2: Band structure of (a) undoped $SrTiO_3$, (b) Rh-doped $SrTiO_3$, (c) La-doped $SrTiO_3$ and (d) (Rh, La)-codoped $SrTiO_3$. Horizontal dashed line indicates Fermi Level.

To investigate this in more details calculation for spin polarized DOS has been carried out. Figure 4.6.3a shows the DOS plot for Rh-doped SrTiO$_3$, indicating the presence of partially occupied and unoccupied states in the spin down part. Analysis of PDOS reveals the contribution of Rh 4d states to both partially occupied and unoccupied states. This is due to the fact that Rh occupying Ti^{+4} lattice site exists as Rh^{+4} and contains unpaired electron (4d^5). Since the acceptor states are well known to play a significant role in promoting electron-hole recombination process, they are undesirable for achieving higher photoconversion efficiency.
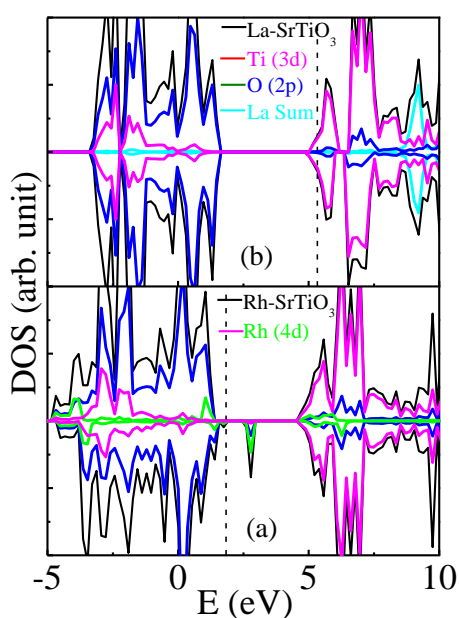
Figure 4.6.3: Density of states of (a) Rh-doped SrTiO$_3$ and (b) La-doped SrTiO$_3$. Vertical dashed line indicates Fermi Level.
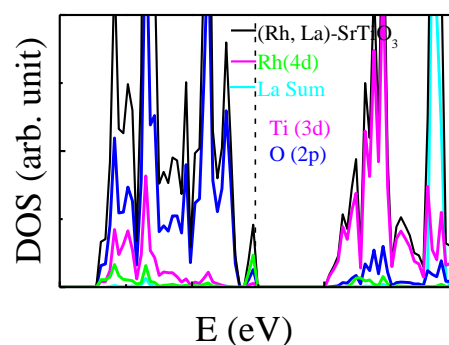
Figure 4.6.4: Density of states of (Rh, La)-codoped SrTiO$_3$

Codoping with another element has been found to be one of the successful strategies to passivate those states. Here, we discuss the unique role of La, which has been employed as a codopant recently in the study of Wang et al.[201] To systematically investigate the effect of La, electronic

structure calculations for both La-doped $SrTiO_3$ and (Rh, La)-codoped $SrTiO_3$ have been carried out. Figure 4.6.2c shows the band structure plot for La-doped $SrTiO_3$, where the Fermi level is found to be shifted into the CB. This is due to donation of one more electron by La ($5s^2$ $5p^6$ $5d^1$ $6s^2$) in comparison to Sr to achieve its formal oxidation state of +3 ($5s^2$ $5p^6$). The energy difference between the VBM and occupied impurity states is calculated as 3.36 eV, which is 0.17 eV higher than that of undoped $SrTiO_3$. Hence, La doping shifts the absorption behavior of $SrTiO_3$ far from visible region, which is consistent with the observation of available experimental report.[202] Figure 4.6.3b shows the DOS plot for La-doped $SrTiO_3$. In contrast to the report of Li et al [202] based on calculation using standard density functional theory, the present study reveals that the band edge of La-doped $SrTiO_3$ is contributed by O 2p states and Ti 3d states, similar to the case of undoped $SrTiO_3$. La states appear in the lower region of the VB and higher energy region of CB, which is rather obvious due to ionic bonding between La and O. The unoccupied Ti 3d state is an indication of localization of extra electron on the Ti center. Now we proceed to discuss the electronic structure of $SrTiO_3$ in presence of both Rh and La. The band structure plot has been shown in Figure 4.6.2d. A clean band structure with complete passivation of localized impurity states is formed, which is responsible for lower rate of electron-hole recombination in (Rh, La)-codoped $SrTiO_3$. Continuum nature of the band structure at both the band edges contributes to the smooth migration of photogenerated charge carriers, thereby improving the solar conversion efficiency. The band gap significantly decreases to 2.57 eV, thus extending the absorption curve towards visible region. The interesting point to be noted is that the CBM is shifted in the upward direction by 0.61 eV, which increases reducing behavior at the CB. This is an important aspect, particularly for achieving higher hydrogen evolution rate during water splitting. The DOS plot for (Rh, La)-codoped $SrTiO_3$ is shown in Figure 4.6.4a. The VBM

is composed of O 2p and Rh 4d states, while the CBM is composed of Ti 3d state. Rh 4d states are found to appear below the Fermi level, adjacent to the VB. In this case, the t_{2g} subset of Rh 4d orbital is completely occupied, as a result of transfer of an extra electron to the Rh center, thereby lowering its oxidation state to +3 ($4d^6$), which is the desirable form of Rh to achieve high photocatalytic activity. This is manifested in the Bader charge analysis, where the Bader charge on the Rh center is found to decrease from 1.64 to 1.43 due to codoping with La. The pairing of Rh 4d electron is also evident in the diamagnetic nature of (Rh, La)-codoped $SrTiO_3$. Thus, the characteristic band structure of (Rh, La)-codoped $SrTiO_3$ ensures longer life time of the photogenerated charge carriers. We also compare the charge density distribution for the Rh-doped $SrTiO_3$ and (Rh, La)-codoped $SrTiO_3$ (Figure 4.6.5). In case of Rh-doped $SrTiO_3$ (Figure 4.6.5a) it is observed that oxygen charge cloud overlaps with the Rh charge cloud, which is a consequence of more extended nature of 4d orbital (Rh) than the 3d orbital (Ti).
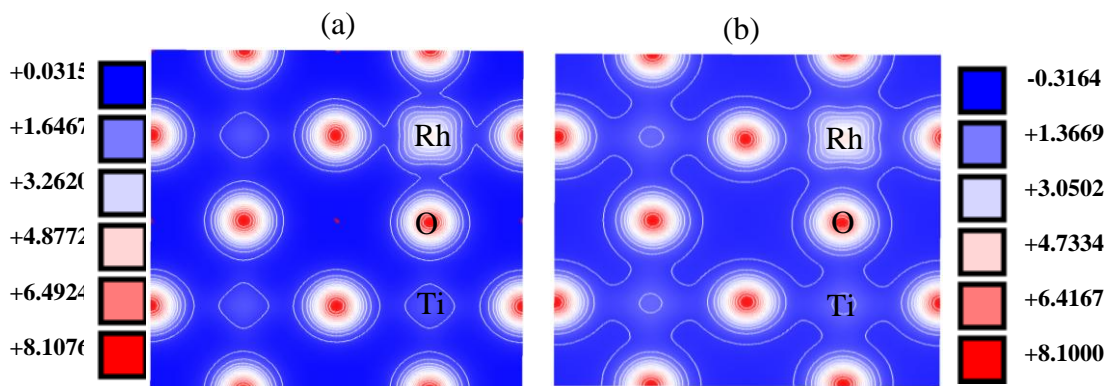
Figure 4.6.5: Part of total charge density distribution for (a) Rh-doped $SrTiO_3$, (b) (Rh, La)-codoped $SrTiO_3$.

However, in case of (Rh, La)-codoped $SrTiO_3$ (Figure 4.6.5b) the overlapping not only increases in between Rh and O, but also in between Ti and O, i.e., the covalent character of metal (Rh/Ti)-oxygen bonding increases. Moreover, Rh^{+3} forms charge compensated system with La^{+3},

thus suppressing the formation of oxygen-vacancy, which is one of the efficient sources of charge carrier loss. Hence, based on this electronic structure description one can explain enhanced photoconversion efficiency of Rh-doped $SrTiO_3$ with the codoping of La.
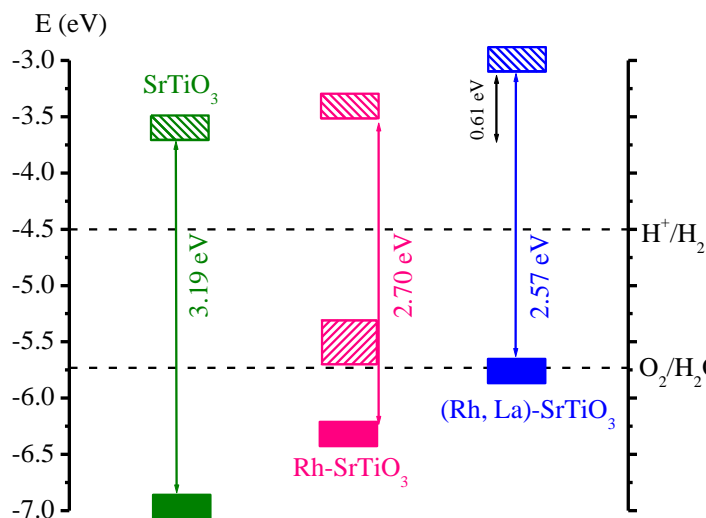
Figure 4.6.6: The band alignment of the undoped, Rh-doped $SrTiO_3$, and (Rh, La)-codoped $SrTiO_3$ with respect to the water redox levels.

4.6.1.4. Effect of Supercell Size

During the discussion of defect formation energy we have already justified our choice of using 2 $\times$ 2 $\times$ 2 supercell. Here we want to discuss how the electronic structure is influenced by change of the dopant concentration. For this purpose, we increase the supercell size to 2 $\times$ 2 $\times$ 3 and 2 $\times$ 3 $\times$ 3 for constructing the (Rh, La)-codoped $SrTiO_3$ model structure. The respective dopant concentration of both Rh and La corresponds to 8.33 % and 5.55 % in the two supercells. In both the cases, VBM is contributed by Rh 4d and O 2p mixed state, and CBM by Ti 3d state. However, the band gap is slightly increased to 2.69 eV and 2.67 eV due to lowering of dopant concentration.

4.6.1.3. Band Edge Alignment

It has been observed in the earlier reports that shifting CBM in the upward direction increases the reducing behavior at the CB, consequently enhancing the hydrogen evolution activity. Hence, knowledge of band edge positions is essential to explain the water splitting efficiency of the material. Doping with only Rh elevates the CBM (although by a small extent (0.18 eV), which may be one of the responsible factors for increasing its the hydrogen release activity with respect to that of undoped $SrTiO_3$. As can be seen from Figure 4.6.6, codoping with Rh and La leads to a significant shifting (0.61 eV) of the CBM in the upwards direction. This is one of the important features of (Rh, La)-codoped $SrTiO_3$ to explain the recent observation of attractive hydrogen evolution activity.

4.6.2. Conclusion

In the present study, using hybrid density functional theory, we have described the effect of La codoping on the geometric and electronic structure of Rh-doped $SrTiO_3$, with the goal of explaining its photoactivity towards hydrogen evolution through water splitting. We have observed that the distortion of the parent crystal structure due to codoping is less significant due to similarity in ionic sizes. However, the electronic structure of Rh-doped $SrTiO_3$ is found be strongly influenced by the presence of La. The localized mid gap states, which were present in the case of Rh-doped $SrTiO_3$ and responsible for lowering the photoactivity, are completely passivated in presence of La. The unique band structure for (Rh, La)-codoped $SrTiO_3$ ensures smooth charge carrier mobility, leading to higher photoconversion efficiency. The presence of La not only suppresses the formation of photochemically inert Rh^{+4} state, but also minimize the oxygen vacancy formation by forming a charge compensated system. According to the

calculated formation energy, (Rh, La)-codoping is energetically more favorable than doping with only Rh. The analysis of electronic energy levels reveals an upward shifting of the CBM by a considerable extent due to codoping with La. We strongly believe that if has a significant role along with passivation of the midgap acceptor states and suppression of vacancy defects for the enhancement of hydrogen evolution activity of Rh -doped $SrTiO_3$ after codoping with La.

4.7. Improving Photocatalytic Activity of Rh-Doped SrTiO$_3$ by codoping with

F: A Hybrid DFT Prediction

In section 4.5 we have seen that Rh-doped SrTiO$_3$ has attracted immense interest due to its excellent photo-absorption behavior. The desirable oxidation state for Rh is +3 to achieve high photoconversion efficiency of Rh-doped SrTiO$_3$. But the Rh-doped SrTiO$_3$ has been reported to contain mixture of both Rh^{+3} and Rh^{+4} states. Hence to keep Rh as Rh^{+3} state by suppressing the formation of Rh^{+4} state in the Rh-doped SrTiO$_3$ sample, has become an active area of research. The strategy of introducing a pentavalent cationic dopant along with Rh has been employed in many recent studies. One of the successful examples include codoping of Sb into the Rh-doped SrTiO$_3$, where significant enhancement of photo-conversion efficiency has been achieved. Since Sb exists as Sb^{+5}, it preferably stabilizes Rh^{+3} state forming a charge compensated system, thereby reducing the rate of electron-hole recombination significantly. The effect of Ta codoping into the Rh-doped SrTiO$_3$ system has been explored in the study of Kang et al for enhancing the hydrogen evolution rate.[203] Very recently, Wang et al observed an increase of hydrogen evolution rate by 3.5 to 3.8 times after doping with La at the Sr lattice site into the Rh-doped SrTiO$_3$.[201] However, cation-anion codoping is believed to be more effective, although it has not been employed so far to improve the photocatalytic activity of Rh-doped SrTiO$_3$. In the recent experimental studies Zhao et al[204] and Li et al [205] have shown that the rate of hydrogen production is significantly higher in case of cation-anion codoped material in comparison to the undoped as well as cation or anion monodoped system.

Here, we have investigated the role of an anionic codopant in stabilizing the lower oxidation state of Rh. We choose F, which can be doped at the O lattice site with minimum lattice

distortion due to similarity in their ionic sizes. As the valence shell of F ($2s^22p^5$) contain one more electron than that of O ($2s^22p^4$), F doping leads to an excess electron in the system. This will ensure the stabilization of Rh $^{+3}$ state in the (Rh, F)-codoped $SrTiO_3$. According to the study of Wang et al, the effective electron mobility in the conduction band increases due to F-doping.[168] They have also observed that the particle size of the F-doped $SrTiO_3$ is associated with relatively smaller particle size and higher specific surface area, leading to higher absorption of the reactant and faster migration of the photo-generated charge carriers to the surface. This reduces the rate of electron-hole recombination. Pan et al arrived at similar conclusion when studied with F-doped TiO_2.[206] It has been observed in the study of Kumar et al that the presence of F facilitates adsorption and photodecomposition water.[207] According to their study, presence of F on the surface of the catalyst significantly reduces the water adsorption energy on the catalyst, which is very much important for efficient photocatalytic process. Besides, adsorption of water molecule on the catalyst surface through the hydrogen atoms elongate the O-H bond length of the water molecule, which enhances the photocatalytic cleavage. In this study, a detailed systematic calculation has been presented using density functional theory (DFT) to explore the role of the individual dopant element as well as dopants in combination, on the geometry and electronic structure of $SrTiO_3$. As the band gap calculated using conventional DFT is highly underestimated, we employ HSE (Heyd, Scuseria, and Ernzerhof) hybrid functional to calculate the electronic properties.

4.7.1. Results and Discussion

The projector augmented wave (PAW) potentials have been constructed using the valence states: Sr ($4s^24p^65s^2$), Ti ($4s^23d^2$), Rh ($5s^14d^8$), O ($2s^22p^4$), and F ($2s^22p^5$).

4.7.1.1. Geometry and Electronic Structure

In the previous section, we have shown that Rh-doping introduces new states above and below the Fermi level. Consequently, the band gap is reduced to 2.70 eV (ignoring the unoccupied mid gap states), which is in excellent agreement with the experimentally reported band gap for Rh^{+4}-doped $SrTiO_3$. Analysis of PDOS indicated that these states are hybridized states formed due to mixing of O 2p and Rh 4d. Hence, in the Rh-doped $SrTiO_3$, photo-excitation of electron from VBM (valence band maxima) to CBM (conduction band minima) occurs via these mid gap states. Although this process requires light of low energy (longer wavelength), it may promote electron-hole recombination, thus reducing the photo-conversion efficiency drastically. Hence, to improve the photocatalytic activity of Rh-doped $SrTiO_3$, one needs to fix the oxidation state of Rh to +3. This can be achieved by introducing another dopant element. In the present study, we want to investigate the role of an anionic dopant, which has not been studied so far. We choose F, which is known to enhance photo-conversion efficiency by reducing electron-hole recombination. It is worthwhile to first investigate the electronic structure description of $SrTiO_3$ doped with only F. Since, F has been found to successfully substitute at the O lattice site, we model F-doped $SrTiO_3$ by replacing one of the O atoms from the 2×2×2 supercell with F (4.17 % dopant concentration). As the ionic size of F is closer to that of O ($R_{O^{-2}} = 1.35$ Å, $R_{F^{-}} = 1.285$ Å), significant change in crystal structure is not observed due to F doping. The Ti-F bond length (2.087 Å) in the F-doped $SrTiO_3$ is found to be slightly longer than the Ti-O bond length (1.974 Å) in the undoped $SrTiO_3$. As the valence shell ($2s^2 2p^5$) of F contains one more electron than that of O ($2s^2 2p^4$), the substitution will add one extra electron. The Fermi level now appears in the CB region. F-doping introduces occupied state at the bottom of the CB. This leads to the reduction in the band gap (difference between the VB and the occupied state adjacent to CB) to

2.96 eV, which is very close to the experimentally reported value. This again justifies the reliability of our computational approach.
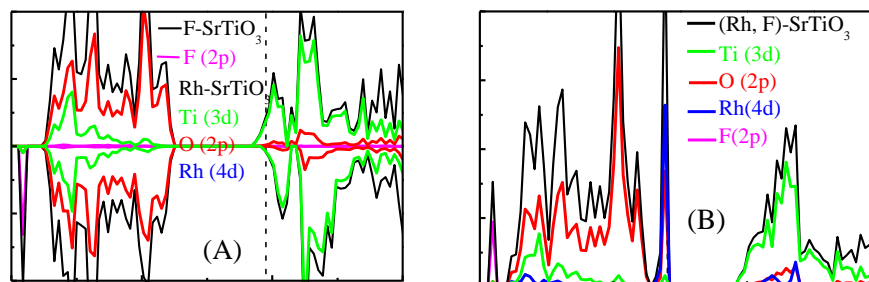
Figure 4.7.1: Density of states of (A) F-doped SrTiO$_3$ and (B) (Rh, F)-codoped SrTiO$_3$

The DOS plot (Figure 4.7.1a) shows that the states adjacent to CB are partially occupied. Analysis of PDOS indicates that the occupied states at the bottom of CB have mainly Ti 3d character, i.e., the extra electron is localized in the Ti 3d orbital. This is also revealed from the magnetic moment calculation. The net magnetic moment for F-doped SrTiO$_3$ is calculated as 0.82 μ_B per supercell, which is mostly contributed by Ti. Now we proceed towards the discussion of (Rh, F)-codoped SrTiO$_3$, which has been modeled by introducing one Rh and one F at the Ti lattice site and O lattice site of 2×2×2 supercell, respectively. We consider two different configurations, obtained by varying the relative distance between Rh and F. In case of configuration I, Rh and F are directly bonded to each other, while they are far away in configuration II. After full geometry relaxation of both the configurations, it is observed that configuration II is energetically more stable and is considered for investigating the electronic structure. It is interesting to observe that in the case of (Rh, F)-codoping, neither unoccupied midgap states nor occupied state at the bottom of the CB appear in the band structure, unlike the

case of Rh/F-monodoping. In presence of both the dopant elements, occupied states are introduced just above the VBM, forming a continuous band structure. Consequently, the VBM is uplifted significantly resulting in a decrease of band gap to 2.50 eV, which will extend the absorption curve towards the visible region. The DOS plot for (Rh, F)-codoped $SrTiO_3$ is presented in Figure 4.7.1b and it is clear that similar to the case of undoped $SrTiO_3$, the spin up and spin down part of the DOS are identical, indicating the absence of unpaired electron in the (Rh, F)-codoped $SrTiO_3$. This is supported by the calculated total magnetic moment value, which is equal to zero. The diamagnetic behavior has also been indicated in case of (Rh, Sb)-codoping in the study of Niishiro et al.[194] Analysis of PDOS (Figure 4.7.1b) indicates that the VBM is contributed by hybridized states, composed of Rh 4d and O 2p states, while the CBM is dominated by the Ti 3d orbital. In the case of (Rh, F)-codoped $SrTiO_3$, the t_{2g} set of Rh 4d orbital is fully occupied. This is the consequence of transferring the extra electron towards the Rh center. We have also calculated the Bader charge using grid based Bader analysis algorithm as implemented in VASP 5.2 program. The calculated Bader charge on the Rh center in the Rh-doped $SrTiO_3$ and (Rh, F)-codoped $SrTiO_3$ are found to be 1.641 and 1.434, respectively. This confirms the existence of rhodium at lower oxidation state in the (Rh, F)-codoped $SrTiO_3$. To get an idea about the chemical bonding in presence of the individual dopant element as well as both the dopant elements, we analyze the total charge density distribution plot (Figure 4.7.2) in each case, where the region with red color indicates low electron density, and pink color represents high electron density region. For F-doped $SrTiO_3$ (Figure 4.7.2a) the charge density around both O and F are spherically distributed. In case of (Rh, F)-codoped $SrTiO_3$ (Figure 4.7.2b), the charge density on Rh is found to be higher than the case of Rh-doped $SrTiO_3$. This indicates the transfer of electron to the Rh center. The continuum nature of the band structure at both the

edges is expected to improve the mobility of charge carriers in the (Rh, F)-codoped SrTiO$_3$, which will significantly enhance the photoconversion efficiency with respect to that of Rh-doped SrTiO$_3$.
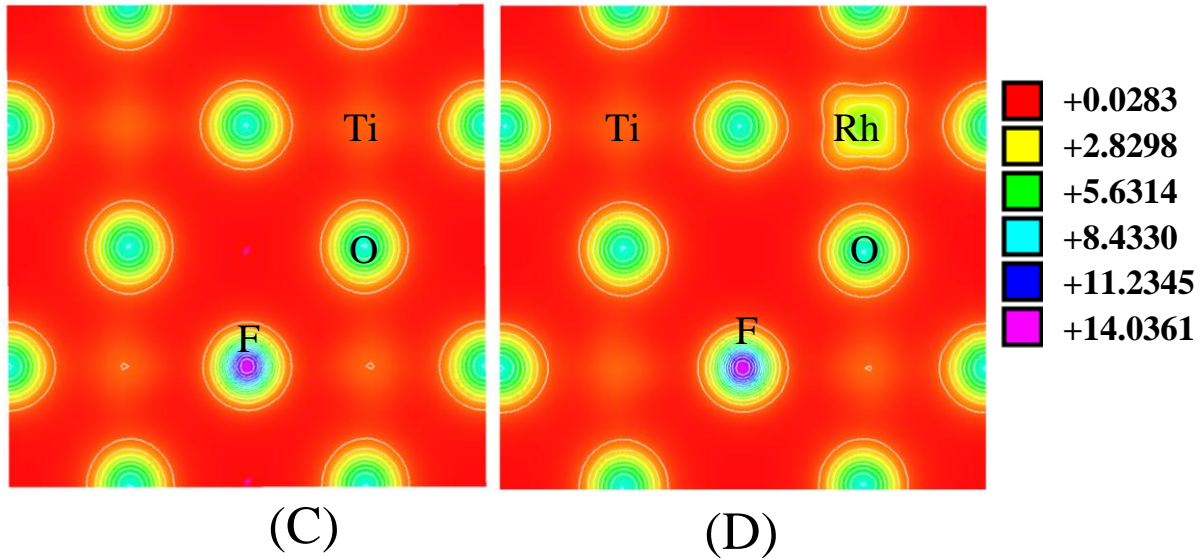
Figure 4.7.2: Part of total charge density distribution for (C) F-doped SrTiO$_3$, and (D) (Rh, F)-codoped SrTiO$_3$. The region with red color indicates low electron density, while pink color represents high electron density region.

4.7.1.2. Defect Pair Binding Energy

To check the stability of the codoped system with respect to that of monodoped system we calculate the defect pair binding energy (E$_b$) using the relation

$$E_b = E_{Rh\text{-}SrTiO3} + E_{F\text{-}SrTiO3} - E_{(Rh, F)\text{-}SrTiO3} - E_{SrTiO3} \qquad (4.7.2)$$

The total energy (E) for the respective system has been calculated using the supercell of identical size. The calculated binding energy for the (Rh, F)-codoped $SrTiO_3$ system is found to be 1.35 eV. The positive value of binding energy is an indication of a stable codoped system.

4.7.1.3. Defect formation energy

When designing new materials, one should check the feasibility to synthesize the material. It will be advantageous for the synthesis purpose, if the favorable growth condition can be predicted theoretically. Hence, we have calculated the defect formation energies for the monodoped as well as codoped $SrTiO_3$ systems using same procedure as discussed in section 4.3.1.3. The relation between the defect formation energy and the chemical potential of the host and guest elements is given by

$$\Delta H_f = E_{doped} + n_O\, \mu_O + n_{Ti}\, \mu_{Ti} - E_{SrTiO3} - n_F\, \mu_F - n_{Rh}\, \mu_{Rh} \qquad (4.7.3)$$

where E_{doped} represents the total energy of the (Rh/F)-monodoped or the (Rh, F)-codoped $SrTiO_3$ system. Here, μ_X defines the chemical potential of the element X, and the number of host/ guest element replaced/added is indicated by n_X. The value of μ_F have been calculated from the energy of an atom ($\mu_F = \frac{1}{2}\, \mu_{F2(gas)}$) in gaseous diatomic molecule, by placing it at the center of a sufficiently large (20 Å × 20 Å × 20 Å) cubical box.

The defect formation energy for the F doping under different O chemical potential (μ_O - $\mu_{O\text{-}gas}$) is shown in the Figure 4.7.3a, which shows that the defect formation energy is highly negative under O-poor condition.
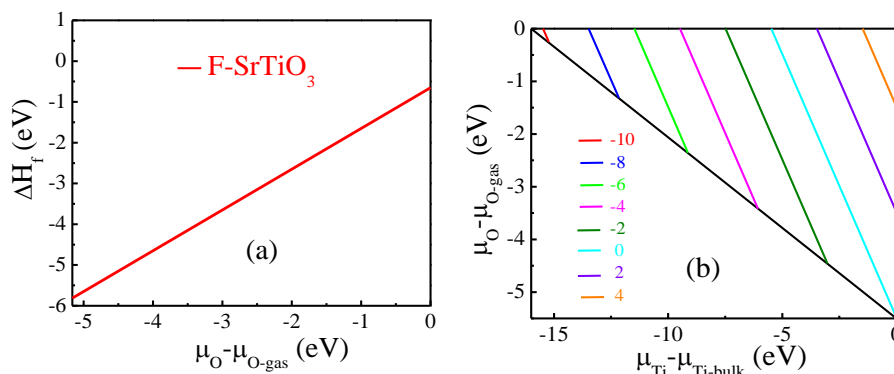
Figure 4.7.3: The variation of defect formation energy with the chemical potential of O (μ_O- $\mu_{O\text{-gas}}$) and Ti (μ_{Ti}- $\mu_{Ti\text{-bulk}}$) for (a) F-doped $SrTiO_3$ and (b) (Rh, F)- codoped $SrTiO_3$. The color lines (b) corresponds to different formation energies for the (Rh, F)- codoped $SrTiO_3$.

Although the defect formation energy increases with the O-chemical potential, it is still negative under O-rich condition. This indicates the feasibility of F-doping in the crystal structure of $SrTiO_3$. Figure 4.7.3b represents the variation of defect formation energy of (Rh, F)-codoped $SrTiO_3$ as a function of both O and Ti chemical potential, with different colors corresponding to different formation energies. As can be seen from Figure 4.7.3b, O-rich condition is more preferable than the Ti-rich condition for the growth of (Rh, F)-codoped $SrTiO_3$. The interesting outcome is that the formation energy for Rh doping decreases significantly in presence of F.
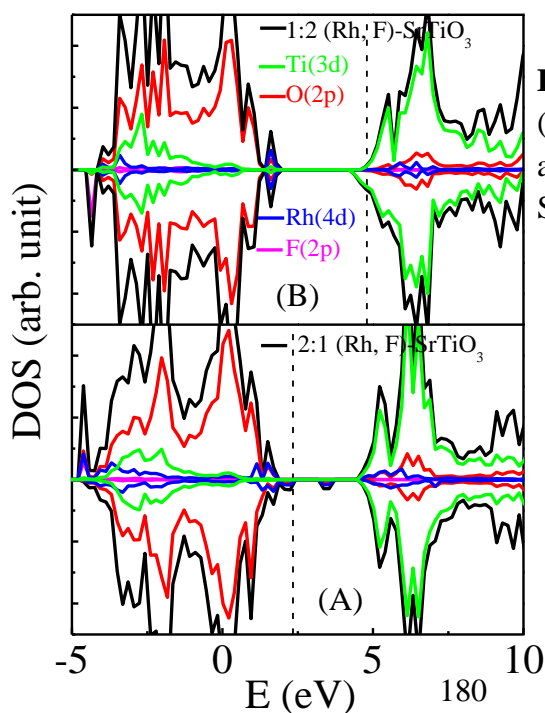
Figure 4.7.4: Density of states of (A) 2:1 (Rh, F)-codoped $SrTiO_3$ and (B) 1:2 (Rh, F)-codoped $SrTiO_3$ using $2 \times 2 \times 3$ supercell.

4.7.1.4. Effect of Dopant Concentration

To investigate the effect of dopant concentration, calculations with 2×2×3 supercell (dopant concentration: 8.33 % Rh, 2.78 % F) and 2×3×3 supercell (dopant concentration: 5.55 % Rh, 1.85 % F), have been carried out. In both the cases, full geometry optimization has been carried out with k-point mesh of 6×6×4 and 6×4×4, respectively. The nature of band edge is found to be unaffected by reduction of the concentration of the dopant elements in equal proportion. The VBM is contributed by hybridized states of Rh 4d and O 2p, and the CBM is dominated by Ti 3d state. However, the extent of overlap of the impurity states with the VBM of the $SrTiO_3$ reduces with decrease in dopant concentration. The band gap calculated using 2×2×3 supercell and 2×3×3 supercell are 2.58 eV and 2.61 eV, respectively. Small difference is due to change in dopant concentration with supercell size.

4.7.1.6. Effect of Different Rh and F Ratio

Till now we have discussed the effect of codoping with equal proportion of Rh and F atoms. In this section, we will investigate the scenario when Rh and F are present in different ratio (2:1 and 1:2) and form charge non-compensated codoped system. The 2:1 (Rh, F)-codoped $SrTiO_3$ is modeled by replacing two Ti and one O from a 2×2×3 supercell with two Rh and one F, respectively (dopant concentration for Rh and F are 16.67 % and 2.78 %, respectively). Full geometry optimization has been carried out with k-point mesh of 6×6×4. The DOS plot for 2:1 (Rh, F)-codoped $SrTiO_3$ (Figure 4.7.4A) shows the presence of partially occupied states above the VB and unoccupied states in the midgap region similar to the case of Rh-doped $SrTiO_3$. This is due to insufficient number of extra electron to completely fill the t_{2g} level of both the Rh centers. Figure 4.7.4A indicates that 2:1 (Rh, F)-codoping introduces unpaired electron. This is

consistent with the calculated total magnetic moment value of 1 μ_B per supercell. Hence 2:1 codoping may show poor photo-conversion efficiency. On the other hand, 1:2 (Rh, F)-codoped SrTiO$_3$ is modeled with same supercell size by introducing one Rh and two F in the Ti and O lattice sites, respectively (dopant concentration for Rh and F are 8.33 % and 5.55 %, respectively). The DOS profile for the 1:2 (Rh, F)-codoped SrTiO$_3$ is presented in Figure 4.7.5B. The Fermi level is located in the CBM region, indicating the presence of excess electron. This is supported by calculated total magnetic moment value of - 0.86 μ_B per supercell. In contrast to the 2:1 codoping, there is no unoccupied mid gap states in this case. The VBM has characteristics similar to the 1:1 (Rh, F)-codoped SrTiO$_3$, and is composed of hybridized states of Rh 4d and O 2p states. Similar to the case of doping with only F, occupied Ti 3d is found to appear just below the CB. Interestingly the band gap is reduced by larger extent than the case of F-monodoping as well as 1:1 codoping. The calculated band gap in this case is 2.31 eV, indicating enhancement of the visible light activity to be more in case of 1:2 codoping. In this scenario, we should mention some points related to charge non-compensated codoping. The charge non-compensated codoping, which introduces local trapping center in the form of discrete occupied or unoccupied states in the forbidden region, reduces the photo-conversion efficiency drastically in spite of significant enhancement in the visible light activity. Fortunately, in the case of 1:2 (Rh, F)-codoping continuum band structure at the band edges is formed. This ensures efficient migration of the charge carriers as well as improved photo-conversion efficiency. Moreover, excess F may be required to increase the possibility of complete conversion of Rh^{+4} to Rh^{+3} in the practical scenario. Thus, one can infer that the 1:2 (Rh, F)-codoped SrTiO$_3$ should show attractive photocatalytic property.

4.7.1.7. Effect of Other Halogen Elements

We now discuss the effect of any of the other halogen elements (Cl, Br and I) as a codopant to improve the photocatalytc activity of Rh-doped $SrTiO_3$ and compare the results with the (Rh, F)-codoped $SrTiO_3$. Similar to the case of (Rh, F)-codoped $SrTiO_3$, we have considered $2 \times 2 \times 2$ $SrTiO_3$ supercell for the calculation of the defect formation energy as well as the electronic structure. The k-point mesh size as well as the convergence criteria have been kept fixed at the earlier values for the geometry optimization and electronic structure calculation of the model structures. As we proceed from (Rh, Cl)-codoped $SrTiO_3$ to (Rh, I)-codoped $SrTiO_3$ deviation from cubic structure increases due to increasing difference in ionic radius of the oxygen ($R_{O^{-2}} = 1.35$ Å) and the codopant element ($R_{Cl^-} = 1.81$ Å, $R_{Br^-} = 1.96$ Å, and $R_{I^-} = 2.20$ Å). This leads to elongation of the Rh-X (X: Cl, Br, and I)bond length (2.22 Å, 2.33 Å, and 2.43 Å, respectively) and Ti-X bond length (2.52 Å, 2.85 Å, and 3.20 Å, respectively) significantly in comparison to the Rh-F bond length (2.06 Å) and Ti-F bond length (2.13 Å). Table 4.7.1 shows the variation of defect formation energy for the codoped $SrTiO_3$ under both O-rich and Ti-rich condition. For all the cases, O-rich condition is found to be more favorable than the Ti-rich condition. The defect formation energy increases in the order (Rh, F) < (Rh, Cl) < (Rh, Br) < (Rh, I). This indicates that the cost of codoping is smallest in case of (Rh, F) pair and highest in case of (Rh, I) pair. The DOS plots for (Rh, Cl/Br/I)-codoped $SrTiO_3$ are shown in Figure 4.7.5. The common features is that the VBM is contributed by Rh 4d and O 2p hybridized state, and the CBM is mainly composed of Ti 3d state. In all the cases, 'p'-state of the codopant appears in the lower energy part of the VB. As can be seen from Table 4.7.1, the calculated band gap for (Rh, Cl)- codoped $SrTiO_3$ and (Rh, Br)- codoped $SrTiO_3$ are higher than that of (Rh, F)-codoped $SrTiO_3$. However, in case of (Rh, I)-codoping, the extent of band gap reduction is found to be

closer to that of (Rh, F)-codoping, which may be correlated with the distortion in the octahedral lattice structure associated with large mismatch between the ionic size of iodine and oxygen.

It is thus clear that the choice of F as a codopant is quite justified over other halogen elements to improve the photocatalytic activity of Rh-doped SrTiO$_3$.

(A)

(B)

(C)
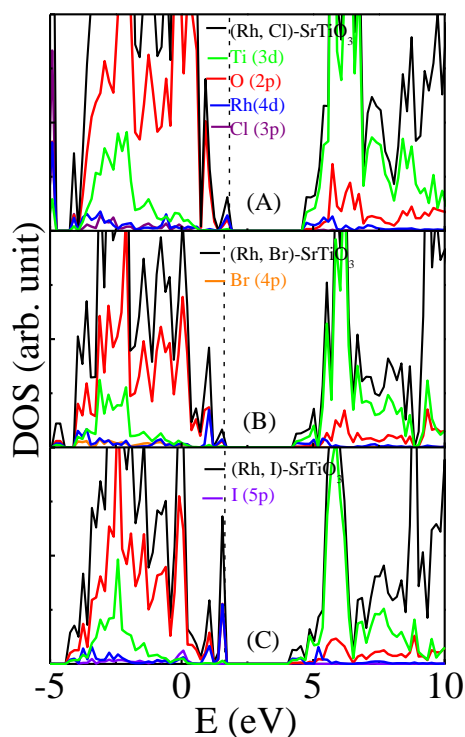
Table 4.7.1. The calculated defect formation energy and band gap for (Rh, X=F, Cl, Br, I)-codoped SrTiO$_3$ using $2 \times 2 \times 2$ supercell

Systems	Formation Energy (eV)		Band Gap
	O-rich	Ti-rich	(eV)
(Rh, F)-SrTiO$_3$	-9.73	0.60	2.50
(Rh, Cl)-SrTiO$_3$	-6.20	4.13	2.74
(Rh, Br)-SrTiO$_3$	-5.04	5.28	2.58
(Rh, I)-SrTiO$_3$	-3.49	6.84	2.46

Figure 4.7.5: Density of states of (A) (Rh, Cl)-codoped SrTiO$_3$ and (B) (Rh, Br)-codoped SrTiO$_3$, and (C) (Rh, I)-codoped SrTiO$_3$ using $2 \times 2 \times 2$ supercell. Vertical dashed line indicates Fermi Level.

4.7.1.7. Band Edge Alignment

While modifying the band gap to improve the visible light activity, one should also pay attention to the extent of band edge shift. We align the band edges of the monodoped as well as codoped-$SrTiO_3$ with respect to water redox levels (Figure 4.7.6) to check whether they are eligible for overall water splitting or not. For Rh-doped $SrTiO_3$, unoccupied midgap state is located above the water oxidation level. This may be responsible for its poor O_2 evolution efficiency, as observed experimentally. In case of F-doped $SrTiO_3$, the band edges are found to be in suitable positions to generate both H_2 and O_2 during water splitting, which is in agreement with the observation of Wang et al. For (Rh, F)-codoped $SrTiO_3$, the positions of the band edges indicate its ability to serve as a photocatalyst for overall water splitting. The upwards shift (0.12 eV) of the CBM will enhance the reducing behavior at the CB (controlling the hydrogen production rate) with respect to that of undoped $SrTiO_3$. On the other hand, among the two non-compensated codoped systems, 1:2 (Rh, F)-codoped $SrTiO_3$ has suitable band edge alignment for overall water splitting.
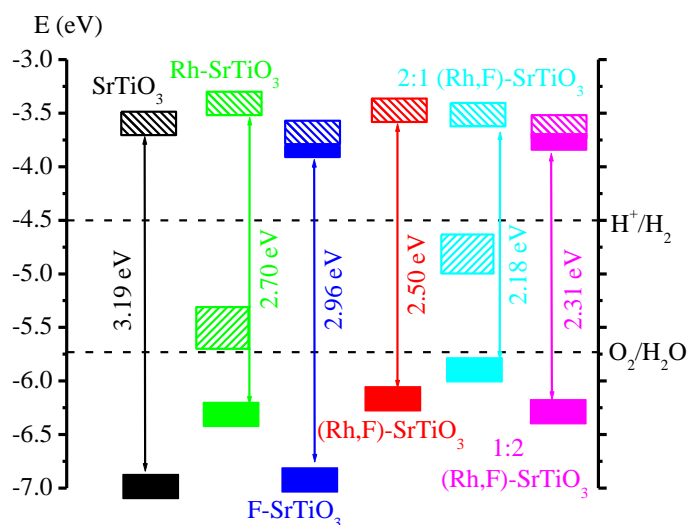
Figure 4.7.6: The band alignment of the undoped, Rh-doped $SrTiO_3$, F-doped $SrTiO_3$, and (Rh, F)-codoped $SrTiO_3$, 2:1 (Rh, F)-codoped $SrTiO_3$, 1:2 (Rh, F)-codoped $SrTiO_3$ with respect to the water redox levels.

4.7.2. Conclusion

In this theoretical study, we investigate the role of F doping in improving the photo-conversion efficiency of Rh-doped $SrTiO_3$. The band gap values for undoped as well as (Rh/ F)-monodoped $SrTiO_3$ obtained in the present study are close to the experimentally reported results, thus justifying our choice of computational methodology. F doping makes the system excess by one electron, which converts Rh^{+4} to Rh^{+3}. The decrease of Bader charge on the Rh center with addition of F supports this view. Electronic structure calculations reveal that the unoccupied localized states are completely passivated in presence of F, forming a continuum band structure at the band edges. Thus, improved charge carrier mobility and lower rate of electron-hole recombination are expected in the (Rh, F)-codoped $SrTiO_3$. The VBM is elevated significantly, reducing the band gap to 2.50 eV, and consequently the visible light activity of $SrTiO_3$ will be enhanced. The nature of band structure of the codoped system is found to be strongly dependent on the ratio of the dopant elements. In case of 2:1 (Rh, F)-codoped $SrTiO_3$, undesirable localized states are found to exist in between the VB and CB, while 1:2 (Rh, F)-codoped $SrTiO_3$ shows clean band structure, with significant reduction of band gap to 2.31 eV. The defect formation energy for Rh doping is found to be reduced considerably in presence of F. The relative positions of the band edges for both 1:1 and 1:2 (Rh, F)-codoped $SrTiO_3$ are such that the condition for overall water splitting is satisfied. Thus, based on the present investigation, we can predict that codoping of F is one of the effective approaches to improve the photocatalytic activity of Rh-doped $SrTiO_3$ under visible light.

4.8. Enhancement of Visible Light Photocatalytic Activity of SrTiO₃ by doping with Pentavalent Cation in combination with other ion

In this section, we investigate the synergistic effect of a pentavalent cation (V, Nb, or Ta) and one more anionic (N) or cationic (Na/K/Rh) dopant element, aiming at improving the photocatalytic activity of $SrTiO_3$ under visible light. Since, V/Nb/Ta acts as a one electron donor, the codopant should be one electron acceptor. We choose N for doping at the O-lattice site, which is one of the most popular nonmetal elements extensively studied by several experimental and theoretical groups for monodoping and codoping purpose. The advantages of choosing nitrogen in this case are (i) valence shell of N contains one less number of electron ($2s^2 2p^3$) than that of oxygen ($2s^2 2p^4$), and hence it can accept the extra electron donated by the metal ion; (ii) formation of charge compensated system in presence of N^{3-} and M^{5+} will minimize the formation of vacancy defects; (iii) it can be doped at the oxygen lattice site with minimum lattice strain due to their similar ionic radius; (iv) N 2p orbital is energetically higher than O 2p orbital, which can elevate the VBM and thus reduce the band gap; (v) availability well known synthetic strategy for the N-doping. Although a few studies in the literature indicate the role of nitrogen as an effective codopant of (V/Nb/Ta)-doped $SrTiO_3$, the valuable informations like actual band gap, relative positions of the band edges with respect to a particular redox level (H^+/H_2, and H_2O/O_2) are still lacking. In the present study, our aim is to extract all these information from the (V/Nb/Ta, N)-codoped $SrTiO_3$ systems. For this purpose, we carry out electronic structure calculation with computationally expensive hybrid density functional theory, as formulated by Heyd, Scuseria, and Ernzerhof (HSE), which has been shown to successfully reproduce the electronic properties of the semiconductor materials.

We have also investigated the effect of cation-cation codoping. There are two types of cationic lattice sites: divalent Sr and tetravalent Ti in the $SrTiO_3$ crystal structure. For the Sr lattice site, mainly non-transition metal elements (except Cr), have been chosen in the previous studies. As for example, doping with La leads to sharp enhancement of photocatalytic activity of $SrTiO_3$ due to formation of particles with smaller size and good crystallinity, which reduces the charge carrier recombination rate. The effective role of La as a charge compensating element has also been involved in many cases, like N-doped, Cr-doped, Rh-doped $SrTiO_3$, etc. However, La also acts as a single donor, and thus may not be suitable as the codopant of (V/Nb/Ta)-doped $SrTiO_3$. In the present study, we choose Na/K as a codopant, which has one less number of electron in the valence shell than that of Sr, and also has similar ionic radius. Na/K mainly exists as monovalent state, and thus will maintain the charge neutrality when doped into the (V/Nb/Ta)-doped $SrTiO_3$. Recently, Xiao et al. investigated the codoping effect of Na/K into the Nb-doped $SrTiO_3$ and observed that the sinterability of the material is improved significantly.[208] They also observed a sharp enhancement of electrical conductivity due to improvement of ionic conductivity with codoping. Qiu et al. observed a significant increase of quantum yield for Mo-doped $SrTiO_3$ during the photocatalytic decomposition of gaseous 2-Propanol under visible light due to codoping with Na.[209] Recently, Kang et al doped Na into the Mo-doped $SrTiO_3$ to maintain the charge neutrality and observed an enhancement of hydrogen evolution rate by 1.5 times in water splitting under visible light.[210] In the present study, we will investigate how the codoping of (Na/K) influences the electronic structure of (V/Nb/Ta)-doped $SrTiO_3$, along with charge compensation.

We also consider a codopant for the Ti lattice site, which has been chosen mostly for the transition metal element doping. As for example, doping with Rh has been studied extensively

due to improvement of visible light activity by a significant extent. Unfortunately, localized Rh 4d acceptor states introduced in the forbidden region drastically affect the photocatalytic activity of Rh-doped $SrTiO_3$. It has been indicated that Rh exist as both Rh^{3+} and Rh^{4+} state in the Rh-doped $SrTiO_3$. Since, Rh^{3+} state is found to be photochemically active and Rh^{4+} state is photochemically inert, lots of effort have been made to increase the Rh^{3+}/Rh^{4+} ratio. The majority of the studies involve addition of Sb, which exists as pentavalent state, and stabilize Rh^{+3} state by forming charge compensated system. Hence, Rh may be a good choice in the present case as a codopant for (V/Nb/Ta)-doped $SrTiO_3$. As V/Nb/Ta acts as a single donor, it will donate one extra electron, which will be utilized to convert Rh^{4+} to Rh^{3+}. Thus in presence of both Rh and (V/Nb/Ta), formation of Rh^{4+} state is expected to be suppressed, and consequently photocatalytic activity will be improved. Although, Sb has been shown to successfully improve the photocatalytic activity of Rh-doped $SrTiO_3$ by reducing the charge carrier recombination rate, the extent of band gap narrowing is limited to only 0.57 eV. This may be due to the fact that being a non-transition element, Sb hardly affects the CBM of the $SrTiO_3$, which is mainly contributed by Ti 3d orbital. However, in the present case V/Nb/Ta will influence the CBM of $SrTiO_3$ due to involvement of their 'd' orbital. For this purpose, we investigate the synergistic effect of both V/Nb/Ta and Rh on the electronic structure of $SrTiO_3$.

4.8.1. Results and Discussion

Dopants are introduced in a $2 \times 2 \times 2$ $SrTiO_3$ supercell (40 atoms). During the geometry optimization, we use k-point mesh of $8 \times 8 \times 8$ generated based on Monkhorst and Pack scheme.

4.8.1.1. Geometry

Now we will discuss the effect of different dopant elements on the crystal structure of $SrTiO_3$.
Previous literature results show that V, Nb, Ta, Rh preferably occupy the Ti lattice site, while
Na, K and N are doped at the Sr and O lattice site, respectively. Hence, in the present study we
model V/Nb/Ta/Rh-doped system by replacing one of the Ti from a $2 \times 2 \times 2$ supercell of
$SrTiO_3$, while for Na (K)-doped system one Sr atom has been substituted by Na (K). In case of
N-doping one of the O atom has been replaced by N. It has been found that the basic crystal
structure of $SrTiO_3$ does not change much in mono-doping as well as codoping cases, which is
also indicated in the calculated lattice parameter value of the model systems (Table 4.8.1). This
may be due to closeness in the ionic radius of the dopant element with that of the host elements.
In case of codoped system two different dopant elements have been introduced simultaneously.
In each case we have considered different model structures, where the dopant-dopant distance
are different. For (V/Nb/Ta, N)-codoped $SrTiO_3$, in one of the configurations the dopant
elements are directly bonded to each other. In case of (V/Nb/Ta, Na/K)-codoped $SrTiO_3$ a bigger
supercell (2 x 2 x 3) has been considered to investigate the dependence of the relative locations
of the dopant elements. For (V/Nb/Ta, Rh)-codoped $SrTiO_3$ also two different geometries have
been considered by varying the distance between the dopant elements. In the case of (V, N)-
codoped $SrTiO_3$ the configuration with the dopant elements occupying the nearest neighboring
lattice site is found to be more stable (by 0.93 eV) than the 'Far' one, while for (Nb, N) and (Ta,
N)-codoped $SrTiO_3$ the energy difference between the configurations is found to be small (0.17
eV and 0.06 eV, respectively). For (V/Nb/Ta, Na/K/Rh)-codoped $SrTiO_3$ the energy difference
between the two types of configurations is found to be still smaller.

Table4.8.1: Ionic Radii, Lattice Parameters, and Calculated Band Gap for undoped and doped-SrTiO₃. (*Lattice Parameter values represent half of the cell length of $2 \times 2 \times 2$ supercell)

	Ionic Radius (Å)	Lattice Parameter(Å)*	Band Gap(eV)
SrTiO₃	R_{Ti}=0.605	3.948	3.19
V-SrTiO₃	0.54	3.937	ΔE_1=1.06 ΔE_2=1.02
Nb-SrTiO₃	0.64	3.968	3.19
Ta-SrTiO₃	0.64	3.965	3.23
N-SrTiO₃	1.46	a=b=3.954 c=3.959	ΔE_1=0.84 ΔE_2=1.13
Na-SrTiO₃	1.39	3.946	3.04
K-SrTiO₃	1.64	3.955	3.07
Rh-SrTiO₃	0.60	3.951	ΔE_1=0.52 ΔE_2=1.79
(V, N)-SrTiO₃		a=b=3.924 c=4.016	2.80
(Nb, N)-SrTiO₃		a=b=3.955 c=4.005	2.78
(Ta, N)-SrTiO₃		a=b=3.955 c=4.005	2.75
(V, Na)-SrTiO₃		3.943	2.98
(Nb, Na)-SrTiO₃		3.966	3.35
(Ta, Na)-SrTiO₃		3.966	3.42
(V, K)-SrTiO₃		3.954	3.01
(Nb, K)-SrTiO₃		3.975	3.34
(Ta, K)-SrTiO₃		3.971	3.44
(V, Rh)-SrTiO₃		a=b=3.945 c=3.929	1.66
(Nb, Rh)-SrTiO₃		a=b=3.971 c=3.965	2.40
(Ta, Rh)-SrTiO₃		a=b=3.967 c=3.964	2.53

4.8.1.2. Formation Energy

The calculation of formation energy has been carried out using the same procedure as in section 4.3.1.3 to compare the stability of the doped system, and lower the formation energy of the system, higher is the possibility to form the compound.
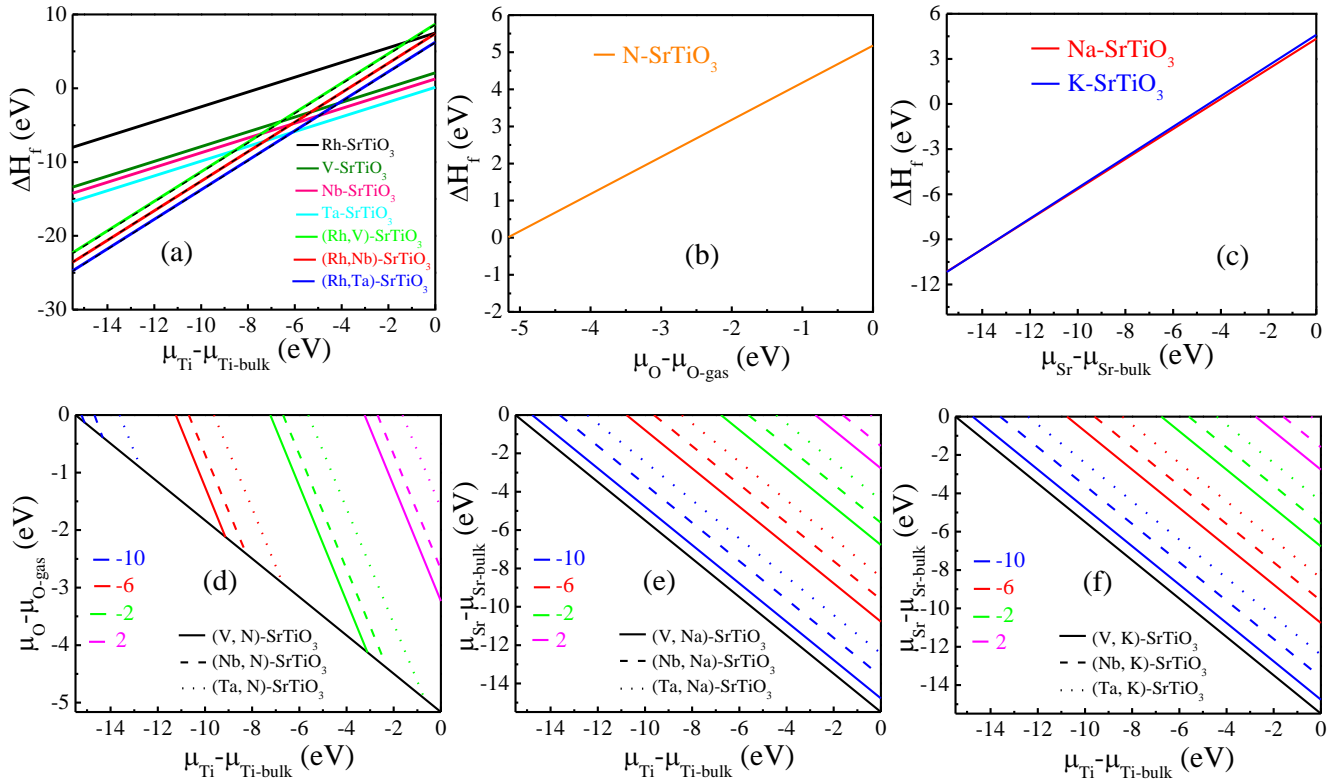
Figure 4.8.1: The variation of defect formation energy with the host chemical potential for (a) (V/Nb/Ta/Rh)-doped SrTiO₃, (V/Nb/Ta, Rh)-codoped SrTiO₃, (b) N-doped SrTiO₃, (c) (Na/K)-doped SrTiO₃ (d) (V/Nb/Ta, N)-codoped SrTiO₃, (e) (V/Nb/Ta, Na)-codoped SrTiO₃, (f) (V/Nb/Ta, K)-codoped SrTiO₃ (calculated using $2 \times 2 \times 2$ supercell). The dotted lines in the panel (c) indicates formation energy calculated using $2 \times 2 \times 3$ supercell. The color lines (d), (e), (f) corresponds to different formation energies.

Figure 4.8.1 shows the variation of defect formation energy of all the doped and codoped $SrTiO_3$. The common feature for V/Nb/Ta-doping is that the formation energy for the substitution of Ti is significantly lower under Ti-poor condition than Ti-rich condition (Figure 4.8.1a). This indicates that the synthesis of all the above doped systems is more feasible under Ti-poor condition. This may be due to difficulty in forming Ti-vacancy under Ti-rich condition. As can be seen from Figure 4.8.1a, the calculated defect formation energy increases in the order Ta< Nb< V, i.e., the cost of doping is minimum for Ta and maximum for V. The defect formation energy profile for N-doped $SrTiO_3$ as a function of oxygen chemical potential has been shown in Figure 4.8.1b, which indicates relatively poorer solubility of N in the $SrTiO_3$ crystal structure. Hence, the cost of the N-doping is expected to be more. Figure 4.8.1c shows the variation of defect formation energy for the Na/K-doped $SrTiO_3$. The defect formation energy is shown to be largely negative under extremely Sr-poor condition. As can be seen from Figure 4.8.1c, the defect formation energy for Na-doping is almost equal to that of K-doping. The variation of defect formation energy for Rh-doping has been shown in Figure 4.8.1a, which indicates that the cost of doping is even larger than that of V-doping. For codoping with (V/Nb/Ta, N), the defect formation energy is found to be more favorable under O-rich condition than Ti-rich condition (Figure 4.8.1d). The calculation of defect formation energy indicates that the codoping of these metal ions hardly shows any influence on the cost of N-doping, except in presence of Ta, which slightly reduces the formation energy. As can be seen from Figure 4.8.1d, the defect formation is more feasible as we proceed from (V, N) to (Nb, N) to (Ta, N)-codoped $SrTiO_3$. This behavior is in contrast to the previous reports in the literature, which indicate that the codoping with (Nb, N) is most feasible among these three systems. The defect formation energy profiles for (V/Nb/Ta, Na) and (V/Nb/Ta, K) have been shown in Figure 4.8.1e and f, as a

function of chemical potential of Ti and Sr. Comparison of Figure 4.8.1e and f indicates that the cost of codoping is almost similar for Na and K cases. The defect formation follows the order (V, Na/K)< (Nb, Na/K)< (Ta, Na/K). As can be seen from Figure 4.8.1e and f, both the environments (Sr-rich and Ti-poor) and (Sr-poor and Ti-rich) are equally favorable for the growth of (V/Nb/Ta, Na/K)-codoped $SrTiO_3$. For codoping with (V/Nb/Ta, Rh), the calculated defect formation energy is found to be smaller (under Ti-poor condition) than that of doping with individual element, which means that the presence of one element is favoring the incorporation of the other element. This may be due to formation of charge compensated system. Figure 4.8.1a shows that the formation energy for codoping becomes larger in the order (Ta, Rh) < (Nb, Rh) < (V, Rh).

4.8.1.2. Electronic Structure

Now, we discuss the effect of dopant on the electronic structure of $SrTiO_3$. We first describe the scenario in presence of only one type of dopant, which is then followed by the case of codoping.
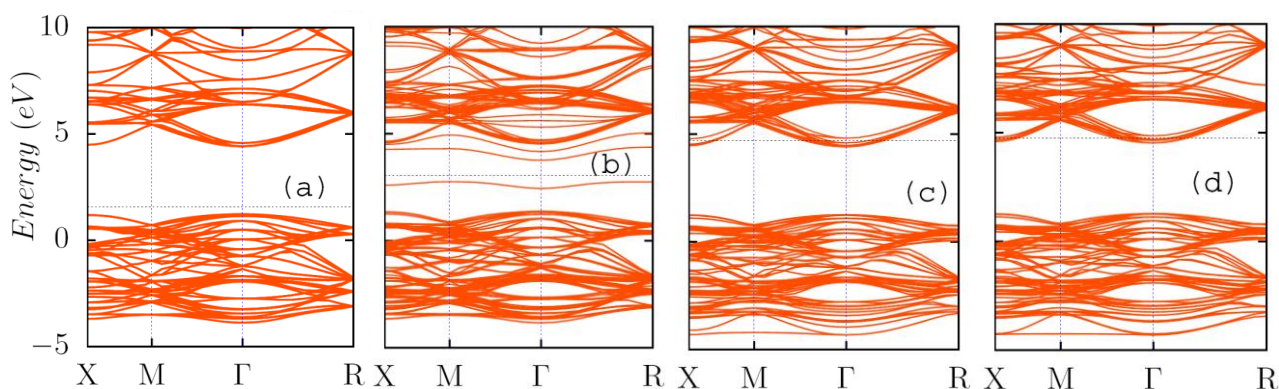
Figure 4.8.2: Band structure plot for (a) undoped $SrTiO_3$, (b) V-doped $SrTiO_3$, (c) Nb-doped $SrTiO_3$, and (d) Ta-doped $SrTiO_3$.
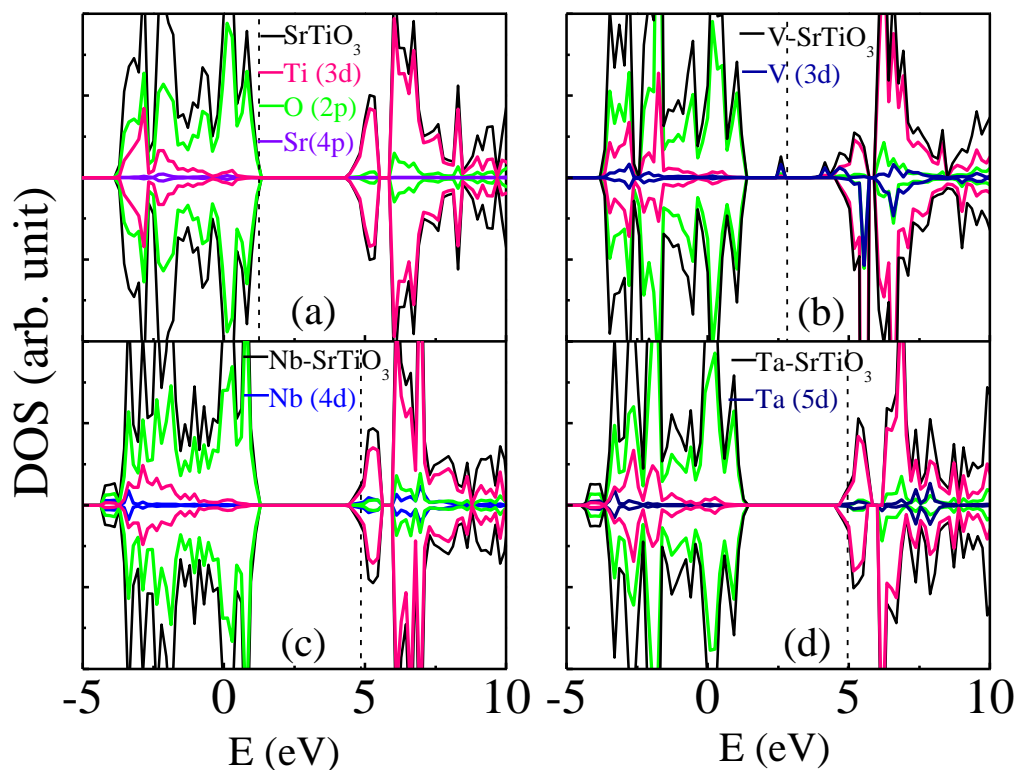
Figure 4.8.3: Density of states of (a) SrTiO$_3$ (b) V-doped SrTiO$_3$, (c) Nb-doped SrTiO$_3$ (d) Ta-doped SrTiO$_3$. Vertical dashed line indicates Fermi Level.

4.8.1.2.1. Monodoped SrTiO$_3$

The stable oxidation state of V, Nb, Ta is +5, and hence their substitution of Ti, which is in the +4 state, will lead to one extra electron in the doped system, resulting into n-type conductivity. The band structure plot for the V-doped SrTiO$_3$ has been shown in Figure 4.8.2b, which indicates the presence of localized occupied impurity states 1.06 eV above the valence band (VB), as well as unoccupied states 1.02 eV below the conduction band (CB). The DOS is unsymmetrical with respect to the spin up and spin down part (Figure 4.8.3b). This may be due to the presence of unpaired electron (3d^5) in the V-doped SrTiO$_3$. Analysis of PDOS indicates that the impurity states are solely contributed by V 3d orbital. The stable oxidation state of V is +5, which leads to one excess electron in the V-doped SrTiO$_3$. Since, the energy of V 3d orbital is lower than the Ti

3d orbital, the extra electron prefers to be located in the V 3d orbital, which is attributed to the appearance of occupied V 3d state. This is supported by the calculated magnetic moment value of 1 μ_B/supercell, which is mainly contributed by V 3d electron. However, the electronic structure of Nb-doped $SrTiO_3$ and Ta-doped $SrTiO_3$ differs significantly with respect to that of V-doped $SrTiO_3$. The band structure for Nb-doped $SrTiO_3$ and Ta-doped $SrTiO_3$ have been shown in Figure 4.8.2c and d, respectively. In both the cases, the Fermi level shifts into the CB, characteristics of n-type semiconductor. The occupied impurity states are found to appear just below the CB. The PDOS analysis (Figure 4.8.3c and d) indicates that the VBM is contributed by O 2p orbital, similar to the case of undoped $SrTiO_3$. The occupied impurity state near the CB have solely Ti 3d character, which may be due to the preference of the extra electron towards Ti 3d orbital over Nb 4d or Ta 5d orbital. This is also manifested in the calculated magnetic moment value of 0.05 μ_B/supercell and -0.32 μ_B/supercell, respectively, mostly contributed by Ti 3d orbital. The calculated energy difference between the VBM and occupied impurity states are 3.19 eV and 3.23 eV, respectively. Therefore, doping with Nb and Ta is not expected to improve the visible light activity of $SrTiO_3$. So we can summarize by saying that, although the doping with each of the three elements V, Nb, and Ta makes $SrTiO_3$ an one electron excess species, the band gap narrowing occurs only in case of V. This is mainly due to the difference in the nature of d orbital of the dopant elements. In the next section, we will see how the electronic structure of (V/Nb/Ta)-doped $SrTiO_3$ is influenced in presence of different codopant elements.
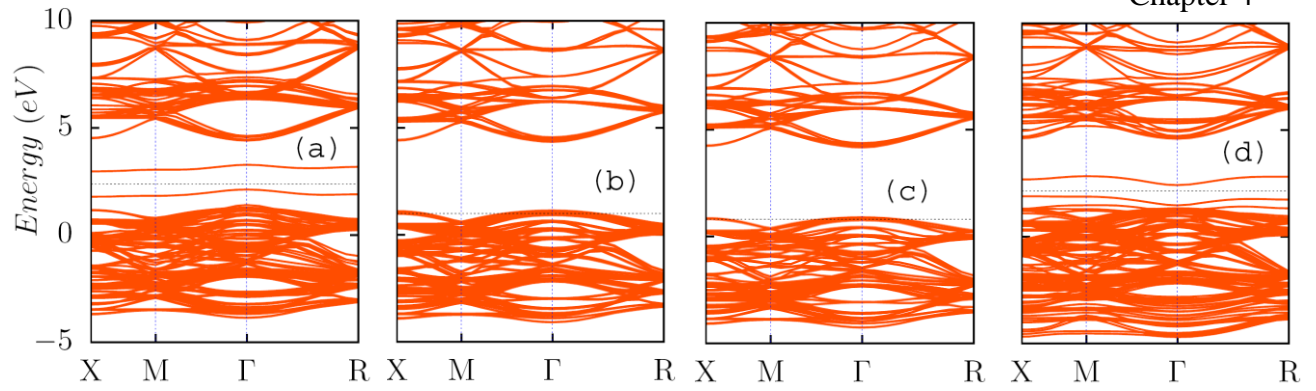
Figure 4.8.4: Band structure plot for (a) N-doped SrTiO$_3$, (b) Na-doped SrTiO$_3$, (c) K-doped SrTiO$_3$, and (d) Rh-doped SrTiO$_3$.
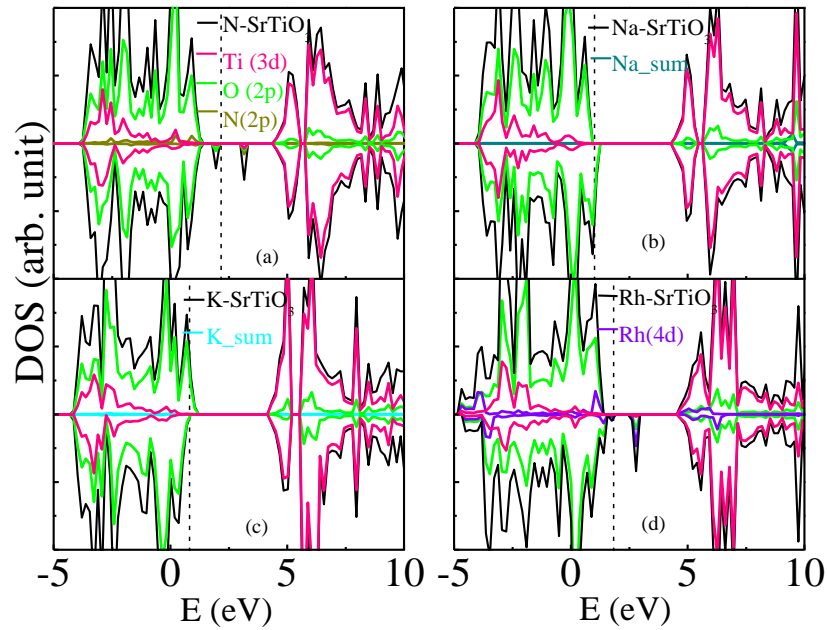
Figure 4.8.5: Density of states of (a) N-doped SrTiO$_3$ (b) Na-doped SrTiO$_3$, (c) K-doped SrTiO$_3$ (d) Rh-doped SrTiO$_3$. Vertical dashed line indicates Fermi Level.

When N ($2s^2 2p^3$) is doped at the O ($2s^2 2p^4$) lattice site it acts as one electron acceptor. This is reflected in the band structure of N-doped SrTiO$_3$ (Figure 4.8.4a), indicating the presence of localized unoccupied state 1.13 eV below the CBM of SrTiO$_3$. N-doping also introduces

localized occupied states 0.84 eV above the VBM of $SrTiO_3$. Both the localized states appear in the spin down part of the DOS plot (Figure 4.8.5a), indicating the presence of unpaired electron in the N-doped $SrTiO_3$. This leads to a magnetic moment of 1 μ_B per supercell. Analysis of PDOS (Figure 4.8.5a) indicates that these states are mainly hybridized states of N 2p and O 2p orbital. The elevation of the VBM can be explained by the higher energy of the N 2p orbital with respect to the O 2p orbital. Thus the effective band gap is significantly reduced due to the presence of these discrete states, leading to sharp improvement of visible light activity of $SrTiO_3$. The major drawback of N-doped $SrTiO_3$ is the presence of those localized states, and charge compensating vacancy defects which can trap the photo-generated charge carriers and accelerates their recombination, thus reducing the photoconversion efficiency of N-doped $SrTiO_3$ drastically. In the course of our discussion, we will see how these states are passivated by codoping with V/Nb/Ta.

Now we discuss the electronic structure of Na (K)-doped $SrTiO_3$. As can be seen from Figures 4.8.4b and c, there is no localized states in the forbidden region, and instead partially unoccupied states are found to appear adjacent to the VBM. A small shift of the CBM level in the downward direction is observed, resulting into a band gap narrowing to 3.04 eV (3.07 eV). The DOS (Figures 4.8.5b and c) is unsymmetrical with respect to spin up and spin down components. This is due to the presence of unpaired electron in the Na (K)-doped $SrTiO_3$ (Na: $2p^6 3s^1$, K: $3p^6 4s^1$, Sr: $4s^2 4p^6 5s^2$). This is evident in the calculated magnetic moment 0.99 μ_B/supercell (-1 μ_B/supercell). Analysis of PDOS indicates that the unoccupied states near the VBM are mainly contributed by the O 2p states. This is due to the replacement of Sr by Na (K) which donates one less number of electron to oxygen than Sr. In both the cases the calculated magnetic moment is found to be contributed mainly by Ti centers and O centers. Figure 4.8.5

indicates no contribution of Na (K)-related states to the band edges of Na (K)-doped SrTiO$_3$. This is expected because there exists ionic type bonding between Na$^+$/K$^+$ and O^{-2}. Small shift of the CBM in the downward direction is found to occur, perhaps due to electron deficiency which perturbs the bonding between Ti and O. The calculated band gap is 3.04 eV (3.07 eV), which leads to smaller improvement of visible light activity of SrTiO$_3$ due to Na (K)-doping.

Let us discuss the effect of doping with Rh. A sharp change in the electronic structure is observed due to Rh doping at the Ti lattice site. The band structure plot for Rh-doped SrTiO$_3$ (Figure 4.8.4d) shows the presence of discrete unoccupied states in between VB and CB. The VBM is elevated by 0.59 eV due to introduction of partially occupied states on the top of VBM. This reduces the effective transition energy for the photo-excited electron from the VBM to CBM, leading to the enhanced visible light activity observed in the experiment. PDOS analysis indicates that these states are mainly composed of Rh 4d states and O 2p states (Figure 4.8.5d). To investigate the origin of these states in details we analyze the electronic configuration of Rh in the Rh-doped SrTiO$_3$. Rh in the +4 state contains five 'd' electrons. In the octahedral crystal field Rh 5d orbitals split into t$_{2g}$ and e$_g$ subsets. The calculated magnetic moment for Rh-doped SrTiO$_3$ is 1 μ_B/ supercell, indicating that Rh^{+4} belongs to be low spin state, i.e., electronic configuration for Rh 5d orbital is t$_{2g}^5$ e$_g^0$. Therefore, the t$_{2g}$ subset appears near the VB, while the e$_g$ subsets is in the CB region. Although these unoccupied states lead to improvement of the optical property, through a reduced effective band gap, they are responsible for faster electron-hole recombination rate, and hence poor photo-conversion efficiency of Rh-doped SrTiO$_3$. In the following section, we will see how these states are passivated in presence of a n-type dopant element (V/Nb/Ta).
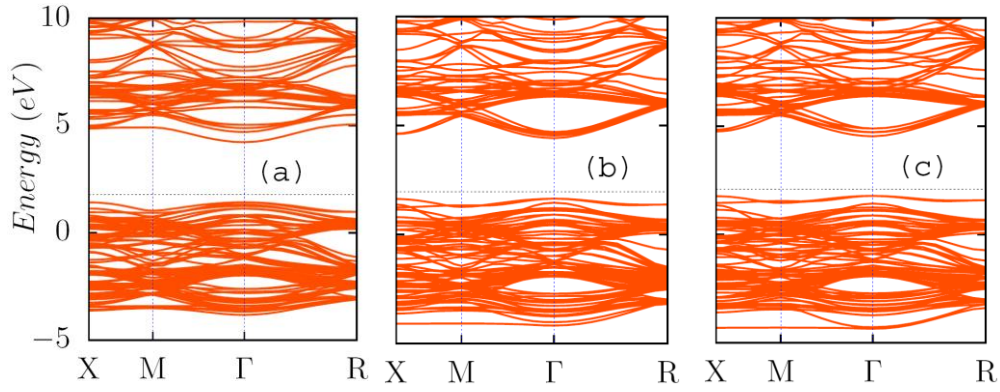
Figure 4.8.6: Band structure plot for (a) (V, N)-codoped SrTiO₃, (b) (Nb, N)-codoped SrTiO₃, and (c) (Ta, N)-codoped SrTiO₃.
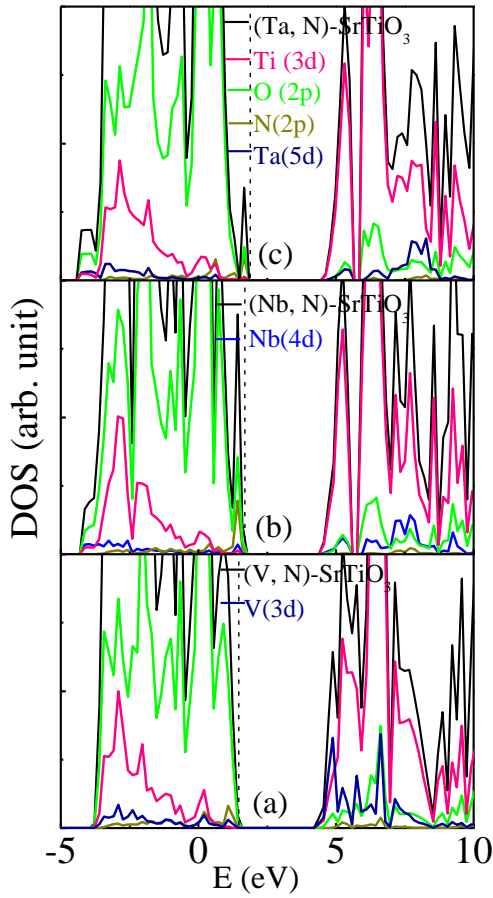
Figure 4.8.7: Density of states of (a) (V, N)-codoped SrTiO₃, (b) (Nb, N)-codoped SrTiO₃, (c) (Ta, N)-codoped SrTiO₃.
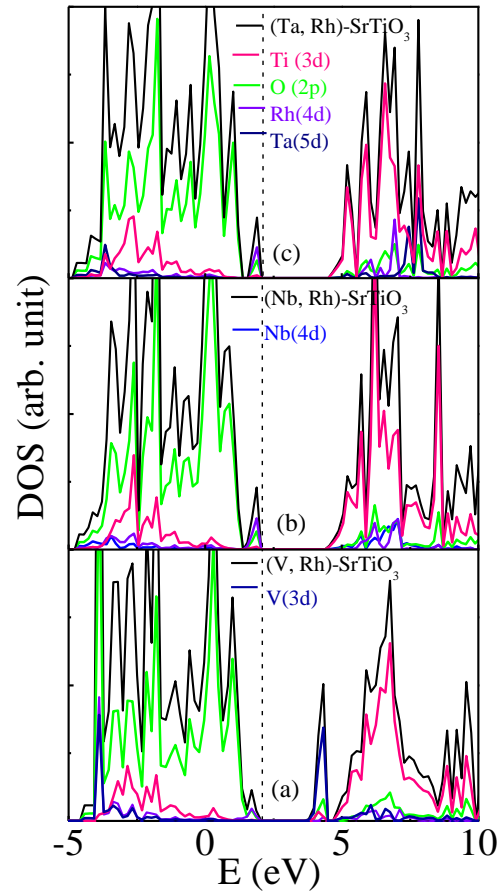
Figure 4.8.8: Density of states of (a) (V, Rh)-codoped SrTiO₃, (b) (Nb, Rh)-codoped SrTiO₃, (c) (Ta, Rh)-codoped SrTiO₃.

4.8.1.2.2. Codoped SrTiO$_3$

In this subsection, the electronic structure of all the codoped SrTiO$_3$ has been described. Let us start this discussion with (V/Nb/Ta, N)-codoped SrTiO$_3$. The band structure plot (Figure 4.8.6a, b, and b) shows complete passivation of the localized N 2p gap states. The Fermi level is pinned to the top of the VB in each case. Neither the N-induced acceptor states nor the occupied Ti-3d states are found to appear in the band structure. This is due to the fact that the extra electron of the cationic dopant is utilized in compensating the electron deficiency of N, forming a charge compensated system. In contrast to the previous study based on standard DFT, we found that the band gap for all the three cases is very close to each other (Table 4.8.1). The calculated band gap in presence of (V, N) pair is 2.80 eV, while the same is 2.78 eV and 2.75 eV for the (Nb, N) and (Ta, N)-codoped SrTiO$_3$, respectively. Analysis of electronic energy levels indicates that there occurs maximum (0.56 eV) elevation of the VBM with respect to that of undoped SrTiO$_3$ in case of codoping with (Ta, N) and minimum (0.20 eV) in case of (V, N)-codoping. On the other hand, CBM in case of (Ta, N)-codoped SrTiO$_3$ is lifted by 0.12 eV, while it remains almost unchanged for (Nb, N)-codoped SrTiO$_3$, and is shifted in the downward direction by 0.19 eV in case of (V, N)-codoped SrTiO$_3$. To investigate this in more details, we analyze PDOS plot for all the cases (Figure 4.8.7a, b, and c). The VBM in the case of (V, N)-codoped SrTiO$_3$ is mainly contributed by O 2p orbital with a small contribution of N 2p orbital (Figure 4.8.7a). However, relative contribution of N 2p states to the VBM increases in case of (Nb, N)-codoped SrTiO$_3$ (Figure 4.8.7b), and becomes almost equal to that of O 2p state in case of (Ta, N)-codoped SrTiO$_3$ (Figure 4.8.7c). Analysis of electronic energy levels indicates that the lowering of the energy of N 2p states is maximum in case of (V, N)-codoping and minimum in case of (Ta, N)-codoping. This may be due to the fact that the strength of dopant-dopant interaction becomes weaker as we

proceed from V (3d) to Ta (5d), due to reduction of interaction between d-orbital and p-orbital. This explains the relative shifts of the VBM level with respect to that of undoped $SrTiO_3$. On the other hand, for (V, N)-codoped $SrTiO_3$ the CBM shows a dominating contribution of V 3d state (Figure 4.8.7a), while for (Nb, N)-codoped $SrTiO_3$ and (Ta, N)-codoped $SrTiO_3$ the CBM is mainly contributed by Ti 3d state (Figure 4.8.7b, c). This may be due to the fact that the V 3d orbital is energetically lower than the Ti 3d orbital, while Nb 4d orbital is energetically closer and Ta 5d is energetically higher than the Ti 3d orbital. This nicely explains the relative shift of the CBM in the codoped systems. In summary, we can tell that the 'd' orbital of the metallic dopant plays a crucial role in shifting the VBM (indirectly) and CBM (directly), resulting into the observed change in the band gap of codoped $SrTiO_3$. Thus the present study, using hybrid DFT, unambiguously explains the electronic structure of (V/Nb/Ta, N)- codoped $SrTiO_3$.
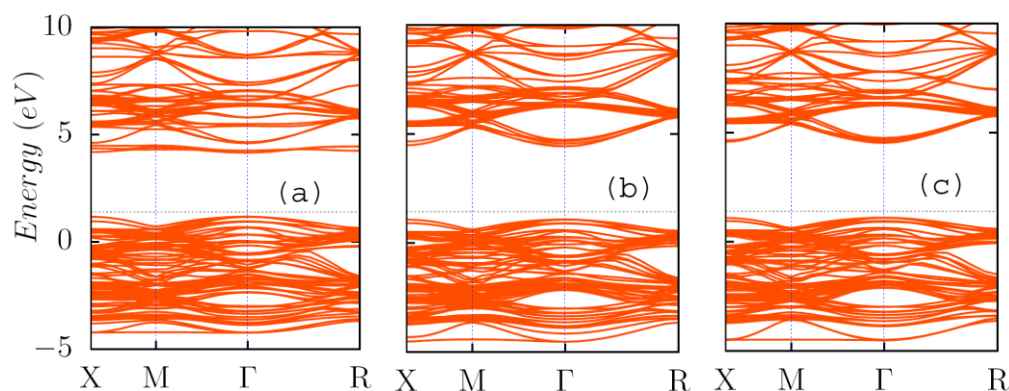
Figure 4.8.9: Band structure plot for (a) (V, Na)-codoped $SrTiO_3$, (b) (Nb, Na)-codoped $SrTiO_3$, and (c) (Ta, Na)-codoped $SrTiO_3$.
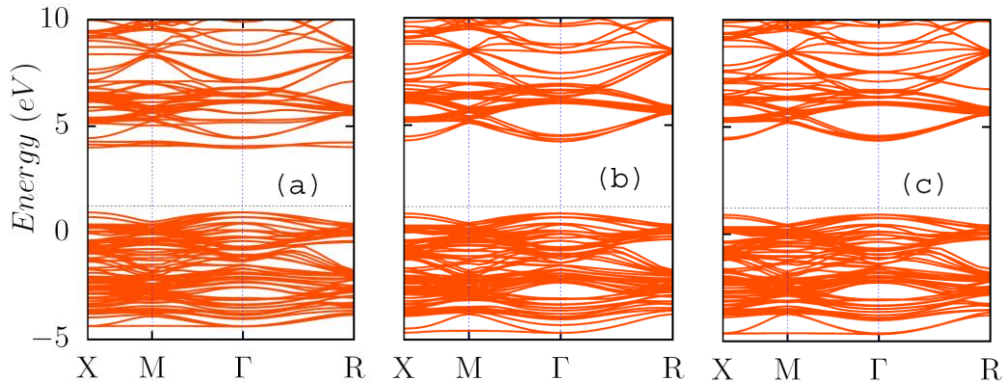
Figure 4.8.10: Band structure plot for (a) (V, K)-codoped $SrTiO_3$, (b) (Nb, K)-codoped $SrTiO_3$, and (c) (Ta, K)-codoped $SrTiO_3$.

Now we present the scenario due to codoping with Na (K) into the crystal structure of (V/Nb/Ta)-doped $SrTiO_3$. As can be seen from Figure 4.8.9a, b, c, 4.8.10a, b, and c, codoping with (V/Nb/Ta, Na/K) also leads to formation of clean band structure. The Fermi level is located on the top of the VBM. In this case, the pentavalent cation dopant (V/Nb/Ta) donates one extra electron than the parent element (Ti), while Na/K donates one less number of electron than Sr, and hence the overall electrical charge remains balanced, thus forming a charge compensated system. In all the cases, both the VBM and CBM are energetically lowered with respect to that of undoped $SrTiO_3$, except (Nb/Ta, Na)-codoped $SrTiO_3$. Codoping with (V, Na) lowers the VBM and CBM by 0.05 eV and 0.26 eV, respectively. Hence, the band gap reduces to 2.98 eV. However, for (Nb/Ta, Na) codoping the VBM is found to be shifted in the downward direction (by 0.14 eV and 0.11 eV, respectively), while the CBM is shifted in the upward direction (by 0.02 eV and 0.12 eV, respectively), resulting into an increase in band gap to 3.35 eV and 3.42 eV, respectively.
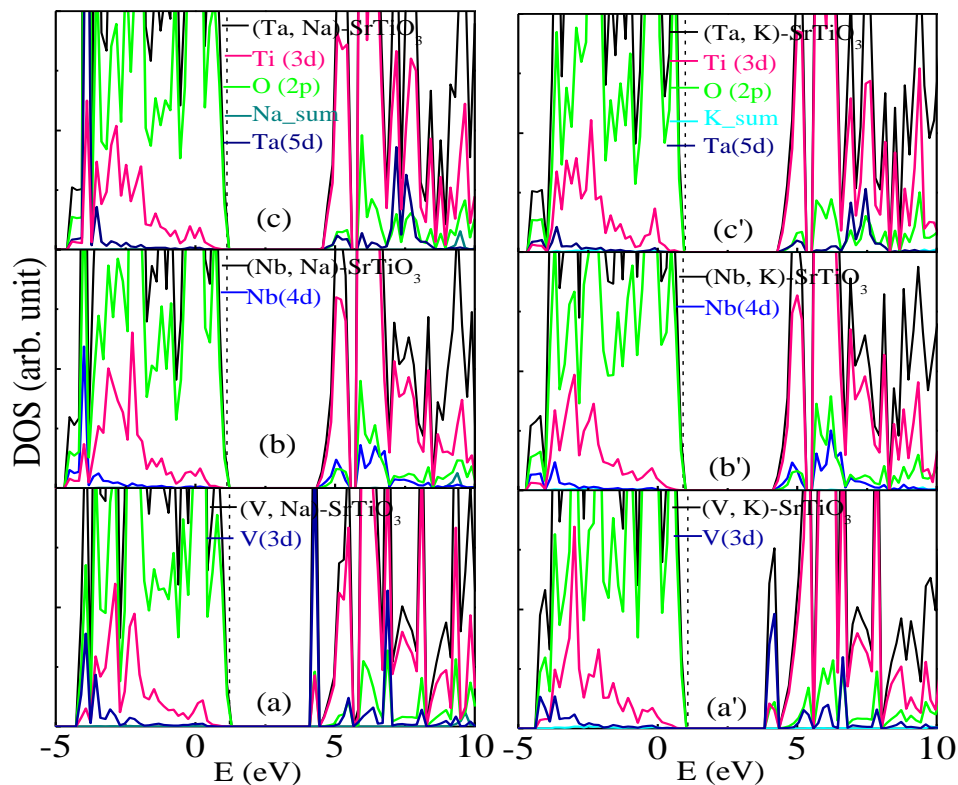
Figure 4.8.11: Density of states of (a) (V, Na)-codoped SrTiO$_3$, (b) (Nb, Na)-codoped SrTiO$_3$, (c) (Ta, Na)-codoped SrTiO$_3$. (a') (V, K)-codoped SrTiO$_3$, (b') (Nb, K)-codoped SrTiO$_3$, (c') (Ta, K)-codoped SrTiO$_3$.Vertical dashed line indicates Fermi Level.

On the other hand, codoping with (V, K) lowers the VBM and CBM by 0.26 eV and 0.44 eV, respectively. Hence, the band gap reduces to 3.01 eV. However, for (Nb/Ta, K) codoping, the extent of shifting the VBM is found to be larger (0.33 eV and 0.32 eV, respectively) than that of CBM (0.18 eV and 0.06 eV, respectively), resulting increase of band gap to 3.34 eV and 3.44 eV, respectively. As can be seen from PDOS analysis (Figure 4.8.11a, b, c, a', b', and c'), there is no contribution of Na (K) to the band edges of the codoped systems. The VBM for all the cases are dominated by O 2p states. The CBM for (V, Na/K)-codoped SrTiO$_3$ is mainly contributed by V 3d states (Figure 4.8.11a, and a'), while in the case of (Nb, Na/K) and (Ta, Na/K)-codoped

SrTiO$_3$ it is mostly contributed by Ti 3d state (Figure 4.8.11b, c, b', and c'). Since, Na/K does not contribute to the band edges due to ionic type bonding, the change in the band gap is mostly controlled by V/Nb/Ta. The CBM of SrTiO$_3$ which is mainly contributed by Ti 3d orbital is found to be affected significantly in presence of V/Nb/Ta due to difference in the 'd' orbital energies. As the V 3d is energetically lower than Ti 3d, codoping with (V, Na/K) lowers the CBM level considerably. However, the presence of mono-valent cation influences the metal oxygen bonding, thus changing the position of the VBM indirectly. Thus based on present theoretical investigation we can predict that codoping with (V/Nb/Ta) and (Na/K) may not be suitable for improving the visible light activity of SrTiO$_3$. However, lowering of the VBM level is expected to enhance the oxidizing power at the VB, which may be important for some catalytic processes.
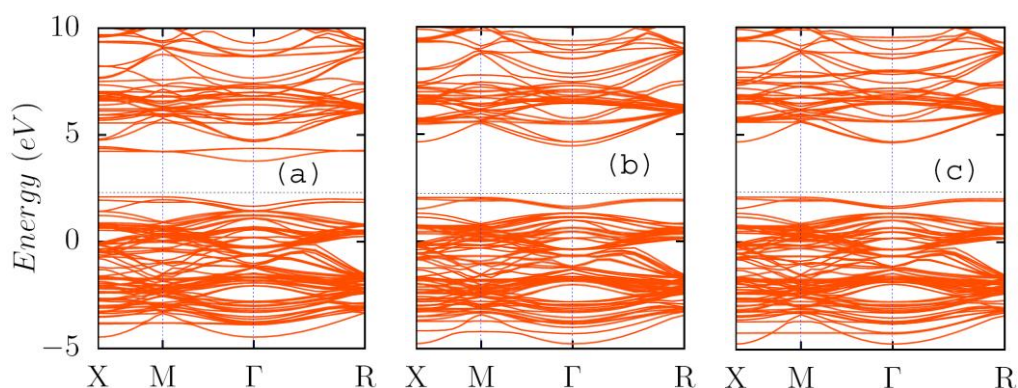
Figure 4.8.12: Band structure plot for (a) (V, Rh)-codoped SrTiO$_3$, (b) (Nb, Rh)-codoped SrTiO$_3$, and (c) (Ta, Rh)-codoped SrTiO$_3$.

Now we come to the discussion of the electronic structure of (V/Nb/Ta, Rh)-codoped SrTiO$_3$. As can be seen from Figure 4.8.12a, b, and c, a clean band structure is produced. In all the cases,

both the acceptor states in the mid gap region and occupied impurity states adjacent to the CB have completely disappeared. This is due to the fact that the extra electron of V/Nb/Ta is utilized in compensating the acceptor states of Rh, forming a charge compensated system. All the electrons are now paired up, and the DOS plot is symmetrical with respect to the spin up and spin down parts. This has also been manifested in the calculated magnetic moment, which is equal to zero for all the (V/Nb/Ta, Rh)-codoped systems. The impurity states now appear on the top of the VB, lifting the VBM with respect to that of the undoped $SrTiO_3$. It has been found that the shifting of the VBM is almost same for all the cases (0.87 eV, 0.83 eV, and 0.87 eV, respectively). This can be explained nicely by analyzing the PDOS plot (Figures 4.8.8a, b, and c) of the codoped $SrTiO_3$, the nature of the VBM is almost similar for all the cases. The VBM for all the (V/Nb/Ta, Rh)-codoped systems is found to be composed of hybridized states of Rh 4d and O 2p orbitals. This is very much identical to the characteristic of Rh^{+3}-doped $SrTiO_3$, where Rh has been found to introduce occupied impurity states above the VB. Here, this situation may arise due to the donation of one extra electron by the other codopant (V/Nb/Ta). Therefore, in all the codoped systems the elevation of VBM is attributed to the presence of Rh. This is a good example, which shows that the VBM of an oxide based semiconductor (normally O 2p character) can be elevated even by a metallic dopant element (Rh). In case of (V, Rh)-codoped $SrTiO_3$ the CBM shifts in the downward direction, and the effective band gap is calculated as 1.66 eV. Analysis of PDOS indicates that the CBM for (V, Rh)-codoped $SrTiO_3$ is mainly contributed by V 3d orbital. Thus lowering of the CBM energy is attributed to the lower energy of the V 3d orbital in comparison to the Ti 3d orbital. This is very much interesting from the point of visible light activity of $SrTiO_3$. To the best of our knowledge, an example of narrowing of the band gap of $SrTiO_3$ by such a large extent without encountering any discrete donor/acceptor state is very

rare till date. Hence, (V, Rh)-codoped $SrTiO_3$ may be one of the promising photocatalysts, although there are other factors still to be tested before drawing a conclusion. Although, the nature of the VBM is found to be similar for all the (V/Nb/Ta, Rh)-codoped $SrTiO_3$, the nature of the CBM in case of codoping with (Nb/Ta, Rh) varies significantly with respect to that of (V, Rh)-codoping. The CBM in case of (Nb, Rh)-codoped $SrTiO_3$ remains almost unchanged (elevated by 0.04 eV), while it is shifted in the upward direction by 0.21 eV for (Ta, Rh)-codoped $SrTiO_3$. This behavior is due to comparable energy of Ti 3d and Nb 3d, while higher energy for Ta 5d in comparison to Ti 3d. The calculated band gap for (Nb, Rh)-codoped $SrTiO_3$ and (Ta, Rh)-codoped $SrTiO_3$ are 2.40 eV and 2.53 eV, respectively. Thus all the three codoping approaches are expected to enhance the photocatalytic activity of $SrTiO_3$ under visible light. Analysis of PDOS (Figures 4.8.8b, and c) indicates that the CBM in both the cases of (Nb, Rh)- and (Ta, Rh)-codoped $SrTiO_3$ is mainly contributed by Ti 3d orbital. This may be due to relatively weaker interaction of O 2p orbital with Nb 4d orbital or Ta 5d orbital in comparison to that with Ti 3d orbital. We also performed Bader charge density analysis for (V/Nb/Ta, Rh)-codoped $SrTiO_3$. The calculated Bader charges on the Rh center are found to be 1.461, 1.452, and 1.452 for the (V, Rh), (Nb, Rh) and (Ta, Rh)-codoped $SrTiO_3$, respectively, while it is 1.641 in case of Rh-doped $SrTiO_3$. A decrease in the Bader charge of Rh in the codoped system is an indication of transfer of extra electronic charge to the Rh center. This leads to difference in the CBM shift for the three codoped systems. The upward shifting of the CBM in case of (Ta, Rh)-codoped $SrTiO_3$ may improve its reducing behavior at the CB, which is very much attractive in the hydrogen generation perspective. Thus based on the present calculation on the electronic structure of (V/Nb/Ta, Rh)-codoped $SrTiO_3$ we can predict that the photogenerated charge carriers have relatively longer life time than in case of individually doped $SrTiO_3$. Since both the

elements together maintain the electrical charge neutrality in the codoped systems, the possibility of formation of charge compensating vacancy defects, which can accelerate the electron-hole recombination rate, will be minimum. Hence, reduced band gap will enhance the visible light activity and clean band structure will improve the photoconversion efficiency, leading to higher photocatalytic response of the (V/Nb/Ta, Rh)-codoped $SrTiO_3$ under visible light.

4.8.1.3. Effect of Concentration

To investigate the effect of dopant concentration on the electronic structure of the (V/Nb/Ta, Rh)-codoped $SrTiO_3$, calculations using larger supercell have been carried out. In this case, we introduce one V/Nb/Ta and one Rh at the Ti lattice sites of 2 x 2 x 3 supercell. The dopant concentration corresponds to 8.33%. All the geometries have been fully relaxed with a k-point mesh of 6 x 6 x 4. We first calculate the defect formation energy for all the cases. The variation of defect formation energy as a function of Ti-chemical potential has been shown in Figure 2a, indicated by dashed lines. As can be seen from Figure 4.8.1a, the dashed lines are almost collinear with the corresponding solid lines (corresponds to formation energy calculated using 2 x 2 x 2 supercell). This indicates that the calculated defect formation energy remains unchanged by increase of supercell size. This also supports our calculation with 2 x 2 x 2 supercell. We have extended our study to further reduce the concentration of the dopant elements. For this purpose, we increase the supercell size for the (V/Nb/Ta, Rh)-codoped $SrTiO_3$ to $2 \times 3 \times 3$ and $3 \times 3 \times 3$, which correspond to dopant concentration of 5.55 % and 3.7 %, respectively, to reach the experimentally achievable concentration range. The geometry optimization has been carried out using the same computational parameter, as discussed earlier, except the k-point mesh of $6 \times 4 \times 4$, and $4 \times 4 \times 4$, respectively. The influence of lowering the dopant concentration on the band

gap has been shown in Table 4.8.2. The calculated band gap of the codoped systems are found to vary with change in the dopant concentration. For (V, Rh)-codoped SrTiO$_3$ the calculated band gap increases to 1.91 eV, and 2.12 eV in case of dopant concentration 5.55 %, and 3.7 %, respectively. Although, the band gap increases it is still in the desirable range of an ideal photocatalyst for solar water splitting. On the other hand, the band gap for the (Nb, Rh)- and (Ta, Rh)-codoped SrTiO$_3$ varies relatively slowly with the decrease of dopant concentration (Table 4.8.2). The calculated band gap for the lowest concentration case (3.7 %) is found to be 2.63 eV and 2.67 eV, respectively, which are still interesting for the utilization of visible light. Thus, based on this calculation we can predict that the codoping with (V/Nb/Ta, Rh) is able to bring significant band gap reduction in SrTiO$_3$ even at low dopant concentration.

Table 4.8.2: Variation of calculated band gap for (V/Nb/Ta, Rh)-codoped SrTiO$_3$ with the dopant concentration

Dopant Concentration	(V, Rh)-SrTiO$_3$ Band Gap (eV)	(Nb, Rh)-SrTiO$_3$ Band Gap (eV)	(Ta, Rh)-SrTiO$_3$ Band Gap (eV)
12.5%	1.66	2.40	2.53
8.33%	1.68	2.44	2.56
5.55%	1.91	2.48	2.60
3.7%	2.12	2.63	2.67

4.8.1.4.Band Edge Alignment

A material to be active for overall water splitting, should have proper band edge alignment with respect to water redox levels. Hence, it is necessary to check the band edge alignment of the modified material with respect to water redox levels before reaching a conclusion related to its photocatalytic water splitting efficiency. It has been reported that the CBM for the undoped $SrTiO_3$ is 0.80 eV above the H^+/H_2 redox level and the VBM is 1.16 eV below the H_2O/O_2 redox level, making it active for overall water splitting process. Since, codoping with (V/Nb/Ta, Na/K) is not able to bring noticeable change in the band gap we are not displaying their band edge alignment. As can be seen from Figure 4.8.13, both (V/Nb/Ta, N)-codoped $SrTiO_3$ and (V/Nb/Ta, Rh)-codoped $SrTiO_3$ are suitable for overall water splitting. Figure 4.8.13 indicates that the reducing behavior at the CB increases in the order (V, N)< (Nb, N)< (Ta, N). The CBM for (V, N)-codoped $SrTiO_3$ lies below that of the undoped $SrTiO_3$, while for (Nb, N)-codoped $SrTiO_3$ it is almost at the same level, and for (Ta, N)-codoped $SrTiO_3$ it is slightly above. Hence the reducing behavior at the CB follows the order mentioned above. On the other hand, the oxidising behavior follows the reverse order. As can be seen from Figure 4.8.13, the oxiding property of (V, Rh)-codoped $SrTiO_3$ at the VBM is nearly same as that of the (Nb, Rh) and (Ta, Rh)-codoped $SrTiO_3$. However, the reducing behavior at the CB follows the trend, (V, Rh)< (Nb, Rh)< (Ta, Rh). For (V, Rh)-codoped $SrTiO_3$, the CBM level is just 0.15 eV above the H^+/H_2 level, while it is 1.01 eV above for the (Ta, Rh)-codoped $SrTiO_3$, which is even above that of the undoped $SrTiO_3$. This will boost the reducing behavior at the CB of (Ta, Rh)-codoped $SrTiO_3$.
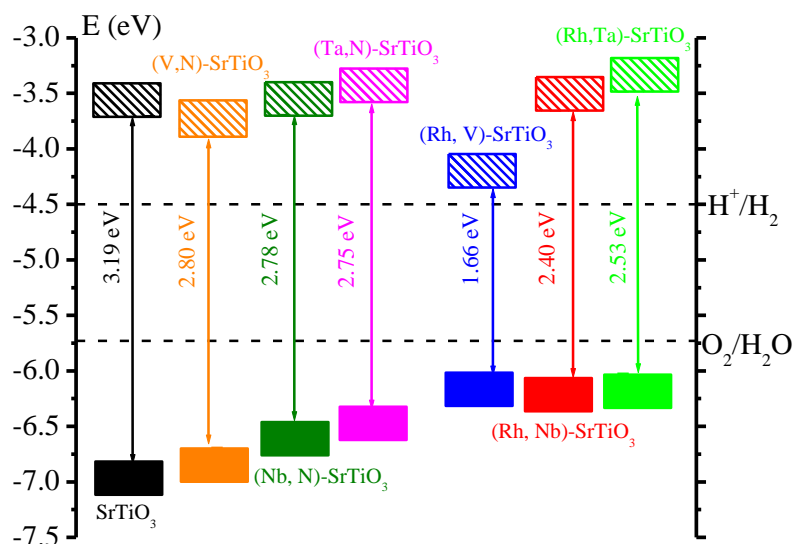
Figure 4.8.13: The band alignment of the undoped, (V, N)-codoped SrTiO$_3$, (Nb, N)-codoped SrTiO$_3$, (Ta, N)-codoped SrTiO$_3$, (V, Rh)-codoped SrTiO$_3$, (Nb, Rh)-codoped SrTiO$_3$ and (Ta, Rh)-codoped SrTiO$_3$ with respect to the water redox levels (H$^+$/H$_2$, O$_2$/H$_2$O).

4.8.2. Conclusion

The geometric and electronic structure of SrTiO$_3$ codoped with pentavalent transition metal element (V/ Nb/Ta) and anionic (N) or cationic (Na/K/Rh) dopant has been calculated using density functional theory. Due to comparable ionic size, the basic crystal structure of the parent and codoped systems are found to be almost similar. In the case of (V/Nb/Ta, Rh)-codoped SrTiO$_3$ the presence of one element has been found to reduce the energy cost of doping with the other element. The precise characterization of the defect states needs a more reliable hybrid density functional theory. All the dopant pairs, studied here maintain charge neutrality and produce clean band structure, thereby leading to reduction of electron-hole recombination rate in

comparison to that in presence of individual dopant elements. Among the codopant pair, (Nb/Ta, Na/K) is found to increase the band gap of $SrTiO_3$, which will lead to poorer visible light activity. However, the presence of alkali metal (Na/K) lowers the VBM energy, which may be important for other catalytic processes due to enhanced oxidising property at the VB. On the other hand, the extent of band gap narrowing lies in the region 0.39 eV to 0.44 eV for codoping with (V/Nb/Ta) and N. The codoping with (V/Nb/Ta, Rh) pair has been found to be most effective in improving the visible light activity of $SrTiO_3$ among the systems studied. Especially, the (V, Rh)-codoped $SrTiO_3$ is shown to be very attractive due to its band gap of 1.66 eV, as calculated here, which is even the lowest band gap among the doped-$SrTiO_3$ capable of releasing both hydrogen and oxygen during water splitting, reported till date (to the best of our knowledge). The pair (Ta, Rh) is also of interest due to its elevated CBM level. It may further boost the reducing property at the CB, which is very much significant in the context of hydrogen generation. In the present case we have shown that the codopant pair involving only the transition element is more suitable than involving transition-nontransition element for the enhancement of the visible light activity of $SrTiO_3$. The present study reveals that in the (V/Nb/Ta, Rh)-codoped $SrTiO_3$, Rh is converted to trivalent state due to donation of one extra electron from the pentavalent ion. This is beneficial for achieving higher photoconversion efficiency, as the probability of charge carrier trapping reduces in absence of tetravalent Rh. Hence, based on the present theoretical results, we can present (V/Nb/Ta, Rh) as one of the promising pair of codopant to enhance the photocatalytic activity of $SrTiO_3$ under visible light.

Chapter 5

Improving Visible Light Photocatalytic Activity of Other Perovskite Materials

5.1. An Efficient Strategy for Controlled Band Gap Engineering of KTaO$_3$

5.1.1. Introduction

Recently, KTaO$_3$ has generated immense interest for the photocatalytic water splitting due to its several unique features. Firstly, the dominating form at room temperature for KTaO$_3$ is perfect cubic ($Pm\overline{3}m$), leading to better delocalization of photogenerated charge carriers, and consequently the electrons and holes have longer life time. Therefore, more number of excited electrons are expected to be available for the photoreaction in case of KTaO$_3$. Moreover, the cubic form for KTaO$_3$ exists over a wide range of temperature, which will not lead to complicated phase behavior in the reaction condition. Secondly, smaller band gap for KTaO$_3$ (3.6 eV) also facilitates to show higher activity under same exposer in comparison to other tantalates. However, band gap engineering of KTaO$_3$ to make it active for visible light absorption is highly restricted by its CBM position. Because, the CBM potential of KTaO$_3$ is not much negative, any attempt to reduce the band gap may further shift the CBM position in the downward direction, which can drastically affect its reducing property (such as, hydrogen evolution ability during photo-splitting of water). This factor limits wide spread applications of KTaO$_3$. Most of the studies carried out so far to enhance the photocatalytic activity of KTaO$_3$ mainly focus on the reduction of the electron-hole recombination rate either by doping with a foreign element or by employing an organic chromophore as a sensitizer. As for example, Ishihara et al found that controlling the charge density with an acceptor dopant significantly improves the photocatalytic activity of KTaO$_3$ for the decomposition of water. In a series of studies, they have investigated the effect of several elements as dopant, including bivalent (Zn^{+2}), trivalent (Y^{+3}, Al^{+3}, Ga^{+3}, In^{+3}), tetravalent (Ti^{+4}, Zr^{+4}, Hf^{+4}, Si^{+4}, Ge^{+4}), pentavalent (Sb^{+5}, Nb^{+5}),

and hexavalent (W^{+6}) species, at the Ta lattice site. Among them, Zr^{+4}, Hf^{+4}, and Ga^{+3} are found to be the most effective in enhancing the rate of hydrogen production. This has been explained by the reduction in charge density, which in turn increases the life time of the photogenerated charge carriers. Hagiwara et al. investigated the effect of codoping with N into Zr-doped $KTaO_3$ and observed a significant improvement of visible light activity.[211] Paulauskas et al attempted to increase the photo-electrochemical performance of $KTaO_3$ by introducing Ca or Ba at the K lattice site.[212] Liu et al observed an enhancement of photoactivity due to doping with La at the K lattice site.[213] This has been attributed to better delocalization of electron and hole in more dispersive and dense band structure of La-doped $KTaO_3$, resulting into improved charge carrier separation. Bajorowicz et al improved the photocatalytic activity of $KTaO_3$ under visible light by forming a ternary composite photocatalyst in combination with CdS, and MoS_2, which works on two photon excitation mechanism.[214] Hagiwara et al demonstrated that photoactivity of $KTaO_3$ for the decomposition of water is significantly enhanced by employing cyanocobalomin dye as a sensitizer, which also facilitates better separation of the electron-hole pair.[215] Later on they modified the catalyst by various porphyrinoids, which increases the photoactivity by a significant extent due to increase of the lifetime of the charge separated state.[216] Recently, Wang et al proposed a strategy to reduce the band gap of several perovskite materials through local rhombohedral to tetragonal structural transition.[217] A significant number of theoretical studies on the undoped $KTaO_3$ have been reported so far using various techniques in order to understand its electronic properties in a better way.[218-226]

Our aim is to lower the band gap of $KTaO_3$ by elevating the VBM only, so that the hydrogen evolution property at the conduction band (CB) remains intact. Because, the VBM and CBM of $KTaO_3$ are contributed by mainly O 2p state and Ta 5d state, respectively, we choose

only anionic type doping in the present study. For this purpose, we involve N, which has been shown to be one of the widely used anionic dopant for improving the visible light activity of various oxide based semiconductor photocatalysts. However, in spite of strong visible light activity, the N-doped systems have several limitations to achieve photoconversion efficiency at a satisfactory level. To overcome this, in the present case, we consider different halogen elements as a codopant. Halogen elements, particularly, F has been widely accepted both for monodoped as well as codoping due to its various unique features. Using density functional theory (DFT) we systematically investigate the effect of all these dopant elements on the geometry and electronic structure of $KTaO_3$. As we all know that the standard DFT, severely underestimates the band gap, and hence we employ the Heyd, Scuseria, and Ernzerhof (HSE) hybrid functional, which has been shown to successfully reproduce the experimental band gap of a wide range of semiconductor materials.

5.1.2. Computational Details

All the calculations have been carried out using Vienna ab initio simulation package (VASP), with projector augmented wave (PAW) potential representing the ionic core and valence electrons interactions. The valence states involved for the construction of the potential are: K ($3p^6 4s^1$), Ta ($6s^2 5d^3$), O ($2s^2 2p^4$), N ($2s^2 2p^3$), F ($2s^2 2p^5$), Cl ($3s^2 3p^5$), Br ($4s^2 4p^5$), and I ($5s^2 5p^5$). The valence electron orbitals are expanded using the plane wave basis set up to an energy cutoff of 500 eV. The doped systems have been modeled with $2 \times 2 \times 2$ supercell (40 atoms) of the cubic $KTaO_3$ crystal structure. All the model structures have been fully optimized by the relaxation of both cell parameters and the ionic positions using the exchange and correlation potentials of Perdew-Burke-Ernzerhof (PBE) under generalized gradient approximation

(GGA).[58] The Brillouin zone sampling has been carried out using Monkhorst and Pack scheme and a k-point mesh of $8 \times 8 \times 8$ has been chosen in the present study. The energy convergence criterion for the self consistent cycle was set to 10^{-6} eV. For electronic structure calculation we employed HSE hybrid functional. In this study, the standard value of the screening parameter (0.2 $\mathring{A}^{-1}$) has been considered. Here, we perform test calculations on undoped $KTaO_3$ with varying proportion of exact HF exchange mixing in the range from 25% to 35 % to find out the best parameter which reproduces the experimental band gap (3.6 eV). The band structure has been plotted along the high symmetric k-path. The calculation for density of states (DOS) has been carried out by using the tetrahedron method with Blöchl correction. Optical spectrum has been drawn by calculating the frequency dependent dielectric function.

5.1.3. Results and Discussion

5.1.3.1. Geometry

$KTaO_3$ exists in the cubic crystalline structure ($Pm\overline{3}m$, space group no. 221) over a wide range of temperature. The basic framework is described by TaO_6 octahedra, as shown in Figure 5.1.1. The calculated lattice parameter is found to be 4.03 $\mathring{A}$ at the GGA_PBE level. In the optimized geometry, the Ta-O-Ta angle is 180° and the Ta-O bond length is 2.01 $\mathring{A}$, which is consistent with the previous theoretical reports. The dopant element (N or X= F, Cl, Br, I) is introduced at the oxygen lattice site of $2 \times 2 \times 2$ supercell of $KTaO_3$ (the dopant concentration corresponds to 4.17%). For codoping two different elements (N, and X) have been simultaneously introduced at the oxygen lattice sites. In this case, we considered two possible configurations (Ta1, O1, O2), and (Ta1, O1, O3), which differ from each other in the distance between the dopant elements.
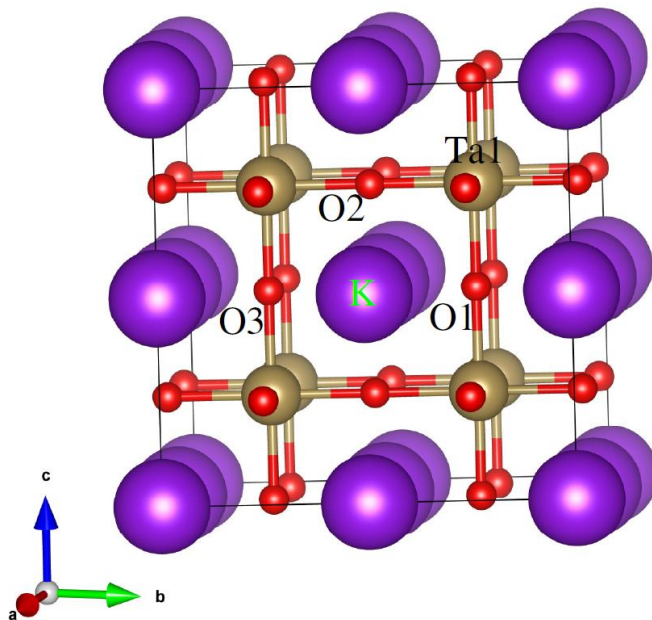
Figure 5.1.1: $2 \times 2 \times 2$ supercell of cubic crystal structure of $KTaO_3$. The numbers indicate positions of the dopant elements.

All the structures have been fully relaxed (i.e., relaxation of both cell parameter and ionic positions) to obtain optimized geometries, which are considered for electronic structure calculations. In case of monodoping with either N or F, the crystal structure is found to be hardly affected due to closeness of their ionic radii with that of oxygen ($R_{O^{-2}} = 1.35$ Å, $R_{N^{-3}} = 1.46$ Å, $R_{F^-} = 1.29$ Å). One of the lattice parameters is increased by 0.03 and 0.06 Å, for N-doped and F-doped $KTaO_3$, respectively. The calculated Ta-N and Ta-F bond distances are found to be 2.03 and 2.14 Å, respectively, which are very close to the Ta-O bond distance in the parent crystal structure. However, a significant change in the geometry is visible in the case of doping with Cl, Br, and I. One of the lattice parameters is enlarged by 0.28, 0.39, and 0.54 Å, respectively. This is the consequence of increased Ta-X bond length (2.31, 2.38 and 2.47 Å, respectively) in

comparison to the Ta-O bond length. This arises due to larger mismatch between the ionic size of the dopant element and the host element ($R_{O^{-2}} = 1.35$ Å, $R_{F^-} = 1.29$ Å, $R_{Cl^-} = 1.81$ Å, $R_{Br^-} = 1.96$ Å, $R_{I^-} = 2.20$ Å). As expected, codoping with N and F leads to negligible distortion in the crystal structure of $KTaO_3$. The two configurations, where N and F are located at 2.88 ('str. I') and 4.03 Å ('str. II') distance away from each other, are energetically very close to each other (ΔE = 0.14 eV). However, the energy difference between the two configurations increases to 1.16, 1.5, and 4.15 eV for the (N, Cl), (N, Br), and (N, I)-codoped $KTaO_3$, respectively. The deviation from the ideal cubic structure also becomes noticeable for these cases. Further calculations have been carried out using the lowest energy structures only, i.e., configuration with smaller N-X distance, except for the case of (N, F)-codoped $KTaO_3$, for which both the configurations are considered.

5.1.3.2. Defect Formation Energy

In order to determine the relative stability of the doped/codoped materials, and find favorable synthetic condition, calculations for the defect formation energy have been carried out using the following relation

$$\Delta H_f = E_{doped} - E_{KTaO3} + n_O \, \mu_O - n_N \, \mu_N - n_X \, \mu_X \qquad (5.1.1)$$

where, E_{doped} and E_{KTaO3} are the energy of doped and undoped $KTaO_3$ calculated by using $2 \times 2 \times 2$ supercell. Here, μ_A stands for the chemical potential of the element, 'A', and n_A is the number of atoms removed or added to the system for the construction of the doped system.

When $KTaO_3$ reaches equilibrium with the reservoir of K, Ta, and O, their chemical potential can be related as

$$\mu_K + \mu_{Ta} + 3\mu_O = \mu_{KTaO3(bulk)} \qquad (5.1.2)$$

The heat of formation can be expressed as

$$\Delta = \mu_{KTaO3(bulk)} - \mu_{K(bulk)} - \mu_{Ta(bulk)} - 3\mu_{O(gas)} \qquad (5.1.3)$$

Because, $KTaO_3$ is a stable compound, Δ is negative. The elemental chemical potential should never cross the value in their bulk/gaseous form, i.e., $\mu_K \leq \mu_{K(bulk)}$, $\mu_{Ta} \leq \mu_{Ta(bulk)}$, and $\mu_O \leq \mu_{O(gas)}$. Hence, one can write the following relations

$$\mu_{K(bulk)} + \Delta \leq \mu_K \leq \mu_{K(bulk)} \qquad (5.1.4a)$$

$$\mu_{Ta(bulk)} + \Delta \leq \mu_{Ta} \leq \mu_{Ta(bulk)} \qquad (5.1.4b)$$

$$3\mu_{O(gas)} + \Delta \leq 3\mu_O \leq 3\mu_{O(gas)} \qquad (5.1.4c)$$

In the present study, chemical potentials for the metallic species, $\mu_{K\ (bulk)}$, and $\mu_{Ta\ (bulk)}$ are obtained by calculating the energy of an atom in their metallic state, while $\mu_{O\ (gas)}$ and μ_N have been calculated from the energy of an oxygen or nitrogen molecule at the center of a 20 Å × 20 Å × 20 Å box ($\mu_{O\ (gas)/N} = \frac{1}{2} E_{O2/N2}$).
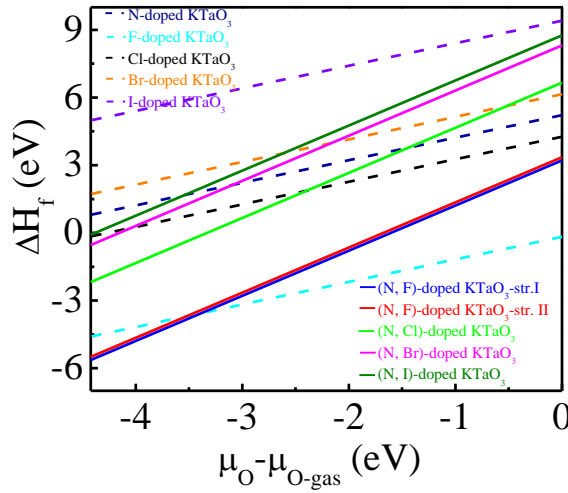
Figure 5.1.2: Variation of formation energy for (N/X)-monodoped and (N, X)-codoped $KTaO_3$ as function of oxygen chemical potential ($\Delta\mu = \mu_O - \mu_{O-gas}$).

The calculated defect formation energy for both the monodoping and codoping cases has been shown in Figure 5.1.2 as a function of oxygen chemical potential. The common feature for all the curves is that the defect formation energy becomes more favorable as we move towards oxygen-poor condition. This can be justified by the requirement of relatively lower energy for the creation of oxygen vacancy under oxygen poor condition. For monodoping with N, the defect formation energy is calculated as 5.22 eV under extreme oxygen-rich condition, which reduces to 0.79 eV at the oxygen-poor condition. In case of doping with halogen element, F is found to be most favorable, as the calculated defect formation energy is found to be negative even under oxygen-rich condition. The defect formation energy for this case increases in the order $F < Cl < Br < I$, i.e., the defect formation becomes less favorable as the lattice mismatch between the host and dopant elements increases. For codoping, the calculated defect formation energy follows the same order as can be seen for monodoping, i.e., $(N, F) < (N, Cl) < (N, Br) < (N, I)$. In case of (N, F)-codoped $KTaO_3$, the calculated defect formation energies for the two different structures are found to be very close to each other. As can be seen from Figure 5.1.2, the defect formation energy for codoping is lower than that of monodoping at the oxygen-poor condition, indicating that the formation of codoping is more favored in comparison to the doping with individual elements.

5.1.3.3. Electronic Structure

5.1.3.3.1. KTaO$_3$

To investigate the effect of doping on the electronic structure of $KTaO_3$, calculations for band structure and DOS have been carried out and results are compared with that of undoped one. To optimize the computational parameters, several test calculations for the determination of band

gap of undoped $KTaO_3$ have been executed with different Hartree-Fock contribution (mixing parameter: 25%, 30%, 34%, and 35%) to the exchange correlation energy in the HSE formalism. As can be seen from Table 5.1.1 that 34% Hartree-Fock mixing with the standard screening parameter value (0.2 Å^{-1}) reproduces the experimental band gap (3.60 eV) of $KTaO_3$ very closely. Hence, throughout the calculations, we use these computational parameters for all the electronic structure calculations. The band structure and density of states plots for undoped $KTaO_3$ have been shown in Figure 5.1.3. Analysis of PDOS indicates that the VBM of $KTaO_3$ is mostly contributed by O 2p orbital, while the CBM has strong Ta 5d character, similar to other metal oxide materials. There is no contribution of K related states found at the band edges. This is due to ionic type bonding between K^+ and O^{2-}. Now we will discuss the influence of the dopant element on the electronic structure of $KTaO_3$. Before presenting the scenario in case of codoping, the electronic structure under the influence of only one type of dopant has been described.

Table 5.1.1: Variation of band gap of undoped $KTaO_3$ with different mixing HF exchange

Screening parameter (Å^{-1})	HF mixing exchange (%)	Band gap (eV)
0.2	25	3.32
0.2	30	3.61
0.2	35	3.89
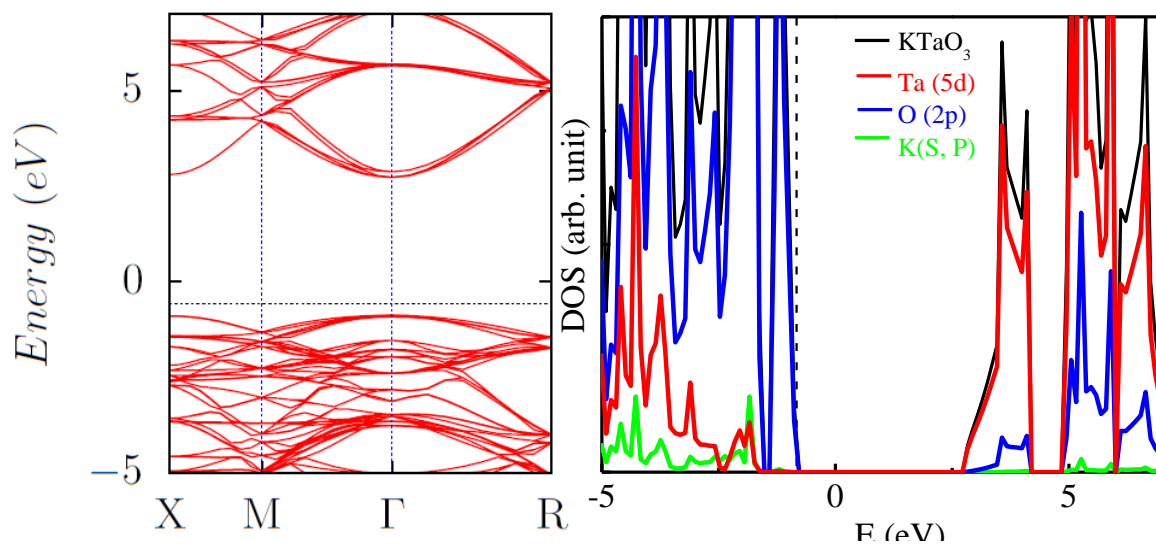
Figure 5.1.3: Band structure and density of states of $KTaO_3$.

5.1.3.3.2. N-doped $KTaO_3$

We start this discussion by investing the effect of N doping, which has been paid maximum attention among the anion dopants for improving the visible light activity of a wide range of oxide based photocatalyst. Figure 5.1.4a shows the band structure plot for the N-doped $KTaO_3$.

Analysis of the energy levels indicates that there occurs a marginal shift of the VBM (Δ= 0.09 eV) and CBM (Δ= -0.03 eV) due to N-doping. However, it introduces occupied states 0.97 eV above the VBM and unoccupied states 1.35 eV below the CBM. As the defect states divide the band gap into three regions with energy gap of 0.97 eV, 0.69 eV, and 1.35 eV, the N-doped $KTaO_3$ should show attractive visible light activity. Unfortunately, these localized states play negative role in achieving good photoconversion efficiency. To investigate the nature of these defect states we analyze the DOS and PDOS for N-doped $KTaO_3$ (Figure 5.1.4a´). The DOS plot is unsymmetric with respect to spin up and spin down parts and both types of the defect states appear in the spin down part of Figure 5.1.4a´. The state below the Fermi level is found to be partially occupied. The presence of unpaired electron is also manifested in the calculated magnetic moment value of N-doped $KTaO_3$ (1 μ_B/ supercell). As can be seen from Figure 5.1.4a´, the defect states are composed of N 2p and O 2p hybrid states. The change in the electronic structure of $KTaO_3$ due to N doping can be correlated with two main factors: (i) the energy of N 2p orbital is higher than that of O 2p orbital; (ii) the number of valence shell electrons for N is less by one with respect to that of oxygen, which makes the system electron-deficient. The major disadvantage of N doping is that electron-hole recombination has been shown to be relatively faster in comparison to that in the undoped system due to localized defect states. Our aim in the present study, is to passivate these states by codoping with different halogen elements, which can provide one extra electron, and therefore, the electron deficiency can be compensated. But before that, we will discuss how these elements influence the electronic structure of the parent $KTaO_3$.
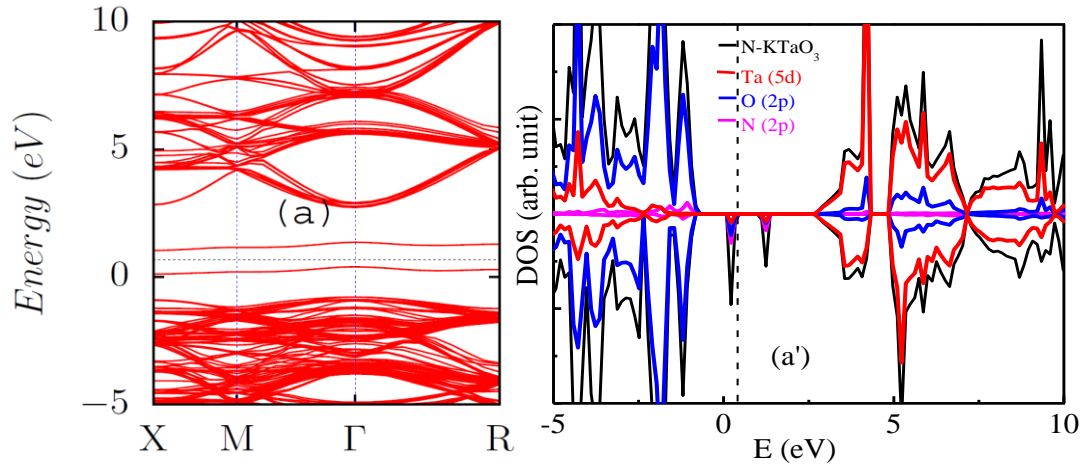
Figure 5.1.4: Band structure and density of states of N-doped KTaO$_3$.
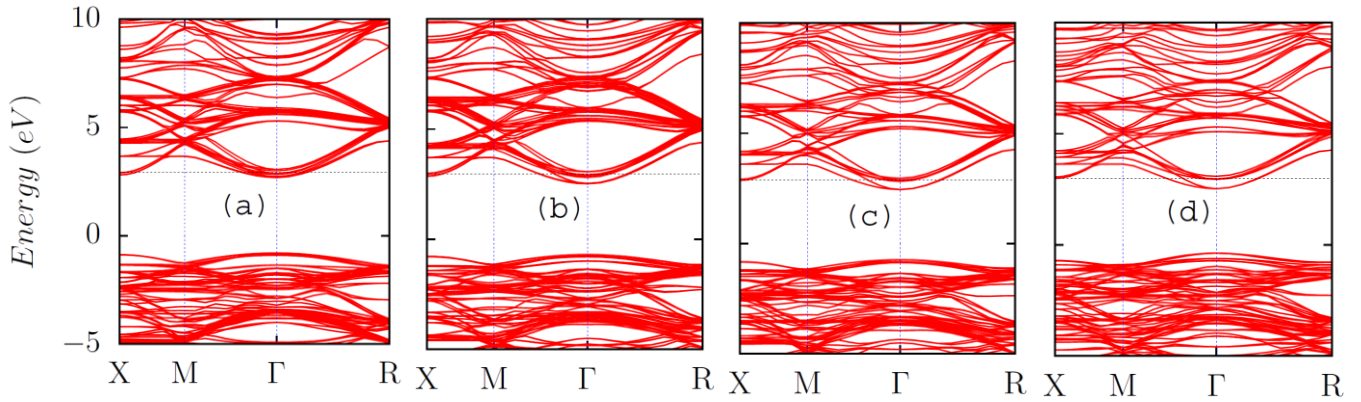
Figure 5.1.5: Band structure of F-doped KTaO$_3$ (a), Cl-doped KTaO$_3$ (b), Br-doped KTaO$_3$ (c), and I-doped KTaO$_3$ (d).
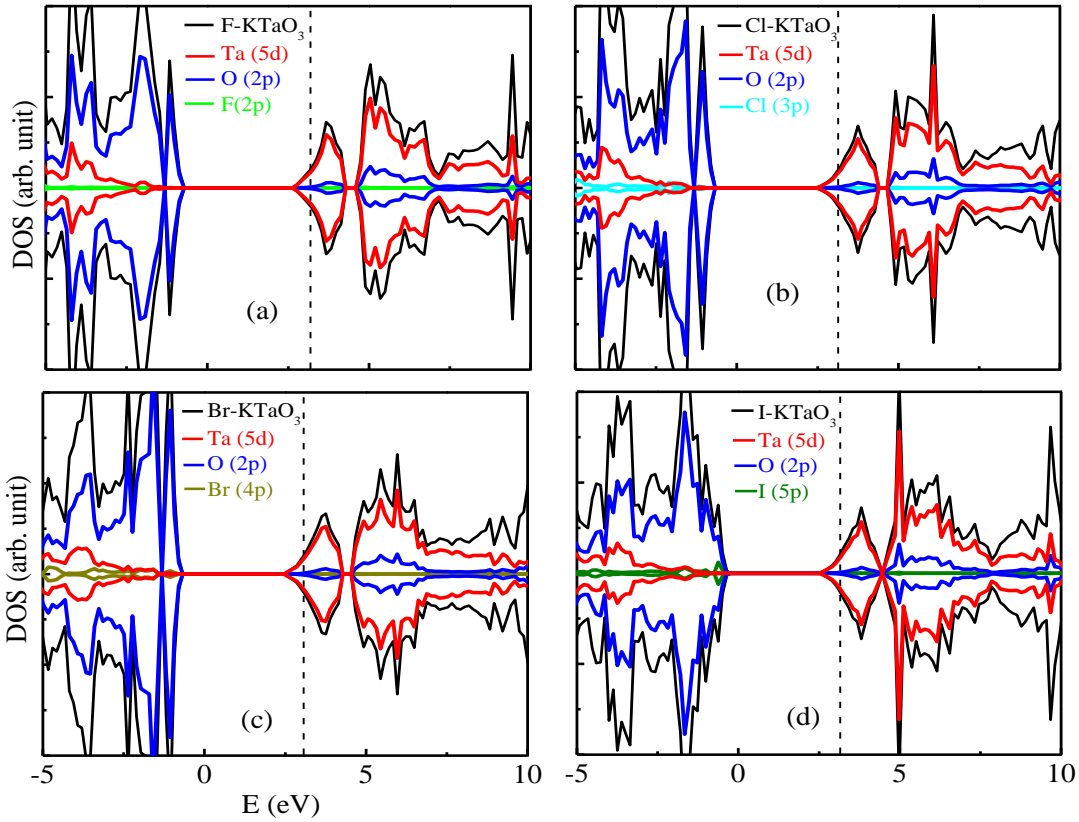
Figure 5.1.6: Density of states of F-doped KTaO$_3$ (a), Cl-doped KTaO$_3$ (b), Br-doped KTaO$_3$ (c), and I-doped KTaO$_3$ (d).

5.1.3.3.3. F/Cl/Br/I-doped KTaO$_3$

The band structure plots for the F/Cl/Br/I-doped KTaO$_3$ have been shown in Figure 5.1.5a-d. In contrast to the N-doped KTaO$_3$, no localized defect states are found in the forbidden region. However, the Fermi level locates itself in the conduction band region, indicating an electron-excess system. This is because of one extra valence shell electron of the halogen element (ns^{2}np^5) in comparison to oxygen atom (2s^{2}2p^4). Hence, codoping of any of the four elements (F, Cl, Br, and I) will remove the electron deficiency. In case of F-doped KTaO$_3$ the band edge is marginally shifted with respect to that of undoped KTaO$_3$, which results into a small reduction of

band gap (by 0.09 eV). However, the extent of band edge shifting increases as we proceed towards I-doped $KTaO_3$. As a consequence, the calculated band gap decreases in the order, Cl-doped $KTaO_3$ (3.28 eV) > Br-doped $KTaO_3$ (3.24 eV) > I-doped $KTaO_3$ (2.91 eV). Hence, doping with only iodine is able to enhance the visible light activity of $KTaO_3$ by a good extent. To investigate this variation of electronic band gap in more details we analyze the PDOS for all the systems. As can be seen from Figure 5.1.6a-d the occupied states adjacent to CB for all the cases are mainly contributed by Ta 5d states. This may be due to localization of the extra electron in the Ta 5d orbital. The VBM for all the cases is composed of O 2p states, except for I-doped $KTaO_3$, where the I 5p state is found to have small contribution to the VB edge. Therefore, the observed change in the band gap can be correlated to the increase in the crystal lattice distortion associated with the increase in the size of the dopant element. Of course, for I-doped $KTaO_3$, participation of I 5p orbital to the VB edge also contributes along with the lattice distortion, resulting into decrease in band gap by a larger extent (0.7 eV). Although, I-doped $KTaO_3$ is quite attractive from the consideration of band gap, distortion of crystal structure by a significant extent is highly undesirable for achieving good photoconversion efficiency as it favors electron-hole recombination process. Now we will discuss the synergistic effect of both halogen elements and nitrogen on the electronic structure of $KTaO_3$.

5.1.3.3.4. (N, F/Cl/Br/I)-codoped $KTaO_3$

The band structure plots for the (N, F/Cl/Br/I)-codoped $KTaO_3$ have been shown in Figure 5.1.7a-b, and 5.1.8a-c. It is interesting to note that the partially occupied mid gap defect states have completely disappeared; instead they appear adjacent to the VBM. Therefore, a clean band structure is formed, which is favorable for achieving high photo-conversion efficiency. This is

attributed to the counter balancing effect of the two types of the dopant elements. In presence of both the dopant elements, the magnetic moment of $KTaO_3$ vanishes. For (N, F)-codoping the calculated band gap using 'str. I' is found to be 2.66 eV, which ensures $KTaO_3$ to show better response towards visible light than in absence of dopoing. More interestingly, this decrease in band gap is found to be solely contributed by the elevation of the VBM. Therefore, band gap narrowing using this approach is very much relevant for $KTaO_3$, because its CBM position is around 0.7 eV above the H^+/H_2 level and hence any other attempt to decrease the band gap by lowering the CBM energy might adversely affect the reducing behavior at the CB. Detailed description of the contributory states to the band structure of (N, F)-codoped $KTaO_3$ 'str. I' is presented in Figure 5.1.7a´.
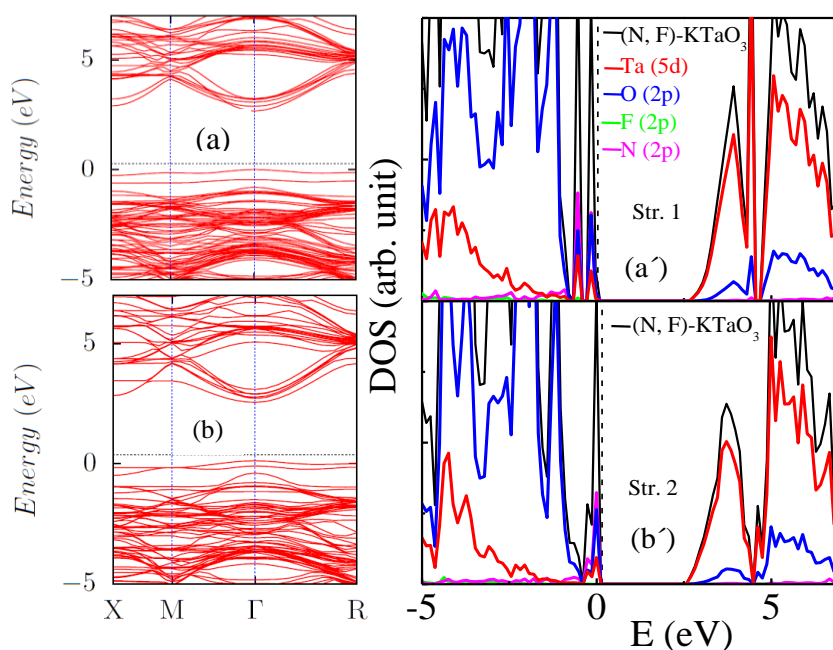
Figure 5.1.7: Band structure and density of states of (N, F)-codoped $KTaO_3$-str.I (a, a´), and (N, F)-codoped $KTaO_3$-str.II (b, b´).

The VBM is composed of hybridized state of N 2p and O 2p, while the CBM shows Ta 5d character. This is as expected due to involvement of non-transition elements. Since, the VBM for $KTaO_3$ is composed of O 2p orbital it is most likely to be perturbed due to the dopant of interest, while the CBM, which is composed of Ta 5d orbital remains unaffected. The calculated band gap is further reduced to 2.43 eV, when the 'str. II' is considered for the (N, F)-codoped $KTaO_3$. Since, 'str. I' and 'str. II' for (N, F)-codoped $KTaO_3$ are found to be energetically very close to each other, coexistence of both the structures is expected in the practical situation. As can be seen from Figure 5.1.7b´, the nature of band edges for the 'str. II' is almost similar to that of 'str. I'. However, the relative shift of VBM is found to be slightly higher in this case, which results into larger band gap reduction. Rest of the codoped systems show relatively lower band gap narrowing than the above case. For all the three (N, Cl/Br/I)-codoped $KTaO_3$ systems, the calculated band gap is close to 3 eV. To investigate this difference, we analyze electronic energy levels, which indicates that the elevation of the VBM in these cases is relatively less than the previous case. Moreover, the CBM is found to move in the upward direction. As can be seen from Figure 5.1.8a-c, there is no significant change in the nature of band edge in comparison to that of (N, F)-codoped $KTaO_3$. However, the electronic charge density distribution is greatly changed with the halogen counterpart (Figure 5.1.9). In case of monodoped system, highest electron density zone is centered on oxygen atoms, while it is shifted to the F center in case of (N, F)-codoped $KTaO_3$. Interestingly, for the rest of the codoped systems the charge distribution again become O-centred. This may be attributed to the combined effect of the difference in the electronegativity as well as nature of the p orbital (p orbital in the valence shell becomes more diffused in the order F < O < Cl < Br < I). We strongly believe that this phenomena have

significant influence on the observed variation in the calculated band gap. Additionally, the distortion in the crystal structure has some contribution to the change in band gap.
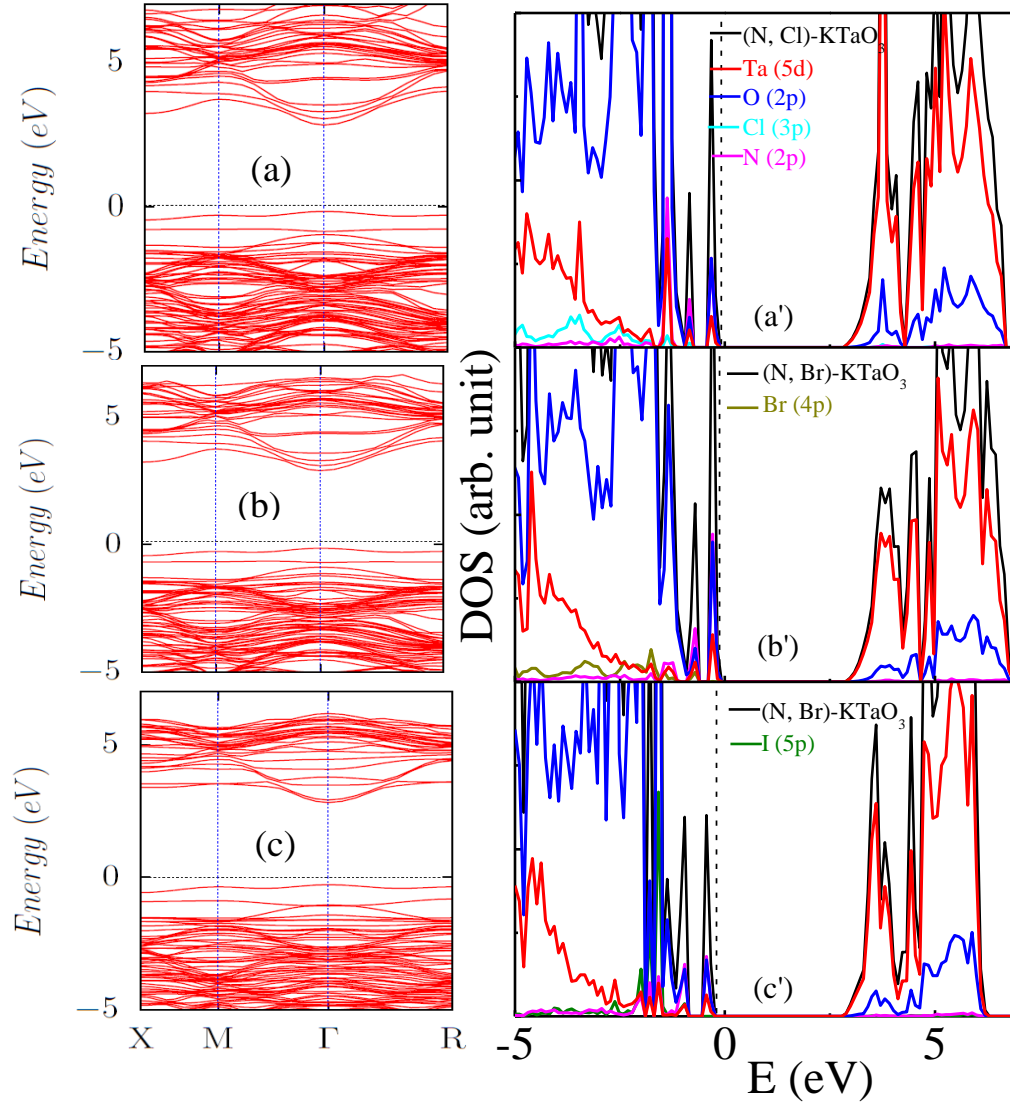
Figure 5.1.8: Band structure and density of states of (N, Cl)-codoped KTaO$_3$(a, a´), (N, Br)-codoped KTaO$_3$ (b, b´), and (N, I)-codoped KTaO$_3$(c, c´).
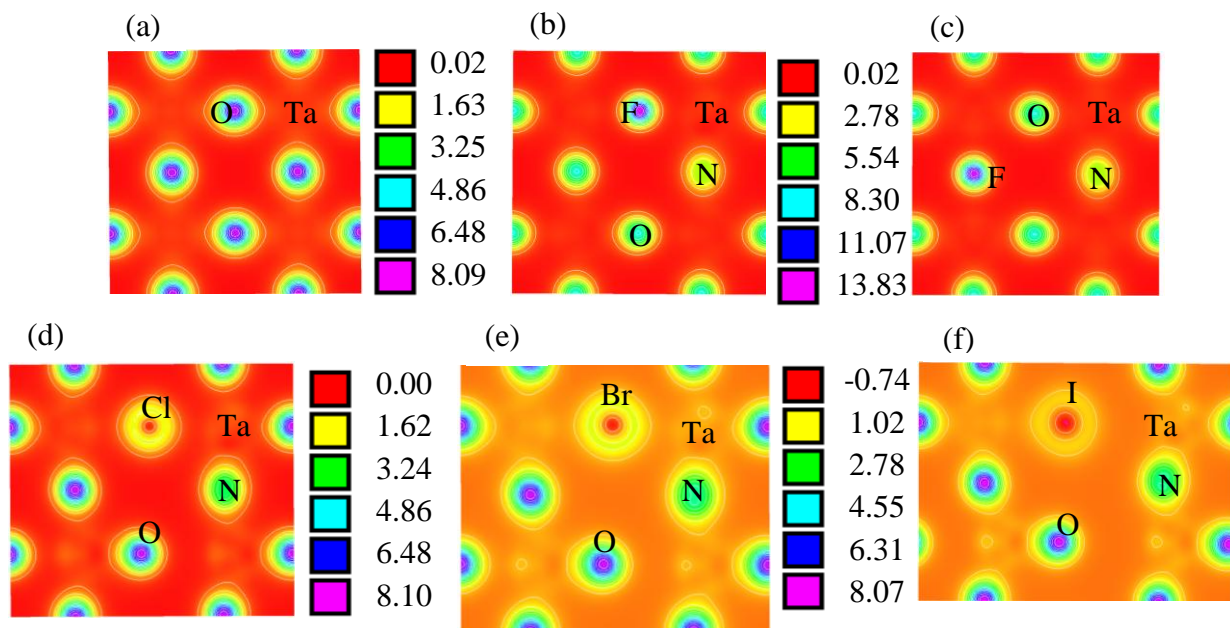
Figure 5.1.9: Charge density distribution for KTaO$_3$ (a), (N, F)-codoped KTaO$_3$-str.1 (b), (N, F)-codoped KTaO$_3$-str.II (c), (N, Cl)-codoped KTaO$_3$(d), (N, Br)-codoped KTaO$_3$ (e), and (N, I)-codoped KTaO$_3$(e).

The common characteristics of the nature of band structure of the (N, X)-codoped KTaO$_3$ is that the 'p' states of the halogen element does not appear at the band edge, thus not contributing directly in the band gap reduction. But the presence of halogen elements lowers the energy of N 2p states, so that it can better mix with O 2p states and appear closer to the top of VB. Not only that, their presence also removes the electron deficiency originated due to N-doping by providing one extra electron, thus passivating those localized defect states. Among the codoped system studied here, (N, F)-codoped KTaO$_3$ should show maximum visible light response.

As per experimental observations, F also offers several other advantages due to its unique feature. Particularly, presence of F in the crystal structure has been found to reduce the rate of electron-hole recombination by a significant extent. This experimental observation has been attributed to the formation of particle with smaller size and higher specific surface area, which increases the quantity of absorbed reactant and accelerates the migration of the charge carriers to the catalyst surface. Enhanced photocatalytic cleavage has been correlated with the elongated O-H bond due to adsorption of water through the H atoms. Thus, the choice of (N, F) pair is quite justified over other pairs.

5.1.3.4. Optical Property

To have a look at the shift in the optical spectrum of $KTaO_3$ due to codoping, calculation for frequency dependent dielectric function has been carried our using HSE hybrid functional. he calculated absorption coefficient has been plotted as a function of wavelength of light in Figure 5.1.10. For $KTaO_3$, the absorption curve is found to be limited to the UV region. This is expected as the band gap for $KTaO_3$ is greater than 3 eV. This behavior is consistent with the experimental observation. However, the curve is found to be extended to the longer wavelength on codoping. As can be seen from Figure 10, the maximum shift occurs in case of codoping with N and F, while for (N, Cl) and (N, Br)-codoped $KTaO_3$ the absorption curves are almost overlapping each other, and for (N, I)-codoped $KTaO_3$ it shows minimum shift towards longer wave length region. This characteristics of the absorption profile for the (N, X)-codoped $KTaO_3$ fully corroborates with the inference drawn during electronic structure discussions. Thus, the choice for N and F pair is again justified.
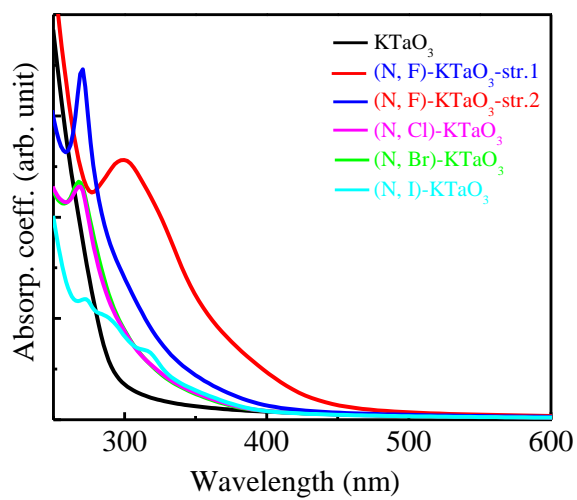
Figure 5.1.10: Absorption spectrum of undoped KTaO$_3$, (N, F/Cl/Br/I)-codoped KTaO$_3$.
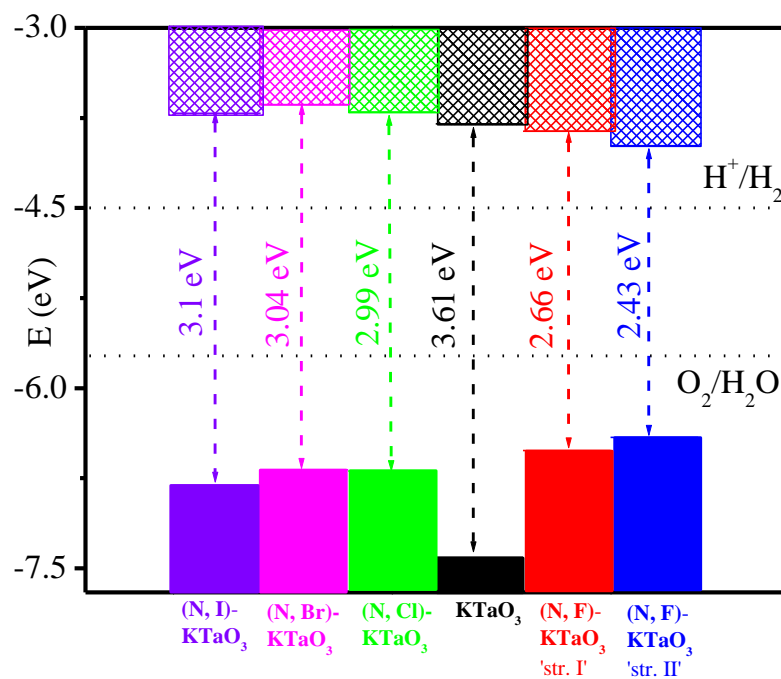
Figure 5.1.11: Band edge alignment of undoped and (N, F/Cl/Br/I)-codoped KTaO$_3$.

5.1.3.5. Band Edge Alignment

While reducing the band gap of a semiconductor photocatalyst, it is always advisable to check its CBM and VBM positions with respect to the redox levels of the desired reaction. A material is considered to be active for hydrogen evolution during water splitting if its CBM is located above the H^+/H_2 level and for oxygen evolution its VBM should be located below the H_2O/O_2 level. As for example, $KTaO_3$ has been experimentally found to be an overall water splitting material due to its appropriate band edge alignment with respect to water redox levels. To check whether this property is still operative in the (N, X)-codoped $KTaO_3$ or not, their band edge positions are aligned. For this purpose, the relative shift of the VBM and CBM of the codoped systems with respect to that of undoped $KTaO_3$ have been determined, for which the absolute positions of the band edge are taken from the experimental database. As can be seen from Figure 5.1.11, the CBM and VBM positions of all the codoped systems are in appropriate positions with respect to the H^+/H_2 level and H_2O/O_2 level, respectively. Therefore, all the codoped systems considered here are suitable for overall water splitting. For undoped $KTaO_3$, the CBM and VBM are located at the distance of around 0.7 and 1.68 eV from the respective the water redox levels. In case of codoping with N and F while considering 'Str. I', the CBM is found to be located at almost same level of that of undoped one ($\Delta E = 0.08$ eV) and the VBM is 0.79 eV below the H_2O/O_2 level. However, for (N, F)-codoped $KTaO_3$ with 'Str. II', the band edges are found to be closer to the reference levels (0.52 and 0.68 eV, respectively) in comparison to the case of 'Str. I'. The interesting observation is that the CBM for the rest of the codoped $KTaO_3$ is located even above that of the undoped one. Therefore, a better reducing behavior at the CB (hydrogen evolution rate) is expected from these codoped systems.

5.1.4. Conclusions

In this hybrid functional based DFT study, our aim has been to find suitable dopant elements for the controlled band gap narrowing of $KTaO_3$. Among the several dopant elements studied here, both individually and in combination, (N, F) pair has been found to be the most effective for improving the photocatalytic activity of $KTaO_3$ under visible light. According to the formation energy calculation, oxygen-poor condition is found to be more favorable for the synthesis of the doped materials, and under this condition the formation energy for the codoped $KTaO_3$ is even lower than that of the monodoped system. Although, monodoping with N reduces the band gap by a large extent, localized defect states created in the forbidden region may promote electron-hole recombination rate. On the other hand, monodoping with F does not bring any noticeable change in the effective band gap, while others do so by a small extent. Combination of N and halogen pair is found to be advantageous because it reduces the band gap without encountering any localized defect states. The enhancement of visible light activity has been manifested in the optical spectrum. More importantly, the narrowing of band gap in the present cases mostly involves elevation of the VBM, and therefore all the codoped systems are found to satisfy the thermodynamic criteria for overall splitting of water. Since, the codopant pair forms charge compensated system, unwanted vacancy formation will be drastically minimized. In addition, they will also counterbalance the adverse effect of each other. Among the four codoped systems studied here, (N, F)-codoped $KTaO_3$ is the most preferred one due to maximum band gap lowering, and unique advantages of F for accelerating photocatalytic water splitting activity over the other halogen elements.

5.2. Improving Visible Light Photocatalytic Activity of KTaO₃ using Cation- Anion Dopant Pair

In this section, the effect of (N, Mo/W) pair on the electronic structure of $KTaO_3$ has been investigated using density functional theory. In case of codoping with (N, Mo/W) pair total electrical charge neutrality is maintained. Therefore, vacancy promoted electron-hole recombination can be avoided. Moreover, the feasibility of N doping into crystal structure of $KTaO_3$ increases in presence of (Mo/W) due to reduction in formation energy. Interestingly, in presence of both cationic (Mo/W) and anionic dopant (N) a clean band structure is produced, which is favorable for good photoconversion efficiency. The reduction in band gap due to codoping is quite significant for enhancement of absorption of visible light, and it is more prominent in the case of (Mo, N) pair. The final conclusion has been drawn by checking the relative positions of the band edges of both the codoped systems with respect to water redox potential. Thus present section explores the role of (Mo/W, N) pair in improving the visible light photocatalytic activity of $KTaO_3$.
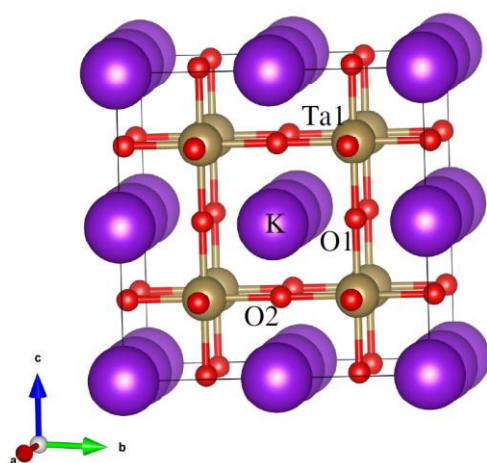
Figure 5.2.1: $2 \times 2 \times 2$ supercell of cubic crystal structure of $KTaO_3$.

5.2.1. Results and Discussion

5.2.1.1. Geometry

In case of codoping, we consider two different model structures obtained by varying the distance between the dopant elements. The structure with the dopant elements directly bonded to each other, occupying the lattice site Ta1 and O1 (Figure 5.2.1) is referred to as 'Str.1', and the structure, where the dopant elements are far away from each other, occupying the lattice site Ta1 and O2 (Figure 5.2.1) is referred to as 'Str.2'. Since, 'Str.1' is energetically lower, this should be the major product under equilibrium condition. Hence, synthetic strategy involving solution method is expected to deliver product with 'Str.1' configuration predominantly. On the other hand, the probability of formation of product with 'Str.2' configuration is considered to be more in the case of synthetic strategy like magnetron sputtering or supersonic cluster beam deposition techniques. The energy difference between the two structures is 1.37 eV for the (Mo, N)-coped $KTaO_3$ and 0.94 eV for the (W, N)-coped $KTaO_3$. Therefore, in the present study, we discuss the electronic structure of both types of products. The calculated Mo-N distance and W-N distance in the respective codoped case ('Str.1') is quite shorter than the Ta-O bond length in $KTaO_3$ (1.73 Å, and 1.76 Å).

5.2.1.2. Electronic Structure

The band structure plots for the (N, Mo)-codoped $KTaO_3$ and (N, W)-codoped $KTaO_3$ have been shown in Figure 5.2.2a, 5.2.2b, 5.2.3a and 5.2.3b. In all the cases, a clean band structure is produced, where the Fermi level is found to be located on the top of the VB. Both the N induced acceptor states and Mo/W induced donor states are completely passivated. Therefore, good photoconversion efficiency is expected for both the cases. Comparison of the nature of

band structure of both the codoped systems indicates that the impurity states in case of (N, W)-codoped $KTaO_3$ appears closer to the band edges. This is due to better mixing of impurity states with the band edges of host, arising from the closeness in d-orbital energy of the host and the dopant element. This leads to difference in the calculated band gap of the two codoped systems (Table 5.2.1). The calculated band gap even differs significantly for 'Str.1' and 'Str.2' of the same material. As for example, for (N, Mo)-codoped $KTaO_3$ the respective band gaps are 2.70 eV and 1.67 eV. This can be correlated with the difference in relative shifting of the band edges. As can be seen from Table 5.2.1, both the VBM and CBM shift to each other considerably (0.86 eV, and 1.08 eV) in case of (N, Mo)-codoped $KTaO_3$ with configuration 'Str.2', resulting into a large reduction in the band gap. However, for 'Str.1', band gap narrowing is responsible for shifting of CBM only. Therefore, the response towards visible light will be more in the case of 'Str.2'. Hence, for the improvement of visible light photocatalytic activity of $KTaO_3$ codoped with the 'Str.2' configuration is more desirable. The difference is investigated in more details by analyzing the PDOS of 'Str.1' and 'Str.2' (Figure 5.2.2a', b'). In case of 'Str.1', (N 2p and O 2p) hybridized states add one new layer on the top of the VB, while they form two new layers in case of 'Str.2'. Thus, the width of the impurity states is relatively broader in case of 'Str.2', causing elevation of VBM by a larger extent. On the other hand, the CBM for both 'Str.1' and 'Str.2' is mainly composed of Mo 4d orbital. This may be due to the difference in bonding pattern of the dopant elements with the host elements. In contrast to the codoping with (Mo, N), the shifting of the CBM in the downward direction is significantly less in case of codoping with (W, N), resulting into relatively smaller band gap narrowing. This is attributed to the difference in energy of Mo 4d, W 5d and Ta 5d orbitals. However, there occurs elevation of VBM for both 'Str.1' and 'Str.2' in this case. This is because both the metal ions involve 5d orbitals, which lead to relatively

weaker bonding with N 2p orbital, than that in case of 4d orbital. As can be shown from Table 5.2.1, the calculated band gap for (N, W)-codoped $KTaO_3$ with configuration 'Str.1' and 'Str.2' are 2.96 eV, and 2.21 eV, respectively. Similar to (N, Mo)-codoped system, the VBM in this case is composed of hybridized state of N 2p and O 2p orbitals (Figure 5.2.3a' and 5.2.3b'). However, CBM is contributed by hybridized states of Ta 5d and W 5d orbitals, where contribution of both Ta 5d and W 5d orbital is found to be almost equal in the case of 'Str.1', while W 5d is dominating in case of 'Str. 2'.

Therefore, codoping with N and Mo/W effectively reduces the band gap of $KTaO_3$ without encountering any localized defect states. Thus, the present strategy should improve the photocatalytic activity of $KTaO_3$ under visible light. We further extended our study to discuss few more points before drawing final conclusions.
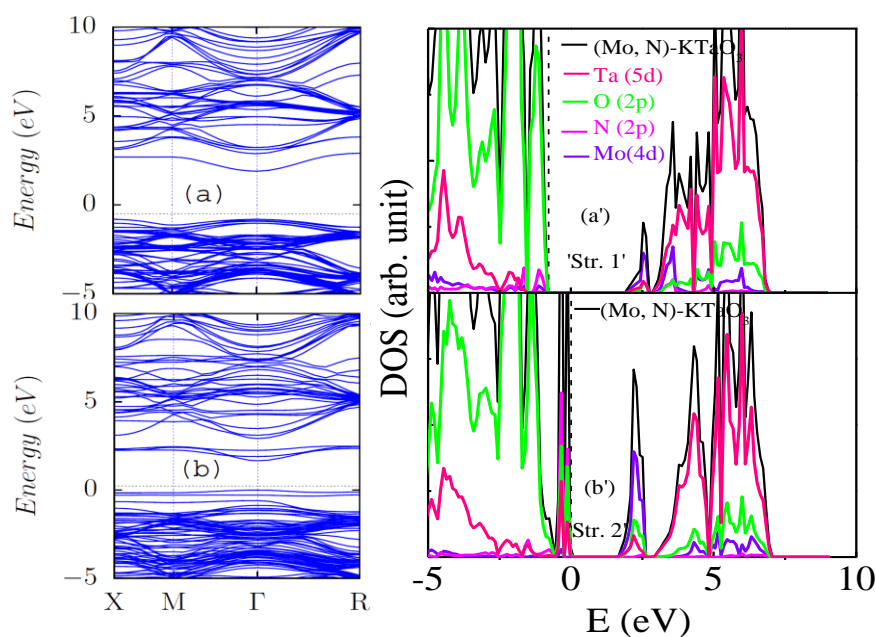
Figure 5.2.2: Band structure and density of states of (N, Mo)-codoped $KTaO_3$-'Str.1' (a, a´), and (N, Mo)-codoped $KTaO_3$-'Str.2' (b, b´).
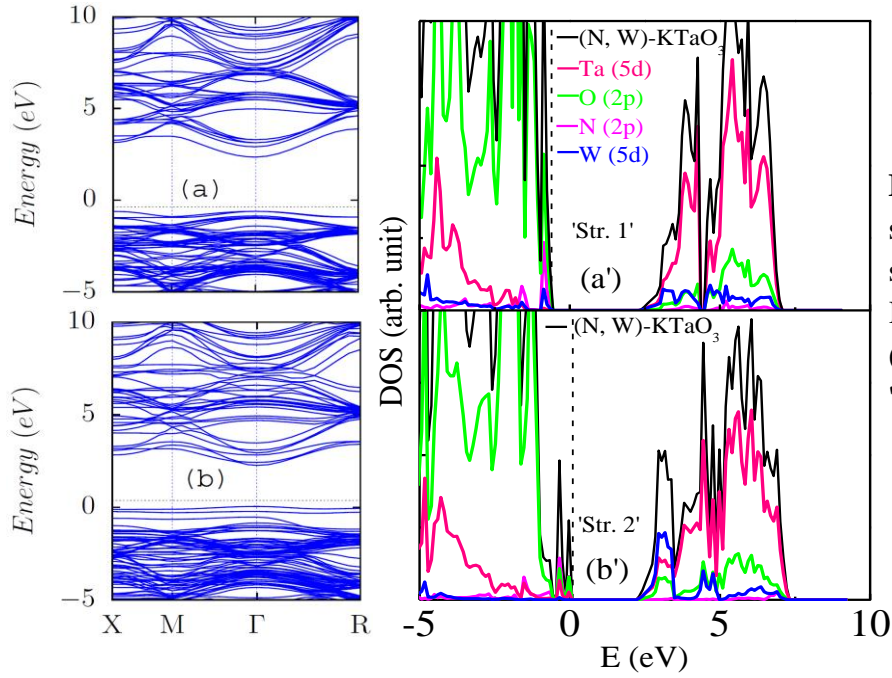
Figure 5.2.3: Band structure and density of states of (N, W)-codoped KTaO$_3$-'Str.1' (a, a´), and (N, W)-codoped KTaO$_3$-'Str.2' (b, b´).

Table 5.2.1: Calculated band gap and band edge shifting (+: upward shifting, − : downward shifting) of (N, Mo)-codoped KTaO$_3$ and (N, W)-codoped KTaO$_3$ at different dopant concentrations.

Dopant Concentration		Configuration	(N, W)-KTaO$_3$			(N, Mo)-KTaO$_3$		
N(%)	W/Mo(%)		Gap (eV)	ΔE_{VBM} (eV)	ΔE_{CBM} (eV)	Gap (eV)	ΔE_{VBM} (eV)	ΔE_{CBM} (eV)
4.17	12.5	'Str. 1'	**2.96**	+0.26	-0.39	**2.70**	+0.06	-0.85
		'Str. 2'	**2.21**	+0.92	-0.48	**1.67**	+0.86	-1.08
2.78	8.33	'Str. 1'	**3.02**	+0.17	-0.42	**2.71**	+0.03	-0.87
		'Str. 2'	**2.22**	+0.98	-0.41	**1.74**	+0.95	-0.92
1.85	5.55	'Str. 1'	**3.14**	+0.19	-0.28	**2.89**	+0.03	-0.69
		'Str. 2'	**2.36**	+0.75	-0.5	**1.85**	+0.74	-1.03

5.2.1.3. Band edge alignment

Based on above discussions one can infer that codoping with (Mo, N) pair is more preferable over (W, N) pair for improving the visible light activity of $KTaO_3$. As we all know that for solar driven photocatalytic water splitting, visible light activity of the material is essential, but not sufficient. The catalyst should have appropriate band edge positions with respect to water redox levels, i.e., CBM should be above the H^+/H_2 level for hydrogen generation, and VBM should be below the O_2/H_2O level to produce oxygen. As for example, $KTaO_3$, which is having the CBM and VBM located at the distance of around 0.7 and 1.68 eV from the respective water redox levels, can split water to generate both hydrogen and oxygen. Since, the CBM is significantly shifted in the downward direction due to codoping with Mo and N, it is questionable whether (N, Mo)-codoped $KTaO_3$ will be applicable for hydrogen generation or not. To check this, we align the band edges for both the codoped systems with two different configurations. As can be seen from Figure 5.2.4, the VBM and CBM positions of the (N, Mo)-codoped $KTaO_3$ in both the configurations are below the respective water redox level. This indicates that (N, Mo)-codoped $KTaO_3$ may not be able to generate hydrogen during splitting of water as it does not meet the thermodynamic criterion for hydrogen release, although it can generate oxygen. On the other hand, for (N, W)-codoped $KTaO_3$ both the band edge positions are such that it should generate both hydrogen and oxygen during water splitting. The important outcome from this section is that, one can now choose the most suitable dopant pair between (N, Mo) and (N, W) to improve the photocatalytic activity of $KTaO_3$ towards solar water splitting.
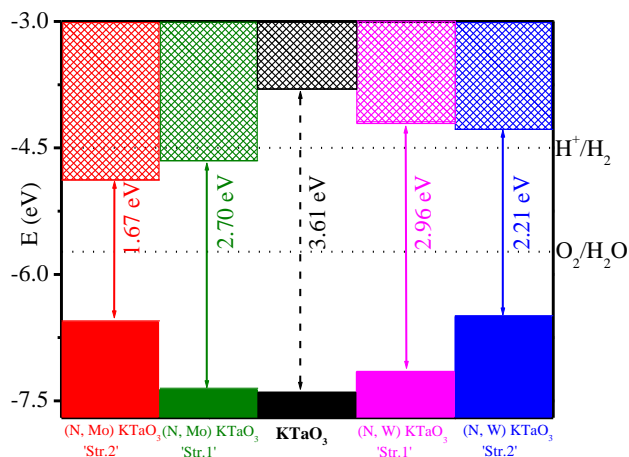
Figure 5.2.4: Band edge alignment for undoped $KTaO_3$, (N, Mo)-codoped $KTaO_3$ and (N, W)-codoped $KTaO_3$ with respect to water redox levels.

5.2.2. Conclusion

We systematically investigate the effect of different cation-anion pair (N, Mo/W) to improve the visible light photocatalytic activity of $KTaO_3$ using hybrid density functional theory as a tool. The advantage of the (N, Mo) and (N, W) dopant pair is that they can reduce the band gap significantly without encountering localized impurity states. Here we want to point out that localized defect state could be also intrinsic and their concentration also depend on the synthetic procedure. This matter should be kept in mind while synthesizing modified material with reduced band gap. Hence, one should choose appropriate synthetic strategy along with suitable dopant elements to achieve an efficient material. Moreover, both the pairs form charge compensated systems, thus reducing the possibility of formation of undesirable vacancy defects, which are known to be efficient source for charge carrier trapping. Besides, the presence of cationic dopant facilitates the introduction of N in the crystal structure of $KTaO_3$, by reducing the formation energy significantly. Although codoping with N and Mo leads to narrowing of band gap by larger extent, it may be important only for other visible light driven photocatalytic processes, and not for hydrogen generation through water splitting. On the other hand, for (N,

W)-codoped $KTaO_3$ the band edges are in suitable positions to satisfy the thermodynamic condition for overall water splitting. Hence, in the present scenario codoping with N and W is more suitable than (N, Mo) pair. Since the band gap narrowing is found to be more prominent in case of 'Str.2' for (N, W)-codoped $KTaO_3$, suitable synthetic strategy should be followed to produce the desired configuration as the major fraction. Thus, the present theoretical study provides valuable information regarding the choice of strategy to improve the photocatalytic activity of $KTaO_3$ towards solar water splitting.

5.3. Improving Photocatalytic Activity of $KNbO_3$ under Visible Light

5.3.1. Introduction

Increasing photocatalytic applications of $KNbO_3$ in different fields motivated us to find efficient strategy to reduce its band gap, so that it can utilize solar spectrum. Recently, $KNbO_3$ has been studied by several groups due to its potential applications in various photocatalytic processes, including hydrogen generation though water splitting, degradation of organic pollutants, CO_2 conversion, etc. $KNbO_3$ exists mainly in three different crystalline phases, viz. cubic, orthorhombic, and tetragonal.[227, 228] The photocatalytic property has been shown to be strongly dependent on the crystal structure. In a recent experimental study by Zhang et al, it has been shown that the cubic form shows highest photocatalytic activity due to highest symmetry in the bulk structure and associated favourable electronic structure.[227] The major drawback for all the forms is their poor photoactivity under visible light exposer due to large band gap (3.24, 3.15, and 3.08 eV, respectively). So far, various strategies have been adopted for improving the photocatalytic activity of $KNbO_3$. As for example, Ding et al synthesized $KNbO_3$ nanowire using hydrothermal method and obtained enhanced photocatalytic activity for water splitting.[229] They have indicated that increased surface area, good crystallinity, and fineness of $KNbO_3$ nanowire are responsible for improved quantum efficiency of water splitting activity. Recently, Zhang et al investigated the structure-photoactivity relationship in $KNbO_3$ nanowire using scanning transmission electron spectroscopy combined with first principles calculations.[230] They concluded that the difference in the reducing behavior due to variation in the conduction band minimum (CBM) potential and the extent of electron-hole separation results into different

photoactivity for the various $KNbO_3$ polymorphs. In a recent study, different $KNbO_3$ nanostructures have been synthesized, including nanowires, nanotowers, nanocubes and nanorods by controlling reactant concentration, temperature, and reaction time.[231] Among the polymorphs, nanocube shows highest photoactivity due to high crystallinity and active surface facet. One dimensional $KNbO_3$ nanowire with Au nanoparticle anchoring onto it has been found to show better photocatalytic response than the commercial variety.[232] The crucial role of surface plasmon resonance and interband transition on gold nanoparticles is responsible for the improved photocatalytic activity. Yan et al utilized similar phenomena by synthesizing $KNbO_3$ microcube deposited with gold nanoparticles, which shows enhanced photocatalytic activity under visible light.[233] An enhancement of the optical property of $KNbO_3$ has been observed by Wang et al due to doping with Na, which reduces the band gap to 3.09 eV.[234] The perturbation of the energy levels associated with lattice distortion and mass effect due to introduction of Na at the K lattice site has been found to be responsible for the change in band gap. Interestingly, the optical property of Na-K mixed niobates has been found to be strongly dependent on the different polymerization agent involved during synthesis.[235] Several attempts by doping with various lanthanide and actinide elements have been made to change the optical property of $KNbO_3$.[236,237] Guo et al observed an enhancement of photocatalytic activity of $KNbO_3$ under visible light towards hydrogen evolution by using $Er^{+3}:Y_3Al_5O_{12}$, which is an upconversion luminescence agent.[238] In a recent study, Wang et al demonstrated hydrogen production under visible light using heterojunction consisting of self (Nb^{+4})-doped $KNbO_3$ and Nb_4N_5.[239] In this case, the heterojunction facilitates separation of photogenerated electron and hole and the Nb_4N_5 unit acts as cocatalyst, leading to improved photocatalytic response. A significant improvement of visible light activity of $KNbO_3$ has been observed in the study of Wang et al by doping with N.[240] It is

well known that N doping into oxide based semiconducting materials has several disadvantages, leading to faster recombination rate. To overcome this, a number of strategies have been developed either by codoping with anionic or cationic dopant elements. In this study, we investigate the effect of introducing a cationic dopant on the electronic structure of N-doped $KNbO_3$. To select suitable codopant we have considered the criteria; (i) the element should form charge compensated system, so that vacancy defect formation can be minimum, (ii) the ionic size of the dopant element should be such that it can easily be fitted into the host lattice site, (iii) the dopant element should not lower the CBM by a significant extent to keep $KNbO_3$ active for hydrogen evolution. Based on these criteria we choose W as a potential codopant for the N-doped $KNbO_3$. The presence of W at the Nb lattice site is not expected to cause downward shift of the CBM by a large extent, because W 5d-orbital is energetically higher than the Nb 4d orbital. To obtain a detailed description of the band structure of $KNbO_3$ in presence of both N and W, we perform calculation using Heyd, Scuseria, and Ernzerhof (HSE) hybrid functional, which has been found to successfully overcome the limitations of standard density functional theory (DFT) for wide range of semiconductor materials. We also address the effect of individual dopant elements on the electronic structure of $KNbO_3$.

5.3.2. Results and Discussion

5.3.2.1. Geometry

$KNbO_3$ exists in different crystal structures, cubic, orthorhombic, and tetragonal. Recent studies have shown that the photocatalytic activity of the cubic form is much higher than that of the other two due to high symmetry in the crystal structure and favorable electronic structure. Therefore in this study, all the calculations have been carried out using cubic $KNbO_3$. As shown

in Figure 5.3.1, the cationic atoms K and Nb are distributed on a simple cubic lattice and the anionic atom O occupies the face centers nearest to Nb. Thus, Nb locates itself at the centre of each oxygen octahedra while K remains at the twelve fold coordinated sites. The lattice parameter for the $2 \times 2 \times 2$ cell is found to be 8.125 Å at the GGA_PBE level of calculation. The Nb-O bond length is 2.03 Å and Nb-O-Nb bond angle exactly equals to 180°. Doping with N results into small change in the parent crystal structure due to the closeness of its ionic size with that of oxygen ($R_{O^{-2}} = 1.35$ Å, $R_{N^{-3}} = 1.46$ Å). However, the introduction of W at the Nb lattice site increases the cell length by 0.29 Å along the c-direction. The W-O bond length is found to be relatively shorter (1.81 Å) than the Nb-O distance in the ideal crystal structure. This increases the adjacent Nb-O distance by 0.46 Å. The bond angles (W-O-Nb and Nb-O-Nb) perpendicularly cutting the c-axis are bent to around 170°, although the angle parallel to the c-axis remains as it is (180°). The cell volume increases by 9 Å^3. In the case of codoping, both N and W are simultaneously introduced into the crystal structure of KNbO$_3$. To consider different configurations for the codoped systems we choose different lattice sites for the dopant pair. In this case, one can generate two different configurations, which are structurally inequivalent to each other. The dopant elements may occupy nearest lattice site (Nb1, O1) or far away from each other (Nb1, O2) in Figure 5.3.1, resulting into the formation of different configurations, 'Str. 1' and 'Str. 2', respectively. In this case, 'Str. 1' is found to be energetically more stable by 0.59 eV than the 'Str. 2'. Depending on the synthetic strategy, the configuration of codoped system may be different. For example, a synthetic route like solution method preferably produces energetically more stable structure, while techniques like magnetron sputtering or supersonic cluster beam deposition, generate structures which may not be the lowest energy configurations. Therefore, in the present study both type of configurations have been considered. In the

optimized geometries, the calculated value of the distance between the two dopant elements is found to be 1.75 and 4.45 Å, in the two structures respectively. The cell volume for both configurations is found to be almost equal. In case of 'Str. 1' the cell length increases by 0.5 Å in the c-direction, while the same is observed along b-direction for 'Str. 2'. The M-O-M' (M= Nb, M'= Nb, or W) bond angle perpendicular to the c-axis is bent to 165° for 'Str. 1', while in 'Str. 2' it occurs for the same bond angle parallel to the c-axis. In the following section we will see how this variation of dopant-dopant separation influences the electronic structure of (N, W)-codoped $KNbO_3$. But before that we will discuss the feasibility of formation of the codoped systems by considering their stability with respect to the individual doping process.
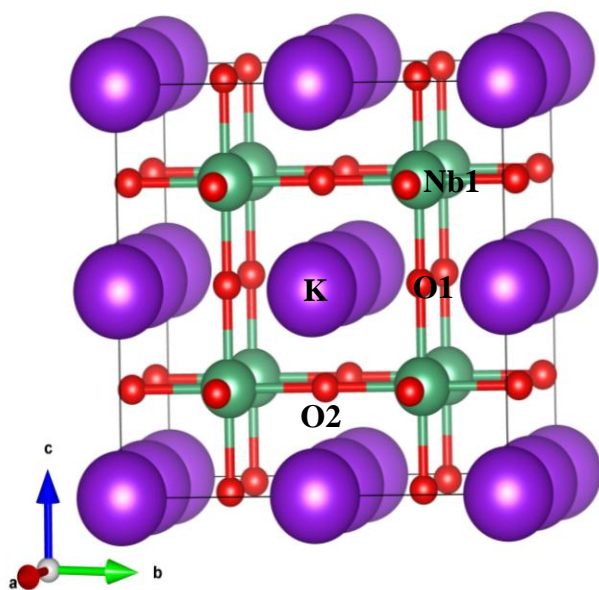
Figure 5.3.1: A $2 \times 2 \times 2$ supercell of KNbO3 cubic crystal structure. Number indicates position of the dopant element.

5.3.2.2. Electronic Structure

In this section we discuss the role of dopant element is modifying the band structure of $KNbO_3$.

For this purpose, we first perform several test calculations with undoped $KNbO_3$ by varying the

computational parameter under HSE formalism. The PBE0 hybrid functional has also been taken

into account. As can be seen from Table 5.3.1, the calculated band gap with screening parameter

of 0.2 $Å^{-1}$ and 36% of mixing of exact HF exchange shows the best match (3.23 eV) with the

experimentally reported band gap of $KNbO_3$ (3.24 eV). Therefore, throughout the calculations

we employ this computational parameter for investigating the electronic structure of the doped

and codoped systems. Figure 5.3.2 shows the band structure plot for the undoped $KNbO_3$ along

the high symmetry K-path. Analysis of PDOS indicates that the valence band (VB) is composed

of O 2p state, while conduction band (CB) is contributed by Nb 4d state. This is similar to the

characteristics of typical metal oxide based materials. Absence of K related states in the band

edge is the consequence of ionic type bonding between K and NbO_6 unit. Now we discuss how

this band structure is influenced in presence of the dopant element. We start this discussion by

describing the electronic structure first in presence of a single dopant element, followed by the

presence of both the dopant elements.
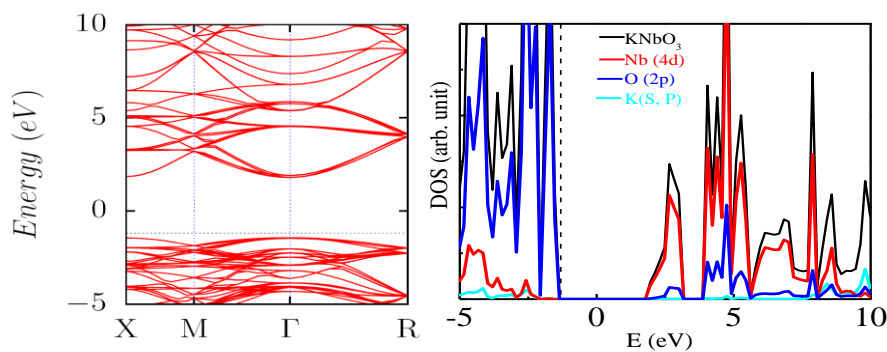
Figure 5.3.2: Band structure and density of states of undoped $KNbO_3$.

5.3.2.2.1. N-doped KNbO$_3$

Doping with N at the oxygen lattice site results into significant changes in the electronic structure of KNbO$_3$. The band structure plot (Figure 5.3.3a) shows the presence of new states at both band edges. Therefore, the effective band gap reduces to 1.91 eV, which can lead to significant enhancement of visible light activity. It is interesting to observe that the new states appear adjacent to the band edges, instead of as discrete states in the forbidden region, that occur for most of N-doped metal oxide materials. The DOS plot (Figure 5.3.3a') is no longer symmetric with respect to spin up and spin down parts. The impurity states near the VB are partially occupied. This is due to one electron deficiency, created by N doping, which contains one less electron in the valence shell ($2s^2 2p^3$) than that of oxygen ($2s^2 2p^4$), leading to paramagnetism (magnetic moment $1\mu_B$/supercell). To obtain detailed description of the impurity states we analyse the PDOS. As can be seen from Figure 5.3.3a', the N 2p and O 2p hybridized states contribute to the VBM of N-doped KNbO$_3$, while the states at the CB edge are composed of O 2p, N 2p and Nb 4d states. One of the main factors behind the change is the higher energy of N 2p orbital with respect to the O 2p orbital, and electron deficiency. The difference in electronegativity between nitrogen and oxygen may also influence the bonding with Nb. It is well known that doping of N into metal oxide semiconductor improves the visible light activity by a significant extent. However, the reported photoconversion efficiency has been found to be far below the expected level. In this case the partial occupancy of the states may be harmful for longer lifetime of the photogenerated charge carriers. Another major issue is the spontaneous formation of charge compensating vacancy defects, which can accelerate the electron-hole recombination. Besides, the impurity states at the CB lower the CBM by a significant extent (0.56 eV), which may in turn lower the reducing behavior (hydrogen evolution reaction during

water splitting). Therefore, to improve the photocatalytic activity of N-doped $KNbO_3$ one needs to introduce another dopant element which can compensate the electron deficiency and form charge compensated system. For this purpose, we choose W as a codopant of N-doped $KNbO_3$. In this next section, description of electronic structure of $KNbO_3$ only in presence of W has been presented.
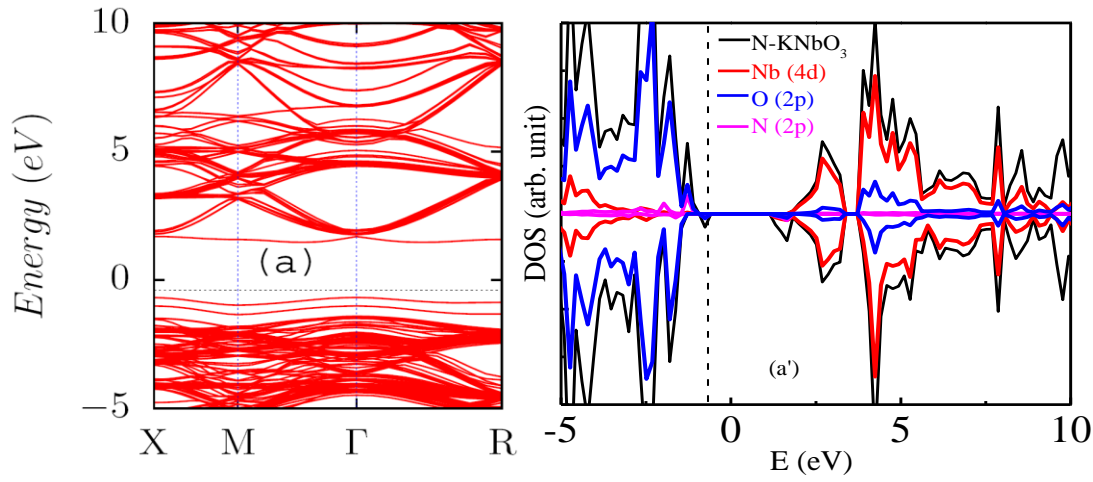
Figure 5.3.3: Band structure (a) and density of states (a') of N-doped $KNbO_3$ (N: 4.17%). The horizontal line in (a), and vertical line in (a') indicates the Fermi level.

5.3.2.2.2. W-Doped KNbO₃

Doping of W at the Nb lattice site results into an n-type semiconductor. The band structure plot (Figure 5.3.4a) shows the presence of Fermi level in the CB region. Calculation of magnetic moment indicates that the total magnetic moment for W-doped $KNbO_3$ is 0.8 μ_B/supercell. The excess electron environment is created due to the presence of one more electron in the valence shell of W than that of Nb. This leads to occupied impurity states adjacent to the bottom of the CB, and consequently the CBM is lower by 0.86 eV with respect to that of undoped $KNbO_3$,

leading to reduction in band gap to 2.21 eV. Hence, significant enhancement of visible light activity is expected in this case also. However, lowering of CBM by such a large extent and the associated charge compensating defects are the main limiting factors for W-doped $KNbO_3$. Because of unpaired electron, the DOS plot (Figure 5.3.4a') is unsymmetrical with respect to spin up and spin down part. To obtain information about the contributory states at the band edge we analyse the PDOS. As can be seen from Figure 5.3.4a', the VBM is composed of O 2p states, while the partially occupied impurity states near the CB are the hybridized states of Nb 4d and W 5d states. Therefore, codoping of W into the crystal structure of N-doped $KNbO_3$ is expected to compensate for the electron deficiency. In the next section the role of both N and W on the electronic structure of $KNbO_3$ is explored.
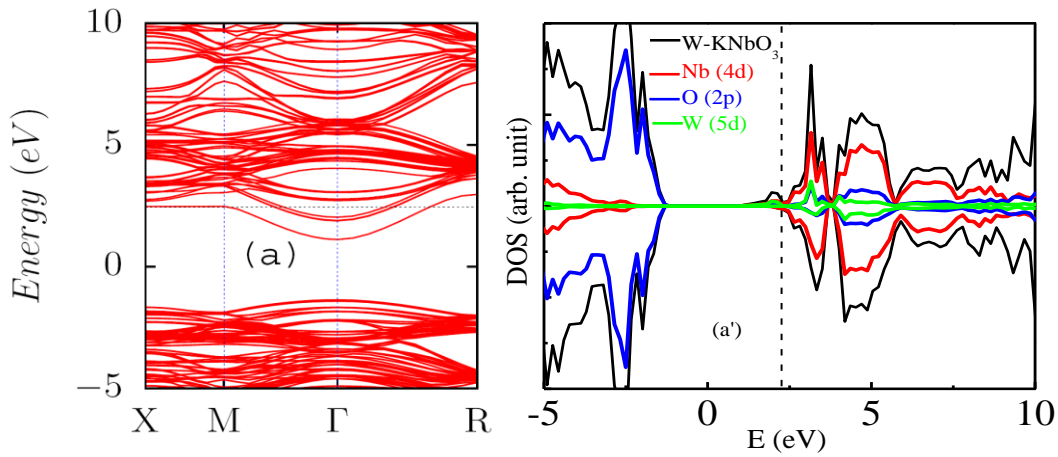
Figure 5.3.4: Band structure (a) and density of states (a') of W-doped $KNbO_3$ (W: 12.5%). The horizontal line in (a), and vertical line in (a') indicates the Fermi level.

5.3.2.2.3. (N, W)-Codoped $KNbO_3$

Here, we consider two different possible configurations for the (N, W)-codoped $KNbO_3$, which differ in the length of dopant-dopant separation. The probability of formation of a particular type

of product in major fraction is strongly dependent on the choice of synthetic strategy. In presence of both N and W, the total electrical charge of the undoped system is maintained. Figure 5.3.5 shows that a clean band structure is produced for (N, W)-codoped $KNbO_3$, where the Fermi level is located on the top of the VB, similar to the case of an intrinsic semiconductor. A considerable reduction in the band gap is observed in case of 'Str. 2' (0.47 eV), while for 'Str. 1' the reduction is rather small (0.1 eV). Analysis of electronic energy levels indicates that the band gap varies due to the difference in relative shift of the VBM and CBM. For 'Str. 1' the VBM is found to be elevated only by a small extent (0.07 eV), while the CBM remains almost unchanged with respect to that of undoped $KNbO_3$. However, in case of 'Str. 2' both the VBM and CBM are elevated by 0.52, and 0.05 eV, respectively. The important observation is that in both the cases the band gap is controlled by the upward shifting of the VBM only, leaving the CBM almost unchanged. Therefore, the present strategy of narrowing the band gap does not sacrifice the reducing behaviour of $KNbO_3$ at the CB. This is very much important for narrowing the band gap of hydrogen evolving photocatalyst. In both the cases, the DOS plot (Figure 5.3.5a' and 5.3.5b') is symmetrical with respect to spin up and spin down parts. To investigate the electronic structure for both the configurations in details we analyze the PDOS. As can be seen from Figure 5.3.5, the nature of VBM and CBM are similar in both the cases. The VBM is composed of hybridized N 2p and O 2p states, while the CBM is contributed by mixed state of Nb 4d and W 5d states. To investigate the change in electronic charge distribution in presence of dopant element we analyse the charge density plot (Figure 5.2.6). As can be seen from Figure 5.3.6a, the charge distribution is almost symmetric in case of undoped $KNbO_3$. In presence of W (Figure 5.3.6b) the symmetric nature is lost, indicating less covalent character between W and O bond. Comparison of charge density plot for the 'Str. 1' and 'Str. 2' (Figure 5.3.6c and d) indicates that

in the latter case N is more covalently bonded to Nb than the first case. This may have important influence on the difference in electronic energy levels of the two different configurations for the codoped systems. Therefore, based on this present investigation, we can conclude that the improvement of visible light activity of $KNbO_3$ by codoping with N and W can only be achieved by choosing appropriate synthetic strategy, like magnetron sputtering or supersonic cluster beam deposition, which is expected to deliver materials of the type 'Str. 2' as a major product.
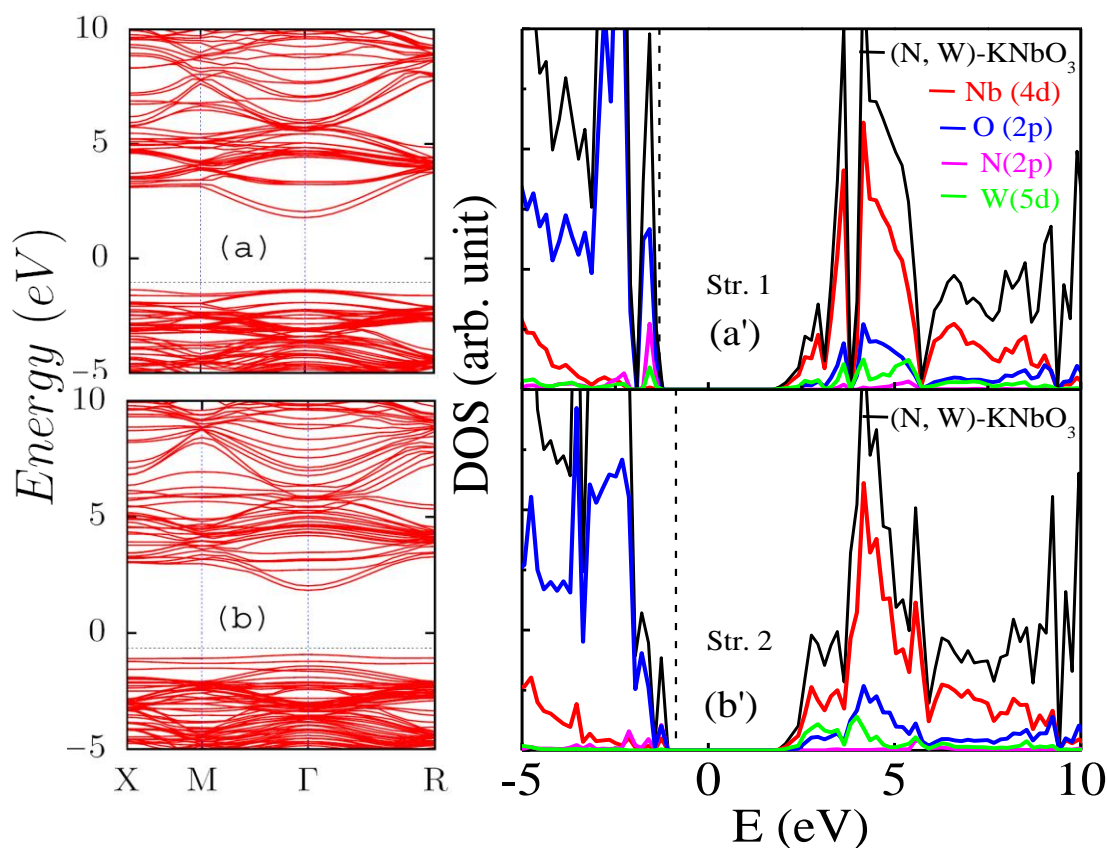
Figure 5.3.5: Band structure and density of states of (N, W)-codoped $KNbO_3$ (N: 4.17%, W: 12.5%) using Str. 1 (a, a') and Str. 2 (b, b'). The horizontal line in the band structure plot and vertical line in the density of states plot indicates the Fermi level.
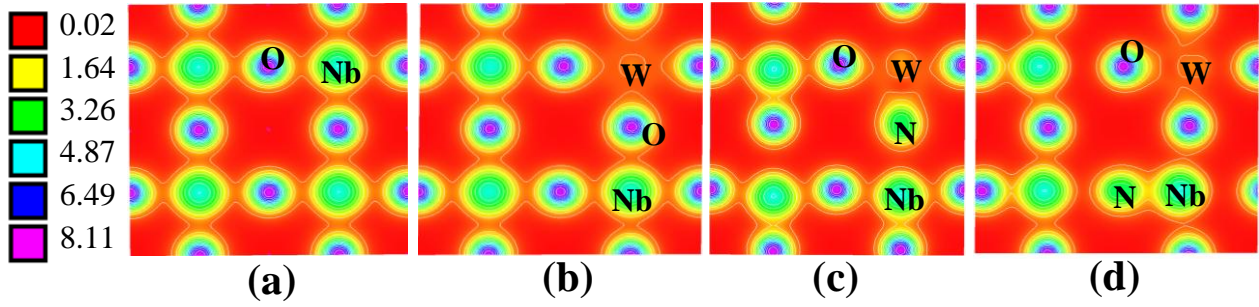
Figure 5.3.6: Charge density distribution for undoped $KNbO_3$ (a), W-doped $KNbO_3$ (W: 12.5%) (b), (N, W)-codoped $KNbO_3$ (N: 4.17%, W: 12.5%) with Str. 1 (c) and Str. 2 (d).

5.3.2.4. Optical Property

In order to observe the change in optical spectrum of $KNbO_3$ due to (N, W) codoping, frequency dependent dielectric function calculation has been carried out by employing HSE hybrid functional. The dielectric function can be expressed in combination of real, $\varepsilon_1(\omega)$ and imaginary, $\varepsilon_2(\omega)$ parts as $\varepsilon(\omega) = \varepsilon_1(\omega) + i\,\varepsilon_2(\omega)$. Here, $\varepsilon_2(\omega)$ is calculated by a summation over sufficiently large number of unoccupied states, and then $\varepsilon_1(\omega)$ from Kramer-Kronig relation, as implemented in VASP 5.2 version. The absorption coefficient, $\alpha(\omega)$, can be calculated using these two parts of the dielectric function as,

$$\alpha(\omega) = \sqrt{2}\omega\left(\sqrt{\varepsilon_1(\omega)^2 + \varepsilon_2(\omega)^2} - \varepsilon_1(\omega) \right)^{\frac{1}{2}}$$

(5.2.5)

Figure 5.3.7 shows the calculated absorption coefficient as a function of wavelength of light. The absorption curve corresponding to undoped $KNbO_3$ is found to be limited to the UV region. This is consistent with the calculation of electronic band gap for $KNbO_3$ (3.24 eV). On codoping the

absorption spectrum is found to be shifted towards the visible region. This indicates that the (N, W)-codoped $KNbO_3$ should have better visible light activity than the undoped $KNbO_3$.
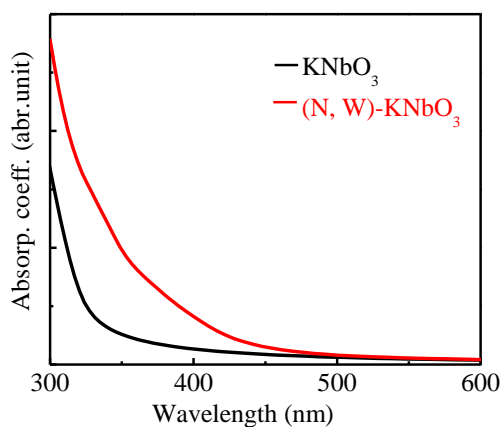
Figure 5.3.7: Optical spectrum for undoped $KNbO_3$ and (N, W)-codoped $KNbO_3$ (N: 4.17%, W: 12.5%).
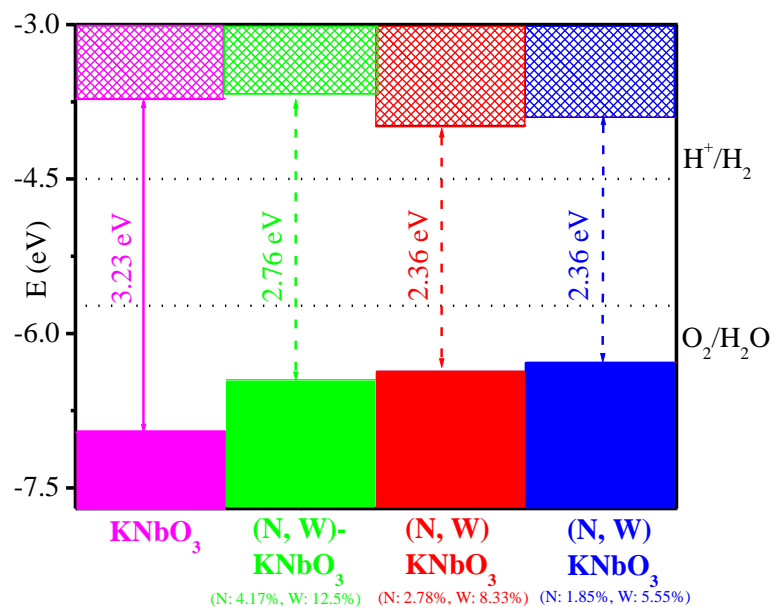
Figure 5.3.8: Band edge alignment of undoped $KNbO_3$ and (N, W)-codoped $KNbO_3$ with different dopant concentration (N: 4.17%, W: 12.5%), (N: 2.78%, W: 8.33%), and (N: 1.85%, W: 5.55%) with respect to water redox levels.

5.3.2.5. Band Edge Alignment

Up to now, we have discussed how the band gap can be reduced to utilize the solar spectrum. But this band gap narrowing may sometimes deactivate the oxidising or reducing behaviour of the parent material. In order to check whether these modified materials are suitable for overall water splitting or not, we align their band edge positions with respect to water redox levels. To be suitable for hydrogen production from water, the CBM of the material must be located above the H^+/H_2 level, while for oxygen generation, its VBM must be located below the H_2O/O_2 level. As for example, for $KNbO_3$ the CBM and VBM are located at around 0.78 eV above and 1.23 eV below from the respective water redox levels. Therefore, $KNbO_3$ is active for overall water splitting, which is evident in several experimental studies. Since the VBM and CBM obtained in DFT calculation are not in absolute scale, one cannot directly align their band edges with respect to water redox levels. For this purpose, we first fixed the location of VBM and CBM for the undoped $KNbO_3$ based on the experimental data. Then we align the band edges of the modified materials by calculating the relative shift of the VBM and CBM with respect to that of undoped $KNbO_3$. Among the different configurations for (N, W)-codoped system, we are interested in only those structures ('Str. 2' in each case) which have lower band gap than the undoped $KNbO_3$. Figure 5.2.9 shows that the CBM and VBM positions of the (N, W)-codoped $KNbO_3$, with different dopant concentration (W: 12.5, 8.33, and 5.55 %). The CBM is found to be 0.83, 0.52, and 0.6 eV above the H^+/H_2 level for the (N, W)-codoped $KNbO_3$ with W-concentration correspond to 12.5, 8.33, and 5.55 %, respectively. On the other hand, the VBM for the respective case lies 0.72, 0.64, and 0.55 eV below the H_2O/O_2 level. This indicates that the band edges are in favourable positions to release both hydrogen and oxygen. Therefore, the (N, W)-codoped $KNbO_3$ is suitable for overall water splitting over a wide range of concentration.

5.3.3. Conclusions

In this theoretical investigation our aim has been to predict an efficient strategy to improve the visible light photocatalytic activity of $KNbO_3$. The present study reveals that the calculated band gap with screening parameter of 0.2 Å^{-1} and 36% of mixing of exact HF exchange shows the best match (3.23 eV) with the experimentally reported band gap of $KNbO_3$ (3.24 eV). Here, we choose (N, W) dopant pair to reduce the band gap of $KNbO_3$. Although, both the elements individually are able to lower the band gap of $KNbO_3$ by a significant extent, the formation of associated vacancy defects due to charge mismatch may accelerate electron-hole recombination. Another factor is the downward shifting of the CBM by a large extent which is not desirable because of the possibility in lowering hydrogen evolution rate. However, these disadvantages are overcome in the case of codoped system, due to the formation of charge compensated system and mainly valence band controlled band gap narrowing. This is the unique characteristics of the (N, W) pair in this case. Moreover, the doping of N is found to be more favoured in presence of W. The calculation of formation energy for codoping under different synthetic conditions provides useful information for practical situations. In addition, the present study has also indicated a strong dependence of the synthetic approach to achieve efficient band gap narrowing with (N, W) pair. Interestingly, the band gap reduction becomes more prominent when the dopant-dopant separation is increased. This leads to the achievement of a considerable band gap reduction even at low concentration. The choice of (N, W) pair is again justified by its ability to narrow the band gap in a controlled way, so that the codoped material can satisfy the thermodynamic criterion for overall water splitting.

5.4. Improving Visible Light Photocatalytic Activity of NaNbO$_3$

Depleting source of fossil fuels and their adverse environmental impact drive global interest to find efficient material for hydrogen generation through solar water splitting. Although, NaNbO3 has several key features to play as an efficient photocatalyst, its large band gap restricts its photoactivity only in the UV-region of solar spectrum. In this theoretical study, we investigate the effect of doping on the electronic structure of NaNbO$_3$ aiming at improving its visible light photocatalytic activity. For this purpose, we employ hybrid density functional theory (DFT), which successfully reproduces the experimental band gap of NaNbO$_3$. Doping with N has been found to reduce the effective band gap significantly by introducing localized acceptor states which however are known to promote electron hole recombination rate. To overcome this, we propose codoping with W at the Nb lattice site. Interestingly this completely passivates those localized acceptor states. The band gap is found to be sufficiently reduced to enhance the visible light activity. The present strategy reduces the band gap in such a controlled way that (W, N)-NaNbO$_3$ satisfies the thermodynamic criteria to execute the overall decomposition of H$_2$O, indicated in the relative position of its band edges with respect to water redox levels. Moreover, doping of N is found to be facilitated in presence of W due to reduction in formation energy. Additionally, spontaneous formation of charge compensated valence defect is expected to be reduced in presence of (W, N) pair in comparison to individual dopant elements due to maintaining the total electrical charge neutrality.

5.4.1. Results and Discussion

NaNbO$_3$ exists in different crystal structures at different temperatures. At room temperature, the most stable form is the orthorhombic structure. But the cubic form ($Pm\bar{3}m$, space group no. 221)

is reported to show best photocatalytic activity among the different forms of $NaNbO_3$. So, in the present study all the calculations have been carried out using the cubic crystal structure only. As can be seen from Figure 5.4.1, the structural framework is based on corner sharing NbO_6 octahedral units. As can be seen from Table 5.4.1, the calculated band gap (3.27 eV) with screening parameter 0.2 $Å^{-1}$ and 34 % of exact HF mixing reproduces the experimental band gap (3.27 eV) successfully. So, all the calculations are carried out using this computational parameter. The band structure plot has been shown in Figure 5.4.2. To analyze the nature of state at the band edge we calculate PDOS for $NaNbO_3$ (Figure 5.4.2). As can be seen from Figure 5.4.2, the VBM is composed of O 2p states and CBM is dominated by Nb 4d state. The contribution of Na related state to the band edge is negligible. This is due to ionic type bonding between Na and NbO_6 unit. We now proceed to the discussion of the effect dopant elements on the geometry and electronic structure of $NaNbO_3$. For a better understanding, we will first present the scenario in presence of individual dopant elements.
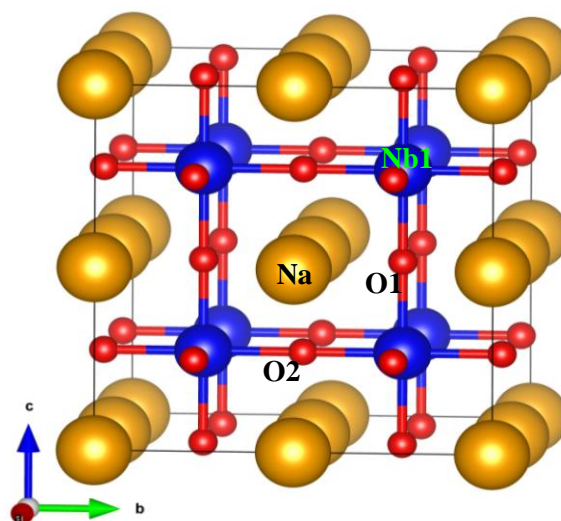
Figure 5.4.1: $2 \times 2 \times 2$ supercell of cubic crystal structure of $NaNbO_3$. The numbers indicate position of the dopant element.

Table 5.4.1: Variation of Band gap of undoped $NaNbO_3$ with different computational parameters.

Mixing HF exchange (%)	Screen Parameter ($\mathring{A}^{-1}$)	Band gap (eV)
25	0.2	2.77
30	0.2	3.05
32	0.2	3.16
34	0.2	3.27
35	0.2	3.33
Experimental		3.29
		3.27
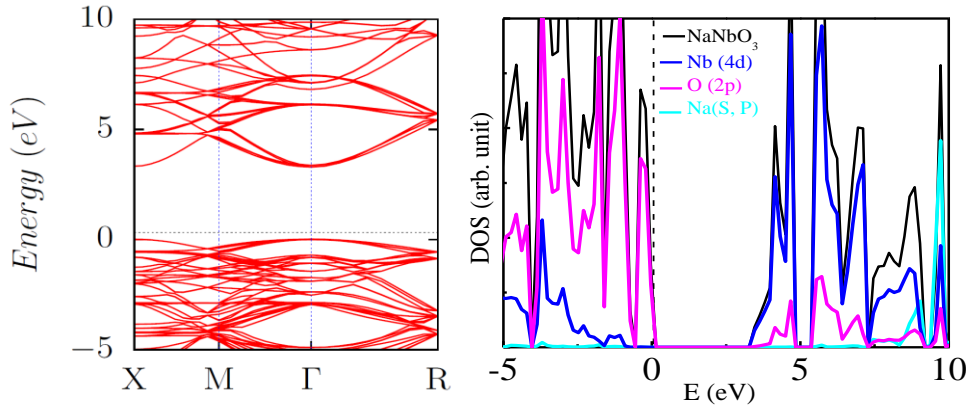
Figure 5.4.2: Band structure and density of states of $NaNbO_3$.

5.4.1.1. N-Doped $NaNbO_3$

The band structure plot for N-doped $NaNbO_3$ is shown in Figure 5.4.3a, indicates that N doping leads to introduction of occupied and unoccupied impurity states in between the VB and CB. The impurity states split the gap region in three parts (0.86 eV, 1.19 eV, and 0.84 eV), leaving the VBM and CBM almost unchanged. To investigate the nature of impurity states in details we analyze DOS and PDOS for N-doped $NaNbO_3$ (Figure 5.4.3a'). Both the impurity states are

composed of hybridized states of O 2p and N 2p orbital. The DOS plot is unsymmetrical with respect to spin up and spin down parts due to partially occupied states. This arises because of presence of unpaired electron in the N-doped $NaNbO_3$, which is also evident in the calculated magnetic moment ($1\mu_B$/supercell). The acceptor states originate due to lesser number of electrons in the valence shell of N ($2s^2 2p^3$) in comparison to O ($2s^2 2p^4$). Although, limitation of visible light activity is greatly overcome by N doping, it fails to deliver photoconversion efficiency at the expected level. This is mainly due to strongly localized nature of the impurity states, which promote electron-hole recombination rate. To overcome this we suggest codoping with W at the Nb lattice site, which can compensate for the electron deficiency by providing one extra electron. Let us now see the effect of W doping on the electronic structure of $NaNbO_3$.
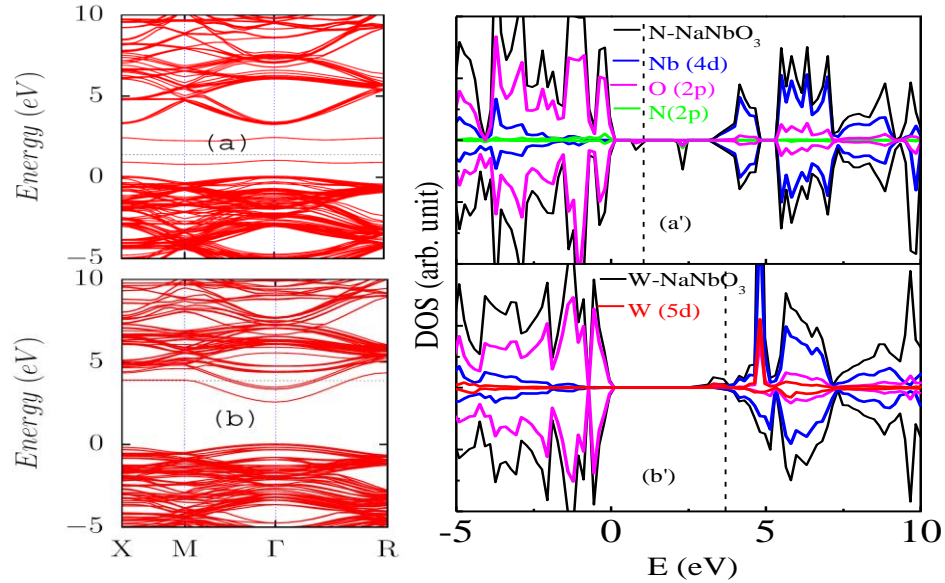
Figure 5.4.3: Band structure and density of states of N-doped $NaNbO_3$ (a, a'), and W-doped $NaNbO_3$ (b, b').

5.4.1.2. W-Doped NaNbO$_3$

In the case of W doping, one of the Nb atoms in the $2 \times 2 \times 2$ supercell is replaced by W (which corresponds to dopant concentration of 12.5 %). The geometry is found to be changed by a small extent after full relaxation. The cell dimension is reduced slightly (0.105 Å) in two directions (along a and b), but is increased by 0.22 Å along 'c'-direction. The Nb-O-W angle reduced to 168°. The average W-O bond distance is 1.872 Å, which is slightly smaller than Nb-O length (2.004 Å) in undoped NaNbO$_3$. The band structure and DOS plot for W-doped NaNbO$_3$ has been shown in Figure 5.4.3 b and 5.4.3b', respectively. In contrast to the case of N doped system, occupied impurity states are introduced here close to the bottom of the CB. The Fermi level is in the CB region, indicating n-type behavior for W-doped NaNbO$_3$. This is due to one extra electron in the valence shell of W in comparison to that of Nb. Interestingly, the calculated band gap (2.27 eV) for W-doped NaNbO$_3$ is almost equal to that of N-doped NaNbO$_3$. The DOS plot (Figure 5.4.3b') is unsymmetrical with respect to spin up and spin down parts due to presence of unpaired electron, which contributes to the calculated magnetic moment of 0.87 µ$_B$/supercell. Analysis of PDOS indicates that the VBM is contributed by O 2p states, and the occupied impurity states at the bottom of CB are composed of hybridized states of W 5d and Nb 4d orbitals. This is due to closeness of the energy of Nb 4d orbital with W 5d orbital. This is also supported by the contribution of Nb 4d orbital (47%) and W 5d orbital (53 %) to the total magnetic moment. This discussion on the effect of W on the electronic structure of NaNbO$_3$ indicates that codoping of W should compensate for the electron deficiency in N-doped NaNbO$_3$. In the following section we discuss the combined effect of both N and W.

5.4.1.3. (W, N)-Codoped NaNbO$_3$

To model the codoped system both N and W are introduced simultaneously at the O and W lattice sites, respectively. With the advent of technology various synthetic strategies have been developed, which may deliver product with different configurations. For example, synthetic route involving solution method is known to generate product with lowest energy configuration due to equilibrium condition, while processes like magnetron sputtering or supersonic cluster beam deposition, may deliver product with other configuration as major fraction. Hence, for (W, N)-codoped NaNbO$_3$ two different configurations have been considered by varying the relative position of N and W. We designate these two configurations as Str.1 and Str. 2, where N and W occupy the nearest neighboring lattice sites (Nb1, O1) and next to nearest neighboring lattice sites (Nb1, O2), respectively. Since, Str.1 is energetically lower than Str.2, it is likely to be formed as a major product in first type of synthetic strategy, while the second type of approach may produce Str.2 predominantly. The structural change due to codoping in both the cases is very much similar to that of doping with only W. The calculated distances between W and N are 1.753 Å and 4.401 Å in Str.1 and Str. 2, respectively. The band structure plot for (W, N)-codoped NaNbO$_3$ with two different configurations (Figure 5.4.4a and 5.4.4b) are nearly same, indicating complete passivation of localized impurity states. This is due to counter balancing effect of both the dopant elements. As we have seen in the previous discussion, N doping results one electron deficiency in NaNbO$_3$, while doping with W leads to one excess electron. So, presence of both the dopant elements maintains the total electrical charge neutrality. Thus, in the case of (W, N)-codoped NaNbO$_3$, it is expected to get photoconversion efficiency at the desired level. The reduction of band gap is quite significant (0.63 eV) for the codoped system with Str.2 configuration, while it is just 0.24 eV for Str.1 configuration. Hence, the codoped system with

Str.2 configuration is more preferable for achieving enhancement of visible light activity by a significant extent. The codoped system no longer contains unpaired electron. This is indicated in the symmetrical nature of DOS plot with respect to spin up and spin down parts, as well as in the calculated zero magnetic moment value. Analysis of PDOS (Figure 5.4.4a' and 5.4.4b') indicates that VBM is contributed by hybridized states of N 2p and O 2p. The mixing of N 2p and O 2p states in this case occurs in such an extent that the impurity states form continuous state with the VB. This is in favor of good charge carrier mobility. The CBM is dominated by Nb 4d state.

The most interesting observation is that the band gap narrowing obtained by using the present strategy is mainly controlled by shifting of VBM only (Table 5.4.2). This feature is very much desirable while modifying the band gap of hydrogen evolving photocatalyst, particularly for material like $NaNbO_3$, where the CBM position is close to the H^+/H_2 level. This justifies the choice of the codoping pair for enhancing the visible light photocatalytic activity of $NaNbO_3$.
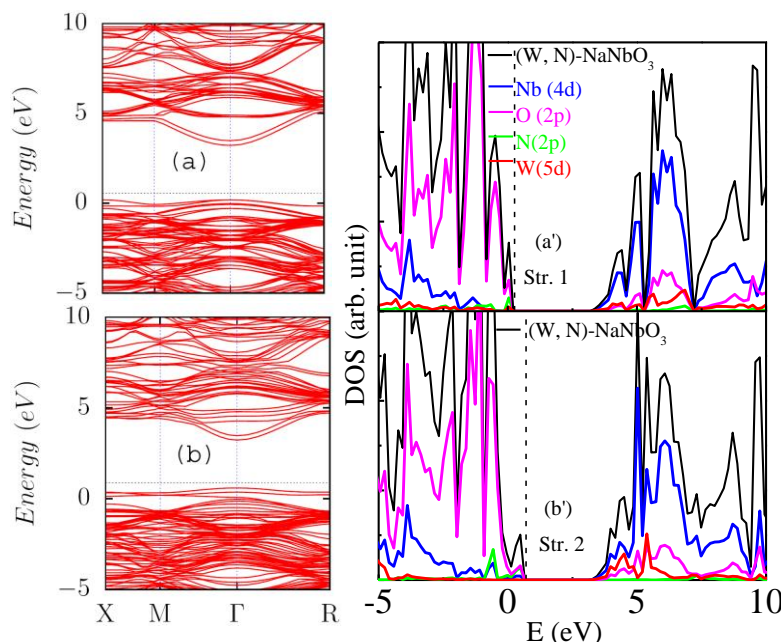
Figure 5.4.4: Band structure and density of states of (W, N)-codoped $NaNbO_3$ with configuration Str. 1 (a, a´), Str. 2 (b, b´).

Table 5.4.2: Calculated band gap and band edge shifting (+: upward shifting, − : downward shifting) of (W, N)-codoped $NaNbO_3$ at different dopant concentrations.

Dopant Concentration		Configuration	(W, N)-NaNbO₃		
N(%)	W (%)		Gap (eV)	ΔE_{VBM} (eV)	ΔE_{CBM} (eV)
4.17	12.5	'Str. 1'	**3.03**	+0.17	-0.08
		'Str. 2'	**2.64**	+0.57	-0.06
2.78	8.33	'Str. 1'	**3.11**	+0.06	-0.11
		'Str. 2'	**2.46**	+0.52	-0.29
1.85	5.55	'Str. 1'	**3.17**	+0.06	-0.05
		'Str. 2'	**2.51**	+0.54	-0.22

5.4.1.4. Band Edge Alignment

A material to be active for overall water splitting must satisfy the thermodynamic criteria, i.e., the CBM should be above the H^+/H_2 level for spontaneous hydrogen evolution and the VBM should be below the H_2O/O_2 level for oxygen evolution. Hence, it is essential to determine the absolute positions of the band edges of the modified catalyst to check its applicability towards water splitting process. Here, we first calculate the absolute position of the CBM (E_{CBM}) of undoped material,

$$E_{CBM} = \left(\chi_{Na} \chi_{Nb} \chi_O^3 \right)^{1/5} - \frac{1}{2} E_g + E_0$$

Then the absolute position of the VBM (E_{VBM}) can be obtained as

$$E_{VBM} = E_{CBM} - E_g$$

Here, E_g indicates the band gap of NaNbO$_3$, and $E_0 = -4.5$ eV, is the scaling factor for relating the reference electrode potential with absolute vacuum scale. χ_{Na}, χ_{Nb}, and χ_O stand for absolute electronegativity, obtained from Pearson electronegativity table. The calculated CBM for NaNbO$_3$ is 0.67 eV more negative than the hydrogen reduction potential and the VBM is 1.37 eV more positive than the water oxidation level. Thus, NaNbO$_3$ fully satisfies the thermodynamic criterion for overall water splitting, which is consistent with the experimental observation. For (W, N)-codoped NaNbO$_3$ the CBM and VBM values are obtained by calculating the relative shift of the band edges with respect to undoped NaNbO$_3$. In Figure 5.4.5, we have shown the band edge alignment of the codoped system with 'Str. 2' configuration, for which band gap narrowing is significant. The VBM is 0.80 eV below the H$_2$O/O$_2$ level and the CBM is 0.61 eV above the H$^+$/H$_2$ level, which is very close to that of the undoped NaNbO$_3$. Thus, the present strategy of band gap narrowing retains the overall water splitting property of NaNbO$_3$. More interestingly, the reducing behavior at the CB for the codoped system is expected to be similar in comparison to that of undoped NaNbO$_3$, which is very much crucial point while developing hydrogen evolving catalyst. We also consider the band edge alignment for the codoped systems with lower dopant concentration. As can be seen from Figure 5.4.5, in both the cases the band edges are in appropriate positions to generate hydrogen as well as oxygen during water splitting. This justifies the codoping of (W, N) pair as an effective strategy for improving the visible light photocatalytic activity of NaNbO$_3$ for practical scenario.
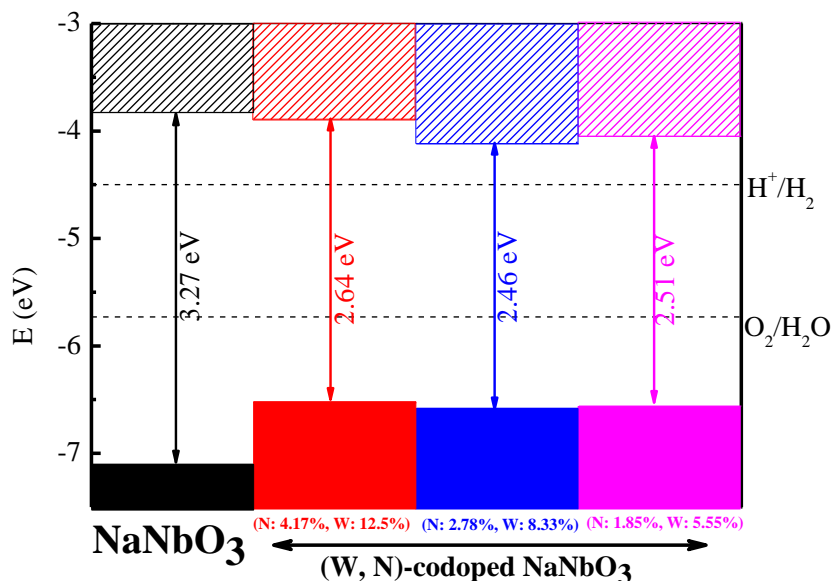
Figure 5.4.5: Band edge alignment of undoped and (W, N)-codoped NaNbO₃ under different dopant concentration.

5.4.2. Conclusion

In this section, we systematically investigate the effect of doping in enhancing the visible light photocatalytic activity of NaNbO₃. The computational parameters used in this calculation successfully reproduce the experimentally reported band gap of NaNbO₃. Although, doping with only N is able to reduce the band gap, localized acceptor states may suppress the photoconversion efficiency. On the other hand, W introduces donor state just below the CB, which may affect the hydrogen evolution property drastically. Interestingly, in presence of (W, N) pair, both the acceptor states and donor states are completely passivated. Formation of clean band structure for (W, N)-codoped NaNbO₃ ensures good photoconversion efficiency. The calculated band gap for (W, N)-codoped NaNbO₃ is in the desirable range to show photocatalytic activity in the visible region even at lower dopant concentration. More interestingly, the band

gap narrowing in the present strategy is mainly controlled by elevation of VBM. Thus, codoping of (W, N) pair retains the overall water splitting property of $NaNbO_3$, which is manifested in the appropriate band edge alignment of both the VBM and CBM with respect to water redox levels. Presence of W not only facilitates introduction of N by reducing the formation energy, but also minimizes the spontaneous formation of vacancy defects by forming charge compensated system. Hence, based on the present theoretical calculation it can be predicted that codoping with N and W is one of the effective approaches to improve the visible light photocatalytic activity of $NaNbO_3$.

Chapter 6

Metal Decorated Porous Graphitic Carbon Nitride (g-C$_6$N$_6$) for Water Splitting

6.1. Introduction

In recent years, polymer semiconductors based photocatalysts like graphitic carbon nitrides have attracted significant research interest to make an efficient catalyst to split water. In 2009, Wang et al.[241] reported the photocatalytic water splitting by metal-free, tri-s-triazine (heptazine) based graphitic carbon nitride, $g\text{-}C_3N_4$. However, the quantum efficiency of the material is reported to be very low. Based on the electronic band structure calculations, the low photocatalytic efficiency of $g\text{-}C_3N_4$ was attributed to the localized valence band states. Apart from water splitting, its photocatalytic activity is also found to have wide applications which include CO_2 reduction to useful organic molecules, decomposition of organic pollutants in water and selective synthesis of H_2O_2. To improve the photocatalytic efficiency of $g\text{-}C_3N_4$, variety of strategies have been suggested, viz. metal decoration, doping with non-metal elements, structure controlled synthesis, making composites with other semiconductors, adsorbing molecules and molecular complexes etc. Through *ab initio* studies, Pan et al.[242] reported $g\text{-}C_3N_4$ nanotubes to be a better choice as compared to the 2D sheets and also shown that further improvements can be attained through functionalization with metal atoms like Pt and Pd. Attempt to dope different non-metal elements, viz. boron, nitrogen, sulphur, phosphorous, iodine etc. into $g\text{-}C_3N_4$ has also been made for tuning its electronic band structure. Martin et al.[243] observed a significant improvement in the quantum efficiency (26.5 %) when $g\text{-}C_3N_4$ was synthesized from the urea precursor and the results were explained based on the surface area as well as the extent of hydrogenated nitrogen species. Graphitic carbon nitride has also been integrated with different inorganic as well as organic materials for making composite materials with improved photocatalytic properties. Very recently, Liu et al.[244] reported a new metal-free photocatalyst based on carbon nitride- carbon nanodot composite materials with a solar to hydrogen conversion efficiency of 2.0 %. They proposed a step wise $2e^-/2e^-$ reduction through the formation of H_2O_2 intermediate and more

interestingly, without the need of any sacrificial reagent. Another form of the graphitic carbon nitride, poly (triazine imide) is also shown to be a potential photocatalyst for solar hydrogen evolution.

In our recent study, we have reported another form of graphitic carbon nitride based on poly s-triazine (g-C_6N_6) as possible photocatalyst for water splitting with appropriate electronic band structure. From our results, though the calculated band gap is found to be 2.89 eV, its optical absorption is mostly limited to the UV region of the solar spectrum. We have also reported the effect of non-metal doping on its electronic structure. Later on, Wang et al.[245] reported the topological insulator states in the same s-triazine based 2D carbon nitride and also indicated that the charge carriers in this system will act like massless Dirac Fermions. This indicates that the mobility of the photo generated charge carriers will be very high in this material and better photo catalytic activity can be expected. In the present study, we are interested in improving the visible light absorption efficiency of the g-C_6N_6 through metal doping. Metal nanoparticles, especially the noble metals, supported on the semiconductor surface are shown to have strong visible light absorption due to the surface plasmon resonance property of the metal nanoparticles which can even be tuned through the size and shape of the nanoparticles. Recently, Samanta et al.[246] synthesized the composites of gold nanoparticles and g-C_3N_4 which had significantly improved the visible absorption and thereby the hydrogen evolution under visible light. The metal atoms decorated not only modulate the electronic band structure but also can create the active reaction centres thereby facilitating the oxidation and reduction reactions of water. We have scanned a range of metal atom decorated g-C_6N_6 surfaces to tune the electronic band structure for designing the g-C_6N_6 based photocatalyst with improved activity. Apart from the single metal atoms, we have also studied the electronic structure of four atom clusters of metals absorbed on the g-C_6N_6 surface.

6.2. Computational Details

All the first principles calculations have been carried out using the spin-polarized periodic density functional theory (DFT) based methods as implemented in the *Vienna ab initio Simulation Package* (VASP) software. The ion-electron interactions have been treated through the projector augmented wave (PAW) potentials. Plane-wave basis sets with a kinetic energy cutoff of 550 eV have been used for expanding the Kohn-Sham equations of the valence electrons. The exchange-correlation energy density functional, E_{xc} [ρ] has been obtained using the Generalized Gradient Approximation (GGA) of Perdew-Burke-Ernzerhof (PBE). An energy cut-off of 1 x 10^{-6} eV has been used for the electronic self-consistent field iterations. Both the cell structure and atomic positions were relaxed using the constant volume constraint until the maximum Hellmann−Feynman force on each atom is less than 0.01 eV Å^{-1}. The Brillouin zone has been sampled using the automatically generated Gamma centered $5 \times 5 \times 1$ Monkhorst−Pack set of k-points. To measure the electronic structure more accurately, we have also performed calculations by using the more accurate hybrid density functional method, developed by Heyd, Scuseria, and Ernzerhof (HSE03 and HSE06) at the PBE optimized structures. The graphical software, p4vasp and VESTA were used for analysing the results and generating the reported figures.

6.3. Results and Discussion

To study the metal decorated systems, we have considered a 2 x 2 x 1 super cell of graphitic carbon nitride (g-C_6N_6) with 24 carbon and 24 nitrogen atoms as shown in Figure 6.1(a). The optimized cell parameter of the super cell using PBE functional is found to be 14.247 Å and the measured C-C and C-N bond lengths are found to be 1.510 Å and 1.341 Å which are consistent with our earlier reported values. The calculated band gap for the pristine g-C_6N_6 by using the HSE03 method is found to be 2.89 eV. The projected density of states

plot for the undoped g-C$_6$N$_6$ calculated using the HSE03 method has been shown in Figure 6.1(b) and it can be observed that the valence band maximum (VBM) is mainly originating from the nitrogen (p_x p_y) states whereas the conduction band minima (CBM) has contributions from p_z states of both carbon and nitrogen. This nature of VBM and CBM indicates that the photo generated electrons and holes will be well separated which can enhance the lifetimes of the charge carriers.
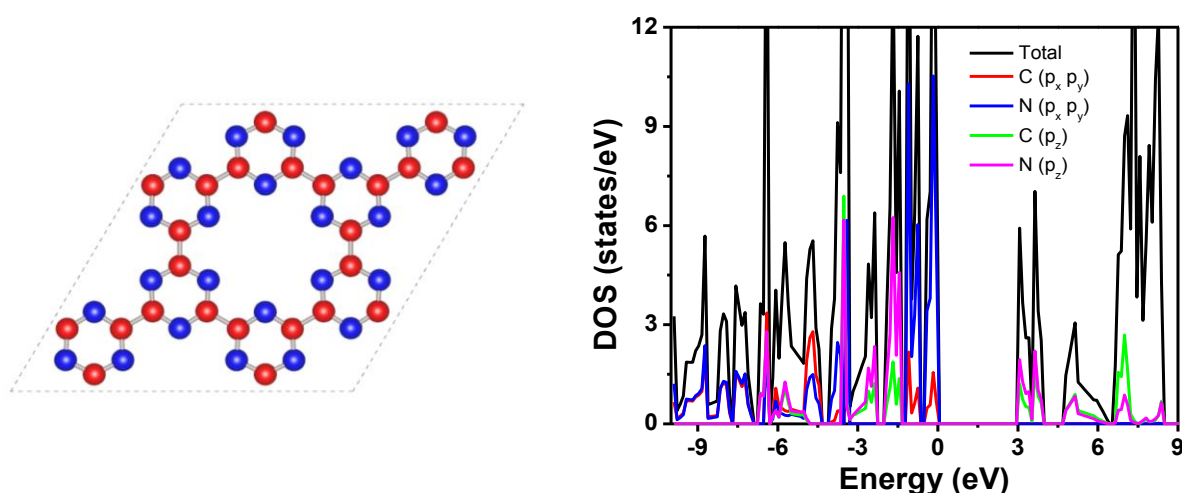
Figure 6.1: (a) Optimized supercell structure and (b) projected density of states of the pristine graphitic carbon nitride (g-C$_6$N$_6$)

For decorating the g-C$_6$N$_6$ surface, a range of metals have been scanned which include the 3d transition metals (Mn, Fe, Co, Ni, Cu and Zn) along with the noble metals (Ag, Au, Pt and Pd). Different possible interaction sites have been considered for metal adsorption such as above the C$_3$N$_3$ ring, above the C-C bond within the N$_6$ cavity and the calculated energies indicated that the N$_6$ cavity as shown in Figure 6.2(a), is the minimum energy site. This can be attributed to the high electron density localised on the six nitrogen sites, forming the N$_6$ cavity, as can be seen from the charge density contour plot reported in Figure 6.2(b).

From the N-M distances reported in Table 6.1, it can be observed that the metal atoms are not located exactly at the centre of the N_6 cavity and are shifted slightly, leading to different M-N distances. This indicates that the size of the cavity is large and hence the metal will not be placed at the centre. The metal binding energies to the carbon nitride surface has been calculated as BE = E($C_{24}N_{24}$-M) - [E($C_{24}N_{24}$)+E(M)]. The calculated metal binding energies to the g-C_6N_6 surface for all the metals considered, by using the PBE method are reported in Table 6.1. From the energetics, it can be observed that in all the cases, the binding energies although are negative, are less than the corresponding metal cohesive energies in some cases. However, for similar metal atoms, the corresponding binding energies to the N_4 type of cavities were reported to be negative. This can be attributed to the larger size of the N_6 cavity where the metal is bonding strongly with the closest nitrogen atoms with remaining nitrogen atoms located somewhat far from the metal. Though the metal binding energies calculated here are less than the metal cohesive energies in some cases, it could be possible to synthesise these metal dispersed systems using advanced experimental techniques (like laser ablation) where the source of the metal precursor is not the bulk metal.
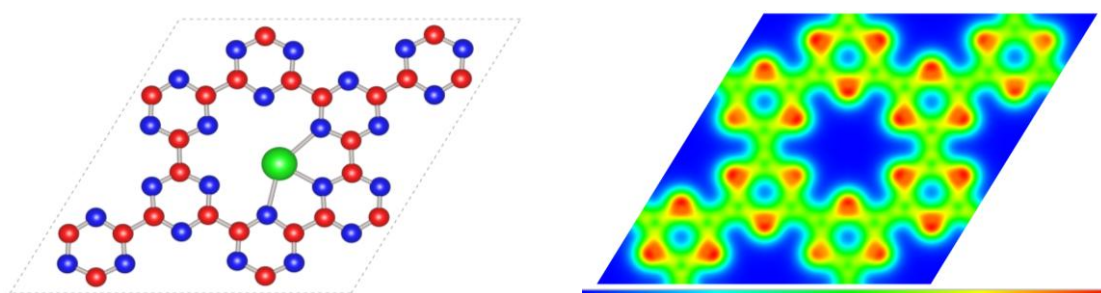
Figure 6.2: (a) Optimized structure of Mn decorated g-C_6N_6 and (b) Charge density contour plot of the g-C_6N_6.

Table 6.1. Metal binding energy to g-C_6N_6 (ΔE_M), range of M-N distances and band gap of the systems calculated using HSE03 method.

System	ΔE_M (eV)	Range of M-N distance (Å)	Band Gap (eV)
g-C_6N_6			2.89
g-C_6N_6 -Mn	-4.23	2.07-3.45	2.56
g-C_6N_6 -Fe	-4.50	1.99-3.61	2.58
g-C_6N_6 -Co	-4.50	1.93-3.63	2.65
g-C_6N_6 -Ni	-4.80	1.92-3.65	2.22
g-C_6N_6 -Cu	-3.00	2.03-3.51	2.32
g-C_6N_6 -Zn	-1.28	1.95-3.70	2.71
g-C_6N_6 -Ag	-2.70		2.76
g-C_6N_6 -Au	-1.87	2.55-2.89	2.19
g-C_6N_6 -Pt	-4.10	1.91-3.91	2.71
g-C_6N_6 -Pd	-2.95	2.13-3.40	2.69
g-C_6N_6 -Ag_4	-2.10		2.53
g-C_6N_6 -Au_4	-2.36		2.32

Now we will discuss the electronic structure of the metal decorated g-C_6N_6. The electronic band gap in all the metal decorated systems are calculated as the energy difference between the valence band maxima and conduction band minima by omitting any donor/acceptor states arising due to metal doping. The projected density of states (PDOS) plots calculated through HSE03 method for all the systems decorated with 3d transition metals considered here are shown in Figure 6.3 and the corresponding band gaps are reported in Table 6.1. Both Mn and Fe decorated systems are found to have almost similar DOS with the band gap of 2.56 eV and 2.58 eV respectively and the reduction in the gap is mainly caused by the elevation of the valence band. Both the systems are found to have donor states

just below the conduction band which arise from the M-N bonding. In the case of Co decorated system, the calculated band gap is found to be 2.65 eV and the difference between the conduction band and donor states is more than the previous case. In the cases of both Ni and Cu decorated systems, though the reduction in band gap is high (2.22 eV 2.32 eV for Ni and Cu respectively), the metal d-states are found to be placed above the valence band. In Zn decorated system, the calculated band gap is found to be 2.71 eV with donor states located below the conduction band. In this case, the occupied Zn *3d*-states are found to be located deep inside the valence band at around 10 eV below the valence band maxima.

As the noble metals are found be advantageous due to their special optical properties like surface plasmon resonance, which can be tuned through shape and size, we have considered Ag, Au, Pt and Pd also for decorating $g-C_6N_6$. From the PDOS plot of Ag decorated system reported in Figure 6.4, it can be observed that Ag doping is not creating any inter band states and the silver *d*-states are located within the valence band. The calculated band gap for this Ag doped system is found to be 2.76 eV which is 0.13 eV less than the pristine $g-C_6N_6$. Based on the nature of DOS, Ag system will be advantageous over earlier discussed systems due to the absence of any mid gap states which can act as recombination centers. In the case of Au decorated system, the band gap is found to be reduced considerably to 2.19 eV and the states corresponding to M-N bonding were found to be placed just above the valence band. In Pt decorated system the calculated band gap is found to be 2.71 eV with donor states below the conduction band. In Pd decorated system, the band gap is found to be 2.29 eV and is found to create mid gap states above the valence band. In all the metal decorated systems, it can be seen that the Fermi level is located just below the conduction band (with donor states below the conduction band) which is characteristic of n-type semiconductors.
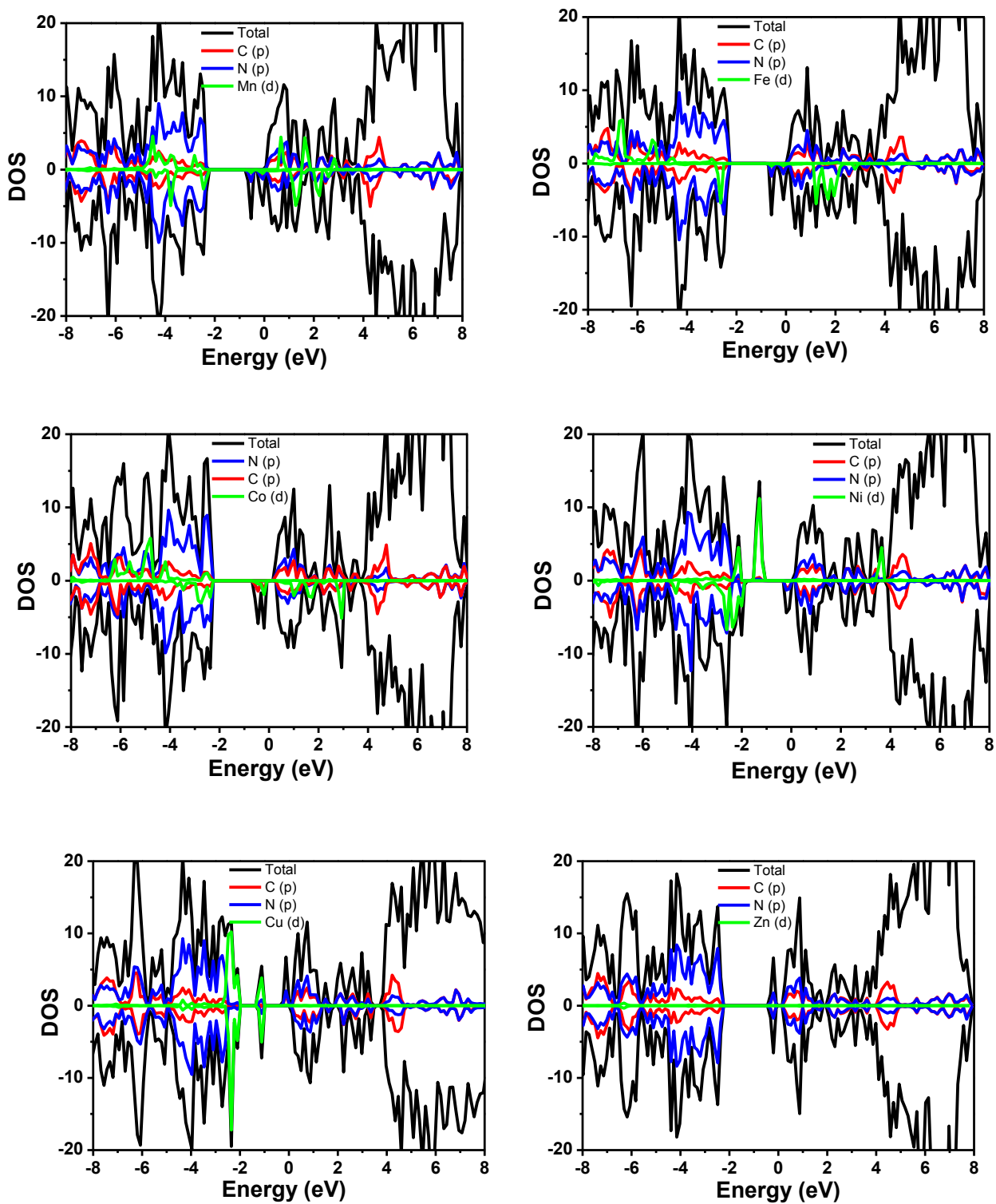
Figure 6.3: Total and projected density of states of (a) Mn (b) Fe (c) Co (d) Ni (e) Cu and (f) Zn decorated g-C_6N_6.
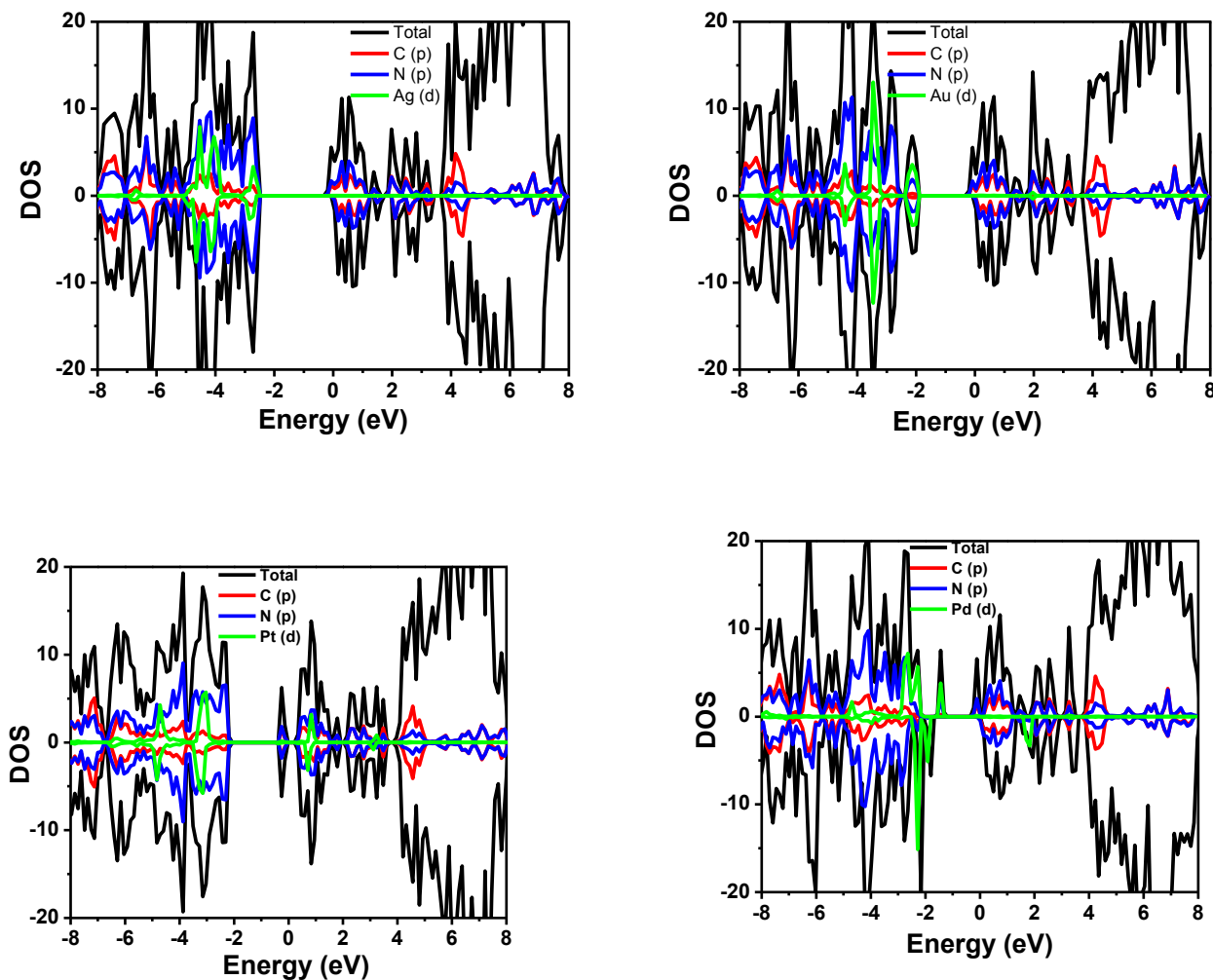
Figure 6.4: Total density of stated and projected density of states of (a) Ag (b) Au (c) Pt and (d) Pd decorated g-C_6N_6.

Apart from the single atom decorated systems, we have also considered decoration the four atom cluster systems of the noble metals, viz. Ag, Au, Pt and Pd. The binding energy has been calculated as BE= $(1/4)*E[(g-C_6N_6-M_4)-\{E(g-C_6N_6)+4*E(M)\}]$ and the calculated binding energies are reported in Table 6.1. The DOS plots for Ag_4 and Au_4 decorated systems are reported in Figure 6.5. The calculated band gap for Ag_4 and Au_4 decorated systems is found to be 2.53 eV and 2.32 eV respectively. Among the four atom cluster

decorated systems, Ag decorated system is found to have a clean band structure without any mid gap states whereas the Au decorated system is found to generate mid gap states originating from the Au-N bonding states.
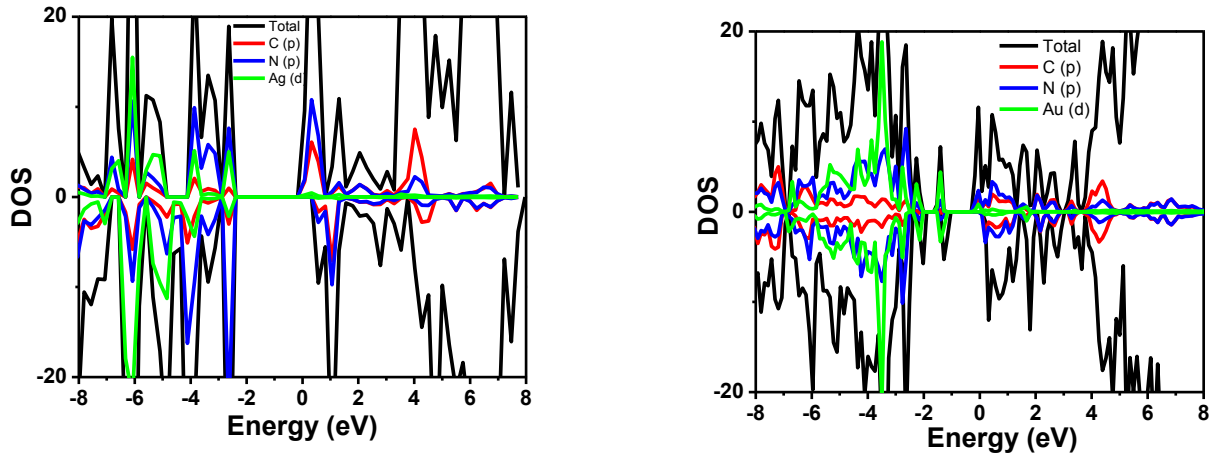
Figure 6.5: Total density of states and projected density of states of systems with (a) Ag_4 and (b) Au_4 cluster adsorbed on g-C_6N_6.

The electronic structure results clearly tells that among all the dopants investigated, silver is the only dopant which does not lead to the formation of any mid gap states and all other systems are found to have either donor or acceptor states which can act as recombination centers for the photo generated charge carriers. Hence Ag could be a better dopant for improving the catalytic activity of g-C_6N_6. However, the extent of band gap reduction is not very high in single atom case but it is better in Ag_4 cluster decorated one.

For investigating the optical absorption properties of these metal decorated g-C_6N_6 systems considered, the complex frequency dependent dielectric function ($\varepsilon(\omega) = \varepsilon_1(\omega) + i\varepsilon_2(\omega)$) has been calculated, where ε_1 and ε_2 represent the real and imaginary parts of the dielectric function, respectively. The absorption coefficient $\alpha(\omega)$ has been calculated using the relation.

$$\alpha(\omega) = \sqrt{2}\omega \left(\sqrt{\varepsilon_1(\omega)^2 + \varepsilon_2(\omega)^2} - \varepsilon_1(\omega) \right)^{\frac{1}{2}}$$

The calculated absorption spectra for pure, as well as four atom metal cluster decorated systems are reported in Figure 6.6. From the absorption spectra, it can be observed that the pristine carbon nitride shows a strong peak in the range of 260-300 nm which is a characteristic peak for π to π^* transition in s-triazine based compounds indicating that the absorption is mainly limited to the UV region. In the metal decorated systems, the absorption peak is found to be broadened slightly towards the visible region. Though the absorption is still limited to the UV region, due to the surface plasmon resonance property of the metal nanoparticles, they can have better visible absorption efficiency which is observed in other carbon nitrides decorated with gold nanoparticles.
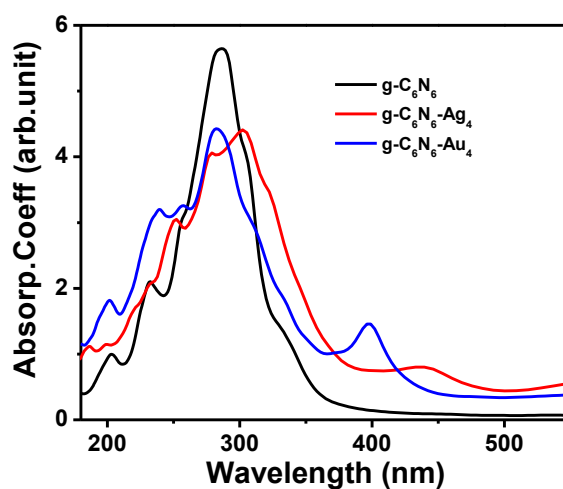
Figure 6.6: Calculated optical absorption spectra of g-C$_6$N$_6$ and its noble metal cluster adsorbed counterparts.

For accomplishing the overall solar driven water splitting, apart from having visible light absorption efficiency, the semiconductor should also have appropriate band edge

potentials with respect to the redox levels of water. As all the DFT calculations carried out here are based on pseudopotental based method along with the periodic boundary condition, the position of the band edges measured are known to be shifted and hence the band edges have been corrected using a standard method. In our earlier work, we have measured the band edge positions of g-C_3N_4 using a similar method and shown that the calculated values are in good agreement with the reported experimental results. The calculated results for pure g-C_6N_6 along with all other metal decorated systems considered here are reported in Figure 6.7. From the results, it can be observed that for all the systems, the valence band maxima is below the water oxidation potential and the conduction band minima is located above the proton reduction potential. The calculated results reveal that theoretically all these systems satisfy the thermodynamic criteria for overall water splitting. On doping with metals, the shift in conduction band minima is found to be less as compared to the shift in valence band maxima. This can be due to the fact that the metal atoms are mainly interacting with the nitrogen atoms of the N_6 cavity, and are placed in the same plane as the carbon nitride sheet, which are the major contributors to the VBM. The best results is observed in Ag_4 decorated system where the CBM is located ~ 0.5 V above the proton reduction potential and the band gap is also 2.53 eV as discussed earlier. Though the shift in the CBM with respect to VBM is less, there is small elevation of CBM for most of the metals and the extent of elevation is maximum in Zn and Ag decorated systems. This small upward shift in the CBM will improve the reduction capacity of the catalyst for better hydrogen evolution.
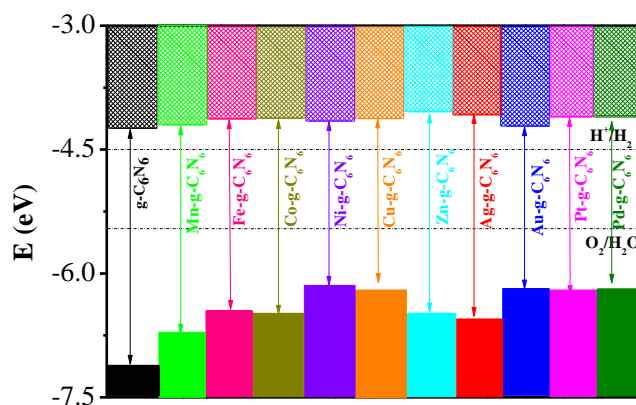
Figure 6.7: Calculated VBM and CBM positions of g-C_6N_6 and the corresponding metal decorated systems.

6.4. Conclusions

In summary, we have investigated the electronic structure of varieties of metal decorated graphitic carbon nitride systems with the aim of improving the visible light absorption efficiency of the graphitic carbon nitride semiconductor photocatalyst. The calculated results reveal that in all the metal decorated systems, the calculated band gap is less than the pristine g-C_6N_6. However, in many cases, the metal doping is found to lead to the formation of interband mid gap states which can act like recombination centers for the photogenerated charge carriers. In the case of Ag doped system, though the reduction in band gap is not much significant, there are no mid gap states. We have also studied the four atom cluster decorated g-C_6N_6 and the results reveal that the Ag_4 decorated system has a band gap of 2.53 eV with appropriate band edge positions for overall water splitting. Our study shows that among the different metals and metal clusters considered for doping, Ag is the best possible dopant as it does not create any mid gap states and it also brings down the band gap for improved visible light activity.

Chapter 7

Metal Decorated Porous Graphitic Carbon Nitride (g-C$_4$N$_3$) as a Hydrogen Storage Media

7.1. Introduction

While the first step towards success in hydrogen energy is generation of hydrogen from natural resources, the second step to make hydrogen energy realizable involves the storage of hydrogen in a safe and cost effective way. So far, large number of materials have been developed for onboard hydrogen storage. Although, the commercial approaches deal with storage of hydrogen as gas under high pressure and liquid under cryogenic temperature, both are neither safe nor cost effective. This leads to the development of other approaches for storage of hydrogen. The strategy through formation metal hydrides has attracted immense interest due to the high gravimetric density of hydrogen in these compounds. Unfortunately, this requires high temperature to desorb hydrogen due to the presence of chemical bond between the metal and hydrogen. The other promising approach is storing hydrogen in a porous framework, which can bind molecular hydrogen through physisorption. Among different materials, carbon based ones have advantage because of the light weight, long term stability, and low cost. The most popular carbon nanomaterials include graphene, fullerene, carbon nanotube, porous carbon materials, etc. However, bare carbon surface hold hydrogen very weakly due to simple van der Waals type interaction between hydrogen molecule and carbon surface. Interestingly, metal decorated carbon surface can hold hydrogen quite strongly. More importantly, the hydrogen adsorption energies for such systems are in the desirable range of energy for hydrogen storage purpose, i.e., which is between chemisorption and physisorption. The metal adatom includes alkali metal, alkaline earth metal, and transition metal which can provide the binding center for the adsorption of hydrogen. As for example, transition metal decorated carbon nanostructures have been extensively studied for ambient hydrogen storage media. These systems adsorb molecular hydrogen through Kubas type of interaction, which involves transfer of electron from the occupied orbital of hydrogen to

the unoccupied d orbitals of the transition-metal atom, and then back-electron transfer from d orbital of the transition-metal atom to the antibonding orbital of the hydrogen molecule.[247-249] But these materials tend to aggregate forming metal clusters instead of being evenly distributed on the surface due to their high cohesive energy.[250] This leads to lowering of the hydrogen storage efficiency significantly. The cluster formation is less prominent in the case of alkali and alkaline earth metal decorated systems due to relatively smaller bulk cohesive energies.[251-253] However, the binding energies of these metals with the carbon nanostructure are also small, making the systems unsuitable for practical applications. This is because, the materials should be stable enough for repeated cycle of hydrogenation and de hydrogenation processes. Many attempts have been made to enhance the binding between these metal elements with the carbon host structures. Popular methods include doping with heteroatom, introduction of vacancy in the host structures, etc.[254, 255] Among different elements, doping with B and N have been well demonstrated to alter the properties of carbon nanomaterials. B and N doped fullerene, carbon nanotube, and graphene have been synthesized by different groups. Lee et al synthesized porphyrin like carbon nanotube using plasma enhanced chemical vapor deposition technique.[256] In this structure, four nitrogen atoms substitute four carbon atoms by truncated doping. However, introducing defects or heteroatom in the carbon nanostructure often requires large amount of energy.[257] This limits the strategy of creation of vacancy in the carbon nanomaterials. Therefore, the major challenge is to find suitable materials which can bind the metal elements so strongly that the clustering of metal atoms can be avoided without sacrificing the hydrogen storage efficiency.

After successful demonstration of single layered graphene, many attempts have been made to synthesize similar graphitic two dimensional layer structure. The most popular class

consists of graphitic carbon nitride.[258-260] There exists different types of graphitic carbon nitrides, obtained by varying the C/N ratio. Particularly, g-C_3N_4, g-C_3N_3, and g-C_4N_3 have gained immense interest due to presence of natural vacancies, which can hold the adatom very strongly. Graphitic carbon nitride of the type g-C_3N_4 is based on tri-s-triazine ring connected through C-N bond, can be easily synthesized by polymerization of cyanamide. The structure of g-C_3N_3 is based on s-triazine ring connected through C-C bond, and this material can be synthesized by using cyanauric chloride as a precursor. On the other hand, g-C_3N_4 has synthesized using fluidic carbon precursors under ambient pressure in presence of ionic liquids. Here, we want to explore this material for hydrogen storage applications using DFT based theoretical calculations.

7.2. Computational Methods

All the calculations have been carried out using Vienna ab initio simulation package (VASP) electronic structure code with projector augmented wave (PAW) potential. The valence shell considered during construction of ion-electron interaction potential are: H ($1S^1$), C ($2s^2 2p^2$), N ($2s^2 2p^3$), Li ($2s^1$), and Na ($2s^2 2p^6 3S^1$). The exchange and correlation energy has been represented by the Perdew-Burke-Ernzerhof (PBE) functional under generalized gradient approximation (GGA). The energy cutoff for the plane wave basis set is chosen to be 550 eV. We employed conjugate gradient algorithm for the geometry optimization. All the structures have been fully relaxed without imposing any symmetry constraints until the Hellmann-Feynman force acting on each elemental constituent is less than 0.01 eV $Å^{-1}$. The tolerance for energy convergence during self consistent iteration was set as 10^{-6} eV. A 2×2 supercell of g-C_4N_3 unit cell is employed for the model structure. To avoid the image interaction between neighboring images, a vacuum layer of 20 Å is considered along the vertical direction of g-C_4N_3 layer. A k-point mesh of $7 \times 7 \times 1$

within Monkhorst and Pack scheme has been found to be sufficient for the sampling of two-dimensional Brillouin zone. Since long range interaction plays an important role in the structure and energetics of the adsorption process, we employed DFT-D3 method, as proposed by Grimme with the inclusion of dispersion correction to take care of the effect of van der Waals interaction.
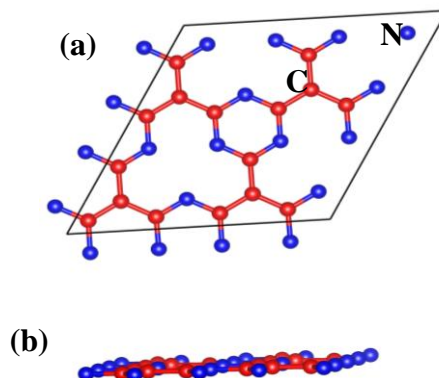
Figure 7.1: Optimized geometry of 2×2 supercell of free-standing g-C$_4$N$_3$ layer, (a) top view and (b) side view.

7.3. Results and Discussion

We start this discussion by describing the supercell of free-standing g-C$_4$N$_3$ layer considered here, which is composed of sixteen carbon atoms and twelve nitrogen atoms. The optimized geometry shows a perfect planar structure for C$_4$N$_3$. The calculated dimension of 2×2 supercell is 9.68 Å, which is in good agreement with the previous reports. Here, we consider Li and Na as two different adatoms. To find out the most possible adsorption site, we have considered four different initial structures. Figure 7.2 shows the possible structures for the Li-C$_4$N$_3$ system, with Li above the cavity, Li inside the cavity in the same plane as the C$_4$N$_3$ structure, Li above the sp^2 C-C bond, and Li above the C$_3$N$_3$ six membered ring. All the structures have been fully relaxed

to get the equilibrium geometry. This structural relaxation results into only two non-equivalent structures, Li above the cavity and Li inside the cavity. Comparison of the total energy indicates that the adsorption of Li is energetically more favorable by 2.07 eV when it is above the cavity than when it is inside the cavity structure. Hence, we investigate the hydrogen adsorption property by taking only this structure. The lattice constant remains unchanged due to loading of Li on the C_4N_3 structure.
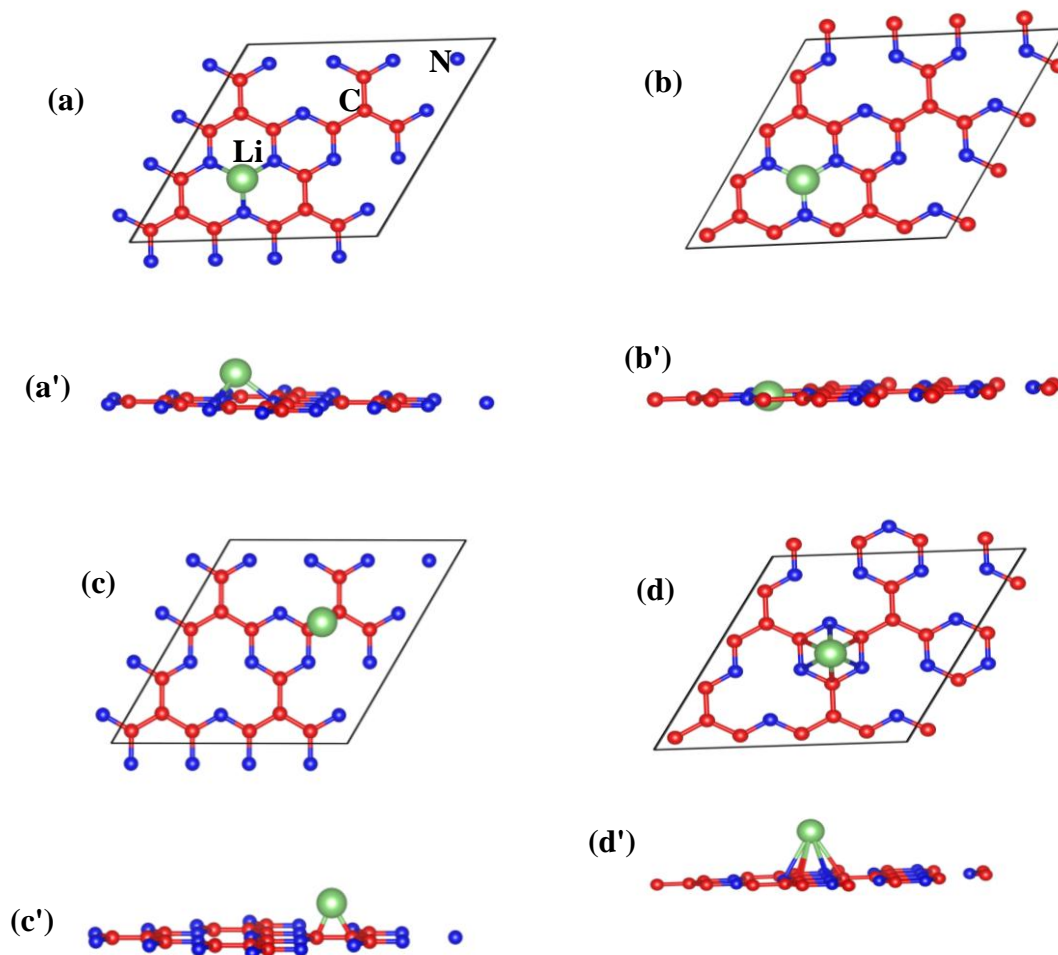
Figure 7.2: Initial structure for Li-C_4N_3 system, (a, a') Li above the cavity, (b, b') Li inside the cavity in same plane as that of the C_4N_3 structure, (c, c') Li above the sp^2 C-C bond, and (d, d') Li above the C_3N_3 six membered ring. (a, b, c, d) top view and (a', b', c', d') side view.
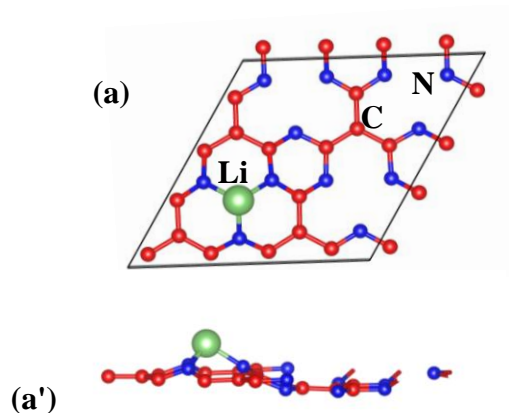
Figure 7.3: Optimized structure for Li-C_4N_3 system (Lowest energy structure among the above four). (a) top view and (a') side view.

Figure 7.3 shows the optimized geometry of Li decorated C_4N_3 systems. This clearly shows that loading Li results into major structural change in the C_4N_3 geometry. The host structure is no longer planar. The three nearest neighboring nitrogen atoms of Li are lifted upwards. The calculated N-Li distance in the optimized geometry is 1.872 Å. In the case of Na also the most preferable adsorption site is found to be above the cavity.

To get an idea about the stability of M-C_4N_3 structure, we calculate the binding energy between the adatom and g-C_4N_3 system, which is defined as,

$$E_b = E_{C_4N_3} + E_M - E_{M-C_4N_3}$$

where, $E_{C_4N_3}$ and $E_{M-C_4N_3}$ indicate the total energy of free standing g-C_4N_3 system and metal loaded g-C_4N_3 system, respectively. E_M represents the energy of a metal atom in the bulk structure. Larger the value of E_b, stronger is the binding of the metal with the g-C_4N_3 system. As

can be seen from Table 7.1, the binding energy of both Li and Na with the g-C_4N_3 system is found to be positive. Thus, the cluster formation can be avoided, and these materials will be suitable for the recyclable hydrogen storage materials.

Table 7.1: Calculated binding energy of metal adatom with g-C_4N_3 system

Metal	E_{BE} (eV)	E_{BE} (eV) (Dispersion corrected)
Li	3.34	4.89
Na	2.36	3.94

We now investigate the adsorption of hydrogen molecule on these two metal decorated g-C_4N_3 systems. We start with the adsorption of one hydrogen molecule at the metal center. The optimized geometry of Li-C_4N_3 with one hydrogen molecule has been shown in Figure 7.4 a, and a'. The calculated average distance (d_{M-H}) between the hydrogen molecule and Li center in Li-C_4N_3 is 2.22 Å. The average distance (d_{M-H}) is defined as the average of the distance between the metal center and two hydrogen atoms of the same hydrogen molecule. The Li-N distance remains almost unchanged due to adsorption of hydrogen molecule. The calculated H-H bond length is 0.753 Å. In the case of Na-C_4N_3 system, the observation is quite similar except that the average metal-hydrogen distance, is longer than that of the Li-C_4N_3 system. The calculated Na-H distance is 2.61 Å, which is due to increase in atomic radius from Li to Na. The distance between the metal center and nitrogen atoms remains unaffected with the increase in number of hydrogen

molecules adsorbed. The same is true for the H-H bond length. However, the average d_{M-H} increases for both Li-C_4N_3 and Na-C_4N_3 systems.
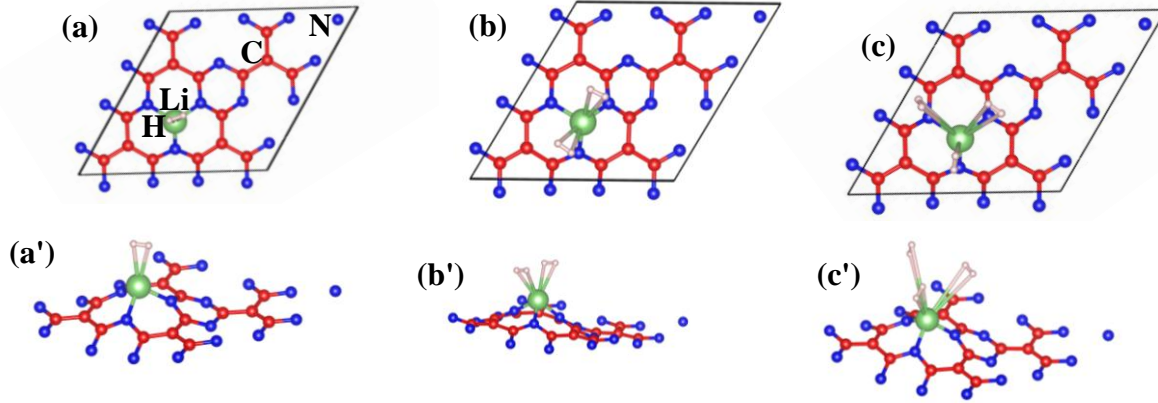
Figure 7.4: Optimized structure for Li-C_4N_3 system with (a) one hydrogen molecule, (b) two hydrogen molecules, and (c) three hydrogen molecules. (a, b, c) top view and (a', b', c') side view.

To obtain a quantitative information about the strength of interaction between the hydrogen molecule and the metal decorated C_4N_3 system, we calculate the adsorption energy per hydrogen molecule, which is defined as

$$E_{ad} = [E_{M-C_4N_3} + nE_{H_2} - E_{(M-C_4N_3+nH_2)}]/n$$

where, n indicates the number of hydrogen molecules adsorbed to the system. $E_{(M-C_4N_3+nH_2)}$ is the total energy of the metal decorated C_4N_3 system with n number of adsorbed hydrogen molecules. E_{H_2} represents the energy of a gaseous hydrogen molecule, calculated by placing at the center of a large cubical box (20 Å × 20 Å × 20 Å).
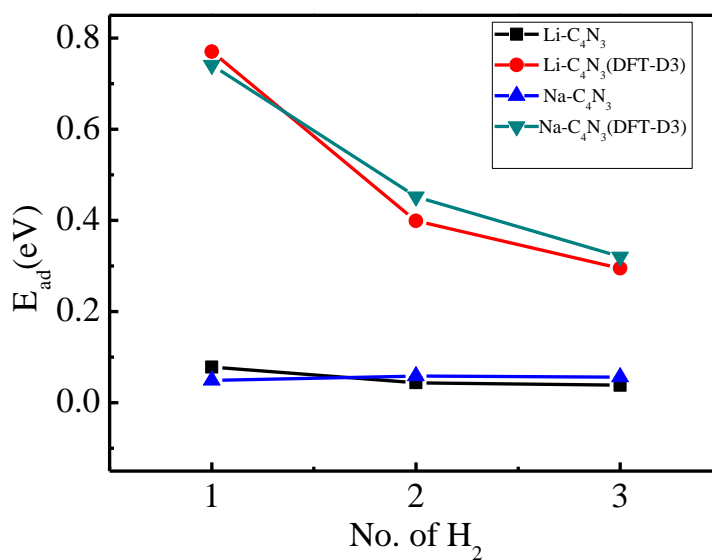
Figure 7.5: Calculated adsorption energy (eV/H$_2$) as a function of the number of adsorbed Hydrogen molecules for Li/Na-decorated C$_4$N$_3$ system.

As can be seen from Figure 7.5, the adsorption energies are very small at the PBE level of calculation. The adsorption energy remains almost unchanged with the increase in number of hydrogen molecules on the metal center according to PBE calculation. However, the values significantly increase when van der Waals correction is incorporated. The adsorption energies in case of Li-C$_4$N$_3$ and Na-C$_4$N$_3$ systems are very close to each other. For the first hydrogen molecule, the calculated adsorption energy is quite high (DFT-D3 method). However, the adsorption energy reduces to around 0.4 eV/H$_2$ for the second hydrogen molecule and 0.3 eV/H$_2$ for the next hydrogen molecule adsorption. This may be due to increase in steric repulsion between the hydrogen molecules. This is quite interesting as the ideal range of adsorption energy for hydrogen storage purpose is considered to be 0.2-0.6 eV/H$_2$. Thus the, present study indicates that these two materials can be of significant interest for hydrogen storage application.

The mechanism of hydrogen adsorption in this case can be explained by the charge transfer from metal to carbon nitride substrate. This partially charged metal ions and C_4N_3 system produce a local electric field, which polarizes the hydrogen molecule. This polarization is the main driving force for the adsorption of hydrogen molecule on the C_4N_3 substrate.

7.4. Conclusion

A systematic DFT study has been carried out to investigate the hydrogen adsorption property of Li and Na decorated C_4N_3 systems. The present study reveals that the binding energies of both Li and Na with C_4N_3 systems are quite strong, and therefore the problem of cluster formation can be avoided. The calculated adsorption energies of hydrogen molecule to the C_4N_3 systems with and without van der Waals correction are found to differ significantly. This justifies the incorporation of van der Waals correction for this type of calculations. Each metal can bind three hydrogen molecules, with adsorption energy in the range of 0.3 eV/H_2. Hence, Li and Na decorated C_4N_3 systems are predicted to be possible hydrogen storage materials with feasibility of operating at ambient temperature and pressure.

Chapter 8

Designing New Catalyst for

Oxygen Reduction Reaction

8.1. Introduction

As discussed in Chapter 1, fuel cell is an important component for using hydrogen directly as a fuel. However, the performance of a fuel cell is largely limited by the slow kinetics of oxygen reduction reaction (ORR) at the cathode. At present the best known catalyst for ORR is the platinum based catalyst. But its high cost and limited availability makes the fuel cell expensive. This drives one to the development of alternate catalyst (to replace Pt) for large scale application of fuel cell. [261-263]

During the past few decades a large number of catalysts have been studied for ORR.[264-283] This includes not only metal oxides, metal carbides based catalysts but also metal free catalyst like doped carbon nanostructure, graphitic carbon nitride of the type g-C_3N_4, etc. As for example, titanium carbide, vanadium carbide etc. show good activity towards ORR. Interestingly, titanium carbide shows better reactivity in the nanowire form than in bulk form. This may be due to the fact that in case of nanowire the reaction proceeds through more efficient four electron path, while in case of bulk material it follows two electron path, which is known to be not so effective due to formation of hydrogen peroxide as an intermediate. Graphene is also a potential material of interest due to wide surface area and high electrical conductivity. Unfortunately, it shows poor activity towards ORR, may be due to extended conjugation. There have been many efforts to enhance the reactivity of graphene mainly by doping with various heteroatoms, including N, O, S, or B.[284-290] Among various metal free catalysts, porous graphitic carbon nitride (g-C_3N_4) has been extensively studied for catalytic purpose. But their poor electrical conductivity limits wide spread application in this field. However, g-C_3N_4 when mixed with other carbon nanomaterials shows enhanced activity. As for example, Zheng et al observed a sharp enhancement of ORR activity of g-C_3N_4 when it is incorporated into a mesoporous carbon, which plays unique role in

efficient transfer of electron.[291] Another efficient strategy to improve the reactivity of g-C_3N_4 is by decorating with different transition metal complexes on the porous sites, forming porphyrine-like structure, which has been shown to play the role of electrocatalyst for ORR. In a recent theoretical study, it has been shown that decorating with different transition metal atoms can make graphyne an efficient catalyst for ORR. However, the property of metal-graphyne complex has been found to be strongly dependent on the nature of the metal. Although, Fe, and Co-graphyne complex can be employed as an effective catalyst for ORR, Ni-graphyne complex is not suitable due to its poor affinity for oxygen. Interestingly, both the Fe and Co-graphyne complex follow more efficient four electron path in acid medium. However, in alkali medium, the behavior of these two complexes is found to be different. Fe-graphyne complex follows four electron path, while Co-graphyne complex follows two electron path. Overall, the Fe-graphyne complex has been predicted to show better reactivity than Co-graphyne complex towards ORR.

Here, we are interested in investigating whether metal decorated fullerene can be useful for ORR, by using density functional theory (DFT) as a tool. Unfortunately, metal loading on fullerene in many cases involves aggregation of metal atoms due to metal-cluster formation. To avoid this, we consider fullerene with consist of porphyrine-like N_4 unit. Recently, Lee et al used plasma enhanced chemical vapor deposition method to synthesize porphyrine-like canbon nanotube, where four carbon atoms are replaced by four nitrogen atoms through truncated doping.[256] Similar type N-doped graphene has been synthesized by taking s-triazine molecule as a precursor. Cao et al reported the formation of porous graphitic carbon nitride and carbon nitride nanotube when cyanuric chloride is heated with Na in presence of $NiCl_2$ catalyst.[292] The basic framework of these two structures is the s-triazine unit connected through C-C bond, which is in contrast to g-C_3N_4, where the basic unit is tri-s-triazine ring connected through C-N bond. This

type of structure can also be generated from fullerene as starting material. As for example, porous fullerene of the type $C_{24}N_{24}$ can be generated through truncated doping of N in C_{60}. The framework of $C_{24}N_{24}$ is based on eight s-triazine ring connected via C-C bond. It contains six N_4 cavities, which can bind various metal elements efficiently. Here, we want to explore the ORR activity of $C_{24}N_{24}$-Fe/Co/Ni complex. For this purpose, a detailed systematic study has been carried out investigating all the intermediate steps involved in the ORR.

8.2. Computational Details

Spin polarized DFT calculation has been carried out using Vienna ab initio simulation package (VASP) with projector augmented wave (PAW) potential. Exchange and correlation energy functionals are defined by Perdew-Burke-Ernzerhof (PBE) under generalized gradient approximation (GGA). Throughout the calculation, energy cut off for plane wave basis set was fixed at 550 eV. The energy convergence criterion during self consistent iteration was set at 10^{-6} eV. To obtain the equilibrium geometry, all the model structures have been fully relaxed under conjugate gradient optimization algorithm at constant volume. The tolerance for Hellmann-Feynman force component on each atom was chosen to be 0.01 eV Å^{-1}. To avoid the image interaction, the simulation cell considered here is sufficiently high. Brillouin zone sampling was done using Γ-point only. The binding energy of the metal atom with $C_{24}N_{24}$ moiety has been calculated using the relation

$$BE(M) = E_{(C_{24}N_{24}+M)} - [E_{C_{24}N_{24}} + E_M]$$

where, the metal energy E_M has been taken from the metal binding energy in its bulk state. The interaction between $C_{24}N_{24}$-metal complex and different molecular species is defined as

$$E_{ads} = E_{(M-C_{24}N_{24}+molecule)} - [E_{C_{24}N_{24}+M} + E_{molecule}]$$

To obtain the free energy plot, we employ the methods developed by Nørskov et al.[293] The change in free energy of the reaction has been calculated by taking the difference between free energies of the initial and final states as

$$\triangle G = \triangle E + \triangle ZPE - T\triangle S + \triangle G_U + \triangle G_{pH}$$

where, $\triangle E$ stands for the reaction energy, ZPE indicates zero point energy, S is the entropy, $\triangle G_U = -eU$ (U represents the electrode potential, measured with respect to standard hydrogen electrode), $\triangle G_{pH} = 2.303k_BT\ pH$ (k_B stands for Boltzmann constant). Here we considered $T=$ 300 K and $pH=0$ (acid medium). For zero point energy correction and entropy calculation we calculate the vibrational frequency by employing density functional perturbation theory. The gas phase entropy values for the different species are used from the NIST data base.[294] The free energy for (H^++e^-) is considered as 1/2 $E(H_2)$ at standard condition ($pH=0$, $U=0$).

8.3. Results and Discussion

The carbon nitride fullerene of the type $C_{24}N_{24}$ is generated through truncated doping with twenty four N atoms at the C sites. To arrive at the $C_{24}N_{24}$ model structure, we consider C_{60} as the starting geometry. First two carbon atoms connecting the two five membered rings are removed and four carbon atoms in the nearest neighboring positions are substituted by N atoms. This leads to the formation of porphyrine-like N_4 cavity. Since there exists six such C-C bonds in C_{60}, total six numbers of N_4 cavities will be formed with twenty four N atoms. The framework of $C_{24}N_{24}$ is based on eight equivalent s-triazine rings connected through C-C bonds (Figure 8.1a). To get the optimized geometry full relaxation has been carried out. The optimized geometry shows octahedral symmetry as in the case of C_{60}. The calculated bond distances for C-C and C-N are found to be 1.555 Å and 1.341 Å, respectively. Previous study based on Hessian calculation

indicated that the $C_{24}N_{24}$ structure is stable as it does not show any imaginary frequency. Besides, it has been found to occupy one of the minima in the potential energy surface. To analyze the electronic structure, calculation of the density of states (DOS) has been carried out. As can be seen from Figure 8.2a, the DOS plot is symmetric with respect to spin up and spin down parts, which is consistent with the calculated value of the magnetic moment as zero. The calculated band gap is 2.11 eV. Analysis of PDOS indicates that the VBM for $C_{24}N_{24}$ is dominated by the N 2p state, while CBM is contributed by both N 2p state and C 2p state. This is corroborated with earlier observation based on band decomposed charge density.

8.3.1. Adsorption of Metal on $C_{24}N_{24}$

Different possible adsorption sites for metal binding on $C_{24}N_{24}$ moiety have been considered and the most energetically preferable site is found to be the porphyrine-like N_4 cavity. As can be seen from Figure 8.1b-d, the metal is located slightly above the N_4 plane, equidistant from all the four N atoms. The calculated M-N bond distance values in the optimized geometry are 1.86, 1.83, and 1.82 Å for Fe-$C_{24}N_{24}$, Co-$C_{24}N_{24}$, and Ni-$C_{24}N_{24}$, respectively. The calculated N-M-N bond angle in the respective cases is 143º, 148º, and 154º. This indicates that as we move from Fe to Co to Ni, the metal atom comes closer to the plane of the N_4 unit. The calculated perpendicular distance between the metal element and the plane of N_4 unit are 0.6 Å, 0.5 Å, and 0.4 Å, respectively. This may be correlated with the decreasing atomic radius of the metal element leading to better fit in the cavity. The increase of strength of interaction between the metal and $C_{24}N_{24}$ unit can be correlated with the increase in electronegativity of the metal element. Incorporation of metal in the N_4 cavity leads to reduction in the nearest C-C bond by a small extent (0.05 Å). This may be due to transfer of charge from metal to $C_{24}N_{24}$ unit, which increases

the covalent character of the nearest C-C bond. This is supported by the charge density distribution plot (Figure 8.3a-8.3d), which shows increase of overlap between the carbon charge clouds in presence of the metal. To investigate the electronic structure of these three metal decorated $C_{24}N_{24}$ systems, we calculated the spin polarized DOS. As can be seen from Figure 8.2b-8.2d, the Fermi level is elevated by 1.45 eV, 1.37 eV, and 1.38 eV due to incorporation of Fe, Co, and Ni, respectively. The calculated band gap (difference between the Fermi level and CBM) is reduced to 0.34 eV, 0.66 eV, and 0.69 eV for Fe-$C_{24}N_{24}$, Co-$C_{24}N_{24}$, and Ni-$C_{24}N_{24}$, respectively. This can facilitate charge transport during the ORR process. Analysis of PDOS indicates that in case of Fe-$C_{24}N_{24}$, states close to the Fermi level are contributed by hybridized state of N 2p and C 2p along with some contribution of metal 3d orbitals. However, the metal 3d contribution gradually decreases as we proceed from Fe-$C_{24}N_{24}$ to Co-$C_{24}N_{24}$, to Ni-$C_{24}N_{24}$ system. As can be seen from Table 8.1, the adsorption energy increases in the order Fe-$C_{24}N_{24}$ < Co-$C_{24}N_{24}$ < Ni-$C_{24}N_{24}$. In all the cases, the calculated metal binding energy is found to be negative indicating its stability towards the aggregation, which indicates that there will be no problem of aggregation of metal atoms that leads to the cluster formation.

(a)   (b)   (c)   (d)
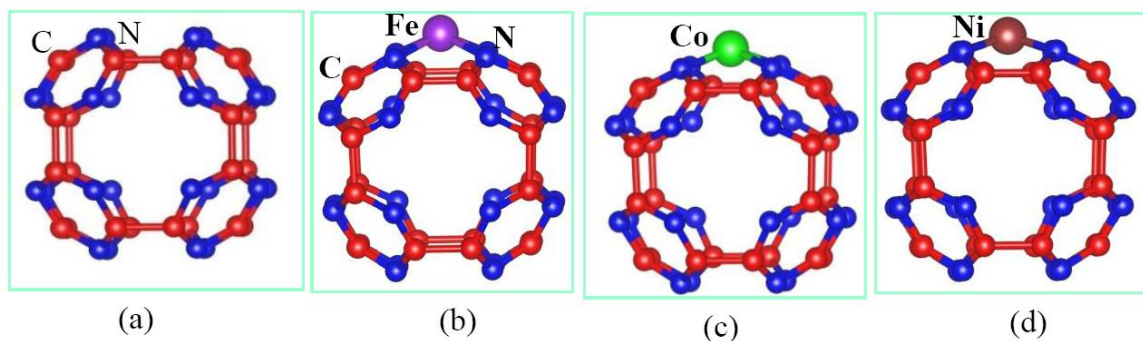
Figure 8.1: Optimized geometries of $C_{24}N_{24}$ (a), Fe-$C_{24}N_{24}$ (b), Co-$C_{24}N_{24}$ (c), and Ni-$C_{24}N_{24}$ (d)
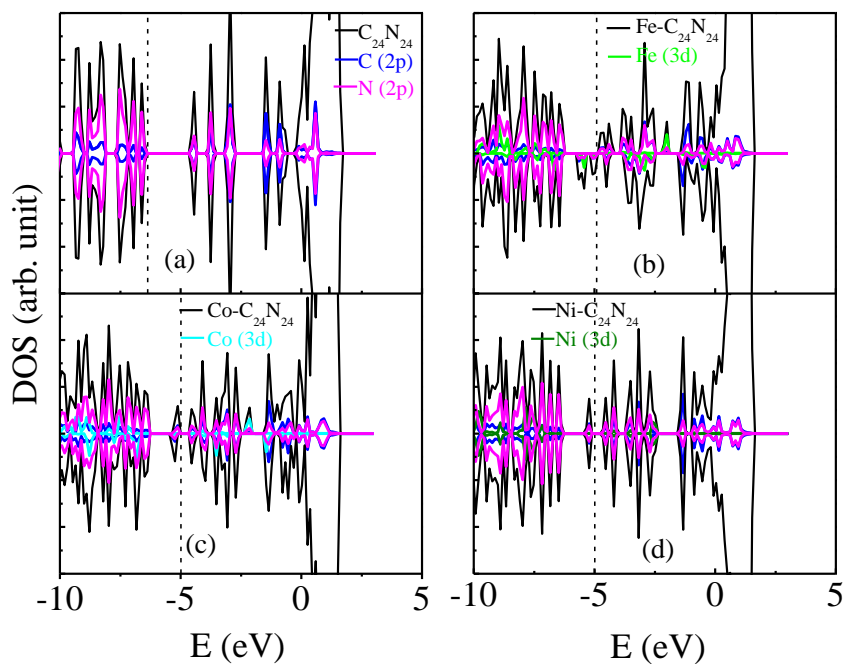
Figure 8.2: Density of states for $C_{24}N_{24}$ (a), Fe-$C_{24}N_{24}$ (b), Co-$C_{24}N_{24}$ (c), and Ni-$C_{24}N_{24}$ (d)
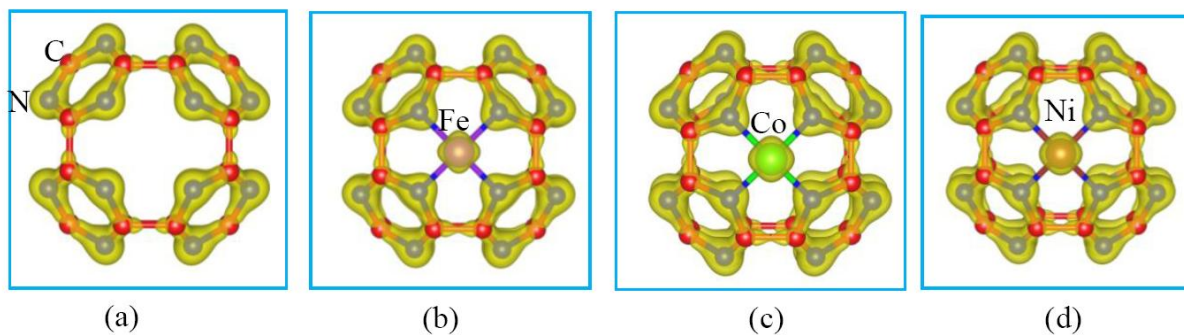
Figure 8.3: Charge density distribution for $C_{24}N_{24}$ (a), Fe-$C_{24}N_{24}$ (b), Co-$C_{24}N_{24}$ (c), and Ni-$C_{24}N_{24}$ (d) (density value considered for the isosurface contour plot is 0.25 electrons per $Å^3$).

Table 8.1: Calculated binding energies for $C_{24}N_{24}$ and metal, and $M-C_{24}N_{24}$ and oxygen molecule.

System	ΔE_M (eV)	ΔE_{O2} (eV)
Fe-C$_{24}$N$_{24}$	-1.77	-1.57
Co-C$_{24}$N$_{24}$	-2.16	-0.68
Ni-C$_{24}$N$_{24}$	-2.31	-0.17

(a) (b) (c)
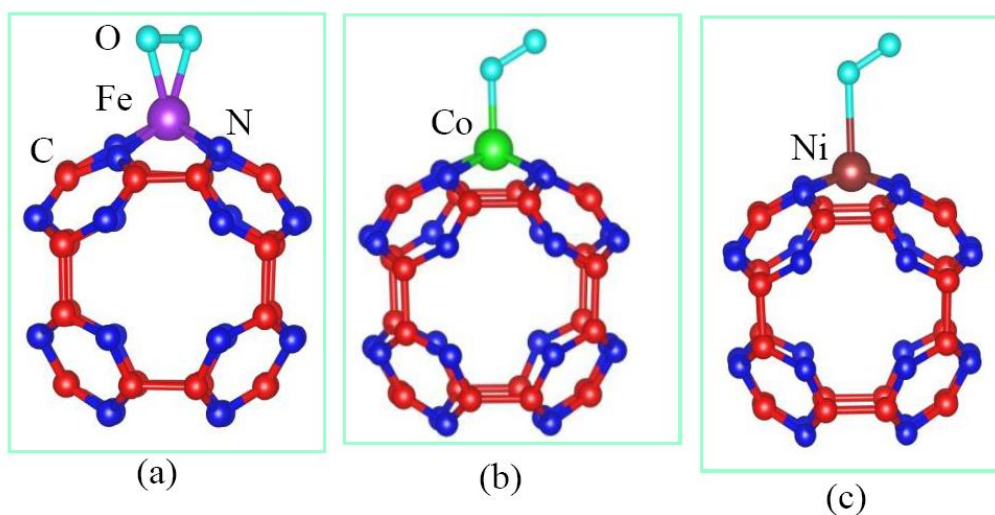
Figure 8.4: Optimized most stable structure of oxygen adsorbed on Fe-C$_{24}$N$_{24}$ (a), Co-C$_{24}$N$_{24}$ (b), and Ni-C$_{24}$N$_{24}$ (c).

8.3.2. Adsorption of Molecular Oxygen on M-C$_{24}$N$_{24}$ Complex

The first necessary step to initiate ORR is the binding of oxygen molecule to the active site of the catalyst. The preferred adsorption site in M-C$_{24}$N$_{24}$ complex is the metal site. Here, we consider

two different geometries for the M-$C_{24}N_{24}$: O_2 adduct. In one case, both the oxygen atoms are attached to the metal centre, and are parallel to the plane of nearest $C_{24}N_{24}$ unit, and the geometry is known as side on mode. The other mode, in which only one of the oxygen atoms is bonded with the metal centre, is known as end on mode. The type of adsorption mode is found to be strongly dependent on the nature of the metal. As for example, in case of Fe-$C_{24}N_{24}$:O_2 adduct both the side on and end on geometries are found. This is consistent with experimental observation of two types of O_2 stretching frequencies for the metal-complex-O_2 adducts. Here, the side on mode is found to be energetically more favorable (Figure 8.4a). The calculated Fe-O distance is found to be 1.88 Å and the O-O bond length is found to be elongated to 1.36 Å, in comparison to 1.23 Å in free oxygen molecule. The elongation of the O-O bond may be correlated to the charge transfer from the Fe 3d-orbital to the antibonding orbital of O 2p, resulting into reduction in the bond order of the adsorbed O_2 molecule. This weakening of the O-O bond is known to facilitate the more desirable four electrons ORR path, which involves splitting of O-O bond in the course of reaction. In case of Co-$C_{24}N_{24}$:O_2 adduct, three types of geometries are found, end on with <Co-O-O= 119º, end on with <Co-O-O= 180º, and the side on mode. However, the end on mode of the first kind is found to be energetically more stable (Figure 8.4b). The calculated Co-O and O-O bond lengths are 1.90 Å and 1.28 Å, respectively. For Ni-$C_{24}N_{24}$:O_2 adduct, the end on geometry with <Co-O-O= 121º and side on geometry are found, where the end on mode is found to be more favorable (Figure 8.4c). The calculated Ni-O and O-O bond lengths are 2.41 Å and 1.25 Å, respectively. This indicates that the interaction of oxygen molecule with M-$C_{24}N_{24}$ system is minima in the case of Ni-$C_{24}N_{24}$. The strength of adsorption of oxygen molecule on the M-$C_{24}N_{24}$ system is also reflected in the binding energy value. Table 8.1 shows the oxygen molecule binding energies to the three M-$C_{24}N_{24}$ systems as -

1.57 eV, -0.68, and -0.17 eV, respectively. According to the Sabatier principle, the O_2 adsorption energy on the catalyst surface should be large enough to prevent desorption of O_2 molecule from catalyst surface and small enough for ORR process to proceed at a significant rate. Hence, Co-$C_{24}N_{24}$ system is expected to be the most suitable among the three systems studied here. However, there are lots of things to be checked before drawing any final conclusion.
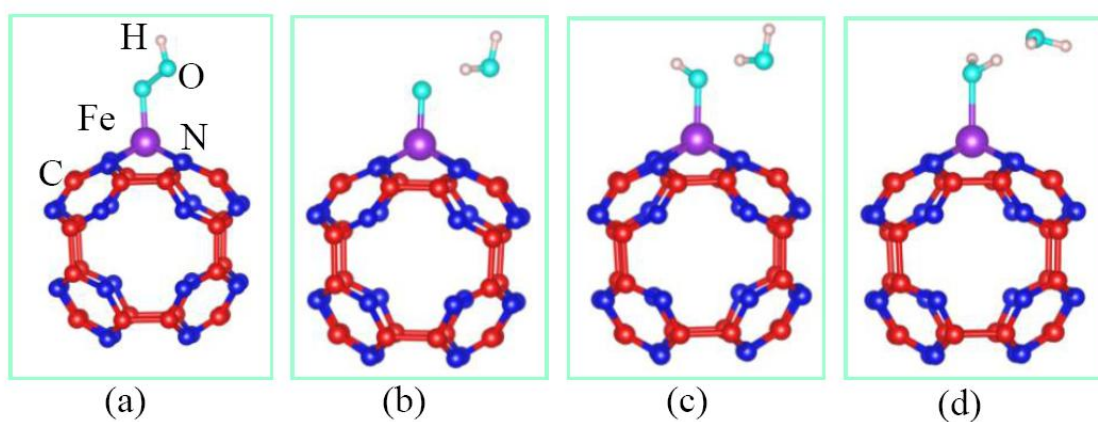
Figure 8.5: Optimized most stable structures of Fe-$C_{24}N_{24}$-OOH (a), Fe-$C_{24}N_{24}$-O-OH$_2$ (b), Fe-$C_{24}N_{24}$-OH-OH$_2$ (c), and Fe-$C_{24}N_{24}$-OH$_2$-OH$_2$ (d).
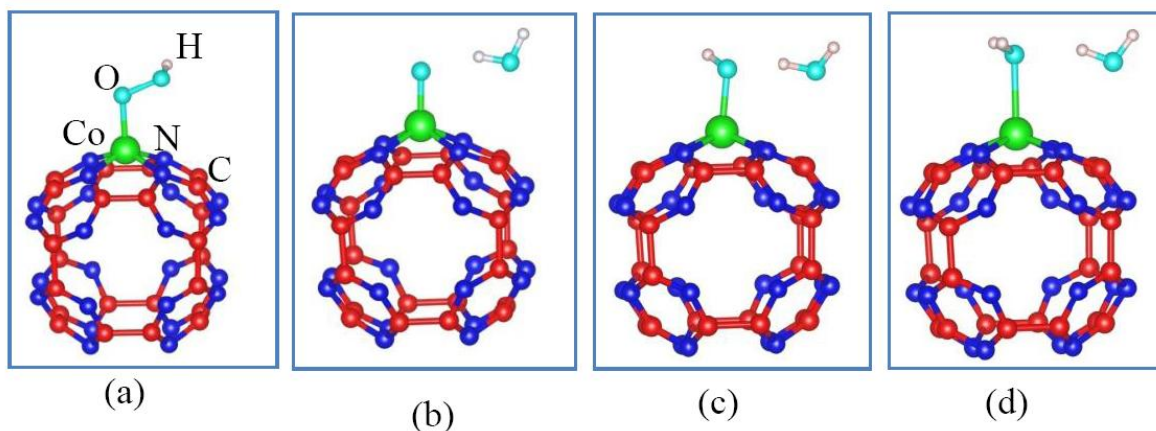
Figure 8.6: Optimized most stable structure of Co-C$_{24}$N$_{24}$-OOH (a), Co-C$_{24}$N$_{24}$-O-OH$_2$ (b), Co-C$_{24}$N$_{24}$-OH-OH$_2$ (c), and Co-C$_{24}$N$_{24}$-OH$_2$-OH$_2$ (d).
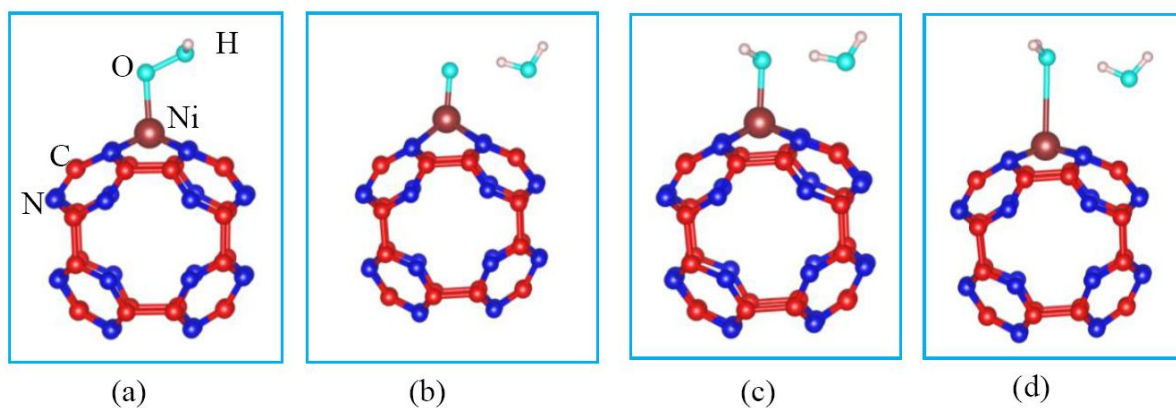
Figure 8.7: Optimized most stable structure of Ni-C$_{24}$N$_{24}$-OOH (a), Ni-C$_{24}$N$_{24}$-O-OH$_2$ (b), Ni-C$_{24}$N$_{24}$-OH-OH$_2$ (c), and Ni-C$_{24}$N$_{24}$-OH$_2$-OH$_2$ (d).

Table 8.2: Calculated free energy change (eV) for different intermediate steps of ORR on Fe-$C_{24}N_{24}$, Co-$C_{24}N_{24}$, and Ni-$C_{24}N_{24}$ systems.

	Fe-$C_{24}N_{24}$	Co-$C_{24}N_{24}$	Ni-$C_{24}N_{24}$
ΔG_1	-1.54	-0.91	-0.37
ΔG_2	-0.36	-0.36	0.13
ΔG_3	-2.11	-1.39	-1.31
ΔG_4	-0.89	-1.46	-1.65
ΔG_5	-0.02	-0.81	-1.72

8.3.3. Oxygen Reduction Path on Fe-$C_{24}N_{24}$ and Co-$C_{24}N_{24}$ systems

The ORR may proceed through either the four electron path or two electron pathways. In the case of four electron path, water is produced as the final product, while the two electron path produces hydrogen peroxide as the final product.

$$O_2 + 4(H^+ + e^-) \rightarrow 2H_2O$$
$$O_2 + 2(H^+ + e^-) \rightarrow 2H_2O_2$$
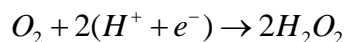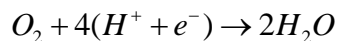
To achieve maximum power output in a fuel cell, the ORR should proceed through four electron path. This is due to more negative free energy change associated with the process:

$$\tfrac{1}{4}O_2 + \tfrac{1}{2}H_2 \rightarrow \tfrac{1}{2}H_2O \qquad \Delta G^o = \text{-118.6 kJ/mol}$$
$$\tfrac{1}{2}O_2 + \tfrac{1}{2}H_2 \rightarrow \tfrac{1}{2}H_2O_2 \qquad \Delta G^o = \text{-67.1 kJ/mol}$$
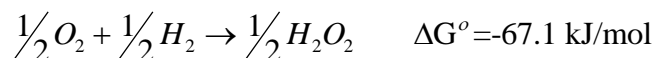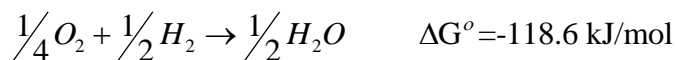
Moreover, the presence of excess hydrogen peroxide can lead to generation of peroxide radicals, which can have adverse effect on cell materials.

Now, we discuss the progress of ORR on the M-$C_{24}N_{24}$ system. The reaction starts with the chemisorption of O_2 molecule on the M-$C_{24}N_{24}$ system. The second step is the hydrogenation of the chemisorbed O_2 to form OOH adsorbed on M-$C_{24}N_{24}$ system. Then the adsorbed OOH undergoes hydrogenation reaction, resulting into splitting of the O-O bond, and formation of first water molecule, leaving one oxygen atom adsorbed on the M-$C_{24}N_{24}$ system. The M-$C_{24}N_{24}$-O system produces a second molecule of water through sequential hydrogenation reaction, and regenerates the catalyst. We have calculated the free energy change of the different steps involved during ORR on the M-$C_{24}N_{24}$ system, and the results are reported in Table 8.2. The free energy of oxygen molecule has been calculated from the total free energy change of the reaction, $H_2 + O_2 \rightarrow 2H_2O$, ($\Delta$G= 4.92 eV), and the free energy values of H_2 and H_2O, calculated by using DFT with PBE functional.

The first step involves the reaction between M-$C_{24}N_{24}$ system and oxygen molecule as

$$M - C_{24}N_{24} + O_2 + 4(H^+ + e^-) \rightarrow M - C_{24}N_{24} - OO + 4(H^+ + e^-)$$
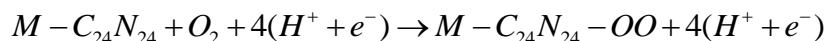
The reaction free energy for Fe-$C_{24}N_{24}$ system is found to be highly negative (exothermic). The calculated free energy change (ΔG_1) in this step is -1.54, -0.91 eV and -0.37 eV for Fe-$C_{24}N_{24}$, Co-$C_{24}N_{24}$, and Ni-$C_{24}N_{24}$ systems, respectively. This is consistent with the inference drawn in previous section based on their oxygen affinity.

The second step is the hydrogenation of the chemisorbed O_2 (Figure 8.5a, 8.6a, and 8.7a) and can be shown as

$$M - C_{24}N_{24} - OO + 4(H^+ + e^-) \rightarrow M - C_{24}N_{24} - OOH + 3(H^+ + e^-)$$
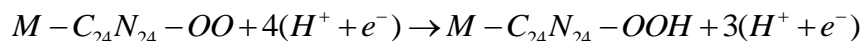
Although, the calculated reaction free energy is negative (exothermic) for Fe-$C_{24}N_{24}$ and Co-$C_{24}N_{24}$ systems, it is positive (endothermic) for Ni-$C_{24}N_{24}$ systems. The free energy change (ΔG_2) for both Fe-$C_{24}N_{24}$ and Co-$C_{24}N_{24}$ systems are found to be equal to -0.36 eV, while for Ni-

$C_{24}N_{24}$ systems it is 0.13 eV. This indicates that this step is unfavorable for the Ni-$C_{24}N_{24}$ system. The O-O bond length increases to 1.47 Å, 1.43 Å, and 1.42 Å, while the Fe-O and Co-O bond length remains almost the same (1.78 Å, 1.86 Å, and 1.96 Å, respectively). The maximum enlargement of the O-O bond for Fe-$C_{24}N_{24}$ system may be due to the side on configuration of the Fe-$C_{24}N_{24}$:O_2 adduct.

The third step involves adsorption of one more hydrogen to the M-$C_{24}N_{24}$-OOH species. There are two possible O-sites for the H, viz. the oxygen directly attached to the metal (O1) and the other oxygen (O2), where one hydrogen is already attached. For all the three systems, Fe-$C_{24}N_{24}$-OOH, Co-$C_{24}N_{24}$-OOH, and Ni-$C_{24}N_{24}$-OOH, the second oxygen (O2) is found to be energetically more preferable (Figure 8.5b, 8.6b, and 8.7b). This indicates that ORR on this system follows the more efficient four electron path. This step can be shown as

$$M - C_{24}N_{24} - OOH + 3(H^+ + e^-) \rightarrow M - C_{24}N_{24} - O + H_2O + 2(H^+ + e^-)$$
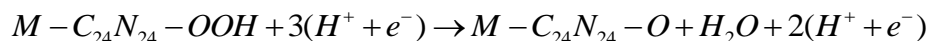
The reaction free energy for the Fe-$C_{24}N_{24}$ system is found to be highly negative (exothermic). The calculated free energy change (ΔG_3) is found to be -2.11, -1.39 eV and -1.31 eV for Fe-$C_{24}N_{24}$, Co-$C_{24}N_{24}$, and Ni-$C_{24}N_{24}$ systems, respectively. The O-O bond cleavage occurs in this step, which leads to reduction of the metal-oxygen bond length to 1.65 Å, 1.70 Å, and 1.72 Å, in Fe, Co, and Ni based systems, respectively.

The oxygen attached to the metal center is now available for reaction with hydrogen, resulting into the formation of M-$C_{24}N_{24}$-OH species (Figure 8.5c, 8.6c, and 8.7c). This step can be expressed as

$$M - C_{24}N_{24} - O + 2(H^+ + e^-) \rightarrow M - C_{24}N_{24} - OH + (H^+ + e^-)$$
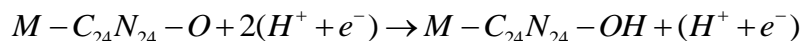
The reaction free energy is more negative (exothermic) for Co-$C_{24}N_{24}$ and Ni-$C_{24}N_{24}$ systems, than the Fe-$C_{24}N_{24}$ system. The calculated free energy change (ΔG_4) for this step is found to be -

0.89 eV, -1.46 eV, and -1.65 eV for Fe-$C_{24}N_{24}$, Co-$C_{24}N_{24}$, and Ni-$C_{24}N_{24}$ systems, respectively. It may be also noted that the adsorption of hydrogen leads to increase in metal-oxygen bond length to 1.83 Å, 1.90 Å, and 1.91 Å, respectively. The M-$C_{24}N_{24}$-OH species again picks one hydrogen to form water molecule (Figure 8.5d, 8.6d, and 8.7d), which is then detached from the system as

$$M - C_{24}N_{24} - OH + H^+ + e^- \rightarrow M - C_{24}N_{24} + H_2O$$
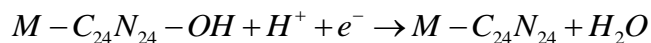
The calculated free energy change (ΔG_5) for this step is -0.02 eV, -0.81 eV, and -1.72 eV for Fe-$C_{24}N_{24}$, Co-$C_{24}N_{24}$, and Ni-$C_{24}N_{24}$ systems, respectively. Large negative value of free energy change for Ni-$C_{24}N_{24}$ system arises due to the weak Ni-O bond.

8.3.4. Effect of Electrode Potential

In the last section, it has been demonstrated that ORR on M-$C_{24}N_{24}$ system can be made to proceed through the more desirable four electron reduction pathway. However, these calculations are carried out in absence of any electrode potential, which is important in practical cases. Therefore, we have also investigated the effect of varying electrode potential on the free energy profiles. For plotting the free energy profiles we considered the gas phase energy of water molecules as the reference energy. As can be seen from Figure 8.8, at zero potential all the ORR steps on Fe-$C_{24}N_{24}$, and Co-$C_{24}N_{24}$ systems are downhill, while the hydrogenation reaction steps for Ni-$C_{24}N_{24}$: O_2 adduct is uphill. Therefore, Ni-$C_{24}N_{24}$ system may not be suitable for ORR. With the increase of potential, some of the reaction steps turn out to be uphill for Fe-$C_{24}N_{24}$, and Co-$C_{24}N_{24}$ systems. As for example, at potential U= 0.4 V all the ORR steps on Fe-$C_{24}N_{24}$ system are downhill except for the last step, i.e., water formation step. This may be due to strong interaction between Fe-$C_{24}N_{24}$ unit and OH. Interestingly, all the ORR steps are downhill for Co-

$C_{24}N_{24}$ system even at U= 0.4 V. However, at potential U= 0.8 V the steps from $*O_2$ to $*OOH$ on $Co-C_{24}N_{24}$ turns out to be uphill. This indicates that the hydrogenation reaction of $Co-C_{24}N_{24}:O_2$ adduct is rate determining. The calculated maximum values of potential at which all the reaction steps are downhill (known as onset potential) is 0.4 V on $Co-C_{24}N_{24}$ system. Thus the present study reveals that the Co-decorated system is more efficient in comparison to Fe and Ni decorated $C_{24}N_{24}$ systems for ORR.
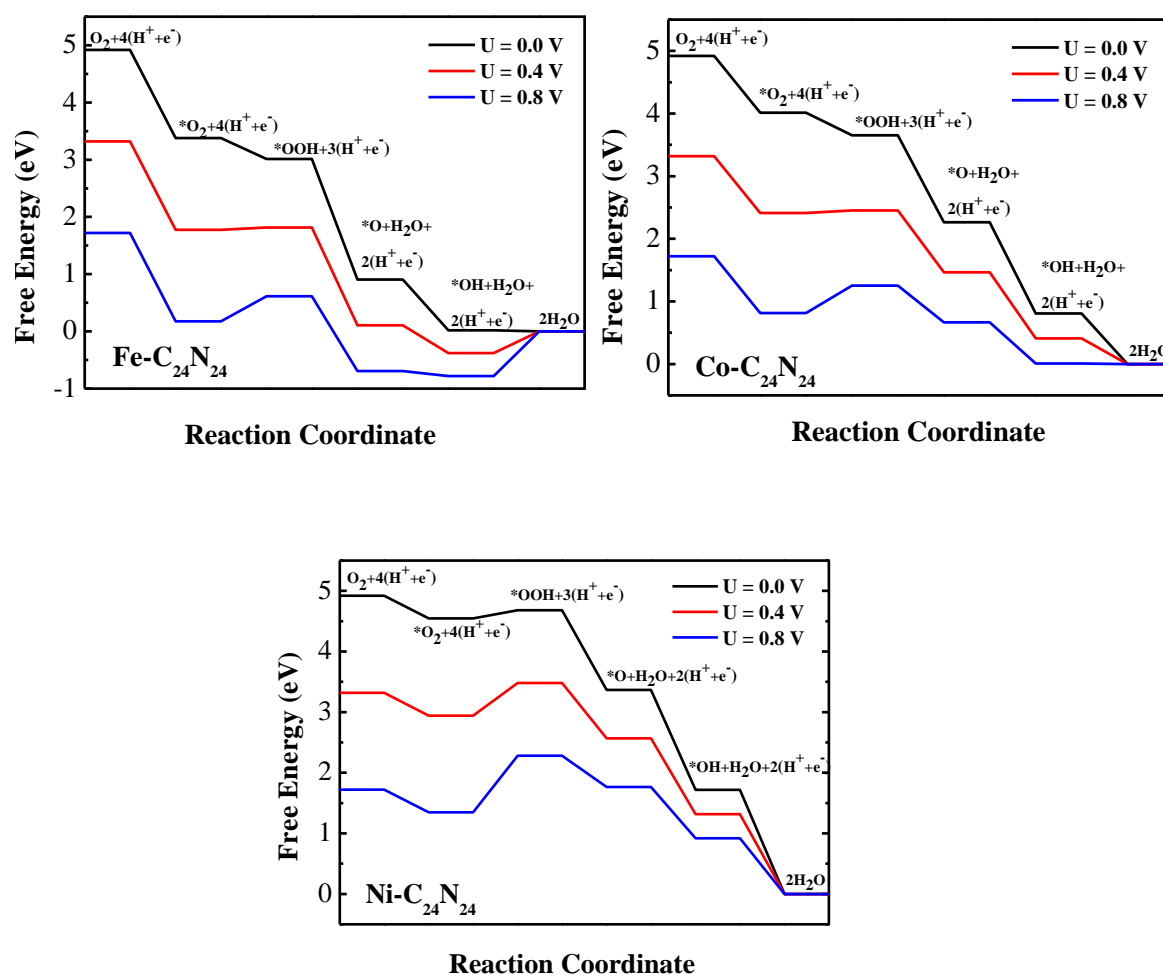
Figure 8.8: Free energy plot of ORR on $Fe-C_{24}N_{24}$, $Co-C_{24}N_{24}$, and $Ni-C_{24}N_{24}$ system.

8.4. Conclusions

In this study, we have explored transition metal decorated $C_{24}N_{24}$ system as a new kind of non-precious catalyst for ORR using DFT as a tool. The metal binding energies to the fullerene-like framework are found to be negative indicating their stability towards metal aggregation. We have systematically investigated the possible mechanism of ORR reaction on Fe, Co and Ni-decorated $C_{24}N_{24}$ systems. This includes calculation of adsorption energies of the ORR species and energetics of all the intermediate steps on the three systems. We have shown that ORR on these three systems proceeds through more efficient four electron reduction path. The present study reveals that among the three systems, the O_2 adsorption energy on the Co-$C_{24}N_{24}$ is in the desirable range to prevent desorption and to sufficiently activate the O_2 molecule to proceed through ORR steps at a significant rate. Our analysis also suggests that hydrogenation of Co-$C_{24}N_{24}$:O_2 adduct is the rate determining step. The free energy profiles for the ORR reaction indicate that, all the steps on Co-$C_{24}N_{24}$ are downhill even at increased electrode potential of U= 0.4 V. Thus, the present theoretical study predicts Co-$C_{24}N_{24}$ as the most efficient catalyst for the ORR as compared to Ni-$C_{24}N_{24}$ and Fe-$C_{24}N_{24}$ systems.

Chapter 9

Outlook and Future Explorations

In this final concluding Chapter we present a brief conclusion of the work described in Chapter 3-8, and also some future extensions of these studies. Using the density functional based electronic structure calculations, we have designed a perovskite based photocatalyst for the generation of hydrogen via visible light driven water splitting. To develop efficient materials for hydrogen storage, we have investigated different the light metal decorated carbon porous nanostructures which can adsorb molecular hydrogen. Finally, calculations for designing new materials for the efficient oxygen reduction reaction have been carried out.

Chapter 3 deal with the effect of codoping with different cation-anion pair and anion-anion pair to form charge compensated and noncompensated $NaTaO_3$ aiming to improve its photocatalytic activity under visible light. In case of charge compensated codoping the localized impurity states are completely passivated, and the impurity states lie just adjacent to the band edges to form a continuum band structure. This ensures improved charge carrier mobility in the codoped system. However, anion-anion pair results narrowing of band gap by a smaller extent than that in presence of cation-anion codoping. Among different pair, copding with (Mo, N) has been found to be the best for improving the visible light photocatalytic activity of $NaTaO_3$.

In chapter 4, we have adopted codoping approach with various dopant pair to improve the photocatalytic behavior of $SrTiO_3$ under visible light. We have shown that codoping with either with pentavalent metal (Sb, V, Nb, and Ta) or hexavalent metal (Mo, W) successfully reduces the band gap without encountering any localized mid gap states, thus ensures enhanced photoconversion efficiency in comparison to that of the monodoped systems. Since the narrowing of band gap is not sufficient to enhance the visible light activity by a significant extent, we further studied with different pair, including (Rh, Sb), (Rh, La), (Rh, F), and (Rh, V/Nb/Ta). The band gap reduces significantly to 1.66 eV on codoping with V

and Rh at the Ti lattice. This is due to lower energy of V 3d orbital with respect to Ti 3d orbital. To the best of our knowledge, calculated band gap for (V, Rh)-codoped $SrTiO_3$ is the lowest among the doped $SrTiO_3$ with overall water splitting capability, reported to date.

Chapter 5 describes a systematic investigation to explore the effect of several anionic dopants on the electronic structure of $KTaO_3$. In all the codoped cases, clear band structure is produced, ensuring good photoconversion efficiency. The present study reveals that the extent of band gap narrowing in case of codoping with N and F is quite significant (almost 1 eV) to improve the visible light activity of $KTaO_3$ effectively. This Chapter also discusses the effect of doping with N and W on the geometry and electronic structure of $KNbO_3$. Interestingly, a highly favourable band structure is produced with reduced band gap when both N and W are simultaneously doped into the crystal structure of $KNbO_3$.

Chapter 6 discusses the strategy of improving the photocatalytic activity of s-triazine based graphitic carbon nitride (g-CN), which is a potential photocatalyst for water splitting, through metal decoration. Our aim is to reduce the band gap in a controlled way by decorating with different noble metal elements, Pt, Pd, Ag, and Au. We have extended this study, to investigate the electronic structure of graphitic carbon nitride decorated with the cluster (Pt_4, Pd_4, Ag_4, and Au_4). Among them Ag_4-graphitic carbon nitride is shown to be the most promising due to reduced band gap as well as suitable for overall water splitting.

Chapter 7 explores porus graphitic carbon nitride of the kind $g-C_4N_3$ decorated with Li and Na as a potential material for hydrogen storage. The unique properties are due to the high adsorption energies of these elements over nitrogen triangular holes. The materials have the additional advantage that they are stable against clustering of the metal elements. The adsorption energies of hydrogen molecules on these metals are in the range for efficient hydrogen storage applications.

Chapter 8 discusses the development of new catalyst for the oxygen reduction reaction (ORR) at fuel cells, which is almost 6 times slower in comparison to the anodic oxidation process, and is considered as the rate limiting step in fuel cell. Here, we have investigated the catalytic activity of the transition metal (Fe, Co and Ni) decorated porphyrene line fullerene ($C_{24}N_{24}$) for the ORR. Present study reveals that the Fe and Co decorated systems are active whereas the Ni decorated system is almost inert due to poor O_2 binding energy in the later case. A systematic study of the possible ORR paths are carried out on both Fe and Co decorated $C_{24}N_{24}$ system. The changes in free energy for all the steps discussed for both Fe and Co systems. The free energy profiles at different electrode potentials are also plotted to see whether all the reaction steps are downhill or not at zero potential, at higher potentials. Present study reveal that both Fe and Co decorated $C_{24}N_{24}$ system are potential materials for ORR in fuel cell.

The present work can be extended to the surface, so that the kinetic of the different steps involved during water splitting can be investigated thoroughly. Besides, heterojunction type materials may be of interest for the photocatalyst for water splitting due to efficient separation of photogenerated charge carriers. In addition, development of efficient cocatalyst is also considered to be one of the potential areas of research in this field.

REFERENCES:

(1) Hoffert, M. I.; Caldeira, K.; Jain, A. K.; Haites, E. F.; Harvey, L. D. D.; Potter, S. D.; Schlesinger, M. E.; Schneider, S. H.; Watts, R. G.; Wigley, T. M. L. Wuebbles, D. J. *Nature* **1998**, *395*, 891.

(2) Raupach, M. R.; Marland, G.; Ciais, P.; Quéré, C.; Canadell, J. G.; Klepper, G.; Field, C. B. *Proc. Natl Acad. Sci. USA* **2007**, *104*, 10288.

(3) Armaroli, N.; Balzani, V. *Chem. Asian J.* **2011**, *6*, 768.

(4) Conway, T. & Tans, P. Trends in atmospheric carbon dioxide. http://www.esrl.noaa.gov/gmd/ccgg/trends (2011).

(5) Züttel, A.: Remhof, A.; Borgschulte, A.; Friedrichs, O. *Phil. Trans. R. Soc. A* **2010**, *368*, 3329.

(6) Coontz, R.; Hanson, B. *Science* **2004**, *305*, 957.

(7) Crabtree, G. W.; Dresselhaus, M. S.; Buchanan, M. V. *Phys. Today* **2004**, *57*, 39.

(8) Lewis, N. S.; Nocera, D. G. *Proc. Natl. Acad. Sci. U.S.A.* **2006**, *103*, 15729.

(9) Midilli, A.; Dincer, I. *Int. J. Hydrogen Energy* **2008**, *33*, 4209

(10) Lubitz, W.; Tumas, W. *Chem. Rev.* **2007**, *107*, 3900.

(11) Ibrahim, H.; Ilinca, A.; Perron, J. *Renewable Sustainable Energy Rev.* **2008**, *12*, 1221.

(12) Schlapbach, L.; Züttel, A. *Nature* **2001**, *414*, 353.

(13) http://www.cleanenergystates.org/

(14) Pagliar M.; Konstandopoulos, A. G. The Royal Society of Chemistry, Cambridge CB4 0WF, UK

(15) Krishnan Rajeshwar, Robert McConnell, Stuart Licht. Spring Street, New York

(16) Russell, C. Chem. World, August 2003. www.rsc.org/chemistryworld/ Issues/2003/August/electrolysis.asp

(17) Turner, J.; Sverdrup, G.; Mann, M. K.; Maness, P.; Kroposki, B.; Ghirardi, M.; Evans,

R. J.; Blake, D. *Int. J. Energy Res*. **2008**, *32,* 379

(18) Funk, J. E. *Int. J. Hydrogen Energy* **2001**, *26*, 185.

(19) Rosen, M. A. *Energy* **2010**, *35*, 1068.

(20) Abanades, S.; Charvin, P.; Flamant, G.; Neveu, P. *Energy* **2006**, *31*, 2805.

(21) Maeda, K.; Domen, K. *J. Phys. Chem. Lett.* **2010**, *1*, 2655.

(22) Navarro, R. M.; Sánchez-Sánchez, M. C.; Alvarez-Galvan, M. C.; del Valle, F.;

Fierro, J. L. G. *Energy Environ. Sci.,* **2009**, *2*, 35.

(23) Fujishima, A.; Honda, K. *Nature* **1972**, *238*, 37.

(24) Chen, X.; Shen, S.; Guo, L.; Mao, S. S. *Chem. Rev*. **2010**,*110*, 6503.

(25) Kudo, A.; Kato, H.; Tsuji, I. *Chem. Lett.*, **2004**, *33*, 1532.

(26) Abe, R. *J. Photochem. Photobiol. C*, **2010**, *11*, 179.

(27) Kudo, A.; Miseki, Y. *Chem. Soc. Rev*. **2009**, *38*, 253–278.

(28) Takanabe, K.; Kamata, K.; Wang, X.; Antonietti, M.; Kubota, J.; Domen, K.

Phys. Chem. Chem. Phys., **2010**, *12*, 13020.

(29) Houlding, V. H.; Gräzel, M. *J. Am. Chem. Soc.*, **1983**, *105*, 5695.

(30) Abe, R.; Sayama, K.; Arakawa, H. *J. Photochem. Photobiol., A*, 2004, **166**, 115.

(31) Abe, R.; Hara, K.; Sayama, K.; Domen, K.; Arakawa, H. *J.Photochem. Photobiol. A*,

200, *137*, 63.

(32) Amano, F.; Prieto-Mahaney, O. O.; Terada, Y.; Yasumoto, T.; Shibayama, T.; Ohtani, B.

Chem. Mater., **2009**, *21*, 2601.

(33) Bu, Y.; Chen, Z.; Li, W.; Yu, J. *ACS Appl. Mater. Interfaces*, **2013**, *5*, 5097.

(34) Cho, I. S.; Chen, Z. B.; Forman, A. J.; Kim, D. R.; Rao, P. M.; Jaramillo, T. F.; Zheng,

X. L. *Nano Lett.*, **2011**, *11*, 4978.

(35) Wang, H.; Quan, X.; Zhang, Y. B.; Chen, S. *Nanotechnology*, **2008**, *19*, 065704.

(36) Chang, H. T.; Wu, N. M.; Zhu, F. *Water Res.*, **2000**, *34*, 407.

(37) Arabatzis, M. I.; Falaras, P. *Nano Lett.*, **2003**, *3*, 249.

(38) Pan, J. H.; Cai, Z.; Yu, Y.; Zhao, X. S. *J. Mater. Chem.*, **2011**, *21*, 11430.

(39) Sameshima, T.; Sakamoto, K.; Asada, K.; Kondo, M.; Matsuda, A.; Higashi, S. *Sol. Energ. Mat. Sol.* **2001**, *65*, 577.

(40) Zhang, X.; Li, H.; Cui, X.; Lin, Y. *J. Mater. Chem.* **2010**, *20*, 2801.

(41) Wang, J.; Tafen, D. N.; Lewis, J. P.; Hong, Z.; Manivannan, A.; Zhi, M.; Li, M.; Wu, N. *J. Am. Chem. Soc.* **2009**, *131*, 12290.

(42) Wu, N.; Lee, M.; Pon, Z.; Hsu, J. *J. Photochem. Photobiol. A: Chem.* **2004**, *163*, 277.

(43) Kawai, T.; Sakata, T. *Nature*, **1979**, *282*, 283.

(44) Kawai T.; Sakata, T. *J. Chem. Soc., Chem. Commun.,* **1979**,1047.

(45) Kawai T., Sakata, T. *Nature* (London, U. K.), 1980, *286*, 474.

(46) Kawai T.; Sakata, T. *J. Chem. Soc., Chem. Commun.,* **1980**, 694.

(47) Kawai T.; Sakata, T. *Chem. Lett.* **1981**, *10*, 81.

(48) Sakata T.; Kawai, T. *Nouv. J. Chim.,* **1981**, *5*, 579.

(49) Fan, W.; Lai, W.; Zhang, Q.; Wang, Y. *J. Phys. Chem. C*, **2011**, *115*, 10694.

(50) Tran, P. D.; Batabyal, S. K.; Pramana, S. S.; Barber, J.; Wong, L. H.; Loo, S. C. J. *Nanoscale*, **2012**, *4*, 3875.

(51) Wu, H.; Xu, M.; Da, P.; Li, W.; Jia, D.; Zheng, G. *Phys. Chem.Chem. Phys.*, **2013**.

(52) Yu, J.; Qi, L.; Jaroniec, M. *J. Phys. Chem. C* **2010**, *114*, 13118.

(53) Jiang, J. Li, H.; Zhang, L. *Chem. Eur. J.* **2012**, *18*, 6360.

(54) Ingram D. B.; Linic, S. *J. Am. Chem. Soc.* **2011**, *133*, 5202.

(55) Ahmadi, T.; Wang, Z. L.; Green, T. C.; Henglein, A. El-Sayed, M. *Science*, **1996**, *272*, 1924.

(56) Maeda, K. *ACS Catal.* **2013**, *3*, 1486−1503

(57) Li, X.; Yu, J.; Low, J.; Fang, Y.; Xiaoc J.; Chen, X. *J. Mater. Chem. A*, **2015**, *3*, 2485–2534

(58) Serpone N.; Emeline, A. V. *J. Phys. Chem. Lett.,* **2012**, *3*, 673–677.

(59) Mocatta, D.; Cohen, G.; Schattner, J.; Millo, O.; Rabani, E. Banin, U. *Science*, **2011**, *332*, 77–81.

(60) Cao, Y. C. *Science*, **2011**, *332*, 48–49.

(61) Asahi, R.; Morikawa, T.; Ohwaki, T.; Aoki, K.; Taga, Y. *Science* **2001,** 293, 269-271.

(62) Khan, S. U. M.; Al-Shahry, M.; Ingler, W. B. J., *Science* **2002**, *297*, 2243-2245.

(63) Srinivasu, K.; Modak, B.; Ghosh, S. K. *J. Phys. Chem. C* **2014**, *118*, 26479−26484.

(64) Gai, Y.; Li, J.; Li, S.-S.; Xia, J.-B.; Wei, S.-H. *Phys. Rev. Lett.* **2009**, *102*, 036402.

(65) Modak, B.; Srinivasu, K.; Ghosh, S. K. *Phys. Chem. Chem. Phys.* **2014**, *16*, 17116−17124.

(66) Modak, B.; Srinivasu, K.; Ghosh, S. K. *J. Phys. Chem. C* **2014**, *118*, 10711−10719.

(67) Modak, B.; Ghosh, S. K. *Chem. Phys. Lett.* **2014**, *613*, 54–58

(68) Modak, B.; Srinivasu, K.; Ghosh, S. K. *Phys. Chem. Chem. Phys.* **2014**, *16*, 24527-24535.

(69) Modak, B.; Srinivasu, K.; Ghosh, S. K. *RSC Adv.* **2014**, *4*, 45703–45709.

(70) Modak, B.; Ghosh, S. K. *J. Phys. Chem. B* **2015**, *119*, 11089−11098.

(71) Modak, B.; Ghosh, S. K. *J. Phys. Chem. C* **2015**, *119*, 7215−7224.

(72) Modak, B.; Ghosh, S. K. *Phys. Chem. Chem. Phys.* **2015,** *17, 15274-15283.*

(73) Modak, B.; Ghosh, S. K. *J. Phys. Chem. C* **2015***, 119,* 23503−23514*.*

(74) Grochala, W.; Edward, P. P. *Chem. Rev.***2004**, *104*, 1283.

(75) Reilly, J. J. *Metal Hydrides as Hydrogen Storage and their Applications*, CRC Press, Cleveland, OH, **1977.**

(76) Fukai, Y. *The Metal–Hydrogen System*, 2nd ed., Springer, Berlin, **2005**.

(77) Chae, H. K.; Siberio-Pérez, D. Y.; Kim, J.; Go, Y.; Eddaoudi, M.; Matzger, A. J.; O'Keeffe, M.; Yaghi, O. M. *Nature* **2004**, *427*, 523.

(78) Yaghi, O. M.; Li, G.; Li, H. *Nature*, **1995**, *378*, 703.

(79) Rowsell, J. L. C.; Yaghi, O. M. *Microporous and Mesoporous Materials* **2004**, *73*, 3.

(80) James, S. L. *Chem. Soc. Rev.*, **2003**, *32*, 276.

(81) Rowsel, J. L. C.; Millward, A. R.; Park, K. S.; Yaghi, O. M. *J. Am. Chem. Soc.*, **2004**, *126*, 5666.

(82) Rosi, N. L.; Eckert, J.; Eddaoudi, M.; Vodak, D. T.; Kim, J.; O'keeffe, M.; Yaghi, O. M. *Science.* **2003**, *300*, 1127.

(83) Rowsel, J. L. C.; Yaghi, O. M. *Angew. Chem., Int. Ed*. **2005**, *44*, 4670. (c) Muller, T.; Ceder, G. *J. Phys. Chem. B* **2005,** *109,* 17974.

(84) Dimitrakakis, G. K.; E.; Froudakis, G. E. *Nano Lett.*, **2008**, *8*, 3166.

(85) Deng, W.; Xu, X.; Goddard, W. A.; *Phys. Rev. Lett*. **2004**, *92*, 166103.

(86) Chandrakumar, K. R. S.; Ghosh, S. K. *Nano Lett.*, **2008**, *8*, 13.

(87) White, C. M.; Steeper, R. R.; Lutz, A. E. *Int. J. Hydrogen Energy* **2006**, *31*, 1292.

(88) Trimm, D. L.; Onsan, Z. I. *Catal. Rev*. **2001**, *43*, 31

(89) Carrette, L.; Friedrich, K. A.; Stimming, U. *ChemPhysChem,* **2000**, *1*, 162, *Fuel Cells*, **2001**, *1*, 5.

(90) Steele, B. C. H.; Heinzel, A. *Nature*, **2001**, *414*, 345.

(91) Debe, M. K. *Nature* **2012**, *486*, 43.

(92) Schrodinger, E. *Phys. Rev.* **1926**, *28*, 1049-1070.

(93) Born, M.; Oppenheimer, J. R. *Ann. Physik.* **1927**, *41*, 457-484.

(94) Hartree, D. R. *Proc. Cambridge. Philos. Soc.* **1928**, *24*, 89-110.

(95) Fock, V. *Z. Physik.* **1930**, *61*, 126-148.

(96) Moller, C.; Plesset, M. S. *Phys. Rev.* **1934**, *46*, 618-622.

(97) Cizek, J. *J. Chem. Phys.* **1966**, *45*, 4256-4266.

(98) Thomas, L. H. *Proc. Cambridge. Philos. Soc.* **1927**, *23*, 542-548.

(99) Fermi, E. *Rend. Accad. Naz. Lincei* **1927**, *6*, 602-607.

(100) Dirac, P. A. M. *Proc. Cambridge. Philos. Soc.* **1930**, *26*, 376-385.

(101) Hohenberg, P.; Kohn, W. *Phys. Rev.* **1964**, *136*, B864-B871.

(102) Kohn, W.; Sham, L. J. *Phys. Rev.* **1965**, *140*, A1133-A1138.

(103) Vosko, S. J.; Wilk, L.; Nusair, M. *Can. J. Phys.* **1980**, *58*, 1200-1211.

(104) Perdew, J. P.; Burke, K.; Ernzerhof, M. *Phys. Rev. Lett.* **1996**, *77*, 3865−3868.

(105) Perdew, J. P.; Wang, W. *Phys. Rev. B* **1992**, *45*, 13244-13249.

(106) Becke, A. D. *Phys. Rev. A* **1988**, *38*, 3098-3100.

(107) Paier, J.; Marsman, M.; Hummer, K.; Kresse, G.; Gerber, I. C.; Ángyán, J. G. Screened Hybrid Density Functionals Applied to Solids. *J. Chem. Phys*. **2006**, *124*, 154709.

(108) F Aryasetiawany and O Gunnarsson. Rep. Prog. Phys. 61 (1998) 237–312

(109) J. Hubbard, Proc. R. Soc. London, Ser. A 276, 238 (1963).

(110) E. Fradkin, Field Theories of Condensed Matter Systems (Westview, 1998).

(111) Slater, J. C. *Phys. Rev.* **1930**, *36*, 57-64.

(112) Gill, P. M. W. *Adv. Quantum Chem.* **1994**, *25*, 141-205.

(113) Kresse, G.; Hafner, J. *J. Phys. Condens. Matter.* **1994**, *6*, 8245.

(114) Troullier N.; Martins, J. L. *Phys. Rev. B* **1993**, *43*, 1993.

(115) Vanderbilt, *D. Phys. Rev. B* **1990**, *41*, 7892.

(116) Louie, S. G.; Froyen, S.; Cohen, M. L. *Phys. Rev. B* **1982**, *26*, 1738.

(117) Kresse, G.; Joubert, D. *Phys. Rev. B* **1999**, *59*, 1758.

(118) Blöchl, P. E. *Phys. Rev. B* **1994**, *50*, 17 953.

(119) Singh, D. J. Plane Waves, Pseudopotentials and the LAPW Method; Kluwer Academic, Norwell, MA, **1994**.

(120) N. W. Ashcroft and N. D. Mermin, *Solid State Physics* (Thomson Learning, Inc., **1976**).

(121) C. Kittel, Introduction to Solid State Physics (New York: John Wiley & Sons, Inc., **1996**).

(122) Fox, M. Optical Properties of Solids; Oxford University Press: New York, **2002**.

(123) Tang, W.; Sanville, E.; Henkelman, G. *Condens. Matter* **2009**, *21*, 084204.

(124) Sanville, E.; Kenny, S. D.; Smith, R.; Henkelman, G. *J. Comput. Chem.* **2007**, *28*, 899−908.

(125) Henkelman, G.; Arnaldsson, A.; Jónsson, H. *Comput. Mater. Sci.* **2006**, *36*, 254−360.

(126) Kresse, G.; Joubert, D. *Phys. Rev. B* **1999**, *59*, 1758.

(127) Kato, H.; Kudo, A. *Chem. Phys. Lett*. **1998**, *295*, 487–492.

(128) Kato, H.; Kudo, *Catal. Lett.* **1999**, *58*, 153–155.

(129) Kato, H.; Kudo, A. *J. Phys. Chem. B*. **2001**, *105,* 4285-4292.

(130) Kato, H.; Asakura, K.; Kudo, A. *J. Am. Chem*. Soc. **2003**, *125*, 3082-3089.

(131) Bouafia, H.; Hiadsi, S.; Abidri, B.; Akriche, A.; Ghalouci, L.; Sahli, B. *Comp. Mat. Sci.* **2013**, *75*, 1-8.

(132) Zhou, X.; Shi, J.; Li, C. *J. Phys. Chem. C*. **2011**, *115*, 8305–8311.

(133) Li, Z.; Wang, Y.; Liu, J.; Chen, G.; Li, Y.; Zhou, C. *Int. J. Hydrogen Energy.* **2009**, *34*, 147–152.

(134) Kang, H. W.; Lim, S. N.; Park, S. B. *Int. J. Hydrogen Energy.* **2012**, *37*, 4026-4035.

(135) Kanhere, P. D.; Zheng, J.; Chen, Z. Site Specific Optical and Photocatalytic Properties of Bi-Doped NaTaO₃. *J. Phys. Chem. C*. **2011**, *115*, 11846–11853.

(136) Kanhere, P. D.; Zheng, J.; Chen, Z. *Int. J. Hydrogen Energy.* **2012**, *37*, 4889-4896.

(137) Su,Y.; Wang, S.; Meng, Y.; Han, H.; Wang, X. *RSC Adv*., **2012**, *2*, 12932–12939.

(138) Fu, H.; Zhang, S.; Zhang, L.; Zhu, Y. *Mater. Res. Bull.* **2008**, *43*, 864–872.

(139) Wang, X.; Liu, G.; Chen, Z.-G.; Li, F.; Lu, G. Q.; Cheng, H.-M. *Chem. Lett.* **2009**, *38*, 214-215.

(140) Liu, D.-R.; Wei, C.-D.; Xue, B.; Zhang, X.-G.; Jiang, Y.-S. *J. Hazard. Mater.* **2010**, *182*, 50–54.

(141) Zhao, Y.-X.; Liu, D.-R.; Li, F.-F.; Yang, D.-F.; Jiang, Y.-S. *Powder Technol.* **2011**, *214*, 155–160.

(142) Liu D.-R.; Jiang, Y.-S.; Gao, G.-M. *Chemosphere* **2011**, *83*, 1546–1552.

(143) Wang, B.; Kanhere, P. D.; Chen, Z.; Nisar, J.; Pathak, B.; Ahuja, R. *J. Phys. Chem. C* **2013**, *117*, 22518- 22524.

(144) Long, R.; English, N. J. *Appl. Phys. Lett*. **2009**, *94*, 132102-3.

(145) Dozzi, M. V.; Selli, E. *J. Photochem. Photobiol. C: Photochem. Rev*. **2013**, *14*, 13– 28.

(146) Irie, H.; Watanabe,Y.; Hashimoto, K. *J. Phys. Chem. B* **2003**, *107,* 5483-5486.

(147) Lin, Z.; Orlov, A.; Lambert, R. M.; Payne, M. C. *J. Phys. Chem. B* **2005**, *109,* 20948-20952.

(148) Batzill, M.; Morales, E. H.; Diebold, U. *Phys. Rev. Lett.* **2006**, *96*, 026103.

(149) Nakano, Y.; Morikawa, T.; Ohwaki, T.; Taga, Y. *Chem. Phys.* **2007**, *339*, 20–26.

(150) Chen, Y.; Cao, X.; Lin, B.; Gao, B. *Appl. Surf. Sci*. **2013**, *264*, 845– 852.

(151) Wei, W.; Dai, Y.; Guo, M.; Yu, L.; Jin, H.; Han, S.; Huang, B. *Phys. Chem. Chem. Phys*. **2010**, *12*, 7612–7619.

(152) Li, D.; Haneda, H.; Hishita, S.; Ohashi, N. *Chem. Mater.* **2005**, *17,* 2588-2595.

(153) Nishar, J.; Wang, B. C.; Pathak, B.; Kang, T.W.; Ahuja, R. *Appl. Phys. Lett*. **2011**, *99*, 051909-3.

(154) Nishar, J.; Pathak, B.; Ahuja, R. *Appl. Phys. Lett.* **2012**, *100*, 181903-5.

(155) Liu, P.; Nishar, J.; Ahuja, R.; Pathak, B. *J. Phys. Chem. C* **2013**, *117*, 5043-5050.

(156) He, Y.; Zhu, Y.; Wu, N. *J. Solid State Chem.* **2004**, *177*, 3868–3872.

(157) Lin, W.-H.; Cheng, C. Hu, C.-C. Teng, H. *Appl. Phys. Lett.* **2006**, *89*, 211904-3.

(158) Li, Z. H.; Chen, G.; Liu, J. W. *Solid State Commun.* **2007**, *143,* 295–299.

(159) Xiong, P.; Tan, G.; Zhang, W.; Xia, A.; Ren, H. *J. Clust. Sci.* **2013**, *24*, 515–522.

(160) ICSD 2013 Inorganic Crystallographic Structural Database, http://icsd.fiz-karlsruhe.de/icsd/; ICSD collection ID numbers are: NaTaO$_3$ (Pcmn) 980.

(161) Zhu, W.; Qiu, X.; Iancu, V.; Chen, X.-Q., Pan, H.; Wang, W.; Dimitrijevic, N. M., Rajh, T.; Meyer, H. M. III; Paranthaman, M. P.; Stocks, G. M., Weitering H. H.; Gu B.;Eres, G.; Zhang, Z. *Phys.Rev. Lett.* **2009**, 103, 226401.

(162) Tkach, A.; Almeida, A.; Agostinho Moreira, J.; Perez de la Cruz, J.; *Appl. Phys. Lett.* **2012,** *100,* 192909-4.

(163) McDonnell, K. A.; English, N. J.; Rahman, M.; Dowling, D. P. *Phys. Rev. B* **2012**, *86*, 115306.

(164) Chiodi, M.; Cheney, C. P.; Vilmercati, P.; Cavaliere, E.; Mannella, N.; Weitering, H. H.; Luca Gavioli, L. *J. Phys. Chem. C* **2012**, *116*, 311–318.

(165) Wrighton, M. S.; Ellis, A. B.; Wolczanski, P. T.; Morse, D. L.; Abrahamson, H. B.; Ginley, D. S. *J. Am. Chem. Soc.,* **1976**, *98*, 2774- 2779

(166) Cardona, M. *Phys. Rev*., **1965**, *140*, A 651.

(167) Xu, Y.; Schoonen, M. A. A. *Am. Mineral*., **2000**, *85*, 543.

(168) Wang, J.; Yin, S.; Komatsu, M.; Zhang, Q.; Saito, F.; Sato, T. *J. Mater. Chem*., **2003**, *13*, 2348-2352.

(169) Kang, H. W.; Park, S. B. *Chem. Eng. Sci*., **2013**, *100*, 384- 391.

(170) Li, N.; Yao, K. L. *AIP. Adv*., **2012**, *2*, 032135-10.

(171) Zhang, C.; Jia, Y.; Jing, Y.; Yao, Y.; Ma, J.; Sun, J. *Comput. Mater. Sci.*, **2013**, *79*, 69-74.

(172) Wang, J.; Yin, S.; Komatsu, M.; Zhang, Q.; Saito, F.; Sato, T. *J. Photochem. Photobiol. A: Chem.*, **2004**, *165*, 149-156.

(173) Mi, Y. Y.; Wang, S. J.; Chai, J. W.; Pan, J. S.; Huan, C. H. A.; Feng, Y. P.; Ong, C, K. *Appl. Phys. Lett.*, **2006**, *89*, 231922.

(174) Liu, P.; Nisar, J.; Pathak, B.; Ahuja, R. *Int. J. Hydrogen Energy*, **2012**, *37*, 11611-11617.

(175) Miyauchi, M.; Takashio M.; Tobimatsu, H. *Langmuir*, **2004**, *20*, 232-236.

(176) Wang, J.; Yin, S.; Komatsu, M.; Sato, T. *J. Eur. Ceram. Soc.*, **2005**, *25*, 3207-3212.

(177) Yu, H.; Yan, S.; Li, Z.; Yu, T.; Zou, Z. *Int. J. Hydrogen Energy*, **2012**, *37*, 12120-12127.

(178) Liu, J. W.; Chen, G.; Li, Z. H.; Zhang, Z. G. *J. Solid State Chem.*, **2006**, *179*, 3704-3708.

(179) Wang, D.; Ye, J.; Kako, T.; Kimura, T. *J. Phys. Chem. B*, **2006**, *110*, 15824-15830.

(180) Wei, W.; Dai, Y.; Jin, H.; Huang, B. *J. Phys. D: Appl. Phys.*, **2009**, *42*, 055401.

(181) Yu, H.; Ouyang, S.; Yan, S.; Li, Z.; Yu, T.; Zou, Z. *J. Mater. Chem.*, **2011**, *21*, 11347-11351.

(182) Reunchan, P.; Umezawa, N.; Ouyang, S.; Ye, J. *Phys. Chem. Chem. Phys.*, **2012**, *14*, 1876-1880.

(183) Shen, P.; Lofaro Jr., J. C.; Woerner, W. R.; White, M. G.; Su, D.; Orlov, A. *Chem. Eng. J.* **2013**, *223*, 200–208.

(184) Konta, R.; Ishii, T.; Kato, H.; Kudo, A. *J. Phys. Chem. B*, **2004**, *108*, 8992-8995.

(185) Bae, S. W.; Borse, P. H.; Lee, J. S. *Appl. Phys. Lett.*, **2008**, *92*, 104107.

(186) Iwashina, K.; Kudo, A. *J. Am. Chem. Soc*. **2011**, *133*, 13272–13275.

(187) Kawasaki, S.; Nakatsuji, K.; Yoshinobu, J.; Komori, F.; Takahashi, R.; Lippmaa, M.; Mase, K.; Kudo, A. *Appl. Phys. Lett.*, **2012**, *101*, 033910-4.

(188) Kawasaki, S.; Akagi, K.; Nakatsuji, K.; Yamamoto, S.; Matsuda, I.; Harada, Y.; Yoshinobu, J.; Komori, F.; Takahashi, R.; Lippmaa, M.; et al. *J. Phys. Chem. C,* **2012**, *116*, 24445−24448.

(189) Chen, H.-C.; Huang, C.-W.; Wu, J. C. S.; Lin, S.-T. *J. Phys. Chem. C*, **2012**, *116*, 7897-7903.

(190) Jia, Q.; Iwase, A.; Kudo, A. *Chem. Sci.*, **2014**, *5*, 1513–1519

(191) Kato, H.; Sasaki, Y.; Shirakura, N.; Kudo, A. *J. Mater. Chem. A*, **2013**, *1*, 12327–12333.

(192) Furuhashi, K.; Jia, Q.; Kudo, A.; Onishi, H. *J. Phys. Chem. C* **2013**, *117*, 19101−19106.

(193) Asai, R.; Nemoto, H.; Jia, Q.; Saito, K.; Iwase A.; Kudo, A. *Chem. Commun.*, **2014**, *50*, 2543–2546.

(194) Niishiro, R.; Tanaka, S.; Kudo, A. *Appl. Catal. B*, **2014**, *150–151*, 187–196.

(195) Bard, A. J.; Fox. M. A. *Acc. Chem. Res.*, **1995**, 141–145.

(196) Sayama, K.; Yoshida, R.; Kusama, H.; Okabe, K.; Abe, Y.; Arakawa, H. *Chem. Phys. Lett.* **1997**, *277*, 387-391.

(197) Zhou, P.; Yu, J.; Jaroniec, M. *Adv. Mater.* **2014**, *26*, 4920–4935.

(198) Tada, H.; Mitsui, T.; Kiyonaga, T.; Akita, T.; Tanaka, K. *Nat. Mater.* **2006**, *5*, 782-786.

(199) Sasaki, Y.; Nemoto, H.; Saito, K.; Kudo, A. *J. Phys. Chem. C* **2009**, *113*, 17536-17542.

(200) Ma, S. S. K.; Maeda, K.; Hisatomi, T.; Tabata, M.; Domen, K. *Chem. Eur. J.* **2013**, *19*, 7480-7486.

(201) Wang, Q.; Hisatomi, T.; Ma, S. S. K.; Li, Y.; Domen, K. *Chem. Mater.*, **2014**, *26*, 4144–4150.

(202) Li, F.; Yu, K.; Lou, Lan-Lan; Su, Z.; Liu, S. *Mater. Sci. Eng. B,* **2010**,*172*, 136–141.

(203) Kang, H. W.; Park, S. B.; *Int. J. Hydrogen Energy*, **2013**, *38*, 823-831.

(204) Zhao, Z.; Li, R.; Li, Z.; Zou, Z. *J. Phys. D: Appl. Phys.,* **2011**, *44,* 165401-5.

(205) Li, X. B.; Liu, Q.; Jiang, X. Y.; Huang, J. *Int. J. Electrochem. Sci.,* **2012**, *7,* 11519 – 11527.

(206) Pan, J. H.; Cai, Z.; Yu, Y.; Zhao, X. S. *J. Mater. Chem.* **2011**, *21*, 11430- 11438

(207) Kumar, N.; Maitra, U.; Hegde, V. I.; Waghmare, U. V.; Sundaresan, A.; Rao, C. N. R. *Inorg. Chem.* **2013**, *52*, 10512-10519.

(208) Xiao, G.; Nuansaeng, S.; Zhang, L.; Suthirakun, S.; Heyden, A.; Loye, H.-C. zur; Chen, F. *Mater. Chem. A* **2013**, *1*, 10546-10552.

(209) Qiu, X.; Miyauchi, M.; Yu, H.; Irie, H.; Hashimoto, K. *J. Am. Chem. Soc.* **2010**, *132*, 15259–15267.

(210) Kang, H. W.; Park, S. B.; Park, A.-H. A. *Int. J. Hydrogen Energy* **2013**, *38*, 9198– 9205.

(211) Hagiwara, H. Kumagae, K. Ishihara, T. *Chem. Lett.* **2010**, *39*, 498499.

(212) Paulauskas, I. E. Katz, J. E. Jellison, G. E. Jr., Lewis, N. S. Boatner, L. A. Brown, G. M. *J. Electrochem. Soc.,* 2009, **156**, B580-B587.

(213) Liu, X. Lv, J. Wang, S. Li, X. Lang, J. Su, Y. Chai, Z. Wang. X. *J. Alloy and Compd.* 2015, **622**, 894–901.

(214) Bajorowicz, B. Cybula, A. Winiarski, M. J. Klimczuk, T. Zaleska, A. *Molecules* **2014**, *19*, 15339-15360.

(215) Hagiwara, H. Ono, N. Inoue, T. Matsumoto, H. Ishihara, T. *Angew. Chem. Int. Ed.* **2006**, *45*, 1420 –1422.

(216) Hagiwara, H. Inoue, T. Kaneko, K. Ishihara, T. *Chem. Eur. J.* 2009, **15**, 12862 – 12870.

(217) Wang, F. Grinberg, I. Rappe, A. M.. *Appl. Phys. Lett.* **2014**, *104*, 152903-1-152903-4.

(218) Zlotnik, S. Sahu, S. K. Navrotsky, A. Vilarinho, P. M. *Chem. Eur. J.*, **2015**, *21*, 5231 – 5237.

(219) Benrekia, A. R. Benkhettou, N. Nassour, A. Driz, M. Sahnoun, M. Lebègue, S. *Physica B*, **2012**, *407*, 2632–2636.

(220) Krasovskii, E. E. Krasovska, O. V. Schattke, W. *J. Electron Spectrosc.*, **1997**, *83*, 121–127.

(221) Sinha, T. P. Dutta, A. Saha, S. Tarafder, K. Sanyal, B. Eriksson, O. Mookerjee, A. *Physica B*, **2012**, *407*, 4615–4621.

(222) Choi, M. Oba, F. *Phys. Rev.* B, **2011**, *83*, 214107-1-214107-6.

(223) Bouafia, H. Hiadsi, S. Abidri, B. Akriche, A. Ghalouci, L. Sahli, B. *Comp. Mater. Sci.* **2013**, *75*, 1–8.

(224) Neumann, T. Borstel, G. Scharfschwerdt, C. Neumann, M. *Phys. Rev.* B, **1992**, *46*, 10623-10628.

(225) Cabuk, S. Akkus, H. Mamedov, A. M. Electronic *Physica B*, 2007, **394**, 81–85.

(226) Zhao, N. Wang, Y.-H. Wang, Q.-X. Hu, W.-J. *J. Solid State Chem.*, **2012**, *194*, 37–42.

(227) Zhang, T. Zhao, K. Yu, J. Jin, J. Qi, Y. Li, H. Hou, X. Liu, G. *Nanoscale* **2013**, *5*, 8375–8383.

(228) Yan, L. Zhang, J. Zhou, X. Wu, X. Lan, J. Wang, Y. Liu, G. Yu, J. Zhi. L. *Int. J. Hydrogen Energy* **2013**, *38*, 3554-3561.

(229) Ding, Q.-P. Yuan, Y.-P. Xiong, X. Li, R.-P. Huang, H.-B. Li, Z.-S. Yu, T. Zou, Z.-G. Yang, S.-G. *J. Phys. Chem. C* **2008**, *112,* 18846–18848.

(230) Zhang, T. Lei, W. Liu, P. Rodriguez, José A. Yu, J. Qi, Y. Liu, G. Liu, M. *Chem. Sci.* **2015**, *6*, 4118–4123.

(231) Jiang, L. Qiu, Y. Yi, Z. *J. Mater. Chem. A* **2013**, *1*, 2878–2885.

(232) Lan, J. Zhou, X. Liu, G. Yu, J. Zhang, J. Zhi, L. Nie, G. *Nanoscale* **2011**, *3*, 5161–5167.

(233) Yan, L. Zhang, T. Lei, W. Xu, Q. Zhou, X. Xu, P. Wang, Y. Liu, G. Today **2014**, *224*, 140–146.

(234) Wang, Z. Gu, H. Hu, Y. Yang, K. Hu, M. Zhou, D. Guan, J. *CrystEngComm*, **2010**, *12*, 3157–3162.

(235) Khorrami, Gh. H. Kompany, A. Khorsand Zak, A. *Modern Phys. Lett. B* **2014**, *28*, 1450224-1-1450224-10.

(236) Zhang, Jun-ji. Zhou, H. Chen, Ji-shi. Tang, T. Hao, Yuan-zheng. *Adv. Mater. Res.* **2014**, *873,* 783-786.

(237) Balakrishnaiah, R. Kim, D. W. Yi, S. S. Kim, K. D. Kim, S. H. Jang, K. Lee, H. S. Jeong, J. H. *ECS Trans.* **2009**, *16*, 23-31.

(238) Guo, Y. Li, Y. Li, S. Zhang, L. Li, Y. Wang. J. *Energy* **2015**, *82*, 72-79.

(239) Wang, J. Wang, X. Cui, Z. Liu, B. Cao, M. *Phys. Chem. Chem. Phys.,* **2015**, *17*, 14185—14192.

(240) Wang, R. Zhu, Y. Qiu, Y. Leung, Chi-Fai. He, J. Liu, G. Lau Tai-Chu. *Chem. Eng. J.* 2013, 226, 123–130.

(241) Wang, X.; Maeda, K.; Thomas, A.; Takanabe, K.; Xin, G.; Carlsson, J. M.; Domen, K.; *Nat. Mater.* 2008, 8, 76-80.

(242) Pan, H.; Zhang, Y. W.; Shenoy, V. B.; Gao, H. *ACS Catal.* **2011**, *1*, 99–104.

(243) Martin, D. J.; Qiu, K.; Shevlin, S. A.; Handoko, A. D.; Chen, X.; Guo, Z.; Tang, J. *Angew.Chem.Int.Ed.* **2014** , *53*, 9240–9245.

(244) Liu, J.; Liu, Y.; Liu, N.; Han, Y.; Zhang, X.; Huang, H.; Lifshitz, Y.; Lee, S-T.; Zhong, J.; Kang, Z. *Science* **2015**, *347*, 970.

(245) Wang, A.; Zhang, X.; Zhao, M. *Nanoscale*, **2014**, *6*, 11157–11162.

(246) Samanta, S.; Martha, S.; Parida, K. *ChemCatChem* **2014**, *6*, 1453–1462.

(247) Kubas, G. J. *J. Organomet. Chem.* **2001**, *635,* 37−68.

(248) Philips, A. B.; Shivaram, B. S. *Phys. Rev. Lett.* **2008**, *100*, 105505.

(249) Hu, X.; Skadtchenko, B. O.; Trudeau, M.; Antonelli, D. M. *J. Am. Chem. Soc.* **2006**, *128*, 11740−11741

(250) Q. Sun, Q. Wang, P. Jena, Y. Kawazoe, *J. Am. Chem. Soc.* **2005**, *127,* 14582.

(251) Ataca C, Akturk E, Ciraci S, Ustunel H. *Appl Phys Lett* **2008**;*93,* 043123.

(252) Wang Y.S, Ji Y, Li M, Yuan PF, Sun Q, Jia Y.*J Appl Phys* **2011**;*110*, 094311.

(253) Wang YS, Li M, Wang F, Sun Q, Jia Y. *Phys Lett A* **2012,** *376,*631.

(254) Bhattacharya A, Bhattacharya S, Majumder C, Das GP. *J Phys Chem C* **2010**, *114,* 10297.

(255) Liu CS, Zeng Z. *Appl Phys Lett* **2010**, *96*, 123101.

(256) Lee, D. H.; Lee, W. J.; Lee, W. J.; Kim, S. O.; Kim, Y.-H. *Phys. Rev. Lett.* **2011**, 106, 175502.

(257) El-Barbary A, Telling R, Ewels C, Heggie M, Briddon P. *Phys Rev B* **2003**;*68*:144107.

(258) Kroke, E.; Schwarz, M.; Horath-Bordon, E.; Kroll, P.; Noll, B.; Norman, A. D. *New J. Chem.* **2002**, *26*, 508−512.

(259) Lee, J. S.; Wang, X. Q.; Luo, H. M.; Dai, S. *Adv. Mater.* **2010**, *22,* 1004−1007.

(260) Du, A.; Sanvito, S.; Smith, S. C. *Phys. Rev. Lett.* **2012**, *108*, 197207.

(261) Greeley, J.; Greeley, J.; Stephens, I. E. L.; Bondarenko, A. S.; Johansson, T. P.; Hansen, H. A.; Jaramillo, T. F.; Rossmeisl, J.; Chorkendorff, I.; Nørskov, J. K. *Nat. Chem.* 2009, 1, 552−556.

(262) Yang, H. *Angew. Chem., Int. Ed.* **2011**, *50*, 2674−2676.

(263) Sha, Y.; Yu, T. H.; Merinov, B. V.; Shirvanian, P.; Goddard, W. A. *J. Phys. Chem. C* **2012**, *116,* 21334−21342.

(264) Suntivich, J.; Gasteiger, H. A.; Yabuuchi, N.; Nakanishi, H.; Goodenough, J. B.; Shao-Horn, Y. *Nat. Chem.* **2011**, *3*, 546−550.

(265) Ham, D. J.; Lee, J. S. *Energies* **2009**, *2*, 873−899.

(266) Zhong, H.; Zhang, H.; Liu, G.; Liang, Y.; Hu, J.; Yi, B. *Electrochem. Commun.* **2006**, *8*, 707−712.

(267) Kim, J. H.; Ishihara, A.; Mitsushima, S.; Kamiya, N.; Ota, K. I. *Electrochim. Acta* **2007**, *52*, 2492−2497.

(268) Wang, S.; Yu, D.; Dai, L. *J. Am. Chem. Soc.* **2011**, *133*, 5182−5185.

(269) Yu, D.; Nagelli, E.; Du, F.; Dai, L. *J. Phys. Chem. Lett.* **2010**, *1*, 2165−2173.

(270) Viswanathan, V.; Hansen, H. A.; Rossmeisl, J.; Nørskov, J. K. *J. Phys. Chem. Lett.* **2012**, *3*, 2948−2951.

(271) Viñes, F.; Sousa, C.; Illas, F.; Liu, P.; Rodriguez, J. A. *J. Phys. Chem. C* **2007**, *111*, 16982−16989.

(272) Yang, S.; Feng, X.; Wang, X.; Müllen, K. *Angew. Chem., Int. Ed.* **2011**, *50*, 5339−5343.

(273) Zheng, Y.; Jiao, Y.; Jaroniec, M.; Jin, Y.; Qiao, S. Z. *Small* **2012**, *8*, 3550−3566.

(274) Yu, D.; Xue, Y.; Dai, L. *J. Phys. Chem. Lett.* **2012**, *3*, 2863−2870.

(275) Wang, S.; Zhang, L.; Xia, Z.; Roy, A.; Chang, D. W.; Baek, J. B.; Dai, L. *Angew. Chem., Int. Ed.* 2012, 51, 4209−4212.

(276) Alder, S. B. *Chem. Rev.* **2004**, *104*, 4791−4843.

(278) Greeley, J.; Nørskov, J. K. *J. Phys. Chem. C* **2009**, *113*, 4932−4939.

(279) Choi, C. H.; Park, S. H.; Woo, S. I. *ACS Nano* **2012**, *6*, 7084−7091.

(280) Choi, C. H.; Park, S. H.; Woo, S. I. *J. Mater. Chem.* **2012**, *22*, 12107−12115.

(281) Tang, Y.; Allen, B. L.; Kauffman, D. R.; Star, A. *J. Am. Chem. Soc.* **2009**, *131*, 13200−13201.

(282) Zhang, L.; Niu, J.; Dai, L.; Xia, Z. *Langmuir* **2012**, *28*, 7542−7550.

(283) Kaukonen, M.; Kujala, R.; Kauppinen, E. *J. Phys. Chem. C* **2012**, *116*, 632−636.

(284) Yang, Z.; Yao, Z.; Fang, G.; Nie, H.; Liu, Z.; Zhou, X.; Chen, X.; Huang, S. *ACS Nano* **2012**, *6*, 205−211.

(285) Byon, H. R.; Suntivich, J.; Shao-Horn, Y. *Chem. Mater.* **2011**, *23*, 3421−3428.

(286) Kong, X.; Chen, Q.; Sun, Z. *ChemPhysChem* **2013**, *14*, 514−519.

(287) Lyth, S. M.; Nabae, Y.; Moriya, S.; Kuroki, S.; Kakimoto, M.; Ozaki, J.; Miyata, S. *J. Phys. Chem. C* **2009**, *113*, 20148−20151.

(288) Choi, H. K.; Chung, M. W.; Kwon, H. C.; Park, H. C.; Woo, S. I. *J. Mater. Chem. A* **2013**, *1*, 3694−3699.

(290) Silva, R.; Voiry, D.; Chhowalla, M.; Asefa, T. *J. Am. Chem. Soc.* **2013**, *135*, 7823−7826.

(291) Zheng, Y.; Jiao, Y.; Chen, J.; Liu, J.; Liang, J.; Du, A.; Zhang, W.; Zhu, Z.; Smith, S. C.; Jaroniec, M.; Lu, G. Q.; Quia, S. Z. *J. Am. Chem. Soc.* **2011**, *133*, 20116−20119.

(292) Cao, C.; Huang, F.; Cao, C.; Li, J.; Zhu, H. *Chem. Mater.* **2004**, *16*, 5213−5215.

(293) Nørskov, J. K.; Rossmeisl, J.; Logadottir, A.; Lindqvist, L.; Kitchin, J. R.; Bligaard, T.; Jónsson, H. *J. Phys. Chem. B* **2004**, *108*, 17886−17892.

(294) Computational Chemistry Comparison and Benchmark Database. http://cccbdb.nist.gov/.